Alexander Pohl

Simulation of Diffraction Based on the Uncertainty Relation

An Efficient Simulation Method Combining Higher Order Diffractions and Reflections

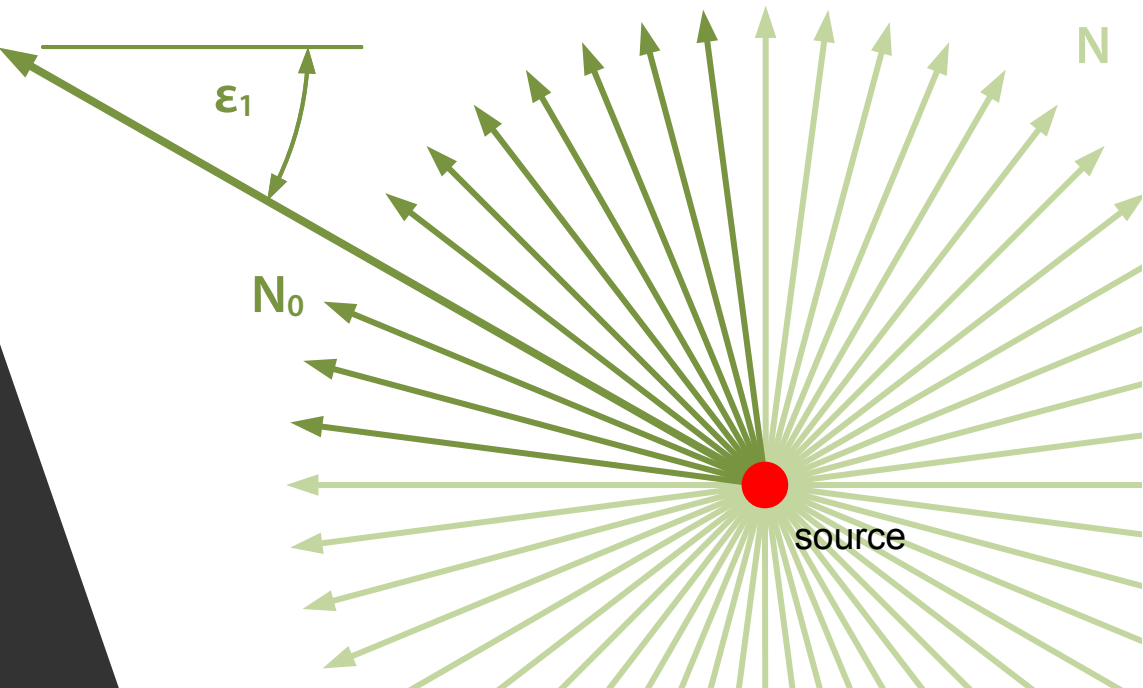

Simulation of Diffraction Based on the Uncertainty Relation – An Efficient Simulation Method Combining Higher Order Diffractions and Reflections

Vorgelegt im Promotionsausschuss der HafenCity Universität Hamburg

zur Erlangung des akademischen Grades

Doktor-Ingenieur (Dr.-Ing.)

Dissertation

von
Alexander Alfred Pohl
aus Prüm

2013

1. Gutachter: Prof. Dr. rer. nat. Uwe Martin Stephenson
2. Gutachter: Prof. Ulf Peter Svensson

Tag der mündlichen Prüfung: 05.07.2013

Impressum:

Copyright: © 2014 Alexander Pohl

Verlag: epubli GmbH
Prinzessinnenstraße 20
10969 Berlin
www.epubli.de

zugl.: Hamburg, Univ., Diss., 2014
Online veröffentlicht auf OPuS, dem Volltextserver der HafenCity Universität Hamburg

ISBN 978-3-8442-9257-2

Contents

Acronyms

BT Beam Tracing
BTM Biot-Tolstoy-Medwin
CT Computation Time
DAPDF Diffraction Angle Probability Density Function
DAPF Diffraction Angle Probability Function
distanceID Distance Identification Number
EDB Edge Diffraction ToolBox
EDS Edge Diffraction Strength
GA Geometrical Acoustic
IE Inner Edge
IV Inner Vertex
MDL Maekawa Detour Law
MFPL Mean Free Path Length
patchID Patch Identification Number
QPBT Quantized Pyramidal Beam Tracing
RUM Reunification Matrix
SPSM Sound Particle Simulation Method
SPR Sound Particle Radiosity
SSM Secondary Source Model
timeID Time Identification Number
UBD Uncertainty relation Based Diffraction
UTD Uniform Theory of Diffraction
VW Virtual Wall

1. Introduction

1.1. Motivation

Today, the exposure of people to noise is one of the most serious problems[BLs95] since it affects the human mental health to a rising extend. In Germany, 54% of the people are disturbed and annoyed by traffic noise, 34% by railway noise and 23% by aircraft noise[RJBJ13]. Here, the Bundesimmissionsschutzgesetz [BIm02] was introduced to protect humans and animals from harmful environmental effects. Since 2002, the environmental noise directive[END02] calls for the monitoring of noise and the creation of action plans in Europe. For the creation of such noise maps, the very simplified sound propagation models, e.g., [ISO96, VDI88, VDI97, DIN02, DIN06, dVV05, RLS90, Sch03] are currently applied. These are implemented in different commercial software products, such as *CadnaA*[CADa], *IMMI*[IMM],*Predictor-LimA*[LIM] and *SoundPLAN*[Sou]. However, these applied estimation methods have to be improved to prevent exceeds of law restrictions. On the contrary, more accurate simulation methods can even reduce costs in the planning stage.

On the other hand, more advanced sound propagation models exist in the field of room acoustics. These models can be separated into wave theoretical approaches and methods of Geometrical Acoustic (GA). The first group handles sound as waves, whereas the second group assumes sound to propagate as energy particles according to the wave-particle duality[Gre01]. Due to their complexity, the wave theoretical simulation methods can only be applied to small frequencies and/or small volumes. GA simulations, such as the Sound Particle Simulation Method (SPSM) or Beam Tracing (BT), propagate sound along straight lines starting at the sound sources to the receivers. The methods of GAs are applicable to larger volumes, such as a large concert hall, or even whole cities. Different programs are known that make use of the GA simulation methods, e.g., *CATT*[CAT], *ODEON*[ODE], *EASE*[EAS], *CadnaR*[CADb] and *RAVEN*[RAV]. Due to the huge range of relevance, GA simulation methods can be applied to both room acoustics and urban noise prognosis.

Traditionally, the GA simulation methods handle only specular reflections and, hence, wave effects like scattering of sound at rough surfaces or diffraction around corners have to be modeled explicitly. While the introduction of scattering is investigated quite well[CDD+06], the development of a general diffraction model is still focus of current research. Especially the problem of higher order diffractions and their combinations with arbitrary reflections is still unsolved. In urban environments, however, sound propagation paths caused by higher order diffraction are most dominant – often times even the only possible propagation paths between a sound source and a receiver. This is further illustrated in Fig. 1.1).

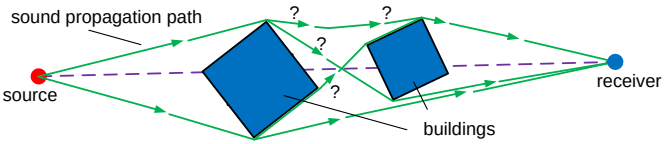

Figure 1.1.: Sound propagation paths between a sound source and a receiver around two obstacles might be possible only by higher order diffraction (after Stephenson[Ste04]).

Here, another major problem is to identify the most relevant sound propagation paths, because it is not clear which sound propagation paths (denoted by question marks in Fig. 1.1) yield relevant contributions to the sound field. In order to find these sound propagation paths, the *straightforward* approach of GA simulations methods can be used directly instead of taking all tedious combinations into account. Due to the straightforward detection technique of SPSM and BT, a diffraction module based on the uncertainty relation[Ste04] seems to be a promising solution to handle diffraction, since it can be combined with these methods. Unfortunately, the Uncertainty relation Based Diffraction (UBD) causes a recursive split-up of particles and, thus, a massive exponential increase of the Computation Time (CT). A reunification of these particles is therefore inevitable. The GA simulation methods Sound Particle Radiosity (SPR)[Ste01, Ste03b] and Quantized Pyramidal Beam Tracing (QPBT)[Ste96, Ste04] have been first proposed by Stephenson and allow this reunification. In addition to his thesis, an unpublished and extended version handles the methods in more detail[Ste03a]. In order to find the most efficient and most accurate method, both methods are implemented for the first time, such that analytical, statistical and numerical comparison can be carried out.

Taking all these considerations into account, the two main goals of this thesis are:

Efficient algorithm with reunification: A GA simulation method has to be formulated that is capable of handling higher order diffraction in combination with reflections. Since the derivation of such a new simulation method goes along with detailed statistical and numerical analysis, the main part of this work is restricted to $2D$ to reduce the geometrical complexity. However, it is also shown that the algorithms can be extended to $3D$.

Extended UBD diffraction model: Highly interconnected with the derivation of an efficient algorithm is the investigation of the UBD module. The theory was already defined by Stephenson[Ste10a], but many general questions remain, which have not been answered yet. Thus, no validation of the diffraction module in combination with reflections is available up to now. The biggest problem, however, is the extension to $3D$.

1.2. Restrictions and Assumptions

Although the boundary conditions of room acoustics and urban noise immission prognosis are very different, the theory of sound diffraction remains the same.

However, both fields of application have quite different aims: while in noise immission prognosis, the spatial distribution of sound is of primary interest, the temporal distribution of sound is more important in room acoustics in order to compute different room acoustical parameters[Got73] (e.g., the reverberation time[Kut09]). In both cases, the sound field is composed by a huge number of contributions (reflections, diffractions)

at each location, where phase differences are often not correlated. Thus, an incoherent addition of these contributions is mostly sufficient. Consequently, this work focuses only on **energetic** simulation results. This is supported by the fact that exact impedances (including phase) of surfaces are often unknown.

Another demanding aspect is the determination of boundary conditions of the GA simulation methods. Geometrical scenes created by architects usually include too many acoustically irrelevant objects. In addition, they do not necessarily form a totally closed polyhedron, which is – in general – an important requirement for many GA simulation methods[SLSC08]. However, the geometrical scenes in this work are always assumed to be defined by a closed polyhedron that is composed by polygons and edges (where diffraction occurs). Furthermore, the quantitative description of the acoustical material properties of those surfaces (especially the scattering coefficient) is standardized, but still a huge source of uncertainty. Both effects are excluded in this work and all material input parameters are assumed to be given correctly.

As the Uncertainty relation Based Diffraction (UBD) used in this work can be seen as a combination of the Kirchhoff approximation[Pie89] and Heisenberg's uncertainty relation[Hei27], it is assumed that sound propagation is only affected by diffraction in forward direction. Kirchhoff's assumption is based on the idea that the incident sound field is not disturbed in front of the wedge[Pie89]. Mostly, the diffraction effect is less important in this region due to the occurrence of direct sound and specular reflections. However, near edges of a building on the source-side, diffraction might play an important role, which is not considered in this thesis.

Evaluations of the reunification algorithms are compared to exact GA methods and in case of the UBD an analytic wave theoretical solution is chosen as reference. This procedure is preferred over the comparison with real world measurements in order to discuss the influences of the applied approximations in a better way.

In summary, the assumptions made in this work are:

1. geometric: the room dimensions are large compared to the wavelength
2. energetic: the results are restricted to intensity echograms and intensity maps
3. polyhedron: a watertight, reduced polyhedron is assumed
4. diffraction behind the wedge: the effect of diffraction is restricted to the receiver-side of the wedge
5. evaluation: comparison to other simulation methods instead of measurements

1.3. Organization of the Work

This work is divided into three parts. In the first part of this thesis, the physical background of sound propagation and energetic sound simulation is briefly presented. The second part discusses the two major goals of this thesis, namely the investigation of the UBD and the construction of an efficient algorithm including reunification. As diffraction is mainly a two dimensional effect, this part is restricted to two dimensional cases. This approach is justified, because also the investigation of an efficient reunification technique is mainly a principle study, such that it is adequate to reduce the complexity of the geometrical operations to $2D$. The respective results and conclusions are then applied to $3D$ in the third part of the thesis. In addition, the respective extensions of the simulation models to $3D$ are further discussed.

Part 1:

Chapter 2: The physical fundamentals of sound are briefly recapitulated, including a wave theoretical description of diffraction.

Chapter 3: GA simulation methods are briefly introduced by presenting their underlying physical models as well as made approximations and restrictions.

Chapter 4: Different spatial sub-division techniques are discussed and a new technique is defined that aims at the introduction of diffraction. The speed-up of the new sub-division technique is derived statistically and verified by numerical experiments.

Part 2:

Chapter 5: The UBD formulation presented by Stephenson is analyzed. It is shown that some assumptions in his previous work are not well founded and alternative formulations are presented. The formulation is extended – and validated – to second order diffraction analytically. Additionally, the combination of diffraction with reflections is validated for the first time.

Chapter 6: By introducing the UBD to GA, particles have to be split-up to achieve a reasonable resolution in space. The exponential growth of the CT by this split-up can only be compensated by a reunification of these particles. The reunification technique QPBT, as proposed by Stephenson[Ste04], is analyzed in detail and different assumptions are proven to be misleading. In contrast, the SPR, which Stephenson argued had serious weaknesses[Ste01][Ste03b], is proven to be both more efficient and more accurate. Therefore, the author concretises and implements both methods, such that an analytical and statistical comparison between both methods can be performed. The numerical errors of the SPR as well as the computational effort are derived in detail and the influence of these numerical errors on the diffraction simulation is evaluated.

Part 3:

Chapter 7: As all former chapters are restricted to $2D$, the results of the former chapters have to be extended to $3D$. Initially, the convex sub-division is discussed for the $3D$ case. In a subsequent step, the most efficient algorithm, namely the SPR, is also extended to the $3D$ case. Fortunately, the complete reunification core algorithm is completely identical to the $2D$ approach, such that only the commonly known geometrical procedures of the SPSM have to be modified. It is shown that the analytical and statistical investigations of the $2D$ case are still valid. The important part of this chapter presents new extensions of the UBD formulation to $3D$ for the first time. Different considerations are presented and the most promising concept is discussed in more detail. Although a complete implementation of the $3D$ method is still missing, first results of analytical evaluations are presented.

The work is concluded by a summary and an outlook discussing the remaining problems. In contrast to other publications, the main chapters 4 - 7 are introduced by separate sections of related work and concluded by separate summaries, too.

2. Physical Fundamentals of Sound

Sound can be interpreted as a wave propagating through a physical medium. In this chapter, the very basics of sound, sound emission and sound propagation are briefly discussed. Sound emission is described by the example of two typical sound sources, i.e., the point source and the line source. Sound propagation of the emitted sound waves is exemplary shown by plane waves. Relevant wave phenomena such as air attenuation, absorption, scattering and diffraction are further discussed. The influence of the propagating waves is investigated with respect to receivers. Often, an energetic approach is sufficient (e.g., for the description of sound sources), but also wave-based derivations are necessary in special cases (e.g., for diffraction). In this work, mainly energetic approaches are considered and an excursion to wave theory is made only if absolutely inevitable. More detailed derivations are given in the literature, e.g., [Kut09, Vor08, Mös08, Pie89].

2.1. Basic Acoustic Equations

The fundamental equation in acoustics is the wave equation. It is a differential equation derived from the law of inertia and the law of mass conservation in fluid media. The overall sound pressure is the sum of the static sound pressure and the dynamic sound pressure p. As only the latter is caused by the sound wave, the wave equation reads

$$\Delta p = \frac{1}{c^2} \cdot \frac{\partial^2 p}{\partial t^2}, \tag{2.1}$$

where Δp represents the three dimensional Laplace operator (in Cartesian coordinates).

$$\Delta p = \frac{\partial^2 p}{\partial x^2} + \frac{\partial^2 p}{\partial y^2} + \frac{\partial^2 p}{\partial z^2}. \tag{2.2}$$

The speed of sound c is given by the ratio of the bulk modulus K and the bulk density ρ. It is rather constant [BoA96], despite a little dependency on the temperature $\vartheta_T[^\circ C]$

$$c = 331.4\sqrt{1 + \frac{\vartheta_T}{273^\circ C}}\frac{m}{s}. \tag{2.3}$$

The sound pressure p appears in a large range of about six decades in-between the threshold of hearing and the theoretical maximum (in air). Therefore, a logarithmical scale is used. The sound pressure level L_p in relation to the standardized reference sound pressure p_0 is defined as

$$L_p = 10\log_{10}\left(\left(\frac{p}{p_0}\right)^2\right) dB = 20\log_{10}\left(\frac{p}{p_0}\right) dB, \text{ with } p_0 = 20\mu Pa. \tag{2.4}$$

In general, all *levels* are given in dB. The reference sound pressure p_0 is equal to $20\mu Pa$, which relates to the hearing threshold of humans, i.e., a sound pressure level of $0dB$. Besides the wave-based formulation using the sound pressure p, the sound intensity $\vec{I} = p \cdot \vec{v}$ is defined as the energetic counterpart. In case of a plane wave or random incidence, an energetic formulation is usually preferred, where the sound intensity is a

scalar. This definition is used in this work. With the free-field impedance Z_0 and the sound energy density w this intensity reads

$$I = \frac{p^2}{Z_0} = c \cdot w. \tag{2.5}$$

As this occurs even in a range of twelve decades, the sound intensity I is transformed to the respective sound intensity level L_I in relation to the standardized reference sound intensity I_0

$$L_I = 10 \log_{10} \left(\frac{I}{I_0} \right) dB, \text{ with } I_0 = 10^{-12} \frac{W}{m^2}. \tag{2.6}$$

In case of a plane wave, the sound pressure level is approximately equal to the sound intensity level

$$L_p \approx L_I. \tag{2.7}$$

2.2. Sources

A sound field can be excited by different kinds of sound sources. In this work, sound sources are generalized to two main types of sound sources. First, point sources are a generalization for different types of spatially restricted sources, whose size is small compared to the other occurring dimensions, e.g., voice, pneumatic hammers, car horns etc. Second, line sources are a generalization of spatial extended sources in one direction, e.g., streets or rail tracks.

2.2.1. Point Sources

In room acoustics, point sources, e.g., musicians, generally spread sound depending on the direction[Mey09]. However, many sound sources can be reduced to point sources without direction dependency. With this assumption, the sound power P of a sound source can be determined by an imaginary sphere around the sound source with the radius r. The sound intensity I is constant over the surface of this sphere ($4\pi r^2$) then (see Fig. 2.1).

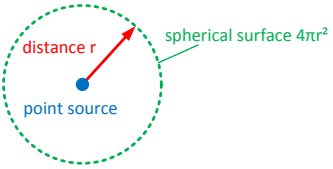

Figure 2.1.: The sound intensity I is constant on a sphere around a point source (after Möser [Mös08]).

Hence, the total sound power is described by the sound intensity over the whole surface

$$I = \frac{P}{4\pi r^2}. \tag{2.8}$$

For this sound power P an equivalent source power level L_W is defined with the standardized reference sound power P_0

$$L_W = 10 \log_{10} \left(\frac{P}{P_0} \right) dB, \text{ with } P_0 = 10^{-12} W. \tag{2.9}$$

Inserting Eqn. 2.8 in Eqn. 2.9 results in (with Eqn. 2.6) the free field sound intensity level for a point source

$$L_I \approx L_W - 20 \log_{10} \left(\frac{r}{m} \right) - 11 dB. \tag{2.10}$$

2.2.2. Line Sources

A line source can be seen as the concatenation of an infinite number of point sources on a thought line. These sources can either be uncorrelated (incoherent), as applied in traffic noise prognosis, or correlated (coherent). This work is restricted to the correlated version, which is needed to create a $2D$ cross-section of a $3D$ scene. Correlated means that the sources forming the line are in phase (i.e., a *pumping line*). These coherent sound sources radially emit their sound intensity outwards, such that I is constant on the lateral surface of a cylinder ($2\pi rh$), where h is the length of that cylinder (see Fig. 2.2).

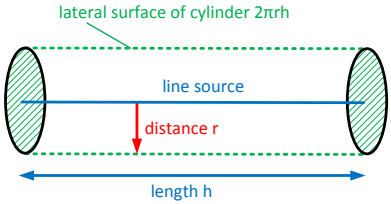

Figure 2.2.: The sound intensity I is constant on a cylinder around a line source (after Möser [Mös08]).

Hence, the total sound power is described by the sound intensity over the whole surface

$$I = \frac{P}{2\pi rh}. \tag{2.11}$$

For infinite line sources ($h \gg r$), it is more descriptive to define a sound power per length P'

$$I = \frac{P'}{2\pi r}. \tag{2.12}$$

Finally, also for infinite line sources, an equivalent source power level L'_W is defined with the standardized reference sound power per meter P'_0

$$L'_W \approx 10 \log_{10} \left(\frac{P'}{P'_0} \right) dB, \text{ with } P'_0 = 10^{-12} \frac{W}{m}, \tag{2.13}$$

which results in

$$L_I = L'_W - 10 \log_{10} \left(\frac{r}{m} \right) - 8 dB. \tag{2.14}$$

Doubling the distance decreases the sound intensity level by $3dB$, in contrast to the point sources with $6dB$ per distance doubling.

2.3. Sound Propagation

The basic sound propagation is described by the wave equation in free field. In this section, first the influence of air attenuation is presented. Furthermore, the boundary conditions of both smooth and rough surfaces are described and their influence on plane waves is briefly described.

In the main part of this section, diffraction of sound *around* objects is physically discussed in more detail, since diffraction modelling is the major focus of this thesis.

2.3.1. Air Attenuation

For sound propagation over large distances, which is especially important for city acoustics, the air attenuation of sound has to be considered. The attenuation is caused by heat conduction, viscosity and thermal relaxation. Therefore, the sound intensity has to be extended by the energetic attenuation coefficient m[BSZ+95, Kut07]

$$I(r) \propto e^{-mr}. \tag{2.15}$$

The energetic coefficient m, however, is frequency-, temperature- and humidity-dependent as shown in Fig. 2.3 [BSZ+95]

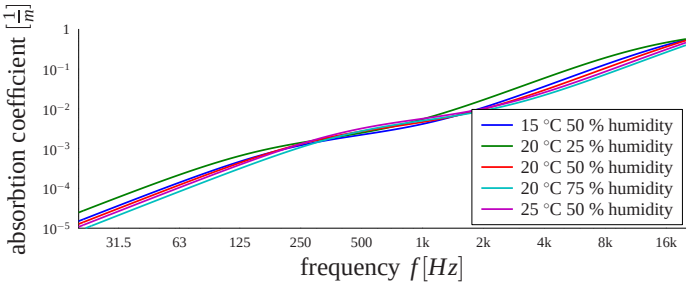

Figure 2.3.: Typical attenuation curves for different temperatures and humidities (after Kuttruff [Kut07]).

2.3.2. Geometrical Sound Reflection and Absorption of Plane Waves

A sound wave in the far field of its source (excitation) can be interpreted as a plane wave for a very small angle range. If such a plane wave intersects with a smooth surface, the wave is geometrically reflected according to *Snell*'s law. This is called *specular* reflection analogues to optics.

For an angle of incidence ϑ between the incident sound wave and the surface normal (here: $-x-direction$), the complex incident sound pressure $\underline{p}_i$ is described in Cartesian coordinates (see Fig. 2.4)

$$\underline{p}_i = \hat{p} e^{j\left(\omega t - k_x cos(\vartheta) - k_y sin(\vartheta)\right)}. \tag{2.16}$$

While the orthogonal component of the incident sound wave velocity $(v_i)_x$ changes the direction, the parallel component $(v_i)_y$ remains unchanged (see Fig. 2.4).

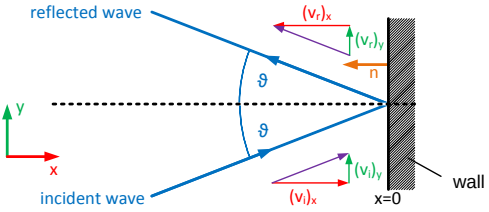

Figure 2.4.: Incident and reflected wave on a smooth surface (after Vorländer [Vor08]).

A common assumption for the boundary condition of a wall is that it is locally reacting[Kut07]. This means that the sound field is only affected by the sound pressure in front of the wall element, but not by the sound pressure at neighbouring wall elements. In other words, no propagation of vibration is allowed parallel to the surface, which is valid, e.g., for porous absorbers. In such cases the reflected sound pressure is written as [Mec08, CD09]

$$\underline{p}_r = \hat{p}\underline{R_\vartheta} e^{j(\omega t + kxcos(\vartheta) - kysin(\vartheta))}. \tag{2.17}$$

Here, $\underline{R_\vartheta}$ is the (angle-dependent) complex reflection factor, which is determined with the complex wall impedance $\underline{Z}$ and the free field impedance Z_0

$$\underline{R_\vartheta} = \frac{\underline{p}_r}{\underline{p}_i} = \frac{\underline{Z}cos\,(\vartheta) - Z_0}{\underline{Z}cos\,(\vartheta) + Z_0}. \tag{2.18}$$

As the complex wall impedance $\underline{Z}$ is often unknown, an energetic (scalar) value is defined with the reflection factor $\underline{R_\vartheta}$. This absorption coefficient α_ϑ reads

$$\alpha_\vartheta = 1 - \left|\underline{R_\vartheta}\right|^2. \tag{2.19}$$

For the simulation of many Geometrical Acoustic (GA) simulation methods, an absorption coefficient independent of the angle of incidence is mainly used, which can be easily measured in a reverberation chamber[CD09, DIN03]. This random incidence reflection factor can also be computed by the angle dependent reflection factor using the Paris formula [CD09]

$$\alpha = \int_0^{\frac{\pi}{2}} \alpha_\vartheta\,(\vartheta)\,sin\,(2\vartheta)\,d\vartheta. \tag{2.20}$$

2.3.3. Sound Scattering

Geometrical reflections are only valid for infinite and plane surfaces. However, for finite surfaces, diffraction deals with the effect of a sound wave *bending* around an obstacle or a finite wall, whereas, for every rough surface, the incident sound wave is scattered. In this section, only the latter effect in discussed, as the former is caused by diffraction (see Sec. 2.3.4).

An incident plane wave is split up into several secondary plane waves. The local phases of these independent secondary waves produce in sum a quite complicated scattered sound field [Vor08].

The scattering effect of *obstacles* on a surface is dependent on their size and structure relative to the wavelength λ. Thus, the structure of a surface acts differently for different frequencies as shown in Fig. 2.5.

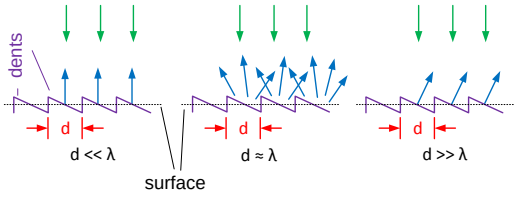

Figure 2.5.: Dependency of sound scattering on the wavelength $\lambda = \frac{c}{f}$ (after Kuttruff [Kut07]).

For *dents* much smaller than the wavelength $\lambda \gg d$, the sound wave is almost solely reflected on the smooth wall surface. In contrast, for *dents* much larger than the wavelength $\lambda \ll d$, the obstacles are seen as separated surfaces by the incident wave and the waves are reflected geometrically on each surface separately. For *dents* in-between these extreme cases, the incident sound wave is scattered.

In general, both specular and scattered reflections for an incident sound wave occur theoretically. A standardized scattering coefficient σ is introduced that describes the portion of the scattered energy that is reflected[CDD+06]. On the contrary, the portion $(1 - \sigma)$ describes the geometrically reflected energy (see Fig. 2.6)[Vor08]. It can be measured according to[VEdG+04, VM00, ISO04].

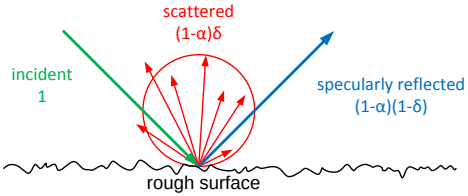

Figure 2.6.: Split-up of incident sound energy into scattered and specularly reflected energy (after Vorländer [Vor08]).

The distribution of the scattered energy σ is strongly dependent on the structure of the scattering surface. However, in most cases a simple Lambertian distribution[LA92] is used which gives good results when applied to real-world scenarios. The Lambert law originates actually from optics and is based on the reciprocity principle, i.e., a surface cannot emit more energy than it would receive[Ste04]. As a surface can only receive energy with its projection area in direction of the incident sound wave, a *cosine* factor has to be used.

Due to the principle of energy conservation, the scattered energy has to be distributed over the complete angle range. Since the scattering distribution is a probability density per (solid) angle[SP13], it follows

$$\text{In } 3D: \int_0^{2\pi} \int_0^{\frac{\pi}{2}} \frac{dp}{d\Omega} d\Omega \stackrel{!}{=} 1 \qquad \text{or} \qquad \text{in } 2D: \int_{-\frac{\pi}{2}}^{\frac{\pi}{2}} \frac{dp}{d\vartheta} d\vartheta \stackrel{!}{=} 1 \tag{2.21}$$

For the $3D$ case, the normalization results in

$$\frac{dp}{d\Omega} = \frac{cos\,(\vartheta)}{\pi}. \tag{2.22}$$

The same consideration holds for the $2D$ case with

$$\frac{dp}{d\vartheta} = \frac{cos\,(\vartheta)}{2}. \tag{2.23}$$

2.3.4. Sound Diffraction

The last two sections of this chapter dealt with the influence of very large walls on sound propagation. The following section handles now the wave phenomenon of diffraction around obstacles. Although diffraction also occurs on the source-side of the obstacle, this thesis focuses on diffraction behind an obstacle. In spite of the fact that diffraction is a more dominant wave phenomenon in acoustics (since the acoustical wavelengths are often in the dimension of occurring obstacles), it was first investigated in optics.

For very small objects (in comparison to the investigated wavelength λ), the sound field is more or less unaffected by the obstacle, i.e., the sound wave is bent around the obstacles, such that the shadow zone behind the obstacles nearly disappears[Kut07].

Today, numerous diffraction theories exist that can be structured by different aspects. In this work, a classification with respect to the applied approximations is chosen. Three degrees of approximations are ascertained: First, wave theoretical methods have to be named. Although all diffraction theories are based on wave theory, this group classifies all diffraction theories that remain completely in the wave pattern without approximations. The second group approximates this wave pattern by Kirchhoff assumptions[Pie89]. Most approaches in this group take only the aperture of an opening into account and the actual shape of the wedge is neglected. Other approaches exist that use the Kirchhoff approximations to compute the reflected sound from a rough surface[Gor75, Tho88, LS09]. However, as the direct (and reflected sound field) is significantly stronger on the source-side of the wedge[Pie89], this work handles only the diffracted sound field behind the aperture. Finally, the third group approximates the diffraction theory even further, such that only the detour is taken into account that sound has to travel around an obstacle. In addition to these three main categories, approaches exist that model diffraction by transmitting sound through a semi-transparent surface[Dam02] or increase the scattering coefficient of a surface close to an edge[Dal02]. The latter, again, handles only diffraction on the source-side and is not considered here.

The quantitative computation is rather complicated, even for simple geometries. Therefore, a qualitative explanation is presented first using the Huygens principle. Then, the three groups mentioned above are further discussed.

2.3.4.1. Huygens Principle

The basic idea of Huygens is that any (optical) wave can be created by the superposition of an infinite number of secondary sources, so called Huygens sources [HLM90]. These secondary sources have to be positioned on a wavefront and radiate sound *spherically*. The superposition of the wavefronts of these secondary sources will create the same wave shape compared to the original wave.

For a plane wave, the sideward components of these secondary sources cancel out each other, whereas the propagating part of the original wave is composed by these secondary sources (see Fig. 2.7 $x_1 \rightarrow x_2$).

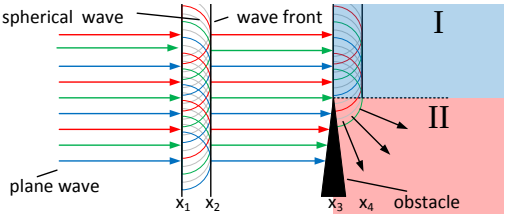

Figure 2.7.: Huygens principle: a plane wavefront (x_1) can be composed by a number of secondary sources on that wavefront ($x_1 \rightarrow x_2$). In case of an obstacle (x_3), the wave is propagating also in the shadow zone (x_4) (after Kuttruff [Kut07]).

By introducing an obstacle orthogonal to the plane wave, the screen shields the lower secondary sources such that only the remaining secondary sources add up to a wavefront behind the screen (see Fig. 2.7 $x_3 \rightarrow x_4$). Qualitatively, energy of the remaining secondary sources propagates in the shadow zone (II), whereas the shielded secondary sources cause a reduction of energy in the view zone (I).

2.3.4.2. Wave Theoretical Diffraction Models

All wave phenomena are frequency dependent. Thus, wave theoretical diffraction models are mainly described in the frequency domain. Here, a large number of contributions exist, e.g., by Bowman and Senior[BSU69], MacDonald[Mac15], Pierce[Pie89] and Sommerfeld[SN04]. A special group of these wave theoretical models are high-frequency asymptotic solutions. On the other hand, the most common solution in the time domain is given by the Biot-Tolstoy-Medwin (BTM) theory[BT57, Med81], which is also the basis of the Secondary Source Model (SSM) (see Sec. 5.1.1). The latter is used as main reference solution in this work. Therefore, the BTM expression is explained in more detail after a short excurse to high-frequency asymptotic solutions.

High-Frequency Asymptotic Solutions Some wave theoretical models are only correct for high frequencies and, thus, are sufficient for describing short waves around an obstacle ($kr \gg 1$)[Pie74, RLBPL04]. Due to their high-frequency application, they are often used in GA simulation methods. Keller presented a Geometrical Theory of Diffraction (GTD)[Kel62] for the Sound Particle Simulation Method (SPSM) (see Sec. 3.4), which was successfully applied to the radiative transfer method[RLBPL04], too. Later, the Uniform Theory of Diffraction (UTD)[KP74] was found, which can be seen as an extension to even higher frequencies (applied, e.g., to Beam Tracing (BT)[TFAC00, TFNC01]). Another approach is the Physical Theory of Diffraction (PTD)[Ufi89], which is based on the usage of elementary edge waves.

Biot-Tolstoy-Medwin The main idea of the solution in time-domain is that the sound pressure level p is the sum of the direct sound p_{direct}, the specular reflections $p_{specular}$ and a diffracted sound field $p_{diffracted}$

$$p = p_{direct} + p_{specular} + p_{diffracted}. \tag{2.24}$$

The BTM handles diffraction around an infinite wedge by normal coordinates[BT57]. Around the infinite edge on the $z - axis$, source (r_S,φ_S,z_S) and receiver (r_R,φ_R,z_R) are positioned in cylindrical coordinates as shown in Figure 2.8.

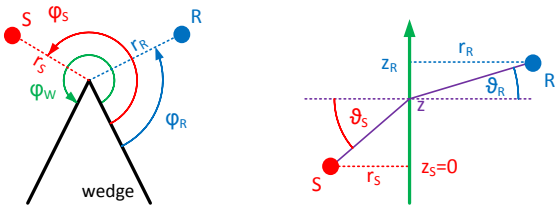

Figure 2.8.: Geometrical definitions of Biot - Tolstoy (after Calamia [Cal09]).

Then, a *displacement potential* is defined for the wedge geometry with the wedge opening angle φ_W. This *displacement potential* is given by the superposition of modes in cylindrical coordinates, such that the boundary conditions of both the rigid wedge surfaces and the source position are fulfilled.

Consequently, the sound pressure $p(t)$ is derived as [Cal09]

$$p_{diffracted}(t) = \frac{\rho_0 c^3}{4\pi\varphi_W} \cdot \frac{t}{r_S^2 r_R^2 sinh^2\left(\eta\left((t\right)\right)} \cdot e^{-\nu\eta((t)} \cdot \sum_{i=4}^{4} \left\{ coth\left(\eta\left((t\right)\right) \frac{sin\left(\nu\varphi_i\right)}{1 - 2e^{-\nu\eta((t)} cos\left(\nu\varphi_i\right) + e^{-2\nu\eta((t)}} + \frac{\pi}{\varphi_W} \frac{\left(1 - e^{-2\nu\eta((t)}\right) sin\left(\nu\varphi_i\right)}{\left[1 - 2e^{-\nu\eta((t)} cos\left(\nu\varphi_i\right) + e^{-2\nu\eta((t)}\right]^2} \right\} \Theta\left(t - \frac{R_0}{c}\right), \tag{2.25}$$

where c is the speed of sound, $\nu = \pi/\varphi_W$ the wedge index, R_0 the length of the shortest path from the sound source to the receiver and $\Theta\left(t\right)$ the Heaviside step function. In contrast to the original publication, the variable names are modified to fit the conventions of this work. Furthermore, $\eta\left((t\right)$ is equivalent to

$$\eta(t) = cosh^{-1}\left(\frac{c^2t^2 - \left(r_R^2 - r_S^2 + z_R^2\right)}{2r_S r_S}\right) \tag{2.26}$$

and φ_i follows

$$\begin{aligned} \varphi_1 &= \pi + \varphi_S + \varphi_R \\ \varphi_2 &= \pi + \varphi_S - \varphi_R \\ \varphi_3 &= \pi - \varphi_S + \varphi_R \\ \varphi_4 &= \pi - \varphi_S - \varphi_R. \end{aligned} \tag{2.27}$$

Note that the sound source is restricted to $z_S = 0$ without a loss of generality.

Instead of a pulse excitation, Medwin extended the Biot-Tolstoy theory by an uniform and instantaneous point source S, such that the sound pressure at the receiver is rewritten [Med81] as

$$p_{diffracted}(t) = -\frac{S\rho_0 c}{4\pi\varphi_W} \cdot \frac{1}{r_S r_R sinh\left(\eta\left((t\right)\right)} \cdot \sum_{i=1}^{4} \beta_i \cdot e^{-\nu\eta((t)} \tag{2.28}$$

with

$$\beta_i\left((t)\right) = \frac{sin\left(\nu\varphi_i\right)}{cosh\left(\nu\eta\left((t)\right)\right) - cos\left(\nu\varphi_i\right)} \tag{2.29}$$

using the same abbreviations as Biot - Tolstoy.

Based on that, Medwin extended the Biot-Tolstoy solution to finite wedges by assuming a reduction of the sound pressure $p(t)$ to one-half, when the smaller detour is reached (see Fig. 2.9, $\overline{SPR}$). Furthermore, the sound pressure is set to zero for distances larger than the greatest detour (see Fig. 2.9, $\overline{SQR}$).

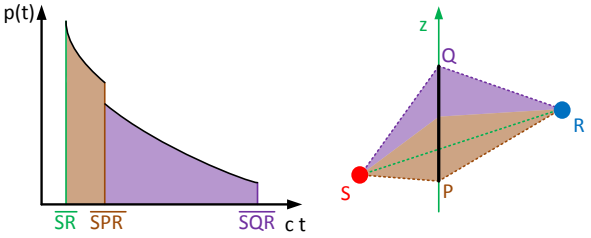

Figure 2.9.: Extension of the Biot - Tolstoy solution to finite wedges (after Medwin [Med81]).

2.3.4.3. Diffraction Models using Kirchhoff Approximations

The second group of diffraction models approximates the exact wave theoretical deviations by applying Kirchhoff's approximation. In contrast to the BTM, these models handle the direct sound p_{direct} and the diffracted sound field $p_{diffracted}$ simultaneously. Due to the approximations made, these models are not asymptotically correct for high frequencies[JM82]. Although the classical Kirchhoff approximation is only valid for small diffraction angles, Stephenson proposed an extension to larger angles, which is presented briefly[Ste10a] (see below). Different approaches exist how to use Kirchhoff approximations in diffraction studies[Emb80, SN81]. The most famous diffraction theories based on Kirchhoff's assumptions are the diffraction theories by Fresnel and Fraunhofer.

A quantitative formulation of Huygens principle is called the Kirchhoff integral theorem. Based on the idea of Huygens, the sound pressure p at any point inside a volume V is described by the sum over all secondary sources on a surrounding surface S of a volume V (see Fig. 2.10).

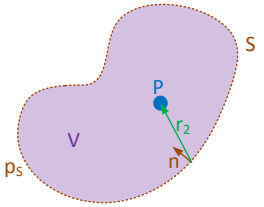

Figure 2.10.: Geometrical definitions of the Kirchhoff integral theorem. The distance r_2 is measured from any point on the closed surface S to a point P inside the volume V defined by the closed surface. The sound pressure p_S as well as the surface normal n pointing inwards are given at any point of the surface.

A complete derivation is found in [Pie89] with the result

$$p(P) = \frac{1}{4\pi} \oiint_S \left[p_S \frac{\partial}{\partial n} \left(\frac{e^{-jkr_2}}{r_2} \right) - \frac{e^{-jkr_2}}{r_2} \frac{\partial p_S}{\partial n} \right] dS, \tag{2.30}$$

where p_S is the sound pressure given at each point of the surface S and n the normal vector at each point of the surface pointing inwards[a)]. In this case, two Green's functions, i.e., solutions of the wave equation with inhomogeneous boundary conditions, occur in the Kirchhoff integral. The right part of Eqn. 2.30 represents a monopole source, while the left part stands for a dipole source directing orthogonal to the surface[Kut07].

This formulation is still exact. In order to apply Kirchhoff's approximations, however, assumptions for the sound pressure of the surface p_S have to be applied. Therefore, the surface S is defined as infinite wall (closing in infinity) and is split up into a solid region as well as a transmitting region S'.

On this surface, the typical Kirchhoff assumptions are:

1. the sound pressure on the rear side of the solid wall is *zero* and

2. the incident sound field is undisturbed in the opening.

Both approximations assume that the opening is large compared to the wavelength, such that the effects of diffraction only take effect inside the volume, i.e., on the rear side of the opening.

When small angles of incidence on the surface and small outgoing angles are assumed[Pie89], the Fresnel - Kirchhoff integral states for the far field ($kr_2 \gg 1$)

$$p(P) \approx \frac{jkp_S}{2\pi} \iint_{S'} \frac{e^{-jkr_2}}{r_2} dS, \tag{2.31}$$

where r_2 this the distance from any point on the aperture to the point of interest P.

Extension of the Kirchhoff Approximation to Larger Angles In order to extend this approximation to larger angles, Stephenson[Ste10a] assumed a plane wave that intersects the aperture with an angle of φ_S, as shown in Fig. 2.11.

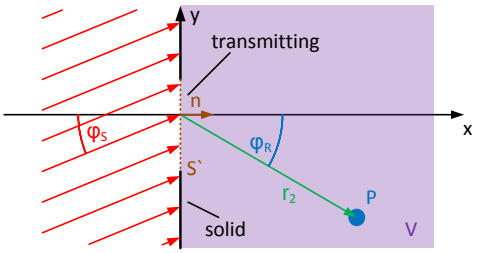

Figure 2.11.: Geometrical definitions for the derivation of the Fresnel-Kirchhoff diffraction through an opening.

The surface normal points in $x-$ direction. The angle φ_R denotes the angle between a connection of the current point on the aperture and the receiving point P relative to

[a)] This equation is only valid for a point P inside the surface S (interior). For P outside S, an exterior problem is solved.

the surface normal n (see Fig. 2.11). If the angles φ_S and φ_R are not too small, Eqn. 2.30 can be modified in a different way.

The first term is simplified to (with far-field approximation $kr_2 \gg 1$)

$$\frac{\partial}{\partial n}\frac{e^{-jkr_2}}{r_2} = \frac{\partial}{\partial x}\frac{e^{-jkr_2}}{r_2} = \left(-\left(jk+\frac{1}{r_2}\right)\frac{e^{-jkr_2}}{r_2}\right)\frac{\partial r_2}{\partial x} \overset{kr_2\gg 1}{\approx} -jk\frac{e^{-jkr_2}}{r_2}cos\left(\varphi_R\right). \tag{2.32}$$

For the second term, a cosine of the angle of incidence φ_S is derived

$$\frac{\partial p_S}{\partial n} = \frac{\partial p_S}{\partial x} = -jkp_S\frac{\partial r}{\partial x} = -jkp_S cos\left(\varphi_S\right). \tag{2.33}$$

If both equations are inserted in Eqn. 2.30, $p(P)$ is written as

$$p(P) \approx \frac{jkp_S}{2\pi}\iint_{S'}\frac{e^{-jkr_2}}{r_2}\cdot\frac{cos\left(\varphi_R\right)+cos\left(\varphi_S\right)}{2}dS. \tag{2.34}$$

This equation is equal to Eqn. 2.31 only for $\varphi_S \approx \varphi_R \approx 0$. The Kirchhoff - Fresnel integral is, so to say, only valid for orthogonal incident $\varphi_S = 0$ and small diffraction angles $\varphi_R \approx 0$.

In all other cases, a factor f must be introduced, found by Stephenson [Ste10a]

$$f = \frac{cos\left(\varphi_R\right)+cos\left(\varphi_S\right)}{2}. \tag{2.35}$$

Fresnel Diffraction at a Half-Infinite Screen A specialization of Eqn. 2.31 is called Fresnel diffraction and refers to diffraction at a half-infinite screen. For this setup, the aperture is defined for $y > 0$ with an infinite length in $z - direction$. Both aperture and screen close at infinity. In addition to the approximations by Kirchhoff, the distance r_2 is approximated by using Taylor approximation in the exponent up to the 2nd order[Pie89]. During the integration over the surface, the current surface element is located at $(x' = 0, y', z')$, whereas the point of interest P is located at (x, y, z), such that the approximation reads

$$r_2 = \sqrt{x^2+\left(y-y'\right)^2+\left(z-z'\right)^2} \approx x + \frac{\left(y-y'\right)^2}{2x} + \frac{\left(z-z'\right)^2}{2x}. \tag{2.36}$$

The denominator r_2, on the other hand, is directly approximated by the Taylor approximation of the 1st order $r_2 = x$.

With Eqn. 2.36 and several conversions, Eqn. 2.31 is written as

$$p(P) \approx \frac{(1+j)}{2}\cdot p_S \cdot e^{-jkx}\left[\left(C\left(\sqrt{\frac{k}{\pi x}}y\right) - jS\left(\sqrt{\frac{k}{\pi x}}y\right)+\frac{1-j}{2}\right)\right]. \tag{2.37}$$

where additionally the Fresnel Integrals[AS64]

$$C\left(z\right) = \int_0^z cos\left(\frac{\pi}{2}s^2\right)ds \qquad \text{and} \qquad S\left(z\right) = \int_0^z sin\left(\frac{\pi}{2}s^2\right)ds \tag{2.38}$$

are used. The computed sound pressure level of the Fresnel diffraction is shown in Fig. 2.12 together with the geometrical shadow zone.

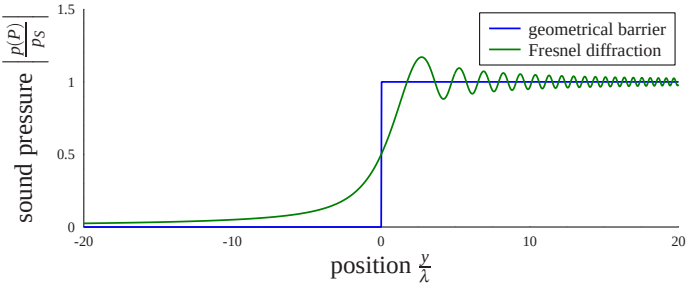

Figure 2.12.: Fresnel diffraction by a rigid half-plane in a distance $\frac{x}{\lambda} = 10$ behind a screen and $\frac{y}{\lambda}$ above the edge (see Fig. 2.11).

Fraunhofer Diffraction at a Slit While the Fresnel diffraction assumes a semi-infinite screen (see previous section), the Fraunhofer diffraction basically deals with diffraction of a finite aperture S in the infinite plane. Fraunhofer diffraction can be interpreted as a further approximation of the Fresnel diffraction assuming an extreme far field and small angles, but historically it has been derived independently.

As this approximation is restricted to even larger distances to the aperture and small angles, such that $y' \ll y$ and $z' \ll z$, Eqn. 2.36 is further simplified by omitting the 2nd order terms

$$r_2 \approx x + \frac{(y-y')^2}{2x} + \frac{(z-z')^2}{2x} \approx x + \frac{y^2 - 2yy'}{2x} + \frac{z^2 - 2zz'}{2x}. \tag{2.39}$$

Hence, the sound pressure of Eqn. 2.31 is further approximated to

$$p(P) \approx \frac{jkp_S}{2\pi x} \int_{-\infty}^{\infty}\int_{-\infty}^{\infty} a(y',z') e^{-jk\left(x + \frac{y^2-2yy'}{2x} + \frac{z^2-2zz'}{2x}\right)} dy'dz'. \tag{2.40}$$

Here, $a(y',z')$ is a transmittance function being either 0 at the solid wall or 1 at the opening. Thus, $a(y',z')$ *filters* an opening from the infinite wall.

This transmittance function reads for a rectangular shape[Hec01]

$$a(y',z') = rect\left(\frac{y'}{Y}\right) \cdot rect\left(\frac{z'}{Z}\right) = \begin{cases} 1 & |y'| < \frac{Y}{2} \quad \text{and} \quad |z'| < \frac{Z}{2} \\ 0 & else \end{cases}. \tag{2.41}$$

This aperture is symmetrical to $(y',z') = (0,0)$ and has a width of Y in $y-$direction and a width of Z in $z-$direction. It is shown that the Fourier transformation[OL07]

$$\mathscr{F}\left(a(y',z')\right) = A(y,z) = Ysi\left(\pi Yy\right) \cdot Zsi\left(\pi Zz\right) \tag{2.42}$$

can be used to describe the sound pressure behind the slit[Pie89]. Although the definition of a symmetrical slit is quite simple, the sound pressure behind the aperture is described by the Fourier transformation of any transmittance function $a(y',z')$ (aperture shape).

The sound pressure behind a rectangular screen is derived with $A(y,z)$ to[Hec01]

$$p(P) \approx jp_S \left(\frac{x}{\lambda}\right) e^{-jk\left(x + \frac{y^2+z^2}{2x}\right)} \frac{Y}{\lambda} si\left(\pi \frac{Y}{\lambda}\frac{y}{x}\right) \cdot \frac{Z}{\lambda} si\left(\pi \frac{Z}{\lambda}\frac{z}{x}\right), \tag{2.43}$$

where $si\,(x) = sin\,(x)\,/x$ is the *si*- function. The result is shown in Fig. 2.13

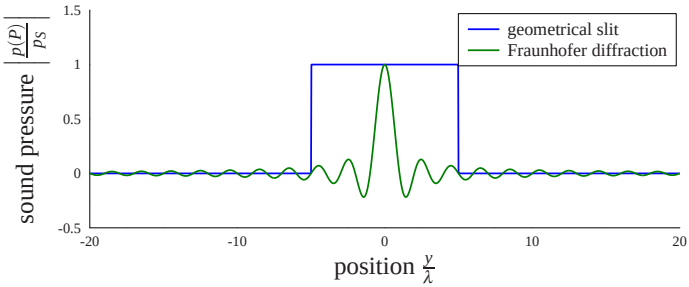

Figure 2.13.: Fraunhofer diffraction at a slit of width $\frac{Y}{\lambda} = 10$ in a distance $\frac{x}{\lambda} = 10$ behind a slit and $\frac{y}{\lambda}$ above the centre of the slit $(z = 0)$

In Eqn. 2.43, two orthogonal diffraction angles ε and η are defined by the ratio of $\frac{y}{x} = tan\,(\varepsilon) \approx sin\,(\varepsilon)$ and $\frac{z}{x} = tan\,(\eta) \approx sin\,(\eta)$ resulting in an energetic formulation of Eqn. 2.43

$$I\,(P) \propto |p(P)|^2 \propto si^2\left(\pi\frac{Y}{\lambda}sin\,(\varepsilon)\right) \cdot si^2\left(\pi\frac{Z}{\lambda}sin\,(\eta)\right). \tag{2.44}$$

2.3.4.4. Diffraction Models using only the Detour

The roughest approximation is to take only the shortest detour into account that sound has to travel around an obstacle. These models are mainly used to compute the screening effect of single noise barriers. Certainly the diffraction theory of Redfearn is to mention here[Red40], which can be derived from the Uniform Theory of Diffraction[Kur74]. Another model is the Maekawa Detour Law (MDL)[Mae68], which was first based on empirical measurements, but has been proven later mathematically[Kur74]. In this work, this method is used as a representative for these most simple diffraction models.

Although the result of Maekawa's experiments is a graph with nonlinear axes, a simple mathematical expression reads with $N = \frac{2d}{\lambda}$[Kur74]

$$\Delta L = 10 \cdot log_{10}\,(20N)\,. \tag{2.45}$$

In this equation, d stands for the detour that sound has to travel around an obstacle, and λ is the wavelength.

2.4. Receivers

A propagating sound field can be evaluated at specified positions, called receivers. The sound field can either be described by the sound pressure p or the (energetic) sound intensity I, which are both dependent on time and space. In room acoustics and city acoustics, different requirements occur for the description of the sound field. In city acoustics, mainly the spatial distribution is of interest, but also the time dependency is important if estimations of annoyance are of interest. Either way, the energetic distribution is sufficient, especially because the exact phase information of the wall impedances is only seldomly known anyway. Nevertheless, when this information is available, an impulse response can be computed. However, if the phase information is not available and only the energetic sound intensity is available, either an intensity echogram or an intensity map can still be computed. All three solutions are presented briefly in the following.

2.4.1. Impulse Response

The impulse response is introduced in system theory to describe the answer of a Linear Time Invariant (LTI) - system to an excitation by a single pulse[OL07]. It is sufficient to define the system completely.

In acoustics, both assumptions for an LTI - system are (at least approximately) fulfilled in practical cases and the respective impulse response can be used to describe the sound propagation of a single pulse from a sound source to a receiver. This impulse response can either be measured or simulated and can be seen as a *fingerprint* of the room[Sch11]. As each excitation signal can be composed of a sum of single delayed and scaled pulses, the signal, i.e., the sound pressure, can be estimated by a convolution of the excitation signal with the impulse response[OL07]. This estimated sound pressure can be used to create a quite authentic auralization of the sound field[Vor08].

2.4.2. Echogram

A sound intensity echogram is the energetic counterpart of the impulse response, when only one source emits a single (energetic) pulse. It describes the sound intensity $I(t)$ up to a maximum time of T_{Max} of different reflection paths at the receiver position for the regarding time delay. Multiple reflection (including scattering and diffraction) paths are possible. From a room acoustical point of view, three main groups of reflections can be named[Vor08]:

- direct sound: the first connection between source and receiver (line of sight). It determines the perceived direction of incidence (precedence effect)[Bla96].

- early reflections: reflections of low-order reaching the receiver (typical $50-80ms$). These reflections are added up to the initial sound event by the human hearing (Haas effect)[Bla96]. They contribute to the direct sound expression and support the speech intelligibility.

- late reverberation: reflections of higher order (typical $> 80ms$). The reverberation tail is quite independent of the receiver position and is used to determine the room shape and size as well as the absorber distribution.

All three groups are described in Fig. 2.14. Here, the sound intensity $I(t)$ is the sum of the energies of single reflection paths at a receiver position up to a maximum time.

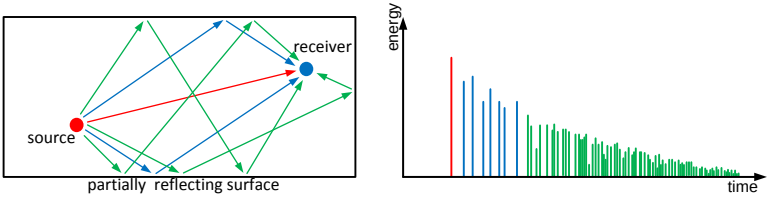

(a) geometrical setup **(b)** time dependent echogram

Figure 2.14.: Composition of direct sound (*red*), early reflections (*blue*) and reverberation (*green*) in an energetic echogram.

Based on the energetic echogram, many room acoustical parameters can be computed. Here, the main parameter is certainly the reverberation time T_{60}. It is defined as the time interval in that the total sound energy in the room is reduced by a factor of 10^{-6} ($-60dB$). Additionally, parameters such as clarity, definition and gain are directly derivable[Got73].

Although many GA simulation methods compute the intensity echogram, an impulse response that is appropriate for auralization purposes can be computed by reconstructing the temporal fine structure from the energetic echogram[Sch11].

2.4.3. Intensity Level Map

For many purposes such as noise immission prognosis, the time dependency of the sound distribution is not of interest. Therefore, a single value is found for the sound intensity I of a specified receiver position by adding up all reflection energies of the echogram. This total intensity (still valid only for a specified receiver position) is drawn in a map. Due to the huge range of the sound intensity, the sound intensity level L_I is used instead of the sound intensity I (see Sec. 2.1). An example of such an intensity level map is given in Fig. 2.15.

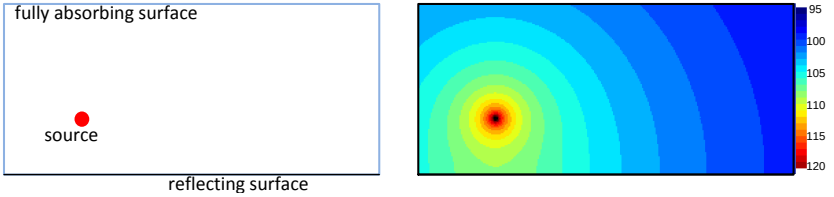

(a) geometrical setup of a single source inside a closed volume with totally reflecting floor and fully absorbing surrounding else.

(b) intensity level map. The sound intensity level L_I is shown as colour from *red* (high) to *blue* (low).

Figure 2.15.: Intensity level map for a geometrical scene with one reflecting surface.

A single source is placed within a closed volume (see Fig. 2.15a). In case of a free-field sound propagation, the sound intensity would decrease radially outwards. However, the specular reflections of the floor increase the sound intensity level L_I right above the surface (see Fig. 2.15b).

3. Geometrical Acoustic Simulation Methods

For high frequencies and small wavelengths, respectively, the wave behaviour can be neglected by part. Instead, the sound energy flow is modelled geometrically just like in geometrical optics[Hec01]. Therefore, this type of wave field modelling is called Geometrical Acoustic (GA). In GA, sound propagation is assumed as the dispersion of rays or particles, similar to the wave-particle-dualism in physics. To apply these GA simulation models, the typical dimensions of the environment have to be large compared to the wavelength. Although there are GA simulation methods that include complex sound pressure[Kel54, Pie89, JIR08], this work restricts GA to complete energetic models. Furthermore, it is assumed that the sound propagation always takes place in a closed polyhedron (a free field is modelled by using only fully-absorbent surfaces).

In this chapter, the physical models as well as algorithmic details of the fundamental GA simulation techniques 1) image sources, 2) ray tracing, 3) beam tracing and 4) acoustic radiosity methods are presented. In general, these methods are applicable in a $3D$ space, but their presentation is restricted to $2D$ cases first. A detailed understanding of these models in $2D$ is required to follow the derivation of the reunification techniques and their evaluation in chapter 6, where only the most efficient and accurate reunification technique is extended to $3D$ later in chapter 7. First an interpretation of the $3D$ space in $2D$ is given. Then, extensions of the common GA simulation methods are introduced in order to simulate multiple frequency bands simultaneously. Finally, the actual implementations of these extended GA simulation methods are presented.

3.1. Interpretation of the 3D Space in 2D

In order to reduce the complexity of the investigated GA simulation methods, the investigations are restricted to $2D$. Therefore, only a two dimensional cross-section of the $3D$ space is discussed. Without loss of generality, this cross-section is defined as the $x-y-$ plane (see Fig. 3.1).

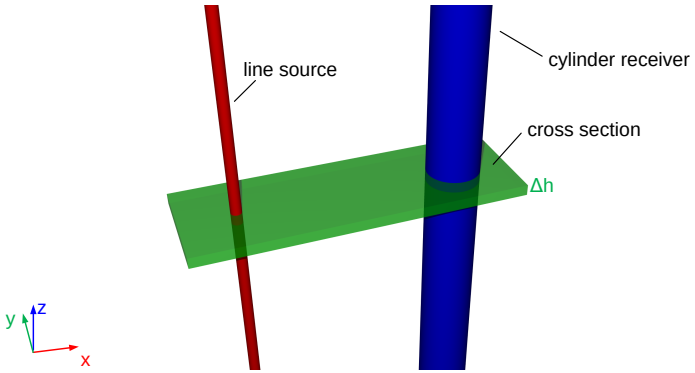

Figure 3.1.: Analogy of $3D$ and $2D$ simulation. The $3D$ scene has to be invariant of a translation in $z-$direction.

In order to compute valid results for this cross-section, the $3D$ scene has to be invariant with respect to a translation in $z - direction$ and, thus, a coherent vertical line source (see Sec. 2.2.2) with a sound power per length P' is assumed. In the case of spatially extended receivers that are used, e.g., in the Sound Particle Simulation Method (SPSM), their shape has to be invariant with respect to a translation in $z-$ direction, too. In this work, a cylindrical shape is chosen to avoid a directivity of the receivers. Thus, the sound propagation in $2D$ is restricted to the propagation in a plane of height Δh (see Fig. 3.1), which can converge to $\Delta h \to 0$.

3.2. Handling Multiple Frequency Bands Simultaneously

In general, the sound propagation is strongly dependent on the frequency. This is especially important since acoustics encompasses a wide range of frequencies from $f = 20Hz$ up to $f = 20.000Hz$. This frequency range is usually split up either into octave or third-octave bands in order to meet the physiology of the human hearing. For acoustics, the following centre frequencies are defined for the frequency bands:

Octave	Third Octave (1)	Third Octave (2)	Third Octave (3)
31.5	20	250	3150
63	25	315	4000
125	31.5	400	5000
250	40	500	6300
500	50	630	8000
1000	63	800	10000
2000	80	1000	12500
4000	100	1250	16000
8000	125	1600	20000
16000	160	2000	
	200	2500	

Table 3.1.: Typical frequency bands used in acoustics.

In building acoustics, only 6 of these octave bands are typically used ($125Hz \leq f \leq 4000Hz$). Classical GA simulation methods handle the sound propagation for each frequency independently. The results of each frequency band are interpreted individually or combined to a full range impulse response[Sch11]. In this work, an octave band resolution is chosen. All bands are computed simultaneously, which means that the sound energy carriers are not only carriers of sound energy, but of multiple energies for each frequency band. This procedure is faster than handling each frequency band independently, but one has to ensure that the geometric sound propagation paths are *independent* of the frequency. Thus, the frequency-dependent effects like scattering, diffraction, absorption and air attenuation result only in a modification of the carried energy, but not of the actual sound propagation path. Solutions for all these cases will be presented in this chapter (in case of diffraction in chapter 5).

3.3. Image Sources

The basic idea of the image source method is that sound sources are mirrored on reflecting walls and specular reflections of the impacting sound are assumed. Early work has been presented for the one dimensional case and the three dimensional case with perpendicular surfaces[Min50]. It has been applied to concert halls[Gib72] and rectangular rooms[Ber75, AB79, Bor84]. The image source method enables the computation

of specular reflections of arbitrary order, whereas the simulation of diffuse reflections is not possible (without further extensions).

The determination of the sound intensity is based on the free-field sound distribution (Eqn. 2.12). Every sound source S is mirrored on a wall with index i to construct the respective image source S_i. The overall path length r_i is equal to the Euclidean distance between the image source and the receiver (see Fig. 3.2).

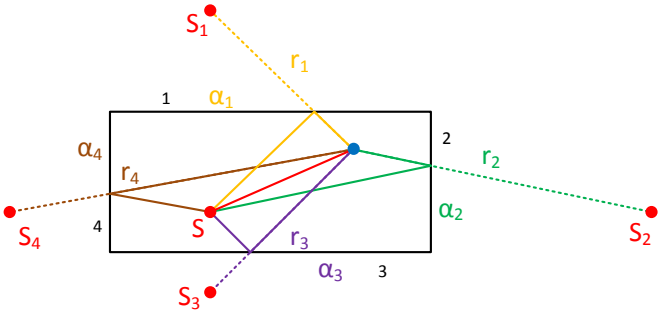

Figure 3.2.: Construction of first order image sources.

The sound intensity after a wall reflection is still computed by simply applying the $\frac{1}{r}$ distance law, where r is the total path length, and a multiplication by the (generally angle- and frequency-dependent) reflection coefficient $(1-\alpha)$, where α is the absorption coefficient (see. Sec. 2.3.2), and the air attenuation m for the distance r_i (see. Sec. 2.3.1). It follows from Eqn. 2.12

$$I = \frac{P'}{2\pi r_i} \cdot (1-\alpha_i) \cdot e^{-mr_i}. \tag{3.1}$$

The overall sound intensity at the receiver position is written as the sum of all these image sources. For the simulation of multiple frequency bands (see Sec. 3.2), the image source positions are identical for each frequency, such that only different α and m have be the used for each frequency band. In case of a real $3D$ simulation, where the source (or the image source) are points rather than lines, an exact time delay between source and receiver is defined. It is computed according to their distance r_i to

$$\Delta t_i = \frac{r_i}{c}. \tag{3.2}$$

The image source method is very accurate within the restrictions of GA and even impulse responses (including phase) can be computed. On the other hand, an introduction of scattering is not possible for the image source method.

As higher order image sources are constructed recursively by mirroring the image sources on additional walls, an exponential growth of these image sources as a function of the reflection order i is derived. For arbitrary polyhedra instead of rectangular rooms [Bor84] with a number of $\overline{n}$ walls, the number of *constructable* image sources n_{CIS} reads[KKF93, Kut09]

$$n_{CIS} = \overline{n}\,(\overline{n}-1)^{i-1} \approx \overline{n}^i. \tag{3.3}$$

Although the number of constructable image sources grows exponentially, the number of *visible* image sources is only a small part of them. Visible, in this context, means

that the constructed path between the image source and the receiver lies within the room boundaries (see Fig. 3.3).

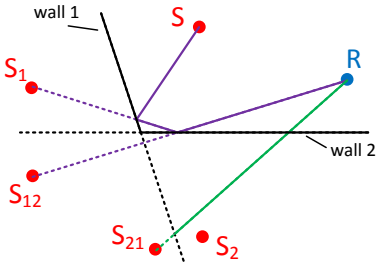

Figure 3.3.: Visibility of 2^{nd}-order image sources. The path construction of S_{12} results in a valid reflection. In contrast, the path connection between S_{21} and R does not intersect the last reflected wall 1 within their boundaries. Thus, S_{21} is invisible (after Vorländer [Vor08]).

Stephenson has estimated the number of *visible* image sources n_{IS} by estimating a visibility probability[Ste90]. On average, an image source of order $n+1$ is one Mean Free Path Length (MFPL) $\bar{l}$[Kos60] farther away than the image source of order n. Hence, the surface S_{IS} where image sources of order i are located, is defined by a ring with $\bar{l} \cdot \left(i - \frac{1}{2}\right) < r < \bar{l} \cdot \left(i + \frac{1}{2}\right)$ (see Fig. 3.4).

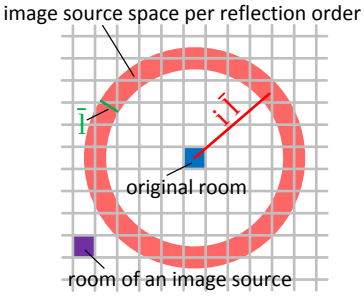

Figure 3.4.: Image rooms. All image sources of reflection order i are statistically within a ring with radius of approximately $i \cdot \bar{l}$ and a width of $\bar{l}$ (after Kuttruff [Kut09]).

The number of visible image sources n_{IS} is found by the ratio

$$n_{IS}(i) = \frac{S_{IS}}{S_R} = \frac{\pi \cdot \left[\bar{l} \cdot \left(i + \frac{1}{2}\right)\right]^2 - \pi \cdot \left[\bar{l} \cdot \left(i - \frac{1}{2}\right)\right]^2}{S_R} = \frac{\pi \cdot \bar{l}^2 \cdot 2 \cdot i}{S_R}, \quad (3.4)$$

because on average one visible image source is in one *image room* of area S_R.

The number of *visible* image sources n_{IS} for one explicit receiver position grows linearly with the reflection order i[a)]. In contrast, the number of constructable image

[a)] only valid for the $2D$ case, for $3D$ the same assumptions yield $\propto i^2$

sources n_{CIS} increases exponentially. Thus, the image source method becomes very inefficient, especially for higher order reflections.

3.4. Sound Particle Simulation Method

Today, many different ray- or sound particle tracing methods exist[KSS68, Gla89]. All these methods have in common that infinitesimally smalls rays are traced along straight lines and are detected by spatially extended receivers. In this thesis, a detection technique is used that takes into account the inner distance, which is called Sound Particle Simulation Method (SPSM). The different techniques of the particle tracing are presented in individual subsections and the main approach for this thesis is chosen.

Sound particles are emitted by a sound source and traced independently through the geometrical scene. These sound particles are reflected either geometrically or diffusely at each wall, until their tracing is aborted. Spatially extended receivers are used to detect the sound intensity at specified receiver locations. These parts of sound particle tracing are described in this section followed by a brief discussion of algorithmic realizations for the processing sequence in $2D$. For the extension to $3D$, see Sec. 7.2.

3.4.1. Emission of Sound Particles

The main configuration parameter of the SPSM is the number of emitted sound particles N. They can be sent out either in N random directions by a Monte Carlo method (see, e.g., [BS66]) or almost equally distributed (see, e.g., [Ste85]).

In this work, equally distributed sound particles are chosen by splitting up the angle range of 2π in N equally spaced angle ranges $2\pi/N$, as this guarantees repeatability (see Fig. 3.5). The sound particle with index i is then emitted in the centre of these region

$$\varphi_i = \frac{i + \frac{1}{2}}{N} \cdot 2\pi. \tag{3.5}$$

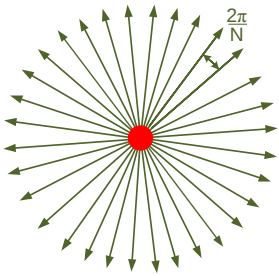

Figure 3.5.: Equal distribution of N sound particles in $2D$ space.

Assuming a continuous sound source with a source power per length P', each sound particle carries a sound power P_i in a plane of height Δh (see Fig. 3.1) with $P_i = \frac{P}{N} = \frac{P' \cdot \Delta h}{N}$. In order to compute an echogram, the sound source emits a single impulse, such that a sound particle carries an energy E_i for a time interval t_{Ref}.

$$E_i = \frac{P' \cdot \Delta h \cdot t_{Ref}}{N}. \tag{3.6}$$

In case of the simulation of multiple frequency bands, one energy for each frequency band has to be carried. In conclusion, an emitted sound particle is defined by

- sound energy
- starting point
- direction vector.

3.4.2. Wall Intersection Test

To find the intersection point between a sound particle and the geometrical scene, four criteria have to be fulfilled. These criteria are visualized in Fig. 3.6.

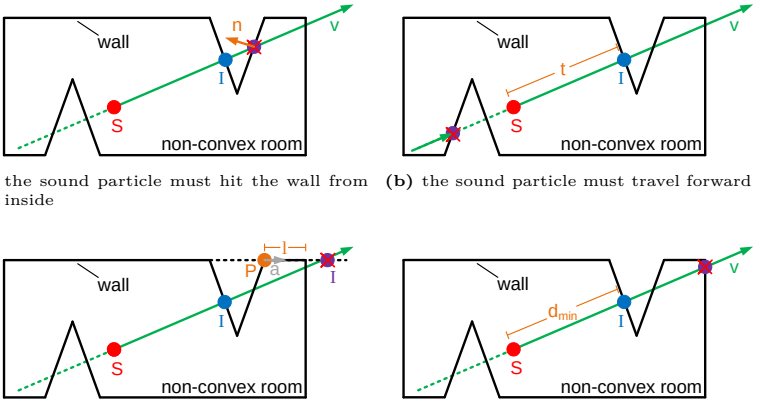

(a) the sound particle must hit the wall from inside

(b) the sound particle must travel forward

(c) the intersection must lie inside a wall

(d) only the intersection with minimum distance to the point of emission is valid

Figure 3.6.: Criteria for valid intersection points of a sound particle (*green*) starting at the sound source (*red*) in non-convex geometry. The valid intersection points are marked *blue*, whereas invalid intersections are indicated in *purple*.

These criteria are computed as follows:

a) hit from inside: whether the particle hits from inside or outside is computed by a scalar product of the surface normal $\vec{n}$ and the particle's direction vector $\vec{v}$

$$\vec{n} \circ \vec{v} = \begin{cases} > 0 & \text{hit from inside} \\ < 0 & \text{hit from outside.} \end{cases} \tag{3.7}$$

b) travel forward: with the distance of the sound particle to the current wall t in the direction of travel (found by a *line-line* intersection test[Gla90]), the particles travel forward for $t > 0$ and backward for $t < 0$

$$t = \begin{cases} > 0 & \text{travel forward} \\ < 0 & \text{travel backward.} \end{cases} \tag{3.8}$$

c) inside wall: with the intersection point $\vec{I}$, the starting point of the current wall $\vec{P}$ of length l and the normalized direction vector $\vec{a}$ in the direction of the wall, the intersection is

$$\left(\vec{I} - \vec{P}\right) \circ \vec{a} = \begin{cases} \geq 0 \wedge \leq l & \text{inside the wall} \\ < 0 \vee > l & \text{outside the wall.} \end{cases} \tag{3.9}$$

d) minimum distance: the intersection point with minimum distance is usually found by defining a large distance $d_{Min} = 1000.000$ as initial minimum distance and updating d_{Min} for each valid intersection with a distance $d < d_{Min}$

$$d_{Min} = d = \left|\vec{I} - \vec{S}\right| \text{ if } d < d_{Min}. \tag{3.10}$$

In a loop over all walls, every wall is tested whether the current particle's direction vector aims in the direction of the surface normal [3.6a]. Then the intersection between the wall and the sound particle is computed and the intersection point is tested whether it lies in the direction of travel of the sound particle [3.6b]. If the sound particle lies in-between the wall boundaries [3.6c], the intersection is a valid intersection point. Out of the set of valid intersection points, the intersection point with the closest distance to the sound particle's starting point is chosen as the resulting intersection point [3.6d].

For convex polygons, the four criteria reduce to two, because criteria *a*) and *b*) as well as *c*) and *d*) are identical for convex polygons. Criterion *b*) is limited to a *line-line* intersection test in $2D$, but a more complicated *point-in-polygon* test[Gla90] has to be performed for $3D$. Thus, in a convex $2D$ geometry only criteria *a*) and *c*) are evaluated. A comparison is shown in List. 3.1.

```
function findWallIntersection() // non convex
Vec IMin // container for intersection
float dMin = 1000.000f; //initialize distance with large value
for (all walls)
  I = findCurrentIntersection(); // line - line - intersection
  if(n * v > 0) // see Eqn. 3.7
    if(t > 0)  // see Eqn. 3.8
      if(0 <= (I-P)*a <= 1) //see Eqn. 3.9
        d = |I-S|; //see Eqn. 3.10
        if(d < dMin) //see Eqn. 3.10
          IMin = I;
          dMin = d;

function findWallIntersection() // convex
Vec I // container for intersection
for (all walls)
  I = findCurrentIntersection(); // line - line - intersection
  if(n * v > 0) // see Eqn. 3.7
    if(0 <= (I-P)*a <= 1) //see Eqn. 3.9
      IMin = I;
      break;
```

Listing 3.1: Pseudocode of the determination of a wall intersection.

3.4.3. Wall Interaction

A sound particle is interpreted as a small fraction of a plane wave propagating in direction of the sound particle. Hence, sound absorption of a plane wave (see Sec. 2.3.2) has to be taken into account. Furthermore, the air attenuation (see Sec. 2.3.1) for the travelled distance since the last wall interaction r has to be considered. In total, the sound energy of the sound particle has to be multiplied with the energy reduction factor

$$e^{-mr} \cdot (1 - \alpha). \tag{3.11}$$

For complete geometrical reflections ($\sigma = 0$, see Sec. 2.3.3) the reflection direction $\vec{v_r}$ is determined according to *Snell*'s law (see Fig. 2.4)

$$\vec{v_r} = \vec{v_i} - 2\,(\vec{v_i} \circ \vec{n}) \cdot \vec{n}, \tag{3.12}$$

where $\vec{v_i}$ is the direction of incidence and $\vec{n}$ the surface normal. The energy of the reflected sound particle computes as in Eqn. 3.11.

For (even partly) scattering surfaces, mainly three different methods[Dal11, SP13] are possible:

direction randomization The scattering coefficient σ is interpreted as a probability. For a random number $z \in]0,1[$ with $z > \sigma$ the sound particle is reflected geometrically, while it is diffusely reflected for $z < \sigma$. In both cases, the sound particle energy is unaffected. For diffuse reflections, a random direction vector for the sound particle is chosen (see Sec. 2.3.3). This method is, e.g., used in [Sch11].

energy weighted addition Another possible realization of scattering is to compute both the specularly and the diffusely reflected vectors independently. Then, both vectors are added up after weighting the diffuse direction vector with σ and the specular direction vector with $(1-\sigma)$ and finally renormalizing the new direction vector [Ste04].

recursive split-up The specular and diffuse reflections are handled independently, where diffuse reflections are realized by additional secondary sound particles, i.e., the incident sound particle is split up[Dal96].

As only the third method results in a split-up of sound particles, the first and the second method seem to be more efficient than the third method. Indeed, both methods can be simply integrated into classical SPSM algorithms by keeping the *nested loops* (see Sec. 3.4.6). On the other hand, the third method is more accurate, because a higher density of sound particles represents the scattered sound distribution better. In order to achieve this accuracy for the two other methods, more sound particles would have to be used.

In addition, the third method is the only one, where the actual directions of the emitted sound particles are independent of absorption and scattering coefficients and, hence, on the frequency. Thus, the energies of different frequency bands are traced simultaneously by using only one particle, where the energy of each frequency band is subsequently multiplied by different factors[PSS+12, SPD+13]. The necessary modification of the entire simulation method to include the split-up of sound particles is discussed in Sec. 3.4.6.

The diffusely reflected sound energy is represented by a number of S additional secondary sound particles. Together with the sound particle for the geometrically reflected sound energy, in total $S+1$ sound particles are emitted from the scattering surface. For the geometrically reflected sound particle, the energy (relative to the incident energy) is

$$e_0 = e^{-mr} \cdot (1-\alpha) \cdot (1-\sigma). \tag{3.13}$$

Because of energy conservation, the energy for the diffusely reflected sound energy is

$$\sum_{i=1}^{S} e_i = e^{-mr} \cdot (1-\alpha) \cdot \sigma. \tag{3.14}$$

The angle range $-\frac{\pi}{2} < \vartheta < \frac{\pi}{2}$ is separated in S equal angle ranges (relative to the surface normal and independent from the incident angle), such that the i^{th} sound particle is emitted in the direction (see. Eqn. 3.5)

$$\vartheta_i = \frac{i+\frac{1}{2}}{S} \cdot \pi - \frac{\pi}{2}. \tag{3.15}$$

According to *Lambert*'s Law (see Sec. 2.3.3), the energy of the i^{th} sound particle is computed with Eqn. 2.23 to

$$e_i = e^{-mr} \cdot (1-\alpha) \cdot \sigma \int_{\frac{i}{S}\pi-\frac{\pi}{2}}^{\frac{i+1}{S}\pi-\frac{\pi}{2}} \frac{cos(\vartheta)}{2} d\vartheta. \tag{3.16}$$

3.4.4. Detection of Sound Particles

In order to detect infinitesimal small sound particles, spatially extended receivers are required. Different ray tracing techniques use different detection techniques, but mainly three methods are in use:

particle counting The most common method for the detection of sound particles is to count the number of sound particles [Vor08]. Whenever a sound particle intersects with the spatially extended receiver, its current energy is added up in the receiver. This is, e.g., used in [Sch11].

back tracing Another method is to use ray tracing only for the detection of valid image sources. Whenever a sound particle intersects a spatially extended receiver, the image source for the sound particle is constructed and the exact reflection path (to the centre of the receiver) is tested for visibility[Vor89]. This method is only a special technique to detect visible image sources and, thus, not directly a ray tracing method.

inner distance weighting The third method is to count not only the detected sound particles, but to weight them with the distance the sound particle travels within the receiver [Ste85, Ste14].

The third method is a generalization of the first method, as the energy is additionally weighted with the distance the sound particles travel in the receiver. While the first method is faster due to less computational effort, the third method is more accurate, as sound particles passing by the receiver position in a larger distance are weighted with lower energy in contrast to a closer hit. Thus, the third method is chosen in this work.

The sound intensity I of a plane wave can be written as $I = c \cdot w$ [Kut07], where w is the energy density per volume and c the speed of sound. Furthermore, a constant energy density w inside the receiver is assumed. The intensity computes with the detected energy E_D in the receiver to

$$I = c \cdot w = c \cdot \frac{E_D}{V_D}, \tag{3.17}$$

where V_D is the volume of the receiver. Due to the invariance of a translation in $z - direction$ (see Fig. 3.1), this volume is written as a surface S_D within the $x - y-$ plane with a height Δh

$$V_D = S_D \cdot \Delta h. \tag{3.18}$$

The detected energy E_D is determined by adding up all energies E_i of all N_0 sound particles crossing the receiver. As the sound source has a certain sound power, it emits sound particles in time intervals of t_{Ref}. Thus, the detected energy is weighted with the time ratio t_i/t_{Ref}, where t_i is the particle's travel time within the receiver volume. Hence, the ratio describes a probability of the sound particle to be inside the receiver.

The sound intensity I is computed by the distance $w_i = c \cdot t_i$ that the sound particle travels inside the receiver and the energy loss e_i of the sound particle since emission (see Eqn. 3.6)

$$I = c\frac{\sum_{i=1}^{N_0} E_i \frac{t_i}{t_{Ref}}}{V_D} = c\frac{\sum_{i=1}^{N_0} \frac{P' \cdot \Delta h \cdot t_{Ref}}{N} e_i \frac{\frac{w_i}{c}}{t_{Ref}}}{S_D \Delta h} = \frac{P'}{N \cdot S_D} \sum_{i=1}^{N_0} e_i \cdot w_i. \tag{3.19}$$

While the energy fraction e_i that the sound particle loses during absorption, air attenuation, scattering and diffraction is computed during the sound particle tracing, the distance w_i is computed during detection.

The determination of such a time-independent sound intensity I is sufficient, e.g., when an intensity map is of interest (see Fig. 2.15). In order to compute a full time-dependent echogram $I(t)$ (see Fig. 2.14), however, the intersection time of the sound particle in the receiver has to be detected, too. Therefore, each summand of Eqn. 3.19 has to reference to an impact time. This impact time is given by the total length of the sound particle's propagation path d_i (between the source and the centre of the inner crossing distance w_i) divided by the speed of sound c. Using Dirac - impulses $\delta(t)$ to shift the single summands to their respective position, the time-dependent echogram concludes to

$$I(t) = \frac{P'}{N \cdot S_D} \sum_{i=1}^{N_0} e_i \cdot w_i \cdot \delta\left(t - \frac{d_i}{c}\right). \tag{3.20}$$

The spatially extended receivers can be realized either by single receivers that estimate the sound field at particular points or by receiver grids in order to determine the sound distribution in a larger area. In either case, each receiver has to detect energy for each frequency band, which is transported by the sound particle.

3.4.4.1. Single Receivers

For single receivers the most common solution is the usage of circular receivers (in $3D$ spheres). If a sound particle hits the receivers, the inner distance in the receiver has to be determined as follows: between receiver centre $\vec{R}$ and the starting point of the sound particle $\vec{S}$, the direct connection $\vec{l} = \vec{R} - \vec{S}$ is separated in a component l_p parallel to the sound particle direction vector $\vec{v}$ and a second orthogonal component l_n (see Fig. 3.7).

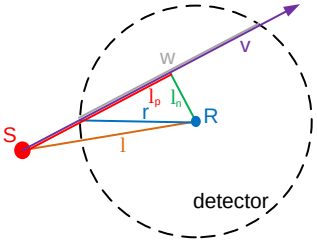

Figure 3.7.: Inner distance of a sound particle in a circular receiver.

The length $\left\|\vec{l}_n\right\|$ equals the bypass distance of the sound particle and, thus, an intersection occurs if $\left\|\vec{l}_n\right\| < r$[b)]. Finally, the inner distance is computed with

$$w = 2 \cdot \sqrt{r^2 - \left\|\vec{l}_n\right\|^2}. \tag{3.21}$$

[b)] the intersection point is only valid, if the intersection is in the direction of travel of the sound particle($l_p > 0$)

3.4.4.2. Receiver Grid

A complete grid of receivers is constructed by a rectangular shape with the dimension w_{grid} in both $x-$ and $y-$ direction[Ste85].

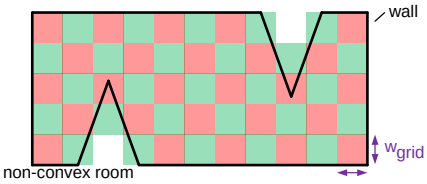

Figure 3.8.: Rectangular grid of receivers. Receivers are coloured *red* and *green*.

Instead of using these receivers independently, their symmetric alignment is used to gain higher efficiency. This technique is similar to the voxel (small cubes) crossing acceleration technique for intersection tests [Gla89, Ste06, Sch11]. The starting point $\vec{S}$ and the end point $\vec{E}$ have to lie within the receiver grid.

The algorithm starts by finding the indices of the starting point's voxel. In $2D$, voxels are defined by $i \cdot w_{grid} < x < (i+1) \cdot w_{grid}$ and $j \cdot w_{grid} < y < (j+1) \cdot w_{grid}$, where the indices i and j describe the indices in $x-$ and $y-$direction. Thus, the tuple (i_T, j_T) of the starting voxel computes[c)]

$$(i_T, j_T) = \left\lfloor \frac{\vec{S}}{w_{grid}} \right\rfloor . \tag{3.22}$$

For the determination of the detected energy, the distances $d_{x,y}$ to the voxel boundary in $x-$ or $y-$ direction read

$$d_x = \begin{cases} \frac{(i+1) \cdot w_{grid} - P_x}{v_x} & v_x > 0 \\ \frac{i \cdot w_{grid} - P_x}{v_x} & v_x < 0 \end{cases} \quad \text{and} \quad d_y = \begin{cases} \frac{(j+1) \cdot w_{grid} - P_y}{v_y} & v_y > 0 \\ \frac{j \cdot w_{grid} - P_y}{v_y} & v_y < 0 \end{cases} , \tag{3.23}$$

where $\vec{v}$ is the direction vector of the sound particle (see Fig. 3.9).

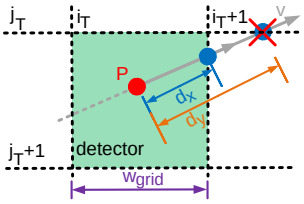

Figure 3.9.: Inner distance of a sound particle in a receiver grid.

The minimum $w = min\,(d_x, d_y)$ indicates the valid intersection and is automatically the inner distance of the sound particle propagation path in the voxel (i_T, j_T). The

[c)] $\lfloor x \rfloor$ is the floor function yielding the largest previous integer

indices of the next tuple (i_N, j_N) are

$$(i_N, j_N) = \begin{cases} (i_T + 1, j_T) & d_x \leq d_y, v_x > 0 \\ (i_T - 1, j_T) & d_x \leq d_y, v_x < 0 \\ (i_T, j_T + 1) & d_x > d_y, v_y > 0 \\ (i_T, j_T - 1) & d_x > d_y, v_y < 0 \end{cases}, \tag{3.24}$$

such that the inner distances of the receivers are found as above. This procedure is repeated until the total inner distance of all voxels w_{total} equals the distance between the starting point and the end point of the particle. The algorithm is summarized in List. 3.2.

```
function gridDetection()
int [iT,jT] = (int) (startingPoint/wGrid); // see Eqn. 3.22
float [dx, dy] = computeDistances(); // see Eqn. 3.23
detectEnergy(iT,jT,min(dx,dy));
while(traveledDistance<=totalDistance)
{
  [dx, dy] = computeDistances(); // see Eqn. 3.23
  detectEnergy(iN,jN,min(dx,dy));
  [iN, jN] = computeNextIndices(); // see Eqn. 3.24
  startingPoint = Vec(iN, jN) * wGrid;
}
```

Listing 3.2: Pseudocode of the detection of a sound particle by a receiver grid.

3.4.5. Abort Criteria

The sound particles are traced until the propagation is aborted, which can be decided by four criteria:

Distance/Time Sound particles are traced until a user-defined maximum propagation time is reached. This maximum time defines the length of the echogram.

Energy Sound particles are traced until the energy of the sound particle is below a certain energy threshold.

Annihilation Whenever a sound particle intersects with a wall, a random number $z \in]0, 1[$ is compared to the local absorption coefficient. For $z < \alpha$, the sound particle is annihilated.

Reflection Order Sound particles are terminated if a user-defined maximum reflection order is reached.

Although the reflection order is the most plausible criterion, it only partially has a physical basis. The distance criterion seems very plausible, but is no secure criterion, as sound particles can get stuck in corners of the geometry. Then, they practically travel no distance anymore which could lead to infinite loops. The energy criterion, however, is the most secure criterion, but the value of the threshold is hard to define safely for every scene, especially with split-up of sound particles. A crucial point is that the number of sound particles in a distant shadow region might be far below a statistical average. Then, even sound particles with less energy might be important in these regions. The annihilation is discussed in detail in [Vor88].

In conclusion, a variation of the energy criterion from the distance criterion is used in this work. However, it has to be checked that enough sound particles are detected in any region.

Starting with the maximum distance $s_{Max} = c \cdot T_{Max}$ given by the energy echogram and the MFPL $\bar{l}$[Kos60], the average number of reflections $\overline{o}$ computes to

$$\overline{o} = \frac{s_{Max}}{\bar{l}}. \tag{3.25}$$

The energy loss of a sound particle is dependent on the sound absorption coefficient α and the number of secondary sound particles S per reflection. With the mean absorption coefficient $\overline{\alpha}$ of the room, the average energy loss per reflection is defined to $\frac{1-\overline{\alpha}}{1+S}$.

From this it follows that the energy threshold (including the air attenuation) is defined by

$$e_{Threshold} = e_{Safety} \cdot e_{Expected} = e_{Safety} \cdot \left(\frac{1-\overline{\alpha}}{1+S}\right)^{\overline{o}} \cdot e^{-m s_{Max}}, \tag{3.26}$$

where s_{Max} is the maximum travel distance and an additional safety factor e_{Safety} is introduced. The latter is introduced to compensate the statistical variations of the average energy loss. However, this safety factor is neglected for statistical evaluations in the following ($e_{Safety} = 1$).

By terminating sound particles within a finite number of reflections (e.g., by thresholds such as minimum energy or maximum travel distance), a small portion of energy is neglected, called *the remaining reverberation energy*[Ste90].

3.4.6. Main Algorithm

The algorithm of the SPSM is classically realized by nested loops. In a loop over all sound sources, a second loop handles all sound particles of the sound source. For each sound particle, a third loop handles the wall reflections including the detection and absorption until the abort criterion terminates the sound particle. The algorithm is summarized in List. 3.3.

```
function soundParticleSimulation()
for (all sources)
  for (all sound particles)
    while(energy > energyThreshold) // see Eqn. 3.26
      findWallIntersection(); // use convex shape, see Sec. 3.4.2
      detectSoundParticle(); // single or grid, see Sec. 3.4.4
      energy = energy * (1 - alpha) * exp(-m * r); // see Eqn. 3.11
      v = v - 2 (v * n) * n // see Eqn. 3.12
```

Listing 3.3: Pseudocode of the Sound Particle Simulation Method algorithm by nested loops.

Unfortunately, this simple algorithm is not applicable for a split-up of sound particles. Instead, a function for the sound propagation between two walls is needed that calls itself recursively. The other procedures are identical to the nested loop version. The recursion is summarized in List. 3.4.

```
function soundParticleSimulation()
for (all sources)
  for (all sound particles)
    traceSoundParticle();

function traceSoundParticle()
findWallIntersection(); // use convex shape, see Sec. 3.4.2
detectSoundParticle(); // either single or grid, see Sec. 3.4.4
energy = energy * (1 - alpha) * exp(-m * r); // see Eqn. 3.11
for (all secondary sound particles) // split-up in S + 1
  if(i==0) // specular reflection
    float newEnergy = energy * (1 - sigma); // see Eqn. 3.13
    v = v - 2 (v * n) * n // see Eqn. 3.12
  else
    float newEnergy = energy * scatteringRatio(); // see Eqn. 3.16
    v = computeScatteredDirection(); // see Eqn. 3.15

  if(newEnergy > energyThreshold) // see Eqn. 3.26
    traceSoundParticle(); // recursive call
```

Listing 3.4: Pseudocode of the Sound Particle Simulation Method algorithm by recursive calls (including split-up).

3.5. Beam Tracing

Although the present work focusses on the SPSM, a brief description of Beam Tracing (BT) is added, as the fundamental ideas are needed later for the discussion of Quantized Pyramidal Beam Tracing (QPBT). BT can be understood as an efficient version of the image source method (i.e., using the $1/r$ law directly) combined with the straight forward detection technique of ray-based simulation methods. It was first introduced in computer graphics[HH84, DKW85] and has later been applied to the computation of acoustics[MMOD96, DL00, FTC$^+$04], too. The main difference to the common ray-based simulation methods is that beams are spatially extended and, thus, the receivers remain point-like for BT. In general, two very different versions of BT exist today.

In the first group, spatially extended beams are mainly defined by a center-ray and an angle range around that direction[Lew93]. In cone tracing [Ama84, VvM86], the cross sections of the beams are restricted to a circular cross shape with a constant angular range. For the $3D$ environment this yields inaccuracies, as circular shaped beams cannot cover the whole angle range homogeneously. Thus, beams are either overlapping or gaps occur in-between them (see Fig. 3.10).

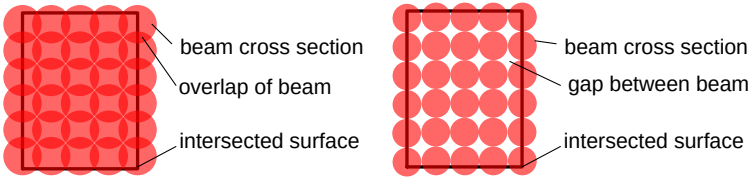

(a) overlap of beams **(b)** gap between beams

Figure 3.10.: Different arrangements of cone tracing fit a rectangular wall.

A major drawback of this approach is that it also computes additional invalid sound paths (which can be cancelled out by back tracing) and ignores valid sound paths. On the other hand, this type of BT can handle diffuse reflections by an application of the energy-weighted addition (see Sec. 3.4.3) to the center-ray.

The second group of BT methods is algorithmically more complicated, but avoids the inaccuracies of gaps and overlaps. One of these methods splits up the beams not exactly, but the wrongly detected beams are eliminated by back tracing[LSLS09]. In contrast to the first group, these BT methods require a split-up of beams and can only handle specular reflections[Far00], but early approaches exist to combine BT with diffraction[WD81]. Due to the exact results, this method is chosen in this work and described in more detail.

Similar to the SPSM, a number of beams are emitted from a sound source and traced through the scene. With each reflection the beams are split up into several secondary beams, such that the secondary beams are reflected geometrically. Receivers within the beams are detected and the energy of the beam is counted by the receivers.

As the computation of propagating beams is even in $2D$ much more complicated than for sound particles, the following description is restricted to convex geometries. For non-convex setups, a sub-division into convex subspaces is required to reduce the geometrical complexity (see chapter 4).

The single steps of BT are described in the following sections.

3.5.1. Emission of Beams

In the exact BT methods, the shape of the beam has to be defined precisely. Therefore, the beam is defined by a polynomial shape[FTC+04], which results in pyramidal beams in $3D$. Here, one beam per wall is emitted for each sound source. While sound particles represent a constant angle range, beams have generally different angle ranges. The sum of all angle ranges of these beams represents the complete angle range of 2π. As the beam is spatially extended, two instead of one direction vectors are needed to define the beam. The region of a beam is defined between the direction vector $\vec{v}_1$ and $\vec{v}_2$ counter-clockwise (see Fig. 3.11). In this initial step, they are set to either the starting point $\vec{S}_i$ or the end point $\vec{E}_i$ of the wall i, with

$$\begin{aligned} \vec{v}_1 &= \vec{S}_i \\ \vec{v}_2 &= \vec{E}_i. \end{aligned} \tag{3.27}$$

The starting point of a beam at emission is defined by the source position. The beam represents a fraction of the sound power per length P'. This is described by the current sound power density per angle $\frac{dP'}{d\alpha}$ multiplied by the angle range spanned by the two direction vectors. This density is stored in the dataset of the beam and set initially to $\frac{P'}{2\pi}$. Again, multiple powers are carried simultaneously for multiple frequency bands. In summary, an emitted beam is defined by

- sound power density
- starting point
- two direction vectors

3.5.2. Wall Intersection Test

At every wall intersection, the intersection points $\vec{Q}_1$ and $\vec{Q}_2$ of the direction vectors $\vec{v}_1$ and $\vec{v}_2$ with the surface have to be determined by independent intersection tests as described in Sec. 3.4.2. As $\vec{v}_1$ and $\vec{v}_2$ intersect different walls in general, the beam has to be split up into one beam per wall between those intersection points (see Fig. 3.11).

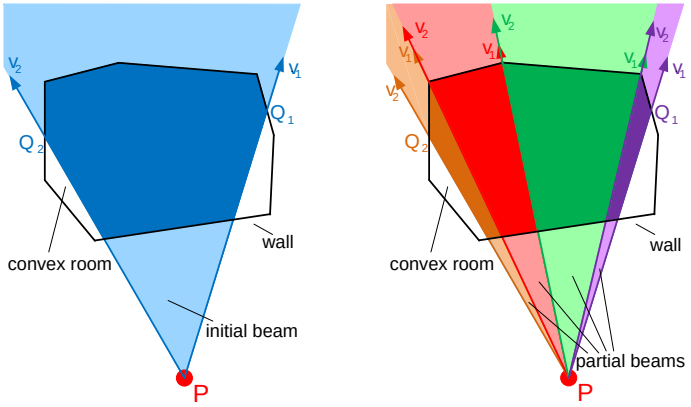

(a) before split-up **(b)** after split-up

Figure 3.11.: Split-up of a beam intersecting with different walls.

Assuming that the intersection $\vec{Q}_1$ lies on the wall a_1 and the intersection $\vec{Q}_2$ on the wall a_2, all walls $a_1 \leq i \leq a_2$ receive a part of the incident beam. In principle, all intersection points of the split beams are set to the starting point $\vec{S}_i$ or the end point $\vec{E}_i$ of the target wall i. For $i = \{a_1, a_2\}$ the walls are only hit by part, such that the computed intersection points have to be inserted. The first intersection point of the beam at $i = a_1$ is retained to be $\vec{Q}_1$ whereas the second intersection point of the beam at $i = a_2$ is retained to be $\vec{Q}_2$ (see Fig. 3.11).

In total, the new direction vectors of the split beams read

$$\vec{v}_1 = \begin{cases} \vec{Q}_1 - \vec{P} & i = a_1 \\ \vec{S}_i - \vec{P} & i > a_1 \end{cases} \quad \text{and} \quad \vec{v}_2 = \begin{cases} \vec{Q}_2 - \vec{P} & i = a_2 \\ \vec{E}_i - \vec{P} & i < a_2 \end{cases} . \tag{3.28}$$

3.5.3. Wall Interaction

The starting point of a beam[d)] is mirrored on the wall after each split-up. This mirrored point equals exactly the image source position for the regarded combination of reflections. In addition, the direction vectors have to be either mirrored or reconstructed by a connection between the image source position and the former intersection points. It should be noted that the sequence of the direction vectors has to be inverted to keep the counter-clockwise definition of the beam region. The power of the beam has to be reduced by the same factor as for the sound particles (see Eqn. 3.11).

3.5.4. Detection of Beams

In contrast to ray tracing methods, the receivers remain point-like due to the spatial extension of the beams. An exact determination of time and location is possible. For the valid detection of a receiver within a beam, the receiver must be located inside the beam, i.e., between $\vec{v}_1$ and $\vec{v}_2$ in counter-clockwise direction. No additional criteria are necessary in case of convex sub-spaces assuming that the receiver is located in the

[d)] source position for beams of order 0

current sub-space. The receivers can be either independent points or aligned in a grid, identical to the SPSM approach.

The energy for each receiver is computed by the $\frac{1}{r}$ law, where r is the distance between the receiver $\vec{R}$ and the beam's starting point $\vec{S}$ (image source position). Without the energy loss due to wall reflections, the beam's power density per angle $\frac{P}{2\pi}$ directly yields the free-field intensity

$$I = \frac{P}{2\pi}\frac{1}{r}. \tag{3.29}$$

3.5.5. Abort Criteria

In principle, the same abort criteria as for the SPSMs are used for BT algorithms. Furthermore, the opening angle of a beam is limited by a lower boundary skipping all beams with an opening angle below a certain threshold α_{Min}. Mathematically speaking, a beam with normalized direction vectors $\vec{v}_{1,2}$ has to fulfil

$$\Delta\alpha = acos\left(\vec{v}_1 \circ \vec{v}_2\right) > \alpha_{Min} \tag{3.30}$$

to be further processed. As the beams opening angle decreases with the reflection order due to the on-going split-up, the opening width (Euclidian distance between the intersection points $\vec{Q}_{1,2}$) can also be tested against a lower boundary a_{Min}. Following this definition, all beams with an opening width of

$$\Delta a = \left|\vec{Q}_1 - \vec{Q}_2\right| > a_{Min} \tag{3.31}$$

are further traced.

In this work, the SPSM energy criterion is combined with an opening width criterion. If at least one of these criteria is not fulfilled, the beam is aborted.

3.5.6. Main Algorithm

The beams are split-up at every wall intersection where a beam hits several walls. Hence, an implementation by nested loops is impossible for BT and only recursive calls can be applied.

In a loop over all sources, a second loop handles all walls of the convex sub-space where the sound source resides. Each wall spans a beam that is traced independently. In order to trace these beams, first (both) wall intersections have to be found and a secondary beam for all walls in-between these intersections (counter-clockwise) has to be constructed. These secondary beams are used to detect all receivers that are located within the beam before their energy is reduced and the beam is mirrored at the respective wall. Finally, if no abort criterion aborts the tracing of the beam, this function is called recursively. The algorithm is summarized in List. 3.5.

```
function beamTracing()
for (all sources)
  for (all walls)
    createBeamDirectionVectors(); // see Eqn. 3.27
    traceBeam();

function traceBeam()
findWallIntersection(); // use convex shape 2x, see Sec. 3.4.2
for (all intersected walls)
  createPartialBeamDirectionVectors();  // see Eqn. 3.28
  detectBeam(); // either single or grid, see Sec. 3.5.4
  float newPower = power * (1 - alpha) * exp(-m * r); // Eqn. 3.11
  v1 = v1 - 2 (v1 * n) * n // see Eqn. 3.12
  v2 = v2 - 2 (v2 * n) * n // see Eqn. 3.12
  switch(v1,v2) // ensure counter-clockwise

  if(newPower > powerThreshold AND aMin > aDelta) // Eqn. 3.26, 3.30
    traceBeam(); //recursive call
```

Listing 3.5: Pseudocode of the Beam Tracing algorithm by recursive calls.

3.6. Acoustic Radiosity

The Acoustic Radiosity method was first formulated for the computation of heat exchange between surfaces[McA54]. Later it has been used in computer graphics to compute the interaction of light between diffuse surfaces[GTGB84] and it was also successfully applied to acoustical problems[Kut71, Lew93, Kut95]. In recent years, a generalization was formulated, called the room acoustic rendering equation[SLKS07].

The method by Miles[Mil84] assumes that after only a few reflections in a closed volume with at least partly scattering walls, the reflections are completely diffuse. Hence, all specular reflections are neglected. In this work, the idea of discretizing the surface into patches is an important part of the reunification of the Sound Particle Radiosity (SPR) and QPBT.

The basic idea of the Acoustic Radiosity is to define energy exchange factors between every point x' to x on a closed circumference C of an acoustic environment (see Fig. 3.12).

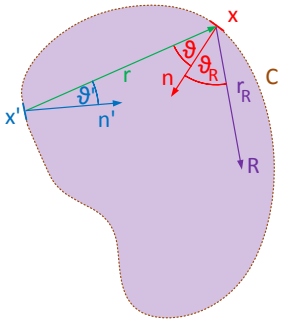

Figure 3.12.: Geometrical definitions of the Acoustic Radiosity method (after Miles [Mil84]).

The energy exchange factor $K(x, x')$ is proportional to two factors: a) the energy distribution from the emission point $\frac{dp}{d\vartheta}$ and b) the projection factor $\frac{d\vartheta}{ds}$. As diffuse reflections are assumed, the energy distribution factor follows Eqn. 2.23. The projection factor, however, is derived graphically from Fig. 3.13a,

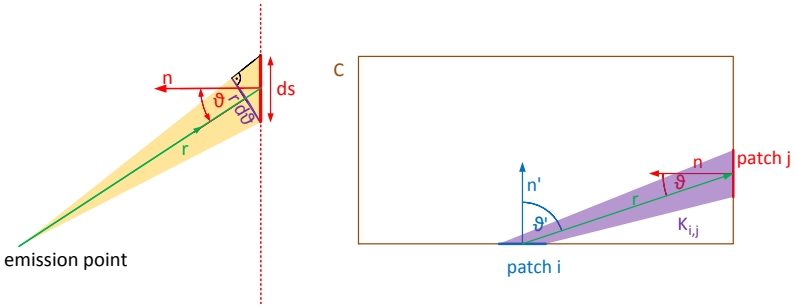

(a) cosine at incidence **(b)** rectangular room

Figure 3.13.: Energy exchange factors $K_{i,j}$ of Acoustic Radiosity between two patches i and j.

such that the energy exchange factor $K(x, x')$ reads[e)]

$$K\left(x, x'\right) = \frac{dp}{d\vartheta} \cdot \frac{d\vartheta}{ds} = \frac{cos\left(\vartheta'\right)}{2} \cdot \frac{cos\left(\vartheta\right)}{r}. \tag{3.32}$$

In both cases, the angles ϑ and ϑ' denote the angles between the connection $\overline{xx'}$ and the surface normals at x' and x, respectively. The distance between x' and x is denoted as r. Due to energy conservation, the total sound energy that is received at all receiving areas x has to be equal to the emitted sound energy at x'. Thus, the energy exchange factor $K(x, x')$ has to fulfil

$$\int_C K\left(x, x'\right) ds = 1. \tag{3.33}$$

To compute the irradiation strength at the circumference $I_C(x, t)$, a differential equation is composed by using the energy exchange factor $K(x, x')$ and the sound irradiation strength due to direct radiation from the sound source $I_D(x, t)$, with

$$I_C(x, t) = \int_C K\left(x, x'\right) \cdot I_C\left(x', t - \frac{r}{c}\right) \cdot (1 - \alpha) \cdot ds' + I_D(x, t). \tag{3.34}$$

Once the sound intensity $I_C(x, t)$ on the circumference is known, $I_C(x, t)$ is reradiated into the room to determine the sound intensity $I(x_R, t)$ at any position x_R inside the circumference.

$$I(x_R, t) = \int_C I\left(x', t - \frac{r_R}{c}\right) \cdot (1 - \alpha) \cdot \frac{cos\left(\vartheta'\right) \cdot cos\left(\vartheta_R\right)}{2 \cdot r_R} \cdot ds' + I_D(x_R, t). \tag{3.35}$$

[e)] in the $3D$ case, the denominator has to be modified to $\pi \cdot r^2$

Analytical solutions to the differential equation only exist for a small range of acoustical setups, but, in general, a numerical solution is required. Along with this numerical solution, the surface has to be discretized in small surface elements called *patches* (see Fig. 3.13b) [NHA04].

For all combinations of the starting patch (with index i) with the end patch (with index j), the propagating energy has to be determined by an energy exchange coefficient $K_{i,j}$. $K_{i,j}$ is computed by integration of Eqn. 3.32 over the surface of both the starting and the end patch and normalized to the length of the starting patch $l_{P,S}$

$$K_{i,j} = \frac{1}{l_{P,S}} \int_{l_{P,S}} \int_{l_{P,E}} K\left(x, x'\right) \cdot ds_j ds_i. \tag{3.36}$$

Even for simple scenes, the energy exchange coefficients are hard to compute, which is the reason why these coefficients are usually calculated my means of numerical methods. In numerical simulations, a large linear equation system has to be solved using the energy exchange factors computed in a pre-processing step.

4. Acceleration of Geometrical Acoustic Simulation Methods

The Computation Time (CT) of Beam Tracing (BT) and the Sound Particle Simulation Method (SPSM) is mainly dominated by the search for intersection points during the computation of sound propagation paths, called collision detection. Therefore, many techniques for the acceleration of these collision detection tests exist. On the other hand, the computation of diffraction with Geometrical Acoustic (GA) simulation methods requires a sub-division of space into convex sub-spaces. Considering Kirchhoff theory (see Sec. 2.3.4.3), diffraction occurs just at these apertures. Algorithmically, a sub-division by Virtual Walls (VWs) prevents the difficult and time consuming search for edges that are passed by closely[PS10b]. Several work has been performed to combine the sub-division technique with diffraction[TFNC01, FTC+04], but these sub-division techniques are not able to detect multiple edges that are passed by simultaneously (see Sec. 5.2.3 for more details).

In this chapter, first a brief overview over the commonly used sub-division techniques is given. Afterwards, a new sub-division technique is presented in $2D$, which is optimized for both the reduction of the CT and the automatic detection of diffraction events. Finally, a statistical approximation of the speed-up of this sub-division technique is shown together with a verification of the approximation.

4.1. Related Work

Collision detection is a fundamental problem in computer graphics, especially in scenarios with a great number of walls n. The three main techniques can be separated in bounding volume hierarchies, sub-divisions in adjacent sub-spaces and binary space partitionings, which are briefly described here. In addition, a sub-division technique by Stephenson is discussed.

4.1.1. Bounding Volume Hierarchy

In order to reduce the CT, bounding volumes can be used to cluster more complex geometrical objects. An intersection test is first performed for this simplified scene, and the hit bounding volume in then inspected further[Eri04]. These bounding volumes can either be spheres[Hub96], axis aligned bounding boxes[vdB98], oriented bounding boxes[GLM96], discrete oriented polytopes of order k (in $3D$: polyhedra)[KHM+98] or convex hulls. More complex bounding volumes yield better culling, whereas more simple bounding volumes yield faster intersection tests. This acceleration method is mainly used for collision tests, where complex objects occur with low density in the geometrical scene. Then, the CT is reduced drastically by skipping all polygons that do not lie within the hit bounding volume. A speed-up cannot be defined generally, as it strongly depends on the density of objects instead of the number of vertices or walls.

4.1.2. Sub-Divisions in Adjacent Sub-Spaces

Another technique is to divide the scene in adjacent, non-overlapping sub-spaces. Uniform grids are constructed by subdividing the complete geometrical scene into small voxels of equal size[Gla89]. For each object of the geometrical scene, all voxels containing the object are computed and a link-up to the object is stored in the voxel. This method can be used best for small objects with high density. For fewer objects, however,

spatial hashing can be used on a uniform grid[THM+03]. By using a hashing table, only the voxels containing objects have to be stored and can be accessed efficiently.

Using a uniform grid, a speed-up from $\mathcal{O}\left(n^2\right)$ to $\mathcal{O}\left(\sqrt{n}\right)$ is achieved[Ste06], but this technique is even more efficient for moving objects, as hashing tables can be updated faster than the bounding volumes or binary space partitioning trees for each translation[Sch11].

4.1.3. Binary Space Partitioning

In binary space partitioning, the geometrical scene is subdivided hierarchically and the scene elements are stored in a tree-like structure[Eri04]. Here, the root node is the entry point to the complete geometrical scene. Each node contains a partitioner that splits the space into two sub-spaces, indicated as *positive* or *negative* halfspace. The names are derived from the position of the halfspaces in relation to the partitioner, i.e., either in front (*positive*) or behind (*negative*) the partitioner. The sub-division is performed recursively until the remaining sub-space is convex (such a node is called *leaf*). A detailed description on how to find the intersection point of ray and the geometrical scene is given in [Sch11]. For a balanced tree, i.e., a tree of minimum height, a speed-up from $\mathcal{O}\left(n^2\right)$ to $\mathcal{O}\left(log_2\left(n\right)\right)$ is achieved.

4.1.4. Convex Sub-Division by Cutting off the Largest Possible Convex Sub-Space

All former sub-division techniques are optimized for an acceleration of the CT and are not capable of diffraction detection directly. Therefore, Stephenson proposed a convex sub-division (in $2D$) by cutting off the largest possible convex polygon recursively[Ste04]. As diffraction occurs basically on protruding wedges, called Inner Edges (IEs) (see Fig. 4.3b), no diffraction has to be computed inside a convex sub-space. Convex sub-spaces are generated by introducing VWs (see Fig. 4.1a, 4.1b).

(a) non convex environment **before** introducing a Virtual Wall

(b) non convex environment **after** introducing a Virtual Wall

Figure 4.1.: Principle of convex sub-division by introducing Virtual Walls.

These VWs are acoustically transparent and connect two convex sub-spaces. As no diffraction occurs in convex sub-spaces, only sound particles that travel from one sub-space to another might be diffracted. Thus, the introduction of VWs makes the detection of diffracted energy very simple (see Sec. 5.2.3).

The principle of Stephenson's approach is to construct a convex sub-space from an arbitrary IE (index i) and a set of adjacent vertices (in counter-clockwise order). Figure 4.2 serves to elucidate this in more detail:

As a first candidate for the insertion of a VW, the vertex with index $i+2$ is chosen (see Fig 4.2a). The index of this vertex is incremented (see Fig. 4.2b) until the constructed polygon is not convex anymore (see Fig. 4.2c). Then, the previous vertex is chosen and

the enclosed polygon (*green*) is cutted off by introducing a VW (see Fig. 4.2d). This procedure is repeated until the remaining polygon is convex, too (see Fig. 4.2e).

Complicated exceptions can occur when other walls intersect the VW to construct even if the polygon to cut off is convex (see Fig. 4.2f).

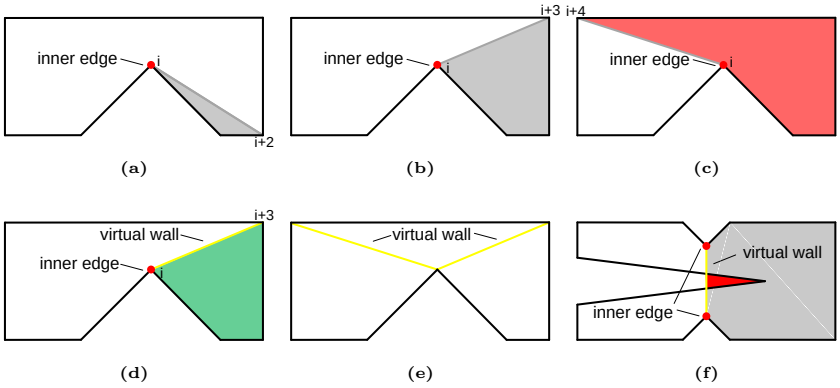

Figure 4.2.: Convex sub-division by cutting of the largest convex polygon possible (after Stephenson [Ste04]).

Although this convex sub-division is capable of detecting diffraction events, three main disadvantages remain:

- the geometrical scene must only consist of one conjunct polygon,
- VWs might be placed far away from the bisecting line, which is not preferable for diffraction detection and
- complicated exceptions can occur by walls intersecting the VWs.

To overcome these issues, a new solution has been found.

4.2. Convex Sub-Division Optimized for the Detection of Diffraction

For the simulation of sound propagation in cities, obstacles, e.g., buildings, hinder the propagation of sound. In a city layout, these obstacles are presented by holes and, thus, the layout has to be described by **multiple, not conjuncted** polygons. Therefore, a convex sub-division allowing non-conjuncted polygons was developed[PS10d], which is optimized for the detection of diffraction.

The positions of the VWs are dependent on the sub-division technique. As an optimized sub-division for the detection of diffraction is aimed at, these VWs have to be located near the bisecting lines of the IEs. Similar to Stephenson's approach, the IEs are chosen as starting point for the insertion of VWs and the sub-division is complete when no IEs remain in the geometrical scene. To find a suitable end point for a VW, a simple form of ray tracing is performed starting with a ray on the bisecting line from the current IE. This VW would introduce an additional vertex at the intersection of the scene with the ray and, thus, increase the complexity. To avoid that, the end point of the VW is moved to either starting or end point of the intersected wall resulting in a smaller change of angle. These steps are described in more detail in the following.

4.2.1. Definition of Inner Edges

In $2D$ the complete scene is defined by a number of closed polygons (4 in Fig. 4.3b). Each of these polygons is constructed from a set of vertices. These vertices enclose the sound propagation environment (*white area*) by connecting them counter-clockwise. As a result, polygons representing obstacles (*black area*) are encountered clockwise. The vectors $\vec{v_i}$ are defined to point from vertex $\vec{P_i}$ to $\vec{P_{i+1}}$ and the normals n_i point outside the sound propagation environment.

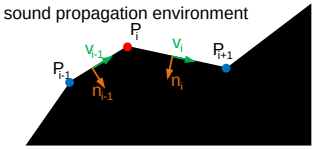

(a) definitions to compute Inner Edges

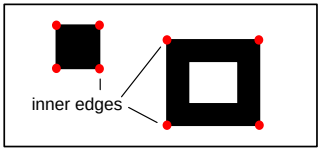

(b) Inner Edges in a city layout

Figure 4.3.: Construction and example of Inner Edges.

As shown in Fig. 4.3a, a vertex $\vec{P_i}$ is an IE if

$$\vec{v}_{i-1} \circ \vec{n}_i \begin{cases} < 0 & \text{IE} \\ \geq 0 & \textbf{no IE} \end{cases} . \tag{4.1}$$

4.2.2. Computation of the End Point of a Virtual Wall

In order to compute the end point of a VW, first the bisecting line of the IE $\vec{P_i}$ has to be determined. The direction vector of the bisecting line $\vec{k}$ reads for a vertex with index i

$$\vec{k} = \frac{\vec{v}_i - \vec{v}_{i+1}}{\|\vec{v}_i - \vec{v}_{i+1}\|}. \tag{4.2}$$

The combination of the IE $\vec{P_i}$ and the direction vector $\vec{k}$ is used as a ray and the intersection point $\vec{K}$ of the ray and the geometrical scene is computed as described in Sec. 3.4.2 (for non-convex geometry). Already constructed VWs are treated as real walls. Although the connection line between the IE $\vec{P_i}$ and the intersection point $\vec{K}$ would result in a valid candidate for the insertion of a VW, one of the already existing vertices is preferred in order to keep the number of vertices of the scene constant. Therefore, the intersection point $\vec{K}$ has to be translated along the intersected wall. The wall is represented by a line segment, such that either the starting point $\vec{S}$ or the end point $\vec{E}$ of the wall is used as new end point $\vec{T}$ for a VW. With the direction vectors $\vec{k}_S = \vec{P_i} - \vec{S}$ and $\vec{k}_E = \vec{P_i} - \vec{E}$, the vertex is chosen that results in a smaller change of angle relative to the bisecting vector $\vec{k}$ (see Fig. 4.4a)[a)]

$$\vec{T} = \begin{cases} \vec{S} & \text{for } \sphericalangle\left(\vec{k}_S, \vec{k}\right) < \sphericalangle\left(\vec{k}_E, \vec{k}\right) \\ \vec{E} & \text{else} \end{cases} \tag{4.3}$$

[a)] The operator $\sphericalangle\left(\vec{x}, \vec{y}\right)$ indicates the (unsigned) angle between two direction vectors.

(a) without intersection **(b)** with intersection

Figure 4.4.: Translation of a Virtual Wall either to the starting point or the end point of the intersected wall.

Due to the translation of the intersection point from $\vec{K}$ to $\vec{T}$, a line of sight between starting point and end point of the VW is not guaranteed anymore and the VW in question might be intersected by other walls. If such an intersection $\vec{J}$ is closer to the starting point than $\vec{T}$ (see Fig. 4.4b), the new intersection has to be translated again either to the starting point or the end point of the intersected wall.

4.2.3. Inserting the Virtual Wall

To insert a VW into the sound propagation environment, two walls are inserted between the starting point and the end point of the VW with reverse vertex order. Each of these walls is used as boundary of the simulation environment. Two cases are possible:

- starting point and end point belong to the same polygon or
- starting point and end point belong to different polygons.

If the starting point and end point belong to the same polygon (see Fig. 4.5a), the polygon has to be split up into two independent polygons. After the creation of a VW (see Fig. 4.5b, *yellow line*), two polygons are created by resorting the vertices (see Fig. 4.5c). Now the VW is duplicated, where one VW is assigned to one newly created polygon (see Fig. 4.5d).

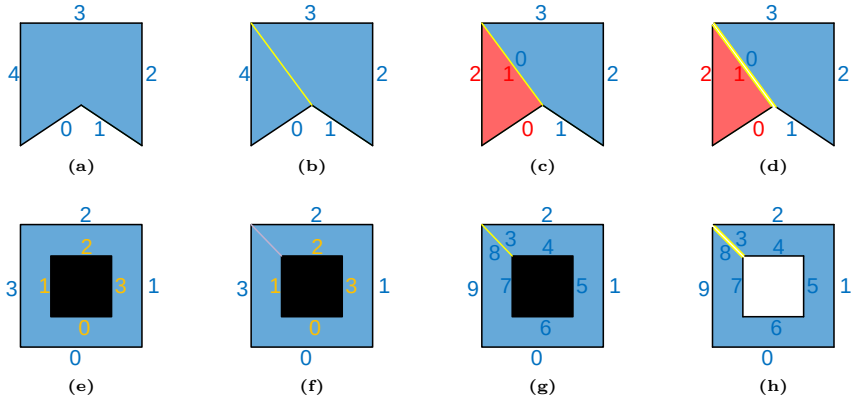

Figure 4.5.: Insertion of a Virtual Wall to divide [(*a*) to *d*)] or combine [(*e*) to *h*)] sub-spaces.

For a VW between different polygons (see Fig. 4.5e), both polygons are connected by the VW (see Fig. 4.5f). The vertices of both polygons are re-arranged such that they construct a closed polygon (see Fig. 4.5g). Again, a duplicate of the VW is used to build a connected polygon that represents the complete sound propagation environment (see Fig. 4.5h).

4.2.4. Main Algorithm

The algorithm of the convex sub-division is based on a loop over all IEs. In each iteration, one IE is processed in a loop until a VW is inserted. In this loop, the intersection of the bisecting line with the scene is computed. The intersection point is translated to either the starting point or the end point of the intersected wall. In case of a new intersection of the translated VW, this routine is repeated until the VW is placed successfully. When a valid VW is found, it is inserted by a rearrangement of the respective vertices. A summary of the algorithm is shown in List. 4.1.

```
function convexSubDivision()
findInnerEdges(); // see Sec. 4.2.1
while(NumerOfInnerEdges!=0)
  Vec P = ChooseInnerEdge(); // random selection
  Vec k = ComputeBisectingDirection(I); // see Eqn. 4.2
  Vec K = findIntersection(I,k); // see Sec. 3.4.2
  while(!VirtualWallConstructed)
    Vec KS = TranslateToStart(K);
    Vec KE = TranslateToEnd(K);
    Vec kS = (KS - P) / length(KS - P);
    Vec kE = (KE - P) / length(KE - P);
    if(angle(kS,k)<angle(kE,k)) // see Eqn. 4.3
      Vec T = KS;
    else
      Vec T = KE;
    Vec J = findIntersection(P,T); // see Sec. 3.4.2
    if(!exist(J))
      insertVirtualWall(P,T); // see Sec. 4.2.3
      VirtualWallConstructed=true;
    else
      K = J;
  updateInnerEdges(); // see Sec. 4.2.1
```

Listing 4.1: Pseudocode of the convex sub-division algorithm optimized for the detection of diffraction.

4.2.5. Example

An example of a convex sub-division is given graphically in Fig. 4.6. Starting with four independent polygons (see Fig. 4.6a), the VWs are inserted directly in Fig. 4.6b, 4.6c, 4.6e, 4.6f, 4.6g and 4.6h. The bisecting line (*orange*) is disconnected in Fig. 4.6d after the translation is interrupted by the inner building (*black*). Then the intersection point is updated accordingly. In Fig. 4.6i a VW is intersected, but handled as a real wall. The final sub-division is shown in Fig. 4.6j. It should be noted that the atrium inside the larger building (*white* square) remains convex, although it is not connected to the remaining simulation environment at all.

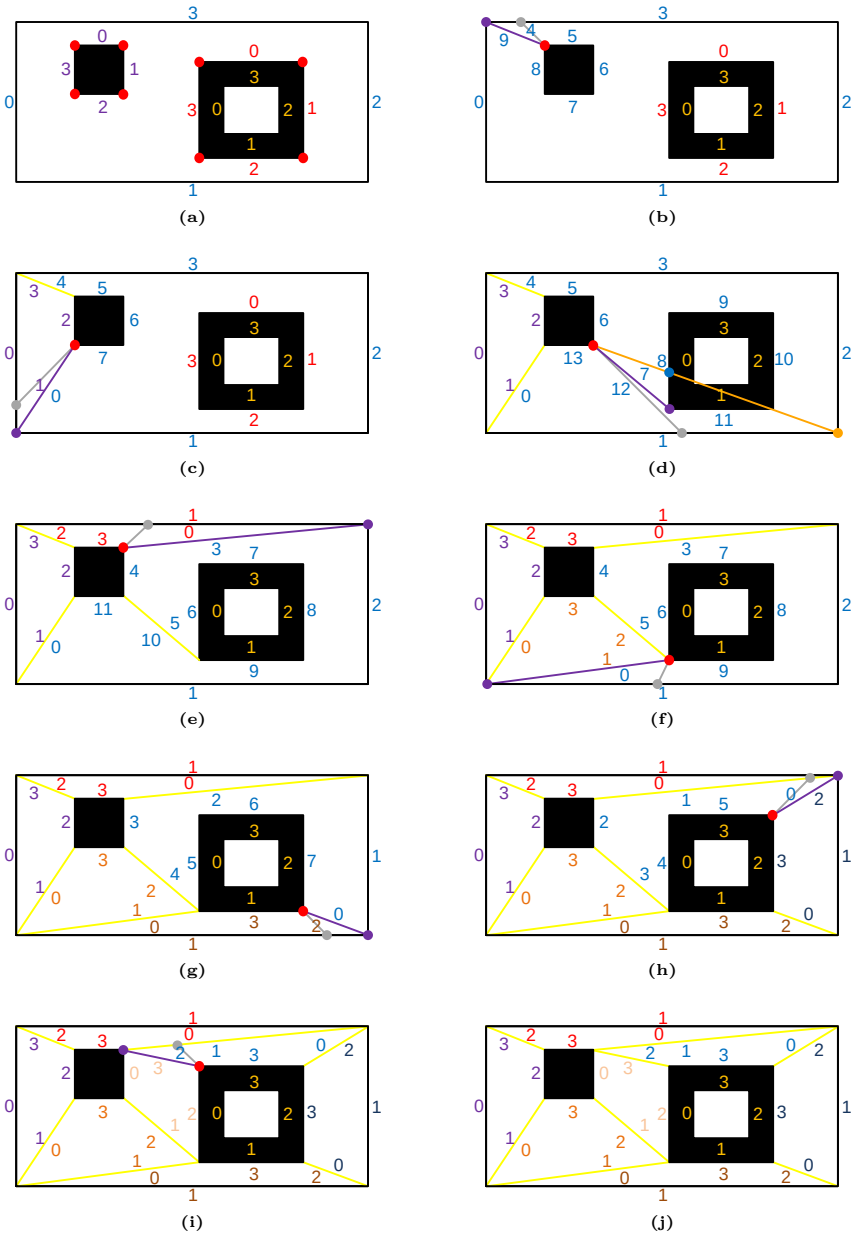

Figure 4.6.: Example sub-division procedure in convex sub-spaces.

4.3. Estimation of the Speed-Up by Convex Sub-Division

The split-up of the geometrical scene into multiple convex sub-spaces has two concurring influences on the CT of the intersection test. First, the number of vertices in a convex sub-space and, thus, the CT to find the next intersection point is reduced (decrease of CT) and, second, sound particles might have to pass one or more VWs until a real wall is intersected (increase of CT).

In order to assess these CTs, two different CTs have to be defined. Both describe the sound propagation from one wall to another, called *iteration* in the following:

- $T_{c,nc}$: The CT for the sound propagation to the physical relevant intersection point (i.e., on a real wall, not a VW) in any convex sub-space and
- $t_{c,nc}$: The CT for the sound propagation to *any* intersection point with a wall (either real or virtual) within the same convex sub-space.

In this section, first the two concurring influences of the convex sub-division are described in more detail and a comparison of both effects is made.

4.3.1. Reduced Computation Time by Convex Sub-Division

The CT for the propagation of a sound particle, an *iteration*, is composed of two parts. One part is to determine the next intersection of the sound particle with the geometrical scene. This part is obviously proportional to the number of walls (and thus the vertices) n. Another part of the CT comes from update- and mirroring processes of the sound particle. This part is independent of the number of walls.

In total, the CT $t_{c,nc}$ (see above) for one iteration is described by two constants $c_{1,2}$ and the number of walls n to

$$t_{c,nc} = c_1 \cdot n + c_2. \tag{4.4}$$

To determine the constants $c_{1,2}$, a sound particle simulation in a regular polygon with different numbers of walls n has been performed. In order to obtain reliable statistical data, a number of $N = 100.000$ sound particles were traced (with no limit on the reflection order). The computations were performed on a standard personal computer (see Tab. 4.1).

CPU:	Intel Core2Quad Q9550 2.83GHz
Level 2 Cache:	2 x 6 MB
Memory:	4 GB
Operating System:	Microsoft Windows Vista Business SP2, 64bit
Development environment:	Microsoft Visual Studio 2008 SP1

Table 4.1.: Personal computer used to determine the Computation Time of the sound propagation by the Sound Particle Simulation Method.

The simulation was performed for different numbers of walls $n = 1..16$, $24, 32, 64$ and with both algorithms (convex (c) and non-convex (nc), see Sec. 3.4.2). The CT for the total simulation is divided by the number of performed *iterations*. The CT $t_{c,nc}$ for one *iteration* is shown in Fig. 4.7.

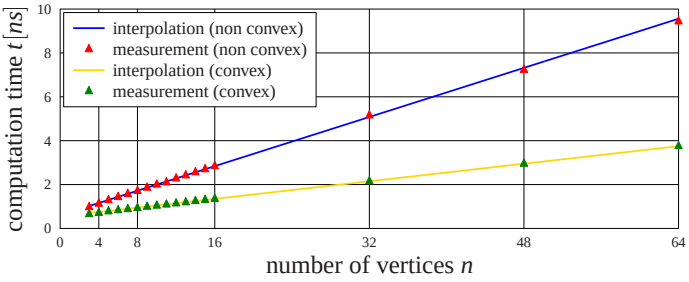

Figure 4.7.: Computation times $t_{c,nc}$ for one *iteration* measured on regular polygons with different numbers of walls compared with the linear regression.

The constants in Eqn. 4.4 are approximated to

$$\begin{aligned} t_{nc} &= 0.14ns \cdot n + 0.6ns \\ t_c &= 0.10ns \cdot \frac{n}{2} + 0.5ns \end{aligned} \tag{4.5}$$

by applying linear regression from the measured CTs for both the convex t_c and the non-convex t_{nc} algorithm. For the convex case, half of the walls are neglected on average, because after a valid intersection point the process is aborted. In addition, the computation in the convex case is accelerated by a factor of 1.5 due to the neglection of criterion d) (see Sec. 3.4.2). The CT c_2, which is independent of the number of walls n, is quite identical for the convex and the non-convex algorithms as the update and mirroring computations are not affected by the convex sub-division.

4.3.2. Increased Number of Wall Reflections

On average more than one *iteration* is needed to find the next real wall due to the insertion of VWs in the sound propagation environment (see Fig. 4.8).

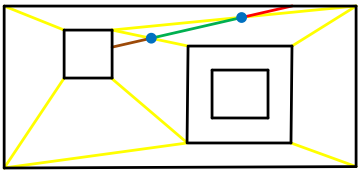

Figure 4.8.: In this example, one *iteration* in the non-convex case is replaced by three *iterations* in the convex case. They are separated by the blue dots at each Virtual Wall intersected.

To estimate this increase, the Mean Free Path Length (MFPL) $\bar{l}$ of both the original and the convex subdivided geometry is investigated.

Assuming a constant surface S of the geometrical scene, the circumference C of the complete geometrical scene is extended by the overall length of the VWs C_{VW}. It should be noted that each VW is counted twice, as each side represents a different sub-space and, thus, can be intersected from both sides (in contrast to a real wall that can only be intersected from inside).

For statistical considerations, a diffuse sound field is assumed, such that

1. the sound energy is distributed homogeneously and
2. each direction of sound propagation is equiprobable.

Thus, the MFPL $\overline{l}$[Kos60] for the complete scene reads

$$\begin{aligned} \overline{l_{nc}} &= \pi \cdot \frac{S}{C} \\ \overline{l_c} &= \pi \cdot \frac{S}{C + C_{VW}}. \end{aligned} \tag{4.6}$$

The smaller the MFPL is, the more *iterations* have to be computed for a sound particle to travel the same distance. The ratio of both MFPLs describes the increase of *iterations*

$$\frac{\frac{1}{\overline{l_c}}}{\frac{1}{\overline{l_{nc}}}} = \frac{l_{nc}}{l_c} = \frac{\pi \cdot \frac{S}{C}}{\pi \cdot \frac{S}{C+V}} = 1 + \frac{C_{VW}}{C}. \tag{4.7}$$

The shape factor $q = \frac{C_{VW}}{C}$ is only dependent on the room shape. It describes the ratio of the length of the VWs relative to the length of the real walls (usually $0 < q < 2$, see Fig. 4.9).

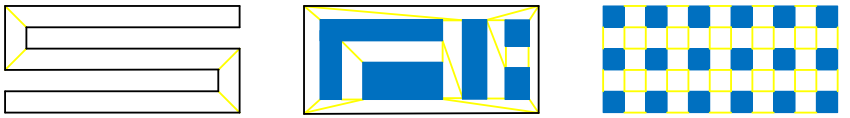

(a) snake shaped room (q = 0.18)

(b) typical city layout (q = 1.11)

(c) rectangular houses (q = 2)

Figure 4.9.: Example of typical shape factors q.

The CT T_{nc}, i.e., the time to find the next real wall, is identical to the CT to find the next wall t_{nc} for a non-convex subdivided scene, whereas for the case of convex sub-division, the shape factor q has to be taken into account

$$\begin{aligned} T_{nc} &= t_{nc} \\ T_c &= t_c \cdot \left(1 + \frac{C_{VW}}{C}\right) = t_c \cdot (1+q). \end{aligned} \tag{4.8}$$

The factor $(1 + q)$ describes the increase of iterations quantitatively.

4.3.3. Comparison of Computation Times in Convex and non-Convex Case

After the determination of the CT in a regular polygon with n walls with and without convex sub-division and describing the increase of *iterations* by a convex sub-division, the total speed-up is computed.

For a complete scene with a total number of walls n_{total}, all these walls have to be tested for intersection. On the other hand, after convex sub-division, only a minor number of walls have to the taken into account for the intersection test *in each sub-space*. On average, a mean number of walls $\overline{n_{convex}}$ is defined. This average number of walls is found to be $\overline{n_{convex}} = 4..5$[Ste04].

For typical geometrical scenes with many perpendicular walls, the average number of walls is even lower ($\overline{n_{convex}} \approx 4$), such that

$$\begin{aligned} T_{nc} &= 0.14ns \cdot n_{total} + 0.6ns \\ T_c &= \left(0.10ns \cdot \frac{\overline{n_{convex}}}{2} + 0.5ns\right) \cdot (1+q) \overset{\overline{n_{convex}} \approx 4}{=} 0.7ns \cdot (1+q)\,. \end{aligned} \tag{4.9}$$

The CT to find the next real wall is, without convex sub-division, proportional to the number of overall walls n_{total} since every wall has to be taken into account. However, (although the single CTs are very low), this is unsustainable for many reflections for complex scenes, where the number of walls can easily be $n_{total} \gg 10.000$.

In contrast, the CT is independent of the number of walls n_{total} after convex sub-division, but increases linearly with the shape factor q. As the shape factor is independent of the number of walls n_{total}, the acceleration of the CT is significant. Both CTs of Eqn. 4.9 are compared in Fig 4.10 in a double logarithmic scale for different shape factors q.

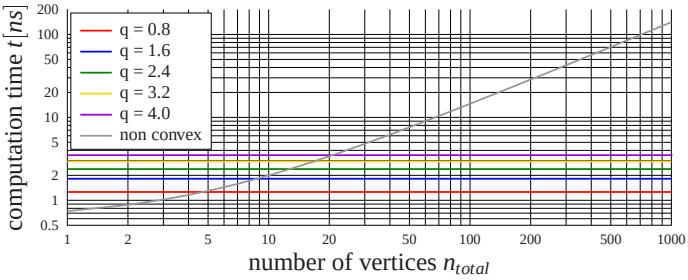

Figure 4.10.: Computation Time $T_{c,nc}$ to find the next real wall for non-convex and convex case for different shape factors q as a function of the number of walls n_{total}.

For very few walls $n_{total} < 20$, the CT after convex sub-division can even be higher than without convex sub-division. This is due to the additional CT by passing the VWs. For a greater number of walls, however, the convex sub-division is very efficient, as the CT is independent of the number of walls.

The CT for convex sub-division itself is in the order of the CT for a first order ray tracing routine, as basically a ray tracing procedure is performed for each IE. This is neglected, as during the simulation many reflections are computed.

The speed-up due to convex sub-division S_{CSD} is defined by the ratio of CT without convex sub-division relative to the CT with convex sub-division. The measure of the achieved speed-up is more meaningful than discussing the actual CTs since it abstracts the underlying architecture and programming language

$$S_{CSD} = \frac{T_{nc}}{T_c} = \frac{0.14 \cdot n_{total} + 0.6}{0.7 \cdot (1+q)} \overset{n_{total} \gg 1}{\approx} \frac{0.14 \cdot n_{total}}{0.7 \cdot (1+q)} = \frac{0.2 \cdot n_{total}}{1+q}. \tag{4.10}$$

The speed-up S_{CSD} increases linearly with the number of walls n_{total} and, therefore, also describes the compensation of the increasing CT without convex sub-division to a constant value.

4.3.4. Numerical Verification of the Statistical Estimations

The speed-up S_{CSD} of Eqn. 4.10 is derived statistically. In order to verify if this still holds for practical use-cases, different geometrical setups have been investigated.

First, the regular polygons are investigated ($q = 0$). As the number of walls is equal in both the initial case and the convex-subdivided case, the approximation $\overline{n_{convex}} \approx 4$ is discarded. Then, the measured speed-up could be verified with a relative error $e < 5\%$ in comparison to the computed speed-up S_{CSD}.

Second, a rectangular room with the dimensions $a : b$ is investigated. A VW is inserted in the middle of a with length b. Here, the shape factor computes

$$q = \frac{C_{VW}}{C} = \frac{2b}{2a + 2b} = \frac{b}{a + b}. \tag{4.11}$$

For a wide range of aspect ratios of the rectangle $0.5 < \frac{a}{b} < 6$ and thus $\frac{2}{3} > q > 0.14$, a relative error of the speed-up is even below 2%. Finally, more complex test cases are computed. Their speed-up S_{CSD} is shown together with their relative error e in Tab. 4.2.

Description	n_{total}	q	S_{CSD}	e [%]
long *snake* (Fig. 4.9a)	12	0.16	2.8	6
city layout (Fig. 4.9b)	26	1.11	2.87	9
city layout (Fig. 4.9c) with 5 x 12 houses	340	2.88	17.74	6
city layout (Fig. 4.9c) with 9 x 12 houses	532	2.04	35.28	5
city layout (Fig. 4.9c) with 12 x 12 houses	676	1.58	52.73	8
city layout (Fig. 4.3b)	16	1.11	1.92	6

Table 4.2.: Speed-up S_{CSD} and relative error e for different setups with different numbers of walls n_{total}.

In total, a very good agreement between the estimated speed-up and the measured speed-up is found, which supports the considerations made.

4.4. Summary of the Convex Sub-Division

The sub-division techniques used in graphics are not optimized to detect diffraction by means of the Uncertainty relation Based Diffraction (UBD) used later. The method proposed by Stephenson, however, was not applicable to urban layouts and the positions of the VWs were not optimized for the detection of diffraction events. Therefore, a new method was proposed and implemented that handles urban layouts and is optimized to detect diffraction events. The reduction of CT was discussed statistically and the CT after convex sub-division was shown to be independent of the number of walls of the geometrical scene. The statistical considerations were verified numerically.

5. Simulation of Diffraction in Geometrical Acoustic Simulation Methods

All Geometrical Acoustic (GA) simulation methods that were presented in this work so far are restricted to energetic approaches (see chapter 3). Thus, they neglect the wave behaviour of sound. Diffraction, however, can only be handled in the wave pattern, which hinders a direct integration of this important wave phenomenon in methods of GA. But diffraction can be introduced to GA methods by applying different modifications.

In this chapter, first the reference methods are presented, which are used to evaluate different types of diffraction simulations later. As diffraction is a two dimensional effect, the two dimensional Uncertainty relation Based Diffraction (UBD) module[Ste10a] is discussed in two dimensions. After a short summary of the fundamental concept of the UBD, the applied assumptions are discussed and many modifications and extensions are introduced that resolve occurring contradictions. An analytical formulation is derived for some basic diffraction scenarios and the fulfilment of the reciprocity principle is investigated. In an extended validation section, the consistency of the model as well as a comparison with the reference models is performed. Additionally, the combination of the Sound Particle Simulation Method (SPSM) with the UBD is validated for some simple test cases.

5.1. Reference Methods

As described in Sec. 2.3.4, the diffraction theories are divided into three classes: a) wave theoretical diffraction models, b) models based on the Kirchhoff assumptions and c) detour based approaches. Because the UBD is a representative of the second group, one exemplary reference solution of the first and the third group is presented, too. It should be noted that the wave theoretical Secondary Source Model (SSM) is the physically correct reference solution, whereas the Maekawa Detour Law (MDL) in only used to demonstrate the need for more accurate methods than this.

In order to formulate diffraction independent of the source power P, the transmission degree T rather than the sound intensity I is used in the following. Therefore, the sound intensity with diffraction is divided by the expected sound intensity without the screen, i.e., the free field sound intensity I_F

$$T = \frac{I}{I_F}. \tag{5.1}$$

The free-field sound intensity I_F differs from $2D$ to $3D$:

$$I_{F,2D} = \frac{P'}{2\pi R} \qquad \text{and} \qquad I_{F,3D} = \frac{P}{4\pi R^2} \tag{5.2}$$

Here, R is the free-field distance between source and receiver and P and P' the sound power and sound power per length, respectively (see Sec. 3.1). By using the transmission level T, the UBD is easily comparable with the reference models.

5.1.1. Secondary Source Model

Svensson et al. propose an analytic SSM for edge diffraction based on the Biot-Tolstoy-Medwin (BTM) solution (see Sec. 2.3.4.2). As result, the sound pressure $p(t)$ is derived [Cal09].

Svensson utilizes the impulse responses of Medwin to derive directivity functions for secondary sources on the edge. The basic idea is that incident sound waves on a wedge are split up when hitting a point of an edge and are reradiated as wavefront in different directions with different amplitudes[SFV99].

Therefore, Svensson derives a directivity function using retarded potentials

$$D\left[\vartheta_S\left(\tau\right),\vartheta_R\left(\tau\right),\varphi_S,\varphi_R\right] = -\frac{\nu\beta\left[\vartheta_S\left(\tau\right),\vartheta_R\left(\tau\right),\varphi_S,\varphi_R\right]}{4\pi}, \tag{5.3}$$

where ϑ_S and ϑ_R are angles between the current point on the edge and the source and receiver relative to the $z-axes$ (see Fig. 2.9). As this directivity function is completely symmetrical with respect to interchanging source and receiver angles, the reciprocity principle is fulfilled automatically. Svensson showed that his implementation of secondary sources using the directivity function exactly matches the analytically derived BTM solution for infinite wedges (half planes) in case of totally reflecting walls (hard or soft). Due to the extension to the secondary sources, also curved wedges are computable and accurate results for the diffraction at a circular disk have been shown[SFV99].

As reference in this work, the Edge Diffraction ToolBox (EDB) by Svensson [Sve10] is used. In order to apply the EDB, a $3D$ setup is needed, such that the wedge setup is extended into the $z-axis$ from $-1000m < z < 1000m$. The complete investigation of the UBD will be performed for distances relative to the wavelength λ, but the toolbox computes impulse response in time domain for given geometrical setups in absolute distances. Thus, the relative distances r are converted to absolute distances $s = r \cdot \frac{c}{f}$ for an arbitrary frequency of $f = 1000Hz$, where c is the speed of sound. The resulting impulse responses are then octave band filtered around $f = 1000Hz$ (as the UBD module is valid for an octave band). Although the impulse response could have been filtered at other frequencies to achieve different equivalent distance combinations by the same impulse response, this is discarded as only single values are of interest at a time. The wedge is defined as *hard*- reflecting with an opening angle of $\varphi_W = 1^\circ$ (both parameters are not relevant for UBD and MDL).

5.1.2. Maekawa Detour Law

Maekawa empirically found the so called detour law. It only takes the shortest detour $d = a+b-c$ between source and receiver across an obstacle into account (see Fig. 5.1a). In case of a receiver in the view zone, the detour is negative ($d < 0$). The detour law can also be analytically derived for small diffraction angles from the Kirchhoff theory as described in Sec. 2.3.4.4.

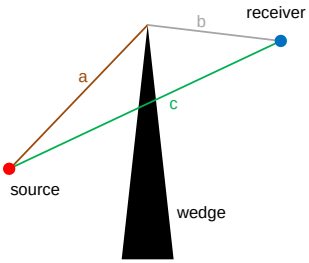

(a) Geometrical definitions of the detour $d = a + b - c$

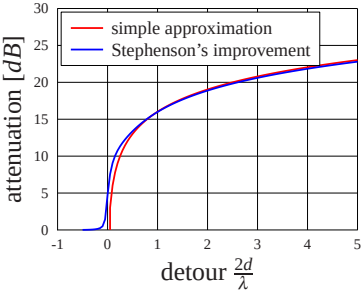

(b) Different approximations of the attenuation as a function of the detour d

Figure 5.1.: Maekawa Detour Law for single diffraction (after Vorländer[Vor08]).

The formulation of Eqn. 2.45 is not defined for a detour of $d = 0$, but a fitted approximation is applied[Ste04] with

$$\Delta L = 10 \cdot log_{10} \left(\frac{1}{2} - \frac{atan\left(\frac{1}{\sqrt{3}} + 6N\left(1 + e^{-3N}\right)\right)}{\pi} \right). \tag{5.4}$$

Both equations are compared in Fig. 5.1b and very good agreements are observed for almost all detours, except for small detours $d \approx 0$ where the numerical error of Eqn. 2.45 is resolved.

The classical detour law is only valid for a single obstacle, but an extension to double diffraction is made by computing the detour around a virtual apex (see Fig. 5.2). As discussed by Pierce[Pie74], a different solution might be to take the *real* detour into account by folding the sound propagation paths at each wedge. However, the first method is used in this work for double diffraction, as it was intended by Maekawa.

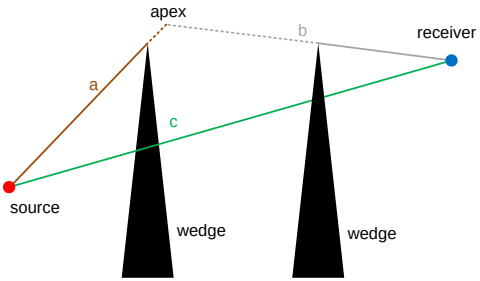

Figure 5.2.: Geometric definitions of the Maekawa Detour Law for double diffraction (after Pierce[Pie74]).

Both Eqn. 2.45 and 5.4 result directly in an average transmission loss, such that no post-processing is needed.

5.2. Uncertainty relation Based Diffraction

In order to combine diffraction with the energetic GA methods SPSM and Beam Tracing (BT), Stephenson uses an energetic approach[Ste04]. It is based on the Fraunhofer diffraction of a slit and the uncertainty relation. For optics, also a particle diffraction method had been derived[HC71, FGH99] using Gaussian functions instead of Fraunhofer related *si* -functions (see Sec. 2.3.4.3), which is, however, wrong in the case of a hard wedge[Ste04]

A main advantage of both methods regarding diffraction is that diffraction is automatically detected by the straight forward detection technique. Thus, a complicated search for valid sound paths is not necessary (in contrast to the SSM[SP09]). In case of the SPSM, sound particles never hit edges exactly, which means that the Uniform Theory of Diffraction (UTD) or BTM cannot be applied without further modifications.

As said before, a complete energetic simulation method is aimed at, but diffraction only occurs in the wave pattern (see Sec. 2.3.4). Therefore, the wave-particle dualism is utilized to bridge the gap between energetic (particle) and wave theory [Ste85]. By this approach, even higher order diffractions are computable directly.

Within the wave-particle dualism, Stephenson uses Heisenberg's uncertainty relation. This relation states that of two complementary values only one can be defined exactly. As an example, the *position* y and the *momentum* p_y can be named. Mathematically, the multiplication of the uncertainty of position Δy and the uncertainty of momentum Δp_y is approximately[Hei27]

$$\Delta y \cdot \Delta p_y \approx \hbar, \tag{5.5}$$

where $\hbar$ is the Planck constant.

Based on this idea, Stephenson postulates for the diffraction module:

1. The closer a sound particle passes by the wedge, the stronger it is deflected (uncertainty in *momentum*)

2. A sound particle *sees* a slit of width b (uncertainty in *position*) that is proportional to the bypass distance a.

Mathematically spoken, these two assumptions yield the two principles of the UBD module[Ste85]. On the one hand, the Edge Diffraction Strength (EDS) describes the attraction of a wedge that is passed in distance a to the sound particle propagation. On the other hand, the Diffraction Angle Probability Density Function (DAPDF) describes the actual diffraction of the sound particle around the wedge by an angle of ε.

This diffraction procedure is outlined in Fig. 5.3.

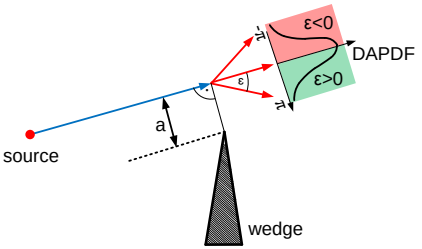

Figure 5.3.: Diffraction of a sound particle passing by a single wedge in a distance a by an angle of ε (after Stephenson [Ste04]).

In order to make the derivations independent of the wavelength, all distances are defined relative to the wavelength λ. In the following, both principles[Ste04] are shortly repeated followed by a discussion of different detection and normalization techniques.

5.2.1. Edge Diffraction Strength

As for the EDS $S(a)$, Stephenson made the following hypotheses[Ste04]:

1. the EDS equals the reciprocal width of an imaginary slit $S_{total} =: \frac{1}{b}$,
2. the EDS is inverse proportional to the bypass distance a (with a factor n) and
3. the EDSs of simultaneously passed wedges add up to $S_{total} = \sum_k S(a_k)$.

Stephenson derived the proportionality factor n by considering the total EDS S_{total} of two simultaneously passed wedges forming a slit of width b. The geometrical setup is sketched in Fig. 5.4.

The total EDS S_{total} is determined using the hypotheses two and three for this setup

$$S_{total} = S_1 + S_2 = \frac{1}{nb_1} + \frac{1}{nb_2} = \frac{1}{ny} + \frac{1}{n(b-y)}. \tag{5.6}$$

The average over all these total EDSs should equal the reciprocal of the width of the real slit (first hypothesis)

$$\frac{1}{b} = \overline{S_{total}} = \frac{1}{b}\int_0^b \frac{1}{n \cdot y} + \frac{1}{n \cdot (b-y)} dy. \tag{5.7}$$

Solving Eqn. 5.7 results in

$$n = \int_0^b \frac{1}{y} + \frac{1}{b-y} dy = \int_0^b \frac{b}{y \cdot (b-y)} dy. \tag{5.8}$$

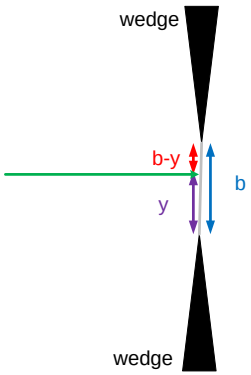

Figure 5.4.: Geometrical definitions of the Edge Diffraction Strength

The found integral diverges for both $y = 0$ and $y = b$, thus, a computation is not possible. To overcome this mathematical problem, Stephenson proposes an averaging over the inverse EDS, i.e., the slit widths, instead of over the original EDS

$$\frac{1}{n} = \int_0^b \frac{y \cdot (b-y)}{b} dy, \tag{5.9}$$

such that the proportionality factor n concludes to $n = 6$. In total, an EDS for the diffraction at a single wedge reads

$$S(a) = \frac{1}{6 \cdot a}. \tag{5.10}$$

Stephenson assumes from the uncertainty relation[Ste04]:
A sound particle passing by a wedge *sees* a slit with a width of six times the bypass distance.

A validation of the diffraction module for the slit[Ste10a] showed that this EDS is too strong for large distances of the edges. Hence, Stephenson disabled diffraction for

sound particles passing by a wedge above an arbitrary distance of 7λ by setting the EDS to *zero* in these cases

$$S(a) = \begin{cases} \frac{1}{6 \cdot a} & a \leq 7\lambda \\ 0 & a > 7\lambda \end{cases} . \tag{5.11}$$

Besides a better agreement with the Fraunhofer diffraction at a slit, a reduction of the Computation Time (CT) is achieved by avoiding a split-up of sound particle above this limit.

Another, more continuous approach by Stephenson was an improved EDS extended by an exponential term[Ste10a]

$$S(a) = \frac{1}{3 \cdot a + e^a}. \tag{5.12}$$

All three EDSs are compared in Fig. 5.5.

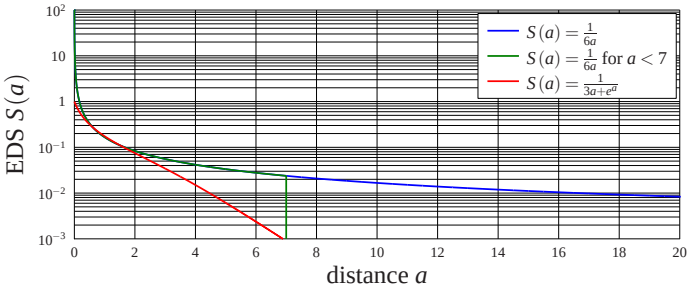

Figure 5.5.: Comparison of the different Edge Diffraction Strength.

In contrast to the mathematically derived EDS, the trimmed and the improved EDSs are based on heuristic observations. By introducing the exponential function into the denominator (see Eqn. 5.12), the EDS decreases significantly faster for larger distances than the former EDS. But also for very close distances, the differences between both EDSs are very great. The errors in the linear EDS for diffraction at a slit are compensated by other improvements, as will be shown in Sec. 5.5.

The mathematical derivation of the EDS wrongly assumes that the result is unaffected by averaging either over the EDS or the inverse EDS (see Eqn. 5.8 and 5.9). Although this assumption has no mathematical and physical basis, the good agreements with the reference models shown in Sec. 5.5 are astonishing. With respect to the heuristical derivation of the trimmed and the improved EDS, the mathematically derived EDS is used in the present work.

5.2.2. Diffraction Angle Probability Density Function

With the Fraunhofer diffraction at a slit (see Sec. 2.3.4.3), the sound intensity is proportional to the squared $si-$function (see Eqn. 2.44). Interpreting the width in one dimension of the slit in wavelength ($\frac{Y}{\lambda}$) as the relative slit width b, Eqn. 2.44 reads

$$I = I_0 \cdot si\,(u)^2 \quad \text{with } u = \pi b sin\,(\varepsilon)\,, \tag{5.13}$$

where I_0 is a reference sound intensity.

The presented Fraunhofer diffraction is only accurate for one specific frequency and, thus, a specific wavelength λ. SPSMs are, one the other hand, valid over a whole frequency band (see Sec. 3.2). Therefore, the diffraction function has to be averaged over the frequency band that the sound particle represents. As all distances are in relative wavelength λ, an averaging over $\frac{b}{\sqrt{2}} < \tilde{b} < \sqrt{2} \cdot b$ has to be performed for an octave band. To avoid a decrease of $sin\,(\varepsilon)$ for angles $|\varepsilon| > 90°$, Stephenson approximates $u = \pi b sin\,(\varepsilon)$ by $u = 2 \cdot b \cdot \varepsilon$. The result is given by

$$D_a\,(\varepsilon, b) = D_0 \cdot \begin{cases} 1 - u^2 & |u| \le u_0 \\ \frac{\frac{1}{2}}{\sqrt{2}-1+u^2} & |u| > u_0 \end{cases} \quad \text{with } u_0 = \sqrt{1 - \frac{1}{\sqrt{2}}} \text{ and } u = 2 \cdot b \cdot \varepsilon, \tag{5.14}$$

where D_0 is a normalization constant. The different variations are shown in Fig. 5.6. The angle range is extended from $-180° < \varepsilon < 180°$ to show the complete angle range. Which range is used in the simulation will be further discussed in Sec. 5.2.4.

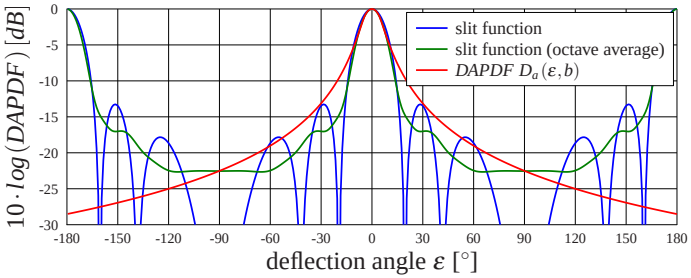

Figure 5.6.: Derivation of the Diffraction Angle Probability Density Function from the (averaged) slit function known from the Fraunhofer diffraction for $b = 3$ and $D_0 = 1$.

Besides this DAPDF, Stephenson proposed many other DAPDFs. These formulations are only summarized without any derivation.

First, an even more simplified DAPDF $D_b\,(\varepsilon, b)$ was presented, yielding even better agreements with the reference models[Ste04]. In order to fulfil the reciprocity principle, Stephenson proposed additional DAPDFs $D_c\,(\varepsilon, b)$-$D_g\,(\varepsilon, b)$ (see Sec. 5.4.2). Lately, Stephenson derived from Fresnel-Kirchhoff theory a DAPDF $D_h\,(\varepsilon, b)$ (not yet published) that depends on the incident angle ε_1 and the outgoing angle ε_2 rather than the total deflection angle $\varepsilon = \varepsilon_1 + \varepsilon_2$ for the first time

$$
\begin{aligned}
D_b(\varepsilon, b) &= \frac{D_0}{1 + 2 \cdot u^2} \text{ with } u = 2 \cdot b \cdot \varepsilon \\
D_c(\varepsilon, b) &= \frac{D_0 \cdot cos(\varepsilon)}{1 + 2 \cdot u^2} \text{ with } u = 2 \cdot b \cdot \varepsilon \\
D_d(\varepsilon, b) &= \frac{D_0 \cdot \frac{1+cos(\varepsilon)}{2}}{1 + 2 \cdot u^2} \text{ with } u = 2 \cdot b \cdot \varepsilon \\
D_e(\varepsilon, b) &= \frac{D_0}{1 + 2 \cdot u^2} \text{ with } u = \pi \cdot b \cdot sin(\varepsilon) \\
D_f(\varepsilon, b) &= \frac{D_0 \cdot cos(\varepsilon)}{1 + 2 \cdot u^2} \text{ with } u = \pi \cdot b \cdot sin(\varepsilon) \\
D_g(\varepsilon, b) &= \frac{D_0 \cdot \frac{1+cos(\varepsilon)}{2}}{1 + 2 \cdot u^2} \text{ with } u = \pi \cdot b \cdot sin(\varepsilon) \\
D_h(\varepsilon_1, \varepsilon_2, b) &= \frac{D_0}{1 + 2 \cdot u^2} \text{ with } u = \pi \cdot b \cdot (sin(\varepsilon_1) + sin(\varepsilon_2)) .
\end{aligned}
\tag{5.15}
$$

These DAPDFs are compared in Fig. 5.7.

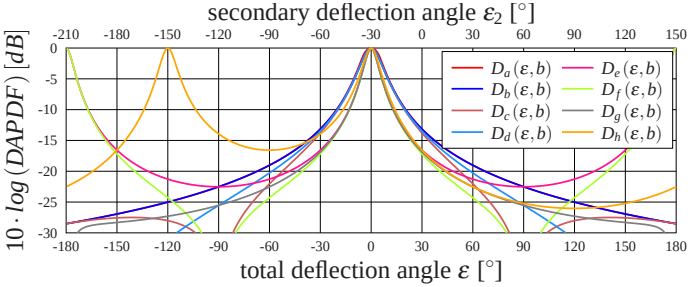

Figure 5.7.: Comparison of different Diffraction Angle Probability Density Functions for $\varepsilon_1 = 30°$, $b = 3$ and $D_0 = 1$.

In order to reduce the number of parameters discussed in the course of this work, some DAPDFs are discarded. It will be shown in Sec. 5.2.4 that results have to be at least plausible for the complete angle range ($-180° < \varepsilon < 180°$). Therefore, both DAPDFs $D_c(\varepsilon, b)$ and $D_f(\varepsilon, b)$ are neglected due to singularities at $\varepsilon = 90°$. In addition, $D_e(\varepsilon, b)$ is also excluded due to the wrongly increasing energy for diffraction angles above $|\varepsilon| > 90°$. The DAPDFs $D_a(\varepsilon, b)$ and $D_b(\varepsilon, b)$ are almost identical for the whole angle range and, thus, the simpler DAPDF $D_b(\varepsilon, b)$ is preferred to $D_a(\varepsilon, b)$. Finally, the DAPDF $D_d(\varepsilon, b)$ decreases by-far too fast for increasing diffraction angles $|\varepsilon| > 90°$.

The latest DAPDF $D_h(\varepsilon, b)$ is identical to DAPDF $D_e(\varepsilon, b)$ for $\varepsilon_1 = 0$, but for $\varepsilon_1 \neq 0$, both angles can cancel out each other, while for all remaining DAPDFs the sign of ε is not influencing the diffraction. As shown in Fig. 5.7, for an angle of incidence $\varepsilon_1 = 30°$, a maximum of diffraction occurs for $\varepsilon_2 = -30°$ as this represents the straight forward direction, but the same maximum occurs also for $\varepsilon_2 = -150°$. The reason is that for $\varepsilon_2 = -150°$ the value of u equals zero for $D_h(\varepsilon, b)$ ($sin(30°) + sin(-150°) = 0$), whereas it remains different from *zero* for, e.g., $D_g(\varepsilon, b)$ ($sin(30° - 150°) \neq 0$). This

behaviour influences the diffraction in a huge angle range, as the DAPDF starts to increase for diffraction angles $\varepsilon < -60°$. An even increasing DAPDF is physically not plausible and, thus, $D_h(\varepsilon, b)$ is not used in this work.

Summing it up, the remaining DAPDFs $D_b(\varepsilon, b)$ and $D_g(\varepsilon, b)$ are further investigated. However, a final DAPDF will be chosen not before a comparison with the reference models (see Sec. 5.5).

5.2.3. Detection of Diffraction Events

Sound particles travel on lines, which intersect with edges with a probability of zero. To overcome this, spatially extended detectors for the detection of diffraction events have to be used, similar to the spatially extended receivers. Stephenson proposed four different detection techniques, which are briefly repeated here[Ste04].

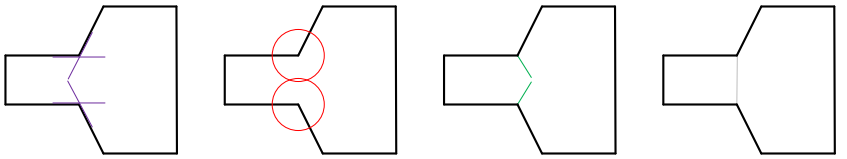

(a) tolerance region **(b)** diffraction cylinders **(c)** diffraction flags **(d)** convex sub-division

Figure 5.8.: Comparison of different detection techniques for diffracted sound particles.

Tolerance region The first approach is a tolerance region of one wavelength λ that extends the adjacent walls in both directions (see Fig. 5.8a). Sound particles are diffracted that intersect with these tolerance regions. As for each wedge two detectors are introduced, this method generates a huge computation overhead. Furthermore, sound particles that hit physical walls in the tolerance region are diffracted, but no bypass distance is defined, i.e., no diffraction procedure is defined.

Diffraction cylinders The most intuitive approach is the usage of diffraction cylinders (see Fig. 5.8b). An intersection of such a cylinder is interpreted as diffraction event and the bypass distance is computed directly. This method is successfully used in [SP09, Sch11]. An advantage of this method is that it always computes the smallest bypass distances of the sound particle and the wedge. One major drawback is, however, that complicated exceptions occur when cylinders intersect each other.

Diffraction flags In this method, additional walls are placed on the bisecting lines (see Fig. 5.8c). An intersection of these flags is interpreted as diffraction. As in the previous case, diffraction is detected exactly on the bisecting line and, thus, the exact bypass distance is computed. All this presented detection methods detect only one edge that is passed. Thus, the important feature of the UBD to handle diffraction at more edges, e.g., two edges forming a slit, cannot be utilized.

Convex sub-division As a consequence of the deficits of the presented detection methods, a global diffraction technique is chosen in this work (see Fig. 5.8d). Stephenson proposes a sub-division of the room into convex sub-spaces.

The convex sub-division technique is the only method that allows the detection of multiple (in $2D$: two) diffraction edges simultaneously by connecting them with a Virtual Wall (VW). Besides the efficient detection of diffraction, the convex sub-division brings in a huge acceleration of the CT instead of an increased CT with the other detection methods. Therefore, the convex sub-division is chosen.

5.2.4. Normalization of Diffracted Energy

In its original definition, the DAPDF is defined as a probability density per diffraction angle. Per definition, the integral over the probability density function has to be equal to one. As a dual definition, the DAPDF has later been used to describe the energy density per diffraction angle, where for energy conservation requirements also the integral over all diffraction angles has to be equal to one. Assuming ε_{Min} and ε_{Max} being the smallest and the largest diffraction angle, respectively, the integral equation reads

$$\int_{\varepsilon_{min}}^{\varepsilon_{max}} D\left(\varepsilon\right) d\varepsilon \stackrel{!}{=} 1. \tag{5.16}$$

With this definition, the normalization constant D_0 is computed. For the normalization range, different diffraction regions are considered. Three of these definitions are discussed in the following.

Normalization symmetrical to the incidence direction The most intuitive approach is to deflect the sound particle in a range $-90° < \varepsilon < 90°$ symmetrically around the incidence direction (see Fig. 5.9). Stephenson defined this range in order to keep the incident sound field undisturbed (Kirchhoff assumption).

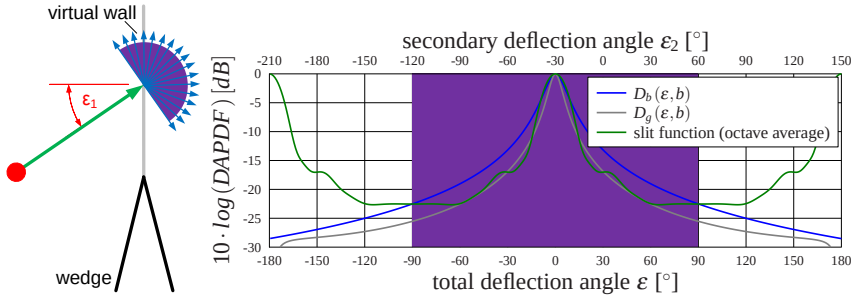

(a) geometrical setting **(b)** normalization range (filled surface) of the Diffraction Angle Probability Density Functions for $\varepsilon_1 = 30°$, $b = 3$ and $D_0 = 1$.

Figure 5.9.: Normalization for the diffraction angle range $-90° < \varepsilon < 90°$ symmetrical around the incidence direction.

This approach has two disadvantages: On the one hand, not all sound particles pass the VW due to the arbitrary position of the VW. Hence, diffracted sound particles might intersect with the same VW several times resulting in multiple diffraction events. From an algorithmical point of view, this also causes a higher effort as the concept of VWs transmitting sound particles from one room to another is lost. One the other hand, sound energy cannot be diffracted into the deep shadow zone, as no diffraction angles larger than $\varepsilon = 90°$ are possible. This is physically not acceptable as in the deep shadow zone diffraction is often the only source of energy.

An advantage of this method is the independency of the angle of incidence ε_1 on the VW. Hence, the normalization constant D_0 is only dependent on the distance a or the effective slit width b, respectively. This algorithmic advantage cannot compensate the disadvantages, such that this method is not used in this work.

Normalization to the complete angle range Another possibility is to allow diffraction to the complete angle range $-180° < \varepsilon < 180°$ (see Fig. 5.10).

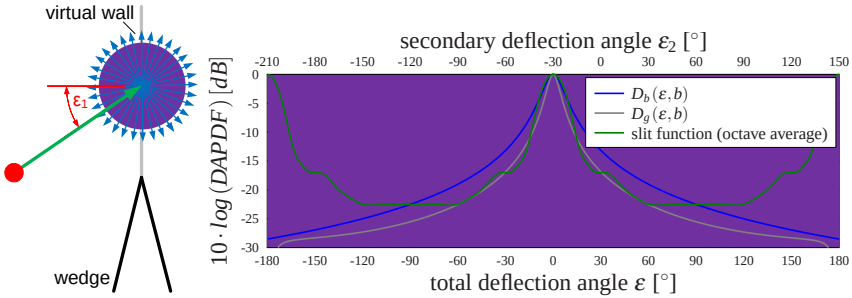

(a) geometrical setting **(b)** normalization range (filled surface) of the Diffraction Angle Probability Density Functions for $\varepsilon_1 = 30°$, $b = 3$ and $D_0 = 1$.

Figure 5.10.: Normalization in the complete diffraction angle range $-180° < \varepsilon < 180°$.

With this approach even more sound particles remain on the source-side of the VW increasing the disadvantage of the first approach, whereas the extension of diffraction to the complete angle range resolves the discrepancy of no sound energy in the deep shadow zone. In contrast to all other methods, this approach completely ignores the Kirchhoff assumption that the incident sound field is undisturbed, as sound particles are diffracted even into the inverse direction. Therefore, this approach is not used in this work, too.

Normalization to the angle range behind the Virtual Wall The combination of both former requirements provides a normalization to the angle range behind the Virtual Wall to $-90° < \varepsilon_2 < 90°$ (see Fig. 5.11).

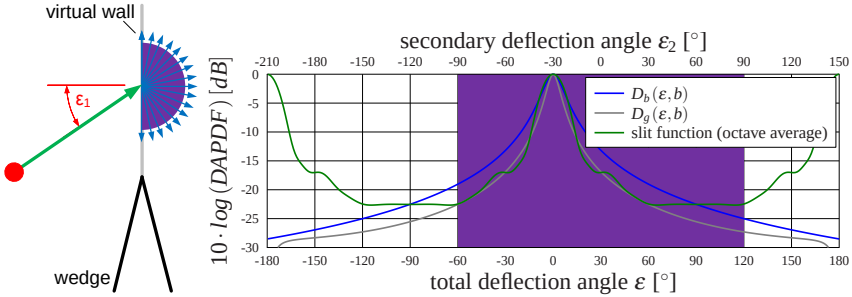

(a) geometrical setting **(b)** normalization range (filled surface) of the Diffraction Angle Probability Density Functions for $\varepsilon_1 = 30°$, $b = 3$ and $D_0 = 1$.

Figure 5.11.: Normalization to the angle range behind the Virtual Wall.

Sound particles are diffracted only into the subspace behind the VW, hence, the algorithmic separation of subspaces is valid. This coincidences with the physical requirements by Kirchhoff to leave the incident sound field unaffected, when the incident found field is defined as the sound field on the source-side of the VW. Sound energy is diffracted into the deep shadow zone behind the obstacle. As the derivation of the DAPDF is based on the diffraction at a slit, this normalization meets this definition best. Only for perpendicular sound incidence, this definition matches the first approach. This approach is used in this work.

The normalization is now additionally dependent on the angle of incidence ε_1. Hence, also the DAPDF itself is dependent not only on the total diffraction angle ε, but also on the angle of incidence ε_1

$$D = D\left(\varepsilon, b, \varepsilon_1\right). \tag{5.17}$$

5.2.5. Combination of the Uncertainty relation Based Diffraction and the Sound Particle Simulation Method

The combination of diffraction with the SPSM is similar to the combination of scattering with the SPSM(see Sec. 3.4.3). Every sound particle that intersects with a VW is split up into S sound particles. These sound particles are equally distributed behind the VW(see Fig. 5.12).

Each sound particle is emitted at the centre of the sound particle's represented angle range (see Eqn. 3.15)

$$\varepsilon_{2,i} = \frac{i + \frac{1}{2}}{S} \cdot \pi - \frac{\pi}{2}. \tag{5.18}$$

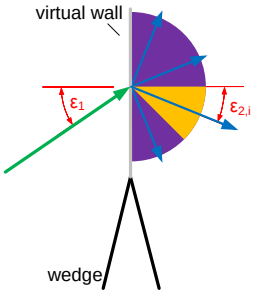

Figure 5.12.: Split-up of sound particles into $S = 4$ secondary sound particles by diffraction.

The energy of the i^{th} sound particle is computed by an integral over the DAPDF. Including the air attenuation (see Sec. 2.3.1), the energy reduction reads

$$e_i = e^{-mr} \cdot \int_{\varepsilon_1 + \frac{i}{S}\pi - \frac{\pi}{2}}^{\varepsilon_1 + \frac{i+1}{S}\pi - \frac{\pi}{2}} D\left(\varepsilon, b, \varepsilon_1\right) \cdot d\varepsilon. \tag{5.19}$$

It has to be noted that the UBD handles both the diffracted sound field and the direct sound (in the view zone). This is a significant difference to the UTD and the BTM, where only the diffracted sound field is computed and the direct sound has to be added separately.

The combination of diffraction with both geometrical and diffuse reflections as well as the extension to higher order diffractions is achieved by combining the diffraction module with the SPSM.

The main algorithm of the SPSM remains unaffected, but the function tracing a sound particle between one wall and another (see List. 3.4) has to be modified such that sound particles intersecting with a wall are scattered and sound particles intersecting with a VW are diffracted. The modified algorithm is shown in List. 5.1.

```
function traceSoundParticle()
findWallIntersection(); // use convex shape, see Sec. 3.4.2
detectSoundParticle(); // either single or grid, see Sec. 3.4.4
energy = energy * exp(-m * r); // see Eqn. 3.11, only air
if(isVirtual(intersectedWall))
  for (all secondary sound particles) // split-up in S
   float newEnergy = energy * diffractionRatio(); // see Eqn. 5.19
   v = computeDiffractedDirection(); // see Eqn. 5.18
   if(newEnergy > energyThreshold) // see Eqn. 3.26
     traceSoundParticle(); // recursive call
else
  energy = energy * (1 - alpha) // see Eqn. 3.11, only alpha
  for (all secondary sound particles) // split-up in S + 1
    if(i==0) // specular reflection
     float newEnergy = energy * (1 - sigma); // see Eqn. 3.13
     v = v - 2 (v * n) * n // see Eqn. 3.12
   else
     float newEnergy = energy * scatteringRatio(); // see Eqn. 3.16
     v = computeScatteredDirection(); // see Eqn. 3.15

   if(newEnergy > energyThreshold) // see Eqn. 3.26
     traceSoundParticle(); // recursive call
```

Listing 5.1: Modified pseudocode for the Sound Particle Simulation Method including diffraction.

5.3. Analytical Formulations for the Simple Scenarios

The combination of the diffraction module with the SPSM causes numerical errors due to the finite number of sound particles and the spatially extended receivers. As these numerical errors (see Sec. 5.5) prevent an exact estimation of the accuracy of the diffraction module, an analytical solution is found (at least for simple scenarios). For the single diffraction at a wedge, Stephenson formulated a *Beam Integration* formula[Ste10a], which combines the UBD diffraction module with BT. In contrast, now a formula is derived from the SPSM and analytical formulations for the diffraction at a slit and double diffraction at two wedges are presented. In order to get results independent of the source power, the transmission level T instead of the intensity is of interest.

5.3.1. Diffraction at a Single Wedge

To analyse the diffraction module analytically, first a derivation of the sound intensity behind a single wedge is determined. Based on the SPSM, analytical substitutions are introduced to achieve both infinitesimally small receivers and an infinite number of primary and secondary sound particles.

Without loss of generality, the diffracting edge is identical to the $z-axis$ and of infinite extend at $(x,y) = (0,0)$. Both the sound source and the receiver are in the $z = 0$ plane at (x_S, y_S) and (x_R, y_R), respectively. The distances of the sound source r_S and the receiver r_R to the edge are counted in wavelength λ and the angles φ_S and φ_R indicate the angles between the $x-axis$ and the source and the receiver. While φ_R is defined relative to the $x-axis$ counter-clockwise, φ_S is defined relative to the $-x-axis$, such that negative angles indicate a position in the shadow zone ($y < 0$) for both the sound source and the receiver (see Fig. 5.13a).

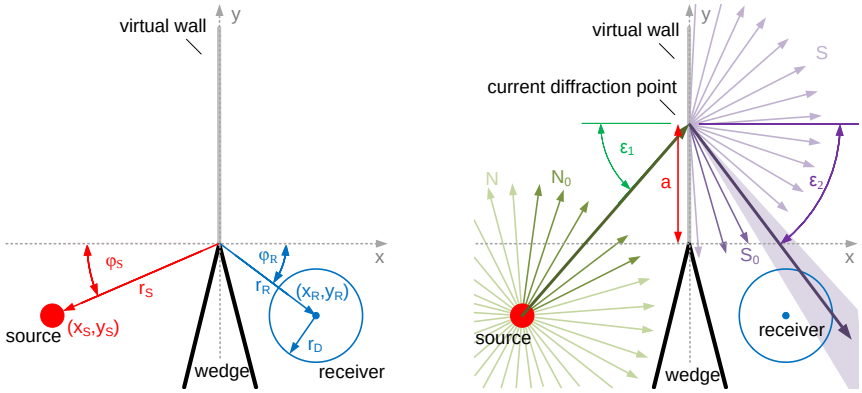

(a) geometrical definitions of source and receiver

(b) definitions of sound paricles

Figure 5.13.: Sound particle diffraction at a single wedge on the $z-axis$.

The SPSM starts by emitting N primary sound particles. Only N_0 of these N sound particles intersect with the VW in the $y-z$ plane for $y>0$. Each of these N_0 sound particles is split up into S secondary sound particles by the diffraction module, where a small number S_0 of these S secondary sound particles intersect with the detector (radius r_D and surface S_D).

The sound intensity I at the receiver is computed regarding Eqn. 3.19 by a double loop over both primary and secondary sound particles to

$$I = \frac{P'}{N \cdot S_D} \sum_{i=1}^{N_0} \sum_{j=1}^{S_0} e_{i,j} \cdot w_{i,j}, \tag{5.20}$$

where $e_{i,j}$ is the relative energy of a sound particle that intersects with the receiver with the inner crossing distance $w_{i,j}$. With the energy loss of a sound particle in Eqn. 5.19 (neglecting air attenuation), the sound intensity reads

$$I = \frac{P'}{N \cdot S_D} \sum_{i=1}^{N_0} \sum_{j=1}^{S_0} w_{i,j} \cdot \int_{\varepsilon_{1,i}+\frac{j}{S}\pi-\frac{\pi}{2}}^{\varepsilon_{1,i}+\frac{j+1}{S}\pi-\frac{\pi}{2}} D\left(\varepsilon, b_i, \varepsilon_{1,i}\right) d\varepsilon. \tag{5.21}$$

The angle of incidence ε_1 as well as the effective slit width b are only dependent on the incident sound particle i. Furthermore, the inner crossing distance w as well as the secondary angle ε_2 depend on the secondary sound particle j.

For infinitesimally small receivers, which will be inserted later, the inner crossing distance $w_{i,j}$ is replaced by the Mean Free Path Length (MFPL)[Kos60] in the detector with circumference C_D to

$$\overline{w} = \pi \cdot \frac{S_D}{C_D} = \pi \cdot \frac{\pi \cdot r_D^2}{2 \cdot \pi \cdot r_D} = \pi \cdot \frac{r_D}{2}. \tag{5.22}$$

Both the inner crossing distance and the surface of the detector are replaced in Eqn. 5.21, such that the sound intensity is written

$$I = \frac{P'}{N \cdot 2 \cdot r_D} \sum_{i=1}^{N_0} \sum_{j=1}^{S_0} \int_{\varepsilon_{1,i}+\frac{j}{S}\pi-\frac{\pi}{2}}^{\varepsilon_{1,i}+\frac{j+1}{S}\pi-\frac{\pi}{2}} D\left(\varepsilon, b_i, \varepsilon_{1,i}\right) d\varepsilon. \tag{5.23}$$

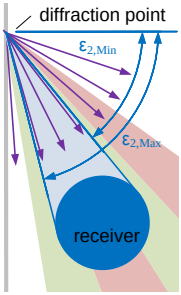

Figure 5.14.: Substitution of the sum over all sound particle angle ranges by the receiver angle range.

The angle ranges of sound particles that intersects with the detector are directly connected to each other. Mathematically speaking, the upper limit of sound particle j is equal to the lower limit of index $j+1$ as long as the sound particles intersect with the detector (see Fig. 5.14). The sum of these partial integrals is replaced by the complete integral over the angle range of the detector as seen from the diffraction point from $\varepsilon_{2,Min,i}$ to $\varepsilon_{2,Max,i}$ to get rid of this sum

$$I = \frac{P'}{N \cdot 2 \cdot r_D} \sum_{i=1}^{N_0} \int_{\varepsilon_{1,i}+\varepsilon_{2,Min,i}}^{\varepsilon_{1,i}+\varepsilon_{2,Max,i}} D\left(\varepsilon, b_i, \varepsilon_{1,i}\right) d\varepsilon. \tag{5.24}$$

This integration over the angle range of a detector is also used as *diffracted rain* by Schröder[Sch11] for both scattering and diffraction.

In the next step, the transition to infinitesimally small receivers is performed by minimizing the angle range of the receiver $\Delta\varepsilon_{2,i} = \varepsilon_{2,Max,i} - \varepsilon_{2,Min,i}$. It is approximated (for small angle ranges) by

$$\Delta\varepsilon_{2,i} = 2 \cdot asin\left(\frac{r_D}{r_{2,i}}\right) \approx 2 \cdot \frac{r_D}{r_{2,i}} \quad \text{or} \quad 2 \cdot r_D \approx \Delta\varepsilon_{2,i} \cdot r_{2,i}, \tag{5.25}$$

where $r_{2,i}$ is the distance between the intersection point on the VW and the receiver (see Fig. 5.15a). For infinitesimally small receivers, the angle range $\Delta\varepsilon_{2,i}$ converges to zero. Thus, the integral over this angle range is approximated by the integrand multiplied with this angle range. As this angle range occurs also in the denominator, it is reduced, with

$$I = \lim_{\Delta\varepsilon_{2,i}\to 0} \frac{P'}{N} \sum_{i=1}^{N_0} \frac{\int_{\varepsilon_{1,i}+\varepsilon_{2,Min,i}}^{\varepsilon_{1,i}+\varepsilon_{2,Max,i}} D\left(\varepsilon, b_i, \varepsilon_{1,i}\right) d\varepsilon}{r_{2,i} \cdot \Delta\varepsilon_{2,i}} = \frac{P'}{N} \sum_{i=1}^{N_0} \frac{D\left(\varepsilon, b_i, \varepsilon_{1,i}\right)}{r_{2,i}}. \tag{5.26}$$

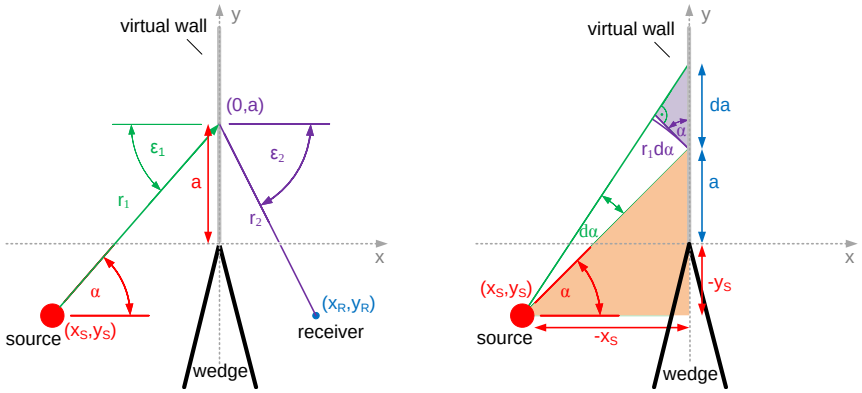

(a) geometrical definitions of current intersection point at $y = a$

(b) substitution of integral over $d\alpha$ to da

Figure 5.15.: Transition of the sound particle diffraction to an integral formulation.

With Fig. 5.15, the following relations are formulated

$$\begin{aligned} r_1 &= \sqrt{x_S^2 + (a - y_S)^2} \\ r_2 &= \sqrt{x_R^2 + (a - y_R)^2} \\ \varepsilon_1 &= \alpha = atan\left(\frac{a - y_S}{-x_S}\right) = acos\left(\frac{-x_S}{r_1}\right) \\ \varepsilon_2 &= atan\left(\frac{a - y_R}{x_R}\right) = acos\left(\frac{x_R}{r_2}\right) \\ \varepsilon &= \varepsilon_1 + \varepsilon_2. \end{aligned} \tag{5.27}$$

To get rid of the numerical value N, the transition to an infinite number of primary sound particles N is made by minimizing the angle between the primary sound particles $\Delta\alpha = \frac{2\pi}{N}$ in Eqn. 5.26

$$I = \frac{P'}{2\pi} \sum_{i=1}^{N_0} \frac{D\left(\varepsilon, b_i, \varepsilon_{1,i}\right)}{r_{2,i}} \Delta\alpha. \tag{5.28}$$

By this replacement, the sum in Eqn. 5.28 is written in integral form. The former sum added up all N_0 sound particles which intersect with the VW, whereas the integral now integrates over the angle range under which the VW is visible from the source position

$$I = \frac{P'}{2\pi} \int_{\alpha_{Min}}^{\alpha_{Max}} \frac{D\left(\varepsilon, b, \varepsilon_1\right)}{r_2} d\alpha. \tag{5.29}$$

Finally, the angle α is substituted by the more general position on the VW, because the integral over a has a direct relation to the scene and is independent of the source position. Assuming that the intersection point on the VW lies at $(0, a)$, an integral in the range of $0 < a < \infty$ is performed to cover the complete VW. By using the derivative of α in Eqn. 5.27 and expanding with the differentials, a substitution is found, with

$$d\alpha = \frac{1}{1+\left(\frac{y_S-a}{x_S}\right)^2}\left(\frac{y_S-a}{x_S}\right)' da = \frac{x_S^2}{x_S^2+(y_S-a)^2}\left(\frac{-1}{x_S}\right) da \qquad (5.30)$$
$$= \frac{r_1 \cdot cos(\varepsilon_1)}{r_1^2} da = \frac{cos(\varepsilon_1)}{r_1} da.$$

This substitution can also be derived graphically from Fig. 5.15b (*purple* triangle). Using this substitution, the intensity follows to

$$I = \frac{P'}{2\pi}\int_0^\infty \frac{D\left(\varepsilon, b, \varepsilon_1\right) \cdot cos(\varepsilon_1)}{r_1 \cdot r_2} da. \qquad (5.31)$$

Using Eqn. 5.1 and Eqn. 5.2, the transmission degree T reads

$$T = \frac{I}{I_F} = \frac{\frac{P'}{2\pi}\int_0^\infty \frac{D(\varepsilon,b,\varepsilon_1) \cdot cos(\varepsilon_1)}{r_1 \cdot r_2} da}{\frac{P'}{2\pi R}} = R\int_0^\infty \frac{D\left(\varepsilon, b, \varepsilon_1\right) \cdot cos(\varepsilon_1)}{r_1 \cdot r_2} da. \qquad (5.32)$$

This equation equals the *Beam Integration* formula for BT [Ste10a]. However, it is derived from a SPSM experiment for the first time. Thus, the diffraction theory is proven to be equivalently applicable to both the SPSM and BT.

5.3.2. Diffraction at a Slit

An analytical formula describing diffraction at a slit is derived to perform a *self-consistency* test. A similar experiment has been performed by Stephenson, but infinite source and receiver distances had been applied[Ste86], such that the results are not comparable. As for the single diffraction event, now both edges are parallel to the $z-axis$ and of infinite extent at $(x,y) = (0, -\frac{d}{2})$ and $(x,y) = (0, \frac{d}{2})$. The positions of the sound source and the receiver are identical to the scenario of single diffraction (see Fig. 5.16a).

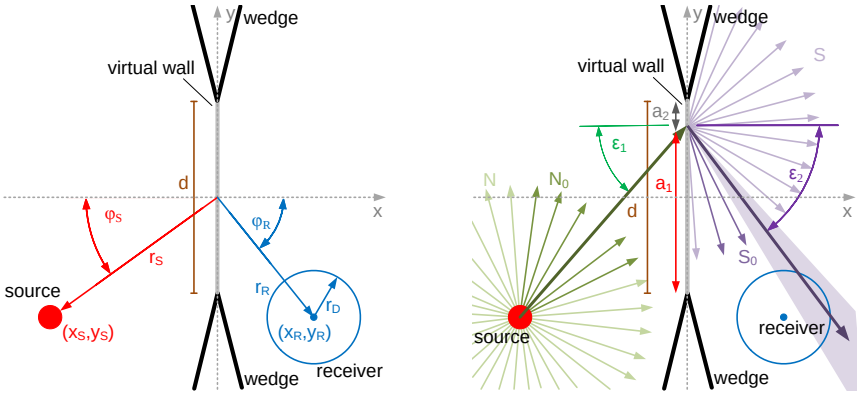

(a) geometrical definitions of source, receiver and slit

(b) definition of sound paricles

Figure 5.16.: Sound particle diffraction at a slit of width d.

For a number of N emitted sound particles, N_0 of these sound particles intersect with the VW in the $y-z$ plane for $-\frac{d}{2} < y < \frac{d}{2}$. The secondary sound particles are handled in the same way as for single diffraction. In contrast to the single diffraction event, two by-pass distances a_1 and a_2 exist simultaneously (see Fig. 5.16b).

The sum of all sound particles is identical to Eqn. 5.20, but the number of sound particles intersecting with the VW is defined differently and the slit width b is now an effective slit width b_{eff}. Hence, the derivation is equal to the single diffraction scenario apart from these small modification, yielding

$$I = \frac{P'}{2\pi} \int_{-\frac{d}{2}}^{\frac{d}{2}} \frac{D\left(\varepsilon, b_{eff}, \varepsilon_1\right) \cdot cos(\varepsilon_1)}{r_1 \cdot r_2} da, \tag{5.33}$$

where the integral covers the slit instead of a semi-infinite plane (compare with Eqn. 5.33). The total EDS is defined (see Sec. 5.2.1) as

$$S_{total} = S_1 + S_2 = \frac{1}{b_1} + \frac{1}{b_2} = \frac{1}{6a_1} + \frac{1}{6a_2} = \frac{1}{b_{eff}}, \tag{5.34}$$

where the by-pass distances a_1 and a_2 are computed by the position on the opening a to

$$a_1 = \frac{d}{2} + a \qquad \text{and} \qquad a_2 = \frac{d}{2} - a. \tag{5.35}$$

It should be noted that the integrant a is no longer a by-pass distance, but the distance to the centre of the slit. Finally, the transmission level reads

$$T = \frac{I}{I_F} = R \int_{-\frac{d}{2}}^{\frac{d}{2}} \frac{D\left(\varepsilon, b_{eff}, \varepsilon_1\right) \cdot cos(\varepsilon_1)}{r_1 \cdot r_2} da. \tag{5.36}$$

5.3.3. Double Diffraction at two Subsequent Wedges

As last analytical derivation, the diffraction at two wedges passed one after another instead of passed simultaneously (described above) is derived[PS12]. While this setup differs only in the position of the second wedge for the SSM derivation, it is a totally different setup in case of the UBD. For the latter, the slit experiment handled one diffraction at two wedges simultaneously, but now two diffractions at one wedge at a time are taken into account. The two edges are parallel to the $z - axis$, this time at $(x, y) = (-\frac{d}{2}, 0)$ and $(x, y) = (\frac{d}{2}, 0)$. In order to avoid single diffraction for sound sources or receivers in-between the wedges, their positions are defined relative to the left or right wedge, respectively (see Fig. 5.17a).

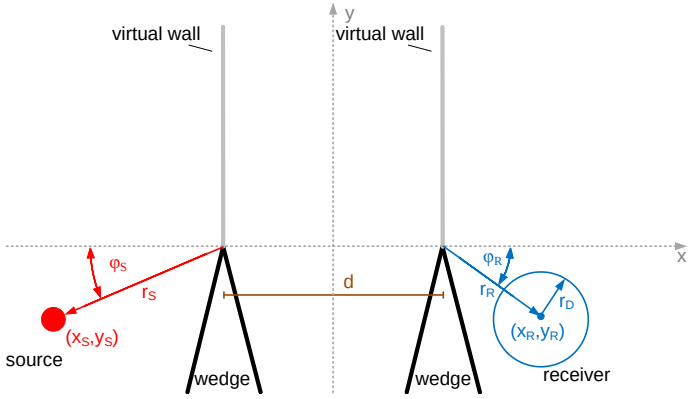

(a) geometrical definitions of source, receiver and wedges

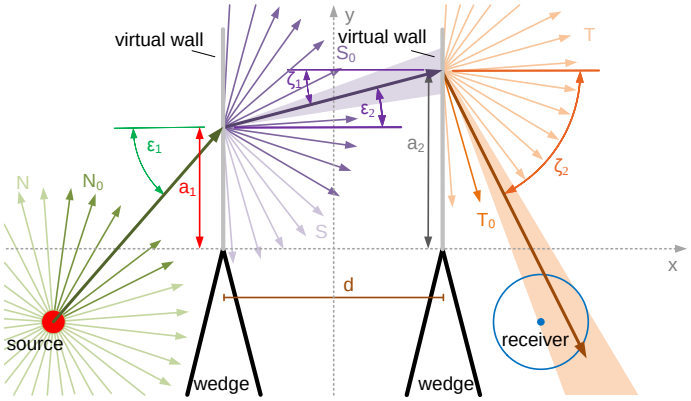

(b) definition of sound paricles

Figure 5.17.: Sound particle diffraction at two wedges in distance d.

The source and receiver positions are defined as follows

$$\begin{aligned}(x_S, y_S) &= \left(-r_S \cdot cos\left(\varphi_S\right) - \frac{d}{2}, r_S \cdot sin\left(\varphi_S\right)\right) \\ (x_R, y_R) &= \left(r_R \cdot cos\left(\varphi_R\right) + \frac{d}{2}, r_R \cdot sin\left(\varphi_R\right)\right).\end{aligned} \tag{5.37}$$

A number of N primary sound particles is emitted from the sound source and N_0 are intersecting with the left VW. The secondary sound particles S are multiplied by an energy factor $e_{i,j}$ and S_0 of these sound particles intersect with the second (right) VW. For each sound particle intersecting with the second VW, a number of T tertiary sound particles are emitted in the direction of the receiver multiplied by another energy factor $f_{i,j,k}$. T_0 of the T sound particles finally intersect with the receiver with an inner

crossing distance of $w_{i,j,k}$ (see Fig. 5.17b). The sound intensity is then described by the following equation

$$I = \frac{P'}{N \cdot S_D} \sum_{i=1}^{N_0} \sum_{j=1}^{S_0} e_{i,j} \cdot \sum_{k=1}^{T_0} w_{i,j,k} \cdot f_{i,j,k}. \tag{5.38}$$

For the analytical solution, the additional geometrical definitions are consequently

$$\begin{aligned}
r_1 &= \sqrt{\left(x_S + \frac{d}{2}\right)^2 + (a_1 - y_S)^2} \\
r_2 &= \sqrt{d^2 + (a_1 - a_2)^2} \\
r_3 &= \sqrt{\left(x_R - \frac{d}{2}\right)^2 + (a_2 - y_R)^2} \\
\varepsilon_1 &= \alpha = atan\left(\frac{a_1 - y_S}{-x_S - \frac{d}{2}}\right) = acos\left(\frac{-x_S - \frac{d}{2}}{r_1}\right) \\
\zeta_1 &= -\varepsilon_2 = atan\left(\frac{a_2 - a_1}{d}\right) = acos\left(\frac{d}{r_2}\right) \\
\zeta_2 &= \zeta_1 = atan\left(\frac{a_2 - y_R}{x_R - \frac{d}{2}}\right) = acos\left(\frac{x_R - \frac{d}{2}}{r_2}\right) \\
\varepsilon &= \varepsilon_1 + \varepsilon_2 \\
\zeta &= \zeta_1 + \zeta_2.
\end{aligned} \tag{5.39}$$

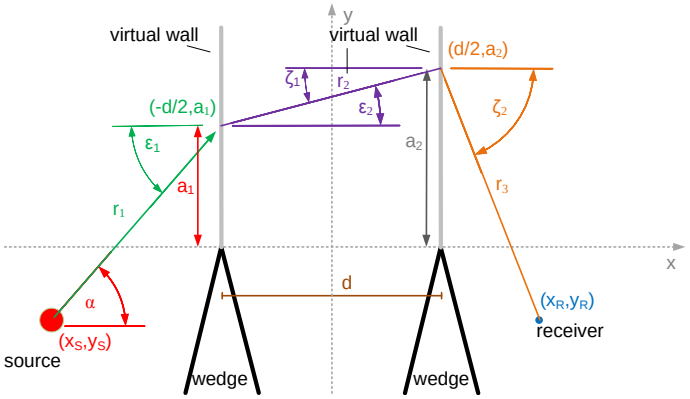

Figure 5.18.: Geometrical definitions for double diffraction.

To determine the energy factors $e_{i,j}$ and $f_{i,j,k}$, an integral is computed over the

respective angle ranges of the sound particles

$$e_{i,j} = \int_{\varepsilon_{1,i}+\frac{j}{S}\pi-\frac{\pi}{2}}^{\varepsilon_{1,i}+\frac{j+1}{S}\pi-\frac{\pi}{2}} D\left(\varepsilon, b_{1,i}, \varepsilon_{1,i}\right) \cdot d\varepsilon \tag{5.40}$$

$$f_{i,j,k} = \int_{\zeta_{1,i,j}+\frac{k}{T}\pi-\frac{\pi}{2}}^{\zeta_{1,i,j}+\frac{k+1}{T}\pi-\frac{\pi}{2}} D\left(\zeta, b_{2,i,j}, \zeta_{1,i,j}\right) \cdot d\zeta.$$

With the MFPL of the tertiary sound particle in the receiver (see Eqn. 5.22), the sound intensity is written as

$$I = \frac{P'}{N \cdot 2 \cdot r_D} \sum_{i=1}^{N_0} \sum_{j=1}^{S_0} e_{i,j} \cdot \sum_{k=1}^{T_0} \int_{\zeta_{1,i,j}+\frac{k}{T}\pi-\frac{\pi}{2}}^{\zeta_{1,i,j}+\frac{k+1}{T}\pi-\frac{\pi}{2}} D\left(\zeta, b_{2,i,j}, \zeta_{1,i,j}\right) \cdot d\zeta. \tag{5.41}$$

Since the sound particles that intersect with the receiver are directly connected to each other (see Fig. 5.14), the sum over the integrals is rewritten as the integral over the complete angle range $\Delta\zeta_{2,i,j}$ under which the detector is visible from the emission point on the second VW. Furthermore, the receiver diameter is expressed by this angle range and the distance between emission point at the second VW and the receiver $r_{3,i,j}$ (see Fig. 5.18) is expressed by $2 \cdot r_D \approx \Delta\zeta_{2,i,j} \cdot r_{3,i,j}$ (see Eqn. 5.25). In total, the sound intensity reads

$$I = \frac{P'}{N} \sum_{i=1}^{N_0} \sum_{j=1}^{S_0} e_{i,j} \cdot \frac{\int_{\zeta_{1,i,j}+\zeta_{2,Min,i,j}}^{\zeta_{1,i,j}+\zeta_{2,Max,i,j}} D\left(\zeta, b_{2,i,j}, \zeta_{1,i,j}\right) \cdot d\zeta}{\Delta\zeta_{2,i,j} \cdot r_{3,i,j}}. \tag{5.42}$$

The transition to infinitesimally small receivers is again performed by the transition to an infinitesimal angle range $\Delta\zeta_{2,i,j} \to 0$. As for the single diffraction case (see Sec. 5.3.1), the integral and the differential $\Delta\zeta_{2,i,j}$ cancel out each other. With $e_{i,j}$ from Eqn. 5.40, Eqn. 5.42 yields

$$I = \frac{P'}{N} \sum_{i=1}^{N_0} \sum_{j=1}^{S_0} \int_{\varepsilon_{1,i}+\frac{j}{S}\pi-\frac{\pi}{2}}^{\varepsilon_{1,i}+\frac{j+1}{S}\pi-\frac{\pi}{2}} D\left(\varepsilon, b_{1,i}, \varepsilon_{1,i}\right) \cdot d\varepsilon \cdot \frac{D\left(\zeta, b_{2,i,j}, \zeta_{1,i,j}\right)}{r_{3,i,j}}. \tag{5.43}$$

To simplify Eqn. 5.43, the transition to an infinite number of secondary sound particles S is performed. By this transition, the integral over the decreasing angle range $\Delta\varepsilon_2 = \frac{\pi}{S}$ is approximated by

$$\int_{\varepsilon_{1,i}+\frac{j}{S}\pi-\frac{\pi}{2}}^{\varepsilon_{1,i}+\frac{j+1}{S}\pi-\frac{\pi}{2}} D\left(\varepsilon, b_{1,i}, \varepsilon_{1,i}\right) \cdot d\varepsilon \approx D\left(\varepsilon_{1,i}+\varepsilon_2, b_{1,i}, \varepsilon_{1,i}\right) \cdot \Delta\varepsilon_2, \tag{5.44}$$

where the current direction is expressed by

$$\varepsilon_2 = \frac{j+0.5}{S}\pi - \frac{\pi}{2}. \tag{5.45}$$

This transition implies for the sound intensity with $\Delta\alpha = \frac{2\pi}{N}$

$$I = \frac{P'}{2\pi} \sum_{i=1}^{N_0} \sum_{j=1}^{S_0} \frac{D\left(\varepsilon, b_{1,i}, \varepsilon_{1,i}\right) \cdot D\left(\zeta, b_{2,i,j}, \zeta_{1,i,j}\right)}{r_{3,i,j}} \Delta\varepsilon_2 \Delta\alpha. \tag{5.46}$$

Now, the transition $\Delta\varepsilon_2 \to 0$ converts the second sum into an integral over the angle range the second VW is visible from the intersection point on the first VW. With the transition to an infinite number of primary sound particles, the remaining sum also converges to an integral (similar to the single diffraction case)

$$I = \frac{P'}{2\pi} \int_{\alpha_{Min}}^{\alpha_{Max}} \int_{\varepsilon_{2,Min}}^{\varepsilon_{2,Max}} \frac{D(\varepsilon, b_1, \varepsilon_1) \cdot D(\zeta, b_2, \zeta_1)}{r_3} d\varepsilon_2 d\alpha. \tag{5.47}$$

This analytical solution is based on two integrals over two angle ranges in the geometrical setup. To generalize the analytical solution, two substitutions are derived from Eqn. 5.39, such that the integrals integrate over the VWs instead of the angles α and ε_2. This substitutions can be derived either mathematically (compare with Eqn. 5.30) or geometrically (compare Fig. 5.15b) to

$$\begin{aligned} d\alpha &= \frac{cos(\varepsilon_1)}{r_1} da_1 = \frac{cos(\alpha)}{r_1} da_1 \\ d\varepsilon_1 &= \frac{cos(\zeta_1)}{r_2} da_2 = \frac{cos(\varepsilon_2)}{r_2} da_2. \end{aligned} \tag{5.48}$$

Hence, an analytical solution for the sound intensity of Eqn. 5.47 is written as

$$I = \frac{P'}{2\pi} \int_0^{\infty} \int_0^{\infty} \frac{D(\varepsilon, b_1, \varepsilon_1) \cdot D(\zeta, b_2, \zeta_1) \cdot cos(\varepsilon_1) \cdot cos(\zeta_1)}{r_1 r_2 r_3} da_2 da_1. \tag{5.49}$$

Finally, after applying the normalization to the free field sound intensity, the transmission level for the double diffraction at two wedges passed one after another is found

$$T = R \int_0^{\infty} \int_0^{\infty} \frac{D(\varepsilon, b_1, \varepsilon_1) \cdot D(\zeta, b_2, \zeta_1) \cdot cos(\varepsilon_1) \cdot cos(\zeta_1)}{r_1 r_2 r_3} da_2 da_1. \tag{5.50}$$

Both integrals integrate over the VWs. In contrast to the transmission level for single diffraction (see Eqn. 5.32), now two DAPDFs are multiplied to fulfil the double diffraction setup. In addition, a factor of $\frac{cos(\zeta_1)}{r_2}$ is added.

It should be noted that all values $\varepsilon_{1,2}$, $\zeta_{1,2}$, $b_{1,2}$ and $r_{1,2,3}$ are at least dependent on one by-pass distance a_1 or a_2.

This derivation can be extended to even higher order diffraction by using the same principles, i.e., adding a factor and an additional integral for each diffraction order. As these diffraction integrals are only solvable numerically, this extension is not performed in this work due to the computational effort. Experiments with higher diffraction orders are therefore carried out by numerical sound particle experiments.

Based on the found analytical description of the diffraction for simple scenarios, the diffraction module is evaluated and discussed in detail for first and second order in the following sections.

5.4. Fulfilment of the Reciprocity Principle

One of the most important principles in sound propagation simulation is to fulfil the principle of reciprocity, i.e., the result has to be independent of an interchanging of the sound source and the receiver. Whereas Stephenson only assumed (without strict proof) the reciprocity to be fulfilled in his first publications [Ste04] and still in 2009[Ste09], an empirical *proof* by sound particle experiments showed that the reciprocity is only fulfilled for $\varphi_S \approx 0°$ and major deviations occur for other angles of φ_S[SP11].

In this section, first the reciprocal scenario is described in short and the discrepancy is determined numerically followed by a brief repetition of Stephenson's attempts to modify the UBD module in order to fulfil the reciprocity. The wrong assumptions of these modifications are analysed and additional modifications to fulfil the reciprocity principle are introduced and discussed. Finally, the numerical deviations of the modified UBD module to reciprocity are determined.

5.4.1. Analysis of the Reciprocal Scenario

For the analysis of the reciprocity principle for diffraction at a single wedge, a sound source is positioned left of the wedge at $\varphi_S = 0°$ in a distance of $r_S = 10\lambda$. The receivers are positioned on the right-hand side of the wedge in a distance of $r_R = 10\lambda$, whereas the receiver angle φ_R is varied (see Fig. 5.19a). The angles φ_S and φ_R are then interchanged, such that the source position is varying and only one receiver at $\varphi_R = 0°$ is used (see Fig. 5.19b). In general, the source and the receiver distances have to be interchanged, but both are identical for this scenario.

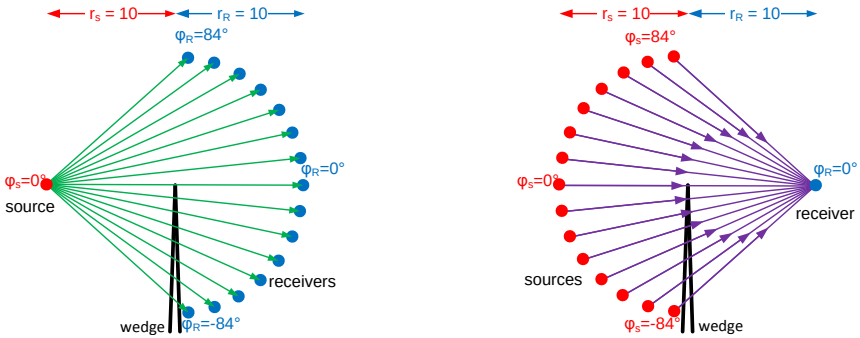

Figure 5.19.: Definition of the normal and the reciprocal scenario for $r_R = r_S = 10\lambda$ (source *red*, receiver *blue*).

As the VW is identical for both scenarios, also the formulation of the transmission level of Eqn. 5.32 is identical for both cases. In the denominator, the source-related and receiver-related distances r_1 and r_2, respectively, are interchangeable without changing the equation. However, the source-related angle $cos\,(\varepsilon_1)$ has no counterpart, which is the reason why a major difference in the results of the normal and the reciprocal scenario is found for both DAPDFs (see Fig. 5.20).

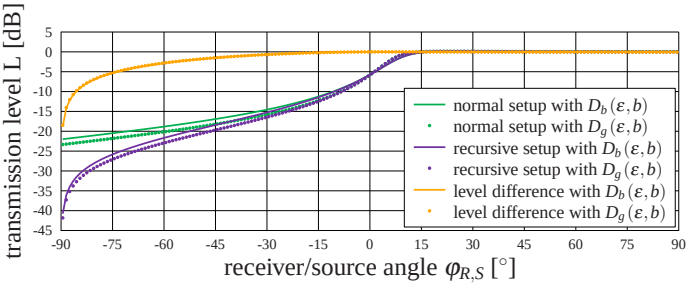

Figure 5.20.: Transmission level for the forward direction and the reciprocal scenario for a single wedge with $r_R = r_S = 10\lambda$. The angle of the fixed source/receiver is $0°$.

In the deep shadow zone $\varphi_{S,R} < -45°$, differences up to $20dB$ occur, which prove that the reciprocity is *not* fulfilled. On the other hand, the difference between the different DAPDFs seem to be very small, such that the mathematical investigation is restricted to the first and more simple DAPDF $D_b(\varepsilon, b)$. The results for this DAPDF are applied to the other DAPDF in the end.

Besides the cosine factor, the applied normalization constant D_0 might also be unreciprocal. With respect to Eqn. 5.16, the normalization constant reads

$$\int_{-\frac{\pi}{2}+\varepsilon_1}^{\frac{\pi}{2}+\varepsilon_1} \frac{D_0(b,\varepsilon_1)}{1+2\,(2\,\cdot\,b\,\cdot\,\varepsilon)^2} d\varepsilon = 1 \rightarrow D_0(b,\varepsilon_1) = \frac{1}{\int_{-\frac{\pi}{2}+\varepsilon_1}^{\frac{\pi}{2}+\varepsilon_1} \frac{1}{1+2(2\,\cdot\,b\,\cdot\,\varepsilon)^2} d\varepsilon}. \quad (5.51)$$

For $b \cdot \varepsilon \gg 1$, which is invalid only for very close by-pass distances a, the normalization constant is found to be only dependent on the effective slit width b and, thus, it is independent of the angle of incidence ε_1

$$D_0(b,\varepsilon_1) \overset{b\varepsilon\gg1}{\approx} \frac{\sqrt{2}\,\cdot\,2\,\cdot\,b}{\pi} = D_0(b). \quad (5.52)$$

As the normalization constant is (approximately) independent of the source and the receiver angles and distances, the factor does not affect the behaviour of the transmission level with respect to reciprocity. Hence, only the $cos(\varepsilon_1)$ factor in the integral is responsible for the inconsistency of the UBD module concerning the reciprocity principle. This complies with Fig. 5.20, where the relation between the reciprocal and the normal scenario is quite identical to a cosine factor of $cos(\varphi_R)$ in the shadow zone ($\varphi_R < 0°$).

5.4.2. Stephenson's Attempts to Achieve Reciprocity

In order to fulfil the reciprocity principle and to diminish the DAPDF in the deep shadow, Stephenson investigated the Fresnel - Kirchhoff diffraction integral in more detail and introduced an additional factor f (see Eqn. 2.35). Since from a physical point of view only the total diffraction angle $\varphi_S + \varphi_R \approx \varepsilon_1 + \varepsilon_2 = \varepsilon$ is relevant, Stephenson substitutes $\varphi_S = \varphi_R \approx \frac{\varepsilon_{1,2}}{2}$ generating a modified factor f' for small $\varepsilon_{1,2}$

$$f = \frac{cos(\varphi_R) + cos(\varphi_S)}{2} \approx \frac{cos\left(\frac{\varepsilon_1}{2}\right) + cos\left(\frac{\varepsilon_2}{2}\right)}{2} = cos\left(\frac{\varepsilon}{2}\right) = f'. \quad (5.53)$$

In the Fresnel - Kirchhoff diffraction integral, this factor is applied to the sound pressure, such that for the energetic approach the factor has to be squared. Furthermore, Stephenson uses another approximation yielding the energetic factor

$$f'^2 = \left(cos\left(\frac{\varepsilon}{2}\right)\right)^2 = \frac{1 + cos\,(\varepsilon)}{2} \approx 1 - \frac{\varepsilon}{2} \approx cos\,(\varepsilon)\,. \tag{5.54}$$

These factors were used to create new DAPDFs (see Sec. 5.2.2, Eqn. 5.15).

Unfortunately, the DAPDF with exactly the factor $f'^2\ D_g\,(\varepsilon, b')$ brings practically no improvement in the fulfilment of the reciprocity (see Fig. 5.20). This behaviour is explained, because the factor f' is itself reciprocal, as it depends only on $\varepsilon = \varepsilon_1 + \varepsilon_2$ and, thus, cannot compensate the $cos\,(\varepsilon_1)$ factor. Therefore, different approaches to fulfil the reciprocity principle are introduced.

5.4.3. Modifications of the Diffraction Angle Probability Density Function to Fulfil the Reciprocity Principle

The attempts of Stephenson to fix the reciprocity were unsuccessful, as only a reciprocal factor was used. In contrast to the former modifications, an unreciprocal factor is now introduced. The first approach is to multiply the DAPDF by the missing cosine factor and the second approach is to divide the DAPDF by the existing cosine factor. Furthermore, an approach that modifies the EDS is discussed.

5.4.3.1. Multiplication of the Diffraction Angle Probability Density Function with $cos(\varepsilon_2)$

In order to create a counterpart for the $cos\,(\varepsilon_1)$ factor, an additional $cos(\varepsilon_2)$ factor is introduced to the DAPDF

$$D_{cos(\varepsilon_2)}\,(\varepsilon, b) = D\,(\varepsilon, b)\ \cdot\ cos\,(\varepsilon_2)\,. \tag{5.55}$$

From a physical point of view, this factor could be argued by the *Lambert* law (see Sec. 2.3.3). A multiplication with the new factor ensures that also the VW emits energy following *Lambert's* law (the maximum contribution must not exceed $cos\,(\varepsilon_2)$) in addition to the diffraction theory.

At first sight, a reciprocal formulation of the transmission level (see Eqn. 5.32) seems to be found

$$T = R\int_0^\infty \frac{D_{cos(\varepsilon_2)}\,(\varepsilon, b)\ \cdot\ cos(\varepsilon_1)}{r_1\ \cdot\ r_2} da = R\int_0^\infty \frac{\frac{D_{0,cos(\varepsilon_2)}(b,\varepsilon_1)\ \cdot\ cos(\varepsilon_2)}{1+2(2\ \cdot\ b\ \cdot\ \varepsilon)^2}\ \cdot\ cos(\varepsilon_1)}{r_1\ \cdot\ r_2} da \tag{5.56}$$

While for the unmodified DAPDF the normalization constant $D_0\,(b)$ has been shown to be (approximately) reciprocal (see Eqn. 5.52), this is not valid after the multiplication of the DAPDF with the cosine factor, as a renormalization is necessary. It is shown mathematically that, at least for $b \gg 1$, an approximation for the new normalization constant is valid, with

$$D_{0,cos(\varepsilon_2)}\,(b, \varepsilon_1) \approx \frac{\sqrt{2}\ \cdot\ 2\ \cdot\ b}{\pi\ \cdot\ cos\,(\varepsilon_1)} = \frac{D_0\,(b)}{cos\,(\varepsilon_1)}. \tag{5.57}$$

Inserting Eqn. 5.57 in Eqn. 5.56 reveals that again the reciprocity is not fulfilled. This time, a $cos\,(\varepsilon_2)$ factor remains without an equivalent counterpart.

$$T = R\int_0^{\infty} \frac{\frac{D_0(b)}{cos(\varepsilon_1)} \cdot cos(\varepsilon_2)}{1+2(2 \cdot b \cdot \varepsilon)^2} \cdot cos(\varepsilon_1)}{r_1 \cdot r_2} da = R\int_0^{\infty} \frac{\frac{D_0(b) \cdot cos(\varepsilon_2)}{1+2(2 \cdot b \cdot \varepsilon)^2}}{r_1 \cdot r_2} da \qquad (5.58)$$

While the mathematical derivation of the normalization factor is quite demanding, the result can also be explained graphically. For $b \gg 1$, as assumed also in the mathematical derivation, the DAPDF is very narrow. By a multiplication of the DAPDF with a factor of $cos(\varepsilon_2) = cos(\varepsilon - \varepsilon_1)$ almost the complete DAPDF is scaled by a quite constant factor due to its narrow shape (see Fig. 5.21).

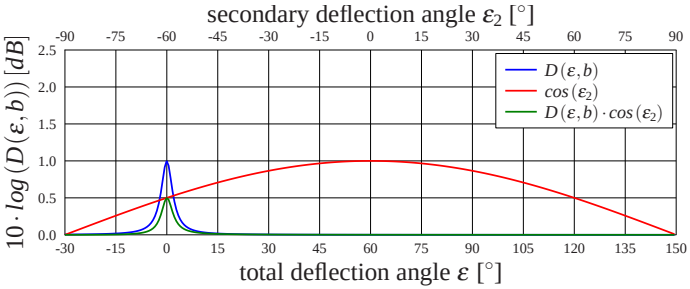

Figure 5.21.: Influence of the multiplication of the Diffraction Angle Probability Density Function with $cos(\varepsilon_2)$ for huge by-pass distances ($b = 10, \varepsilon_1 = 60°$).

The DAPDF is symmetrical to $\varepsilon = 0°$ (see lower $x - axis$), which correlates to $\varepsilon_2 = -60°$ for $\varepsilon_1 = 60°$ in the given example. The cosine factor $cos\,(\varepsilon_2)$, on the other hand, is symmetrical to $\varepsilon_2 = 0°$ (see upper $x - axis$) and almost constant in the range of the DAPDF for $b \gg 1$. This constant occurs at $\varepsilon = 0°$, which relates to $cos\,(-\varepsilon_1) = cos\,(\varepsilon_1)$. Due to the energy conservation criterion, the factor has to be compensated by the renormalization and automatically extends the DAPDF by a factor $\frac{1}{cos(\varepsilon_1)}$.

For smaller by-pass distances ($b \leq 1$) this approximation is a bit too rough as shown in Fig. 5.22.

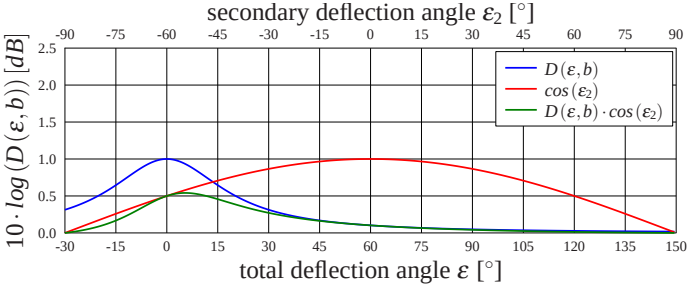

Figure 5.22.: Influence of the multiplication of the Diffraction Angle Probability Density Function with $cos(\varepsilon_2)$ for small by-pass distances ($b = 1, \varepsilon_1 = 60°$).

The DAPDF is by far broader than for huge by-pass distances, such that the multiplication with a *constant* factor is invalid for the complete range of the DAPDF. The maximum of the DAPDF is shifted in the direction of $\varepsilon_2 = 0°$. Besides these restrictions, the rescaling behaviour of the DAPDF is approximately valid here.

Even more, the introduction of the $cos(\varepsilon_2)$ factor can be interpreted as a new DAPDF modified by a factor of $\frac{cos(\varepsilon_2)}{cos(\varepsilon_1)}$. However, there is no physical argumentation for such a factor.

5.4.3.2. Division of the Diffraction Angle Probability Density Function by $cos(\varepsilon_1)$

Another approach to fulfil the reciprocity principle is to divide the DAPDF by a factor of $cos(\varepsilon_1)$ to compensate the existing cosine factor. Hence, a new DAPDF reads

$$D_{cos(\varepsilon_1)}(\varepsilon, b) = \frac{D(\varepsilon, b)}{cos(\varepsilon_1)}. \tag{5.59}$$

No physical argumentation is found for this procedure, but from a mathematical point of view all former numerical evaluations stay approximately valid, because $\varphi_S = 0°$ results in $\varepsilon_1 \approx 0°$. Again, the reciprocity seems to be fulfilled at a first glance

$$T = R \int_0^\infty \frac{D_{cos(\varepsilon_1)}(\varepsilon, b) \cdot cos(\varepsilon_1)}{r_1 \cdot r_2} da = R \int_0^\infty \frac{\frac{D_{0,cos(\varepsilon_1)}(b, \varepsilon_1)}{cos(\varepsilon_1)}}{r_1 \cdot r_2} \cdot cos(\varepsilon_1) da. \tag{5.60}$$

In order to approve the reciprocal behaviour of the integral, the normalization constant has to be recomputed. In contrast to the multiplication by a $cos(\varepsilon_2)$ factor, this time the normalization constant is computed without further approximations, with

$$D_{0,cos(\varepsilon_1)}(b, \varepsilon_1) = D_0(b) \cdot cos(\varepsilon_1). \tag{5.61}$$

Here, the normalization constant is multiplied by a factor of $cos(\varepsilon_1)$. For Eqn. 5.60 this yields again a formulation that does not fulfil the reciprocity principle

$$T = R \int_0^\infty \frac{\frac{D_0(b) \cdot cos(\varepsilon_1)}{cos(\varepsilon_1)}}{r_1 \cdot r_2} \cdot cos(\varepsilon_1) da = R \int_0^\infty \frac{D_0(b)}{r_1 \cdot r_2} \cdot cos(\varepsilon_1) da. \tag{5.62}$$

This formulation equals exactly Eqn. 5.32, such that the results are completely unaffected by the modification. This is explained graphically as shown in Fig. 5.23

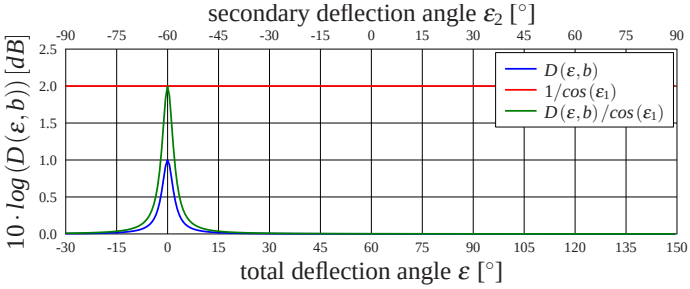

Figure 5.23.: Influence of the division of the Diffraction Angle Probability Density Function by $cos(\varepsilon_1)$ ($b = 10, \varepsilon_1 = 60°$).

The DAPDF is multiplied by a *constant* factor $\frac{1}{cos(\varepsilon_1)}$, such that the complete energy is scaled by the same factor. As the normalization assures that the total energy equals 1, this multiplication is withdrawn.

As the result equals the former equation, again no improvement to the reciprocity is achieved. Even more it is stated that any modification of the DAPDF cannot fix the reciprocity due to the renormalization of the DAPDF, because any needed asymmetrical solution is cancelled by the normalization (at least for not too small distances). Hence, a different approach has to be applied.

5.4.3.3. Usage of a *Projected* Slit Width

As the approach to modify the DAPDF has failed, the second function of the UBD is investigated, i.e., the EDS $S(a)$, which only depends on the by-pass distance a.

Up to now, the evaluated by-pass distance and, hence, the proportional slit with b, are completely independent of the angle of incidence ε_1. It is not the shortest by-pass distance. This behaviour, on the other hand, is only correct for the perpendicular sound incidence on a slit. For an oblique incidence, also the shortest by-pass distance may be considered to be relevant for the uncertainty relation. Thus, a *projected* slit width b' is introduced (see Fig. 5.24a), such that the sound particles see a narrower slit.

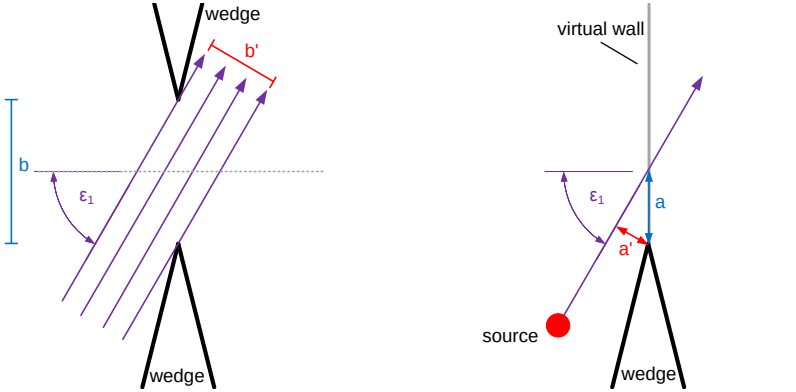

(a) *projected* slit width b' **(b)** *projected* by-pass distance a'

Figure 5.24.: Graphical explanation for projection of an angle of incidence $\varepsilon_1 = 60°$.

For the *projected* slit width it is followed geometrically

$$b' = b \cdot cos(\varepsilon_1). \tag{5.63}$$

This correction of the actual slit width b is applied to the by-pass distance a in the same way (see Fig. 5.24b). The result is a *projected* by-pass distance a'

$$a' = a \cdot cos(\varepsilon_1). \tag{5.64}$$

As a and b are proportional to each other, both models yield the same modification. Due to the usage of the EDS inside the DAPDF, a modified DAPDF is formulated

$$D_{b'}(\varepsilon, b) = D(\varepsilon, b \cdot cos(\varepsilon_1)). \tag{5.65}$$

The transmission level of Eqn. 5.32 then reads

$$T = R \int_0^\infty \frac{D_{b'}(\varepsilon, b) \cdot cos(\varepsilon_1)}{r_1 \cdot r_2} da = R \int_0^\infty \frac{\frac{D_{0,b'}(b,\varepsilon_1)}{1+2(2 \cdot b \cdot cos(\varepsilon_1) \cdot \varepsilon)^2} \cdot cos(\varepsilon_1)}{r_1 \cdot r_2} da, \tag{5.66}$$

where an unreciprocal formulation occurs by this modification also in the denominator of $D_{b'}(\varepsilon, b)$ for the first time. Before the equation is analysed further, the normalization constant for the particular case has to be computed (using Eqn. 5.52)

$$D_{0,b'}(b, \varepsilon_1) = D_0\left(b'\right) = D_0\left(b \cdot cos\left(\varepsilon_1\right)\right) \approx \frac{\sqrt{2} \cdot 2 \cdot b \cdot cos\left(\varepsilon_1\right)}{\pi} = D_0\left(b\right) \cdot cos\left(\varepsilon_1\right). \tag{5.67}$$

For the transmission level of Eqn. 5.66, this modification delivers

$$\begin{aligned} T &= R \int_0^\infty \frac{\frac{D_{0,b'}(b,\varepsilon_1)}{1+2(2 \cdot b \cdot cos(\varepsilon_1) \cdot \varepsilon)^2} \cdot cos(\varepsilon_1)}{r_1 \cdot r_2} da \\ &= R \int_0^\infty \frac{\frac{D_0(b) \cdot cos(\varepsilon_1)}{1+2(2 \cdot b \cdot cos(\varepsilon_1) \cdot \varepsilon)^2} \cdot cos(\varepsilon_1)}{r_1 \cdot r_2} da. \end{aligned} \tag{5.68}$$

Appling the approximation $b \cdot \varepsilon \gg 1$, the transmission level simplifies to

$$T \approx R \int_0^\infty \frac{\frac{D_0(b) \cdot cos(\varepsilon_1)}{2(2 \cdot b \cdot cos(\varepsilon_1) \cdot \varepsilon)^2} \cdot cos(\varepsilon_1)}{r_1 \cdot r_2} da = R \int_0^\infty \frac{\frac{D_0(b)}{2(2 \cdot b \cdot \varepsilon)^2}}{r_1 \cdot r_2} da. \tag{5.69}$$

Finally, a complete reciprocal formulation (assuming $b \cdot \varepsilon \gg 1$) for the transmission level is found, as neither ε_1 nor ε_2 remain in the equation. Both radii r_1 and r_2 are completely interchangeable. Although the made approximations are actually not valid for small by-pass distances a or small diffraction angles ε, the reciprocity is proven analytically in a wide range.

At first glance, it seems doubtful to achieve reciprocity by taking the slit width into account which is seen from the sound source and neglecting the slit width which is seen from the receiver. However, this definition meets the idea of a straight-forward simulation technique based on the Kirchhoff approximation, since diffraction has to be independent of the receiver position (which is not yet known).

5.4.4. Numerical Difference after Introducing the Modifications

The introduction of a *projected* slit width shows, in principle, a reciprocal equation for the transmission level. This transmission level is computed for three distance combinations $r_S = r_R = 1\lambda, 10\lambda$ and 100λ in Fig. 5.25.

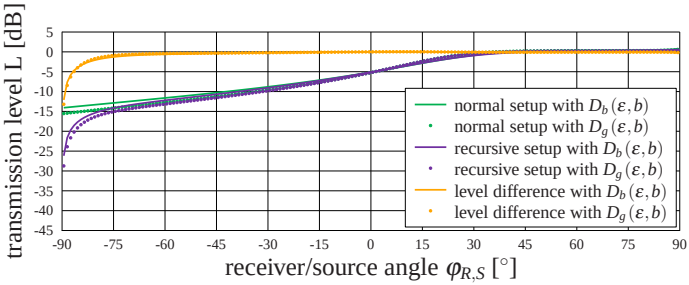

(a) $r_R = r_S = 1\lambda$

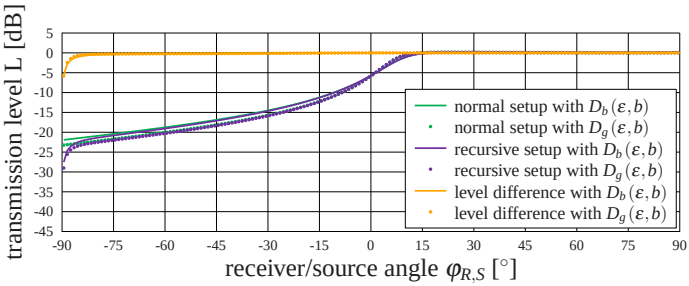

(b) $r_R = r_S = 10\lambda$

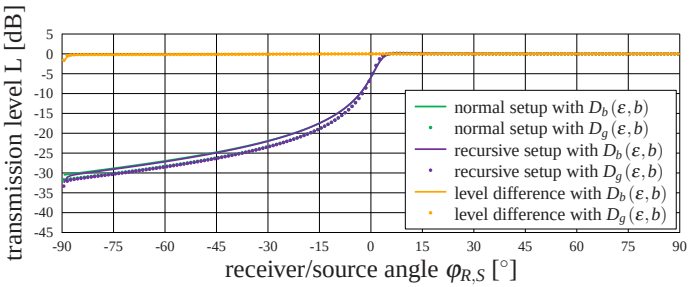

(c) $r_R = r_S = 100\lambda$

Figure 5.25.: Transmission level for the forward direction and the reciprocal scenario for a single wedge after introduction of the *projected* slit width b'.

Fig. 5.25 shows that the reciprocity is fulfilled in all scenarios $r_R = r_S \geq 10$ for the complete angle range (difference$< 0.7dB$). Only for very close sound sources and receivers ($r_R = r_S = 1$) greater differences occur below $\varphi_R < -75°$. For larger receiver angles, the difference is below $1dB$ even for such close distances that the approximations made are not valid anymore.

Even for the second DAPDF $D_g(\varepsilon, b)$, which has not been investigated mathematically, the results are completely applicable, as the results of both DAPDFs are almost identical (difference $< 0.1dB$).

In summary, the *projected* slit width b' solves the reciprocity problem for almost

all cases. Only for very close source and receiver positions and simultaneous very low receiver positions differences above $1dB$ remain. Nevertheless, a huge improvement has been achieved also in these regions. The modified EDS is used for the rest of this work.

5.5. Validation and Comparison with Reference Models

The former UBD module was validated by Stephenson in detail for the single wedge and a slit. Due to the modifications of the EDS (to fulfil the reciprocity principle) as well as the new normalization range, these results became outdated. Furthermore, both the presented extension to higher order diffraction and the combination of the diffraction module with reflections have not been evaluated yet.

In this section, first the analytical solution for the UBD module is compared with three simple scenarios (screen, slit and cascade) using the MDL (only for screen and cascade) as well as Svenssons SSM as references. Based on this results, the final DAPDF for this work is chosen. With this DAPDF, the module is tested on consistency when some non-geometrical parameters are varied. Finally, the integration of the UBD module into a SPSM is performed and validated for some critical setups.

5.5.1. Comparison of Simple Scenarios with Reference Models

In a first investigation, analytical formulations of the three simple scenarios of a single wedge, a slit and two subsequent wedges (see Sec. 5.3) are validated against the reference models. In order to fulfil the reciprocity principle, the EDS is used that utilizes the *projected* slit width. Although eight different DAPDFs were presented in total, it was shown that only two of them are physically reasonable (see Sec. 5.2.2). In the following, the UBD with the former DAPDF $D_b\left(\varepsilon, b\right)$ is denoted as UBD_b and the UBD with the new DAPDF $D_g\left(\varepsilon, b\right)$ is denoted as UBD_g. As reference models both the SSM and the MDL are used.

After discussing the three scenarios single wedge, slit and cascade independently from each other, this section concludes with the selection of a final DAPDF for this work.

5.5.1.1. Single Wedge

The geometrical setup of a single wedge is given in Fig. 5.26. The geometrical variables are the source distance r_S, the receiver distance r_R, the source angle φ_S and the receiver angle φ_R. The transmission levels are directly computed regarding Eqn. 5.32. In all experiments, the source and the receiver distances as well as the source angles are fixed, whereas the receiver angle is varied in steps of 1° (in contrast to 15°[Ste04]). The methods are analysed in four regions (see Fig. 5.26).

- *region0*: $-90^\circ < \varphi_R \leq -60^\circ$ (deep shadow zone)
- *region1*: $-60^\circ < \varphi_R \leq -30^\circ$ (medium shadow zone)
- *region2*: $-30^\circ < \varphi_R \leq 0^\circ$ (high shadow zone)
- *region3*: $-90^\circ < \varphi_R \leq 90^\circ$ (complete range)

The mean differences between different models are computed for these regions. In addition, the maximum and minimum differences between the different models are computed.

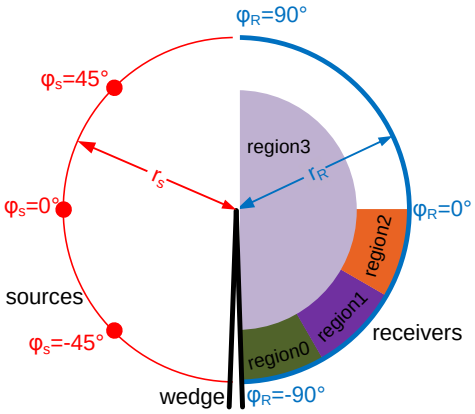

Figure 5.26.: Definition of the investigated regions of the single wedge.

In a first reference experiment, the source and the receiver distances are set to $r_S = r_R = 10\lambda$ and the source angle is set to $\varphi_S = 0°$. The results of the transmission level $L = 10 \cdot log_{10}(T)$ of the UBD, the MDL and the SSM are shown in Fig. 5.27.

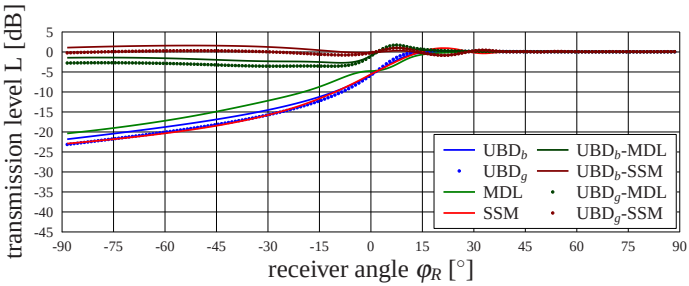

Figure 5.27.: Validation of a single screen as a function of φ_R, with $r_S = 10\lambda$, $\varphi_S = 0°$ and $r_R = 10\lambda$.

The main difference between the two UBDs is that the UBD$_g$ diffracts fewer energy into the shadow zone, such that a greater transmission loss (smaller transmission level) of about $1dB$ is gained quite constantly in the shadow zone (closer to the SSM).

Investigations of Stephenson[SS07] (using the former DAPDF with beam diffraction) showed a standard deviation (in contrast to the mean difference in this work) between UBD and SSM of $0.39dB$, but without the EDS with the *projected* slit width.

The UBD$_g$ fits very well to the SSM (*region0* - *region1*). Only in the transition from the shadow zone to the view zone at approximately $\varphi_R = 20°$, the SSM causes a transmission level above $0dB$, hence, an increasing transmission level after the introduction of the wedge. This effect is caused by *ripples* from interference effects (see Fig. 2.12). Here, this effect is smoothed due to the applied octave band averaging. In contrast, the MDL and the UBD cannot model this effect as both methods are energetic models. Therefore, at $\varphi_R = 21°$, the difference of transmission levels between the UBD and the SSM reaches its minimum ($0.8dB$). Between this *ripple* and the boundary to the

shadow region ($\varphi_R = 0°$), the transmission level decreases stronger for the UBD than for the SSM, such that a maximum difference of $1.0dB$ is observed. For the UBD$_b$, this difference vanishes almost completely, but the maximum difference between the UBD$_b$ and the SSM is $1.6dB$ at $\varphi_R = -52°$ due to the difference in the shadow zone. This difference is almost constant in the shadow zone (*region0* - *region1*) yielding an overall mean difference (*region3*) of $0.6dB$, whereas the UBD$_g$ delivers a mean difference of $0.0dB$ (*region3*). The MDL, on the other hand, overestimates the diffracted energy in a wide angle range. Quantitatively, the MDL results in a $2.0dB$ greater transmission level in comparison to the UBD$_b$ and a $3.0dB$ greater transmission level in comparison to the UBD$_g$ (*region0* - *region2*). Nevertheless, the UBD$_g$ brings in more accurate results compared to the SSM. For the MDL a saddle point is noted a $\varphi_R = 0°$, as the detour itself has a saddle point there. Due to this saddle point, the minimum difference between the UBD$_b$ is $-2.7dB$ at $\varphi_R = -9°$ and the maximum difference $1.0dB$ at $\varphi_R = 8°$ quite symmetrically. In case of the UBD$_g$, the minimum is shifted to $\varphi_R = -29°$ with $-3.6dB$. On average, the mean difference (*region3*) is $-0.9dB$ (UBD$_b$) and $-1.4dB$ (UBD$_g$), respectively.

To achieve more general results, the parameters r_S, r_R and φ_S are modified independently, before all distances are modified simultaneously, which equals the modification of the frequency for fixed distances and finally the source angle is varied. For the interested reader, all graphical comparisons are shown in appendix A.2.1. In addition, tables summarizing the differences quantitatively are given.

Changing Source Distances As first parameter, the source distance is varied within $r_S = 0.1\lambda, \lambda, 10\lambda, 100\lambda, 1000\lambda$. For distances $r_S > 10\lambda$, a far field approximation is defined for all three models, such that the occurring differences from modifying the source distance do not affect the transmission level anymore. For sound sources coming closer to the wedge, the transmission level of the SSM increases faster than the transmission level of the UBD in the shadow zone. Therefore, the UBD underestimates the diffracted sound energy in comparison to both the MDL and the SSM for $r_S \leq 1\lambda$ (see Fig. 5.28). However, the transmission level was in-between them for distances $r_S > 1$.

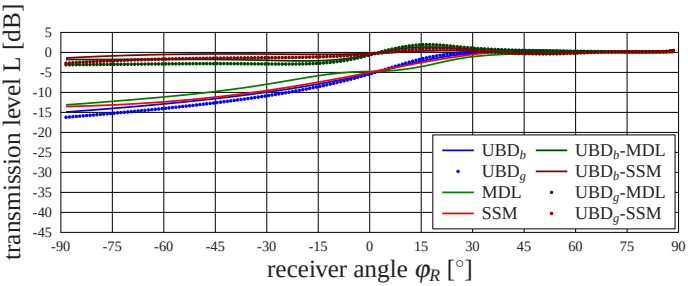

Figure 5.28.: Validation of a single screen as a function of φ_R, with $r_S = 1\lambda$, $\varphi_S = 0°$ and $r_R = 10\lambda$.

For all distances, the UBD$_g$ is approximately $1dB$ below the UBD$_b$ in the shadow zone. For very close sound sources $r_S = 0.1$ this means that the mean difference (*region3*) between the UBD$_b$ and the SSM is smaller ($-0.6dB$) compared to the UBD$_g$ ($-1.0dB$). Nevertheless, the agreements are better than expected for very close distances, as interference effects (not handled by the energetic UBD) were expected to dominate. A mean value over the *region3* values of all source distances shows that the

UBD_g is only a little closer ($0.2dB$) to the SSM than the UBD_b ($-0.3dB$). As shown in Tab. A.1, the difference of the UBD_g comes mainly from differences in close sound source scenarios. As larger distances are of higher importance, the UBD_g yields better results than the UBD_b.

Changing Receiver Distance In this investigation, the receiver distance r_R is varied, whereas the source distance is fixed at $r_S = 10\lambda$. As for the variation of the source distance, again, the convergence to a far field approximation for $r_R > 10\lambda$ seems to be fulfilled, since no variation is found for $r_R > 10\lambda$. Basically the same effects occur for closer receivers as for the variation of the source distance r_S. In the transition to the near field, the transmission level of the SSM rises faster than the transmission level of the UBD. Due to this effect, the difference between the UBD_g and the SSM decreases down to a minimum of $-3.5dB$ at $\varphi_R = -89°$ for $r_R = \frac{1}{10}$ (see Tab. A.2). However, a good agreement between the SSM and the UBD can still be found, as this difference occurs only for extreme angles. The mean difference (*region3*) over all receiver distances is quite similar for the different DAPDFs (UBD_b:$0.3dB$, UBD_g:$-0.2dB$), but again the discrepancy between the UBD_g and the SSM occurs only for very close distances. The MDL overestimates the diffracted energy in contrast to the UBD_b by $-0.2dB$ ($-0.9dB$ in case of the UBD_g) (average over *region3* for all distances).

Changing All Distances Frequency is often very important in practical scenarios. Therefore, all distances are varied simultaneously in the next experiment. A doubling of the relative distance, for instance, is directly interpreted as a doubling of the frequency. In the deepest shadow zone (*region0*), transmission levels range from $-7dB$ for $r_S = r_R = 0.1\lambda$ up to $-42dB$ for $r_S = r_R = 1000\lambda$ for the SSM. This is explained by the detour law, too (see Tab. A.3). The UBD_g follows this strong variation quite well, but again with a smaller slope. Thus, the UBD_g overestimates the diffraction by $+2.8dB$ at 1000λ and underestimates the diffraction by $-2.4dB$ at 0.1λ (*region0*). For *region3*, the mean discrepancy is only $+1.6dB$ and $-0.9dB$, respectively. The UBD_b behaves quite similar but produces again approximately a $1dB$ greater transmission level in the complete shadow zone (*region0-region2*). This yields better agreements with the SSM for close distances and worse agreement for far distances.

The maximum underestimation of the transmission level of the UBD in the interference region is located at $\varphi_R = 21°$ for $r_S = r_R = 10\lambda$, but shifts in the direction of $\varphi_R \to 0°$ for increasing distances. For $r_S = r_R = 100\lambda$, the minimum is shifted to $\varphi_R = 7°$ (see Fig. 5.29), whereas it stayed almost constant for the previous experiments.

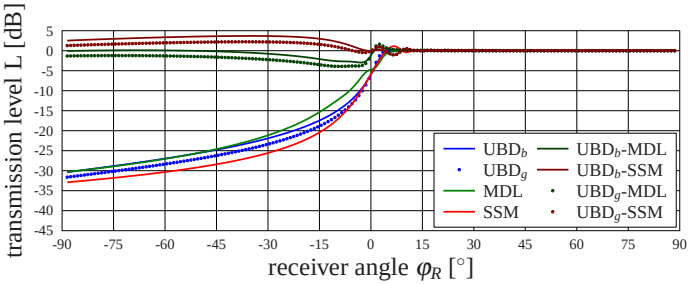

Figure 5.29.: Validation of a single screen as a function of φ_R, with $r_S = 100\lambda$, $\varphi_S = 0°$ and $r_R = 100\lambda$.

Here, the transmission level of the UBD$_g$ is in-between the transmission levels of the SSM and the MDL. The average difference between the UBD and the SSM (*region3*) is $0.9dB$. Although the largest difference is expected to be in the deepest shadow zone (*region0*), the medium shadow zone (*region1*) has a $0.5dB$ greater difference than the deep shadow zone. This effect occurs qualitatively for all distances larger than 10λ and can also be seen in the maximum difference of $2.2dB$ at $\varphi_R = -37°$. There is no physical explanation for this effect and, thus, the effect can only be argued by the totally different underlying diffraction theories. Finally, the average over all *region3* setups shows that the UBD$_g$ fits the SSM better ($0.2dB$) than the UBD$_b$ ($0.7dB$).

Changing Source Angle As a final experiment for the single wedge setup, the distances are now fixed with $r_S = r_R = 10\lambda$ and the source angle φ_S is varied in steps of 15°. These experiments have never been performed by Stephenson, as he expected these experiments to be covered already by the reciprocity principle. Indeed these experiments are important, because, on the one hand, the UBD was not reciprocal before and, on the other hand, these experiments now include total diffraction angles above 90°, which are very important in practical cases. Without the introduction of the *projected* slit width (see Sec. 5.4) the UBD would cause errors of up to $20dB$ for sound sources in the shadow zone. With the introduction of the *projected* slit width, the difference between the UBD$_g$ and the SSM is only $2.3dB$ in *region3* for sound sources in the deep shadow zone $\varphi_S = -75°$ (see Tab. A.4). These angles correlate with a total diffraction angle of $\varepsilon \approx 150°$. The good agreements between the UBD and the SSM are even more astonishing, as the derivation of the diffraction module uses the Kirchhoff approximation which is only valid for small diffraction angles[Pie89]. Hence, the introduction of the *projected* slit width to the UBD is interpreted also as an extension of the Fraunhofer diffraction to greater diffraction angles (see Sec. 2.3.4.3). Diffraction angles above ±90° were not possible before the redefinition of the normalization (see Sec. 5.2.4). The interference effect for the SSM as well as the saddle point of the MDL are shifted on the φ_R axis by the source angle as shown in Fig. 5.30.

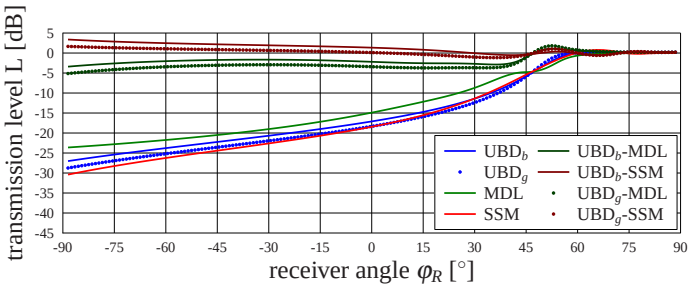

Figure 5.30.: Validation of a single screen as a function of φ_R, with $r_S = 10\lambda$, $\varphi_S = -45°$ and $r_R = 10\lambda$.

For $\varphi_S = -45°$, the transition from the shadow zone into the view zone is at $\varphi_R = 45°$, where the saddle point of the MDL is identified. The interference point is also shifted from $\varphi_R = 21°$ ($\varphi_S = 0°$) to $\varphi_R = 66°$ ($\varphi_S = -45°$) (as the angles are counted in different directions). The UBD$_g$ yields about $1dB$ smaller transmission levels than the UBD$_b$ for all source angles in the (now extended) shadow zone. As the UBD$_g$ matches the SSM quite well for $\varphi_S = 0°$ and $r_S = r_R = 10\lambda$, the averaged difference in *region3* is $0.0dB$ and $0.6dB$ for the UBD$_b$.

5.5.1.2. Slit

The geometrical setup for the slit is composed by two wedges where both diffraction wedges are parallel to the $z-axis$. In addition to the parameters of the single wedge experiment, the distance between the wedges d is varied, too. The regions of interest are the same as before (see Fig. 5.31). The MDL is not defined for the diffraction at a slit and is, thus, not considered here. The EDB is used to compute the SSM again and the UBD is computed according to Eqn. 5.36.

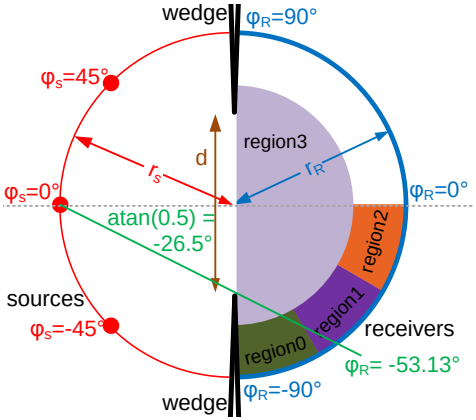

Figure 5.31.: Definition of the investigated regions of the slit. *Green* angles are only valid for $r_S = r_R$.

The reference experiment for the slit setup is defined as follows: the sound source is located on axis ($\varphi_S = 0°$) and all distances are set to $r_S = r_R = d = 10\lambda$. Stephenson validated the received sound intensity relative to the total diffracted sound energy for parallel incidence, i.e., $r_{S,R} \to \infty$. In order to stay conform to both other experiments in this section, the transmission degree T is defined as the received sound intensity relative to the free-field sound intensity (as for the single wedge). The transmission levels are shown in Fig. 5.32.

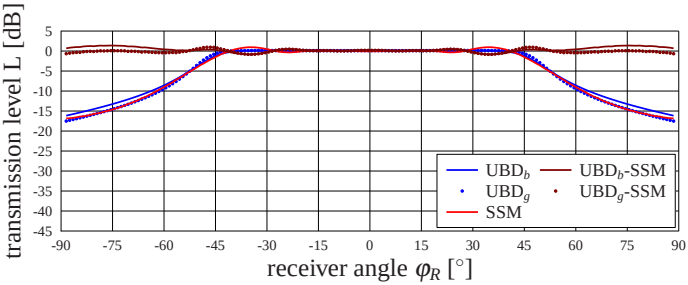

Figure 5.32.: Validation of a slit ($d = 10\lambda$) as a function of φ_R, with $r_S = 10\lambda$, $\varphi_S = 0°$ and $r_R = 10\lambda$.

The transmission level is completely symmetrical to $\varphi_R = 0°$ for the SSM and for both

UBDs. In the angle range $-35° < \varphi_R < 35°$, the transmission level is almost exactly $0dB$ for both DAPDFs (compare with total illumination area $-53.13° < \varphi_R < 53.13°$, see Fig. 5.31). For the SSM, in the transition region between the shadow and the view zone again the interference effect is modelled yielding an overestimation of the diffraction of $+0.8dB$ at $\varphi_R = \pm 36°$. In the actual shadow zone, the UBD_g yields again an approximately $1dB$ smaller transmission level than the UBD_b. The UBD_g fits the SSM better in the shadow zone of *region0* ($-0.2dB$ in contrast to $+1.1dB$). The maximum difference of $+1.0dB$ at $\varphi_R = \pm 47°$ as well as the minimum difference of $-0.8dB$ at $\varphi_R = \pm 36°$ reveal a very good agreement between the SSM and the UBD_g. Furthermore, the overall difference between these transmission levels is $\pm 0.0dB$ in *region3*. In short, the good agreements of the single wedge experiment are also obtained for the slit experiment.

Based on this reference case, only one of the distances r_S, r_R and d is changed. Then, all distances are changed simultaneously to perform a variation of the frequency. Finally, a variation of the source angle φ_S is investigated. The numerical results as well as the plots are given in appendix A.2.2.

Changing Source Distance The source distance r_S is varied within the same range as in the single wedge experiment. For distances $r_S > 10\lambda$, the results converge to a far field distribution and the UBD differs only slightly from the SSM. In contrast to the perfect match for $r_S = 10\lambda$, the SSM matches the UBD_g still very well in the view zone and in the deepest shadow zone, but the SSM computes smaller transmission levels between $\varphi_R = \pm 75°$ and $\varphi_R = \pm 45°$ of up to $+1.3dB$ at $\varphi_R \approx \pm 64°$ (see Tab. A.5). Hence, a mean difference of $+0.9dB$ is noticed in *region0* resulting in a total difference of $+0.5dB$ in *region3*. With the UBD_b, this difference is $+1.3dB$ due to the constantly greater transmission levels. For shorter source distances $r_S < 10\lambda$, the angle range of the view zone increases drastically ($\Delta\varphi_R = 150°$ for $r_S = 1\lambda$, see Fig. 5.33).

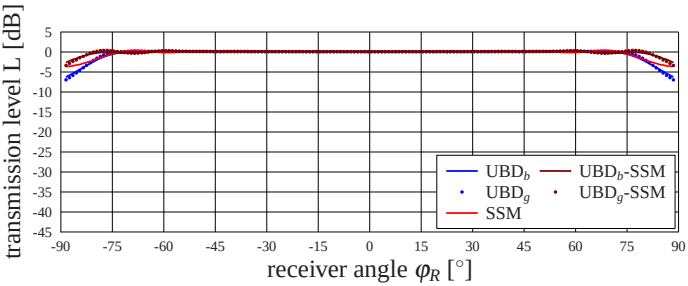

Figure 5.33.: Validation of a slit ($d = 10\lambda$) as a function of φ_R, with $r_S = 1\lambda$, $\varphi_S = 0°$ and $r_R = 10\lambda$.

For these short distances that are not covered by Kirchhoff theory, almost no difference between the different DAPDFs is found. Both show good agreement with the SSM with $L \approx 0dB$. For the closest distance of $r_S = 0.1\lambda$, the SSM computes a transmission level of $L \approx 0dB$ over the complete angle range of the receivers, whereas the UBD yields transmission levels up to $3dB$ below this threshold for receiver positions in the deep shadow zone, $|\varphi_R| > 80°$. Minimum differences between the UBD and the SSM of $-3.4dB$ occur at $\varphi_R = \pm 89°$. In the deep shadow region, sound energy is diffracted for sound particles passing the edge closely, hence, some energy is missing for receivers in the straight forward direction of these sound particles. This effect decreases with de-

creasing source distances with the result that again a match between the SSM and the UBD is expected for even shorter source distances $r_S < 0.1\lambda$. However, the agreements are still better than expected, because the underlying Kirchhoff theory is derived for large distances. The average of all the experiments in *region3* shows better agreement between the UBD$_g$ and the SSM ($0.2dB$) than in case of the UBD$_b$ ($0.5dB$).

Changing Receiver Distance In the second experiment, the receiver distance r_R is varied, while both source and wedge distances are constant $r_S = d = 10\lambda$. The source angle is again on axis ($\varphi_S = 0°$). For receiver distances of $r_R \leq 1\lambda$, all receivers are completely in the view zone of the slit (see Fig. 5.31). For $r_R = 1\lambda$, the transmission level is almost constant with $L \approx 0dB$ ($\pm 0.2dB$, see Tab. A.6). Due to this, no numerical values are computed for receivers even closer to the slit. With increasing receiver distances, the transmission level of both the SSM and the UBD gradually turns to a far field transmission level that is almost independent of the distance (see Fig. 5.34 for $r_R = 1000\lambda$).

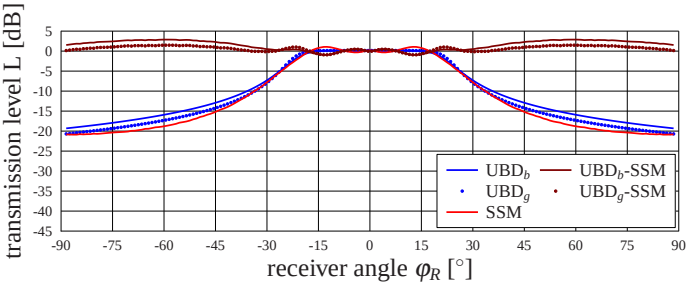

Figure 5.34.: Validation of a slit ($d = 10\lambda$) as a function of φ_R, with $r_S = 10\lambda$, $\varphi_S = 0°$ and $r_R = 1000\lambda$.

For $r_R = 1000\lambda$, the compatibility between the SSM and the UBD$_g$ is good with almost no discrepancy in both the view zone and the deepest shadow zone. However, for the transition from *region0* to *region1*, the UBD overestimates the transmission level. The maximum difference of $+1.5dB$ occurs at $\varphi_R = \pm 60°$ and the mean differences are $+1.0dB$ in *region0* and $+0.8dB$ in *region1*. The differences between the SSM and the UBD$_b$ are again about $1dB$ greater than between the SSM and the UBD$_g$. The mean average over all experiments in *region3* reveals better agreement of the UBD$_g$ ($0.3dB$) in contrast to the UBD$_b$ ($0.8dB$) with the SSM.

Changing Slit Width For constant source and receiver distances $r_S = r_R = 10\lambda$ and a source angle of $\varphi_S = 0°$, the influence of the wedge distance d (aperture size) is investigated in the following. For wedge distances above $d > 10\lambda$, the slit is too large to observe diffraction phenomena for the given source and receiver distances. Hence, the transmission level equals $L \approx 0dB$ for both diffraction methods. For wedge distances below $d < 10\lambda$, shadow regions occur. The difference in-between these methods is in the range between $-0.8dB$ and $+1.0dB$ in case of $d = 10\lambda$ (see Tab. A.7). For smaller distances of the wedges (aperture size), almost no agreement between the SSM and the UBD was expected, because strong side-lobes occur for small aperture sizes with Fraunhofer diffraction (see Sec. 2.3.4.3). Indeed, the maximum difference over all distances occurs for $d = 1\lambda$ with $2.3dB$ in the same order of magnitude as before at $\varphi_R = \pm 62°$. The transmission level is shown for $d = \frac{1}{10}\lambda$ in Fig. 5.35.

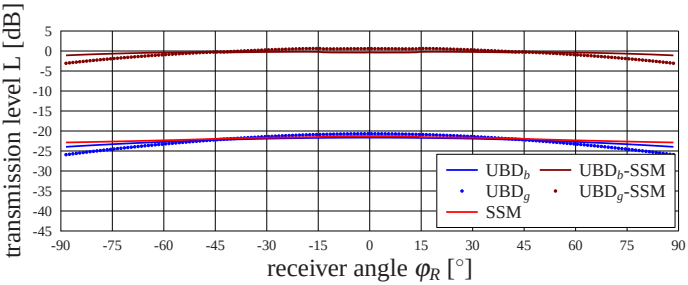

Figure 5.35.: Validation of a slit ($d = \frac{1}{10}\lambda$) as a function of φ_R, with $r_S = 10\lambda$, $\varphi_S = 0°$ and $r_R = 10\lambda$.

The transmission level computed with the SSM is quite constant at $-22dB$ for the complete angle range $-89° < \varphi_R < 89°$. The UBD$_b$ matches the SSM for the complete angle range, whereas the UBD$_g$ underestimates the diffracted energy with about $-3.1dB$ at $\varphi_R = \pm 89°$. Although the UBD$_b$ matches the SSM better for $d = \frac{1}{10}\lambda$, the UBD$_g$ matches the SSM around $1dB$ better for all larger distances. The mean difference in *region3* averaged over all distance combinations shows better results for the UBD$_g$ ($0.0dB$) than the UBD$_b$ ($0.5dB$) in comparison to the SSM.

Changing All Distances In order to investigate the frequency behaviour of diffraction at a slit, all distance combinations $\frac{1}{10}\lambda < r_S = r_R = d < 1000\lambda$ are computed. As in the previous experiments, the UBD$_b$ computes slightly greater transmission levels than the UBD$_g$, which, again, matches the SSM better - at least for larger distances. For small distances, i.e., low frequencies, quite constant transmission levels are found again similar to the experiment with small apertures ($d \leq 1$), but fixed source and receiver positions $r_S = r_R$. In this experiment, however, the transmission level is around $L \approx 0dB$ for $\varphi_R = 0°$. The quite constant transmission level for $d = \frac{1}{10}\lambda$ converges to transmission levels down to $-10dB$ at $d = 1\lambda$ in *region0* (see Tab. A.8). For larger distances, i.e., higher frequencies, a plateau is found between $-45° < \varphi_R < 45°$ (as shown in Fig. 5.36 for $r_S = r_R = d = 100\lambda$).

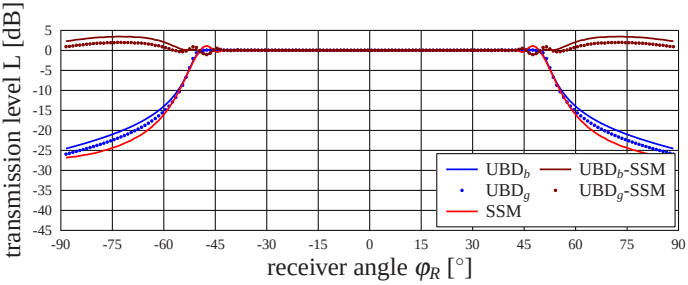

Figure 5.36.: Validation of a slit ($d = 100\lambda$) as a function of φ_R, with $r_S = 100\lambda$, $\varphi_S = 0°$ and $r_R = 100\lambda$.

For $r_S = r_R = d = 100\lambda$ identical results are computed in the view zone except for the interference effect yielding a difference of $-1.1dB$ between the UBD with both DAPDFs

and the SSM at $\varphi_R = \pm 47°$. However, the SSM computes smaller transmission levels in the deep shadow zone (*region0*) with a difference of $+1.6dB$ in comparison to the UBD_g and $+3.0dB$ in comparison to the UBD_b. The maximum difference between both models is again not obtained for the lowermost angle $\varphi_R = \pm 89°$, but for $\varphi_R = \pm 74°$. In the regions *region1* and *region2* almost no difference between the UBD_g and the SSM is found ($\pm 0.0dB$) and only slight differences occur in the case of the UBD_b (*region1*:$0.2dB$, *region2*:$0.0dB$). In the complete angle range, on the other hand, the discrepancy between the UBD_b and the SSM ($0.6dB$) is significantly greater than with the UBD_g ($0.3dB$).

Changing Source Angle In a last experiment for the slit setup, the source angle is modified in steps of 15° in-between $-75° \leq \varphi_S \leq 75°$. In the appendix A.2.2.5 only the figures for the angles $-75° \leq \varphi_S \leq 0°$ are shown as greater angles equal the shown graphs with inverted $x - axis$ due to the complete symmetrical geometry. The UBD_g yields almost identical transmission levels for $\varphi_S = 0°$ in comparison to the SSM, whereas the UBD_b overestimates the transmission levels in the shadow zone. Similar to the single wedge experiment, this behaviour stays almost unaffected by a rotation of the sound source up to extreme angles. For all possible combinations of source and receiver angles, the difference between the SSM and the UBD_g is always between $-1.9dB$ and $+2.2dB$ (see Tab. A.9) whereas it is in the range of $-0.9dB$ up to $+4.9dB$ using the UBD_b. The difference is explained by the general overestimation of diffraction by the previous DAPDF. It should be noted that the extreme discrepancies occur only in the outermost receiver positions at $\varphi_R = \pm 89°$. As an example, a comparison for $\varphi_S = -45°$ is shown in Fig. 5.37.

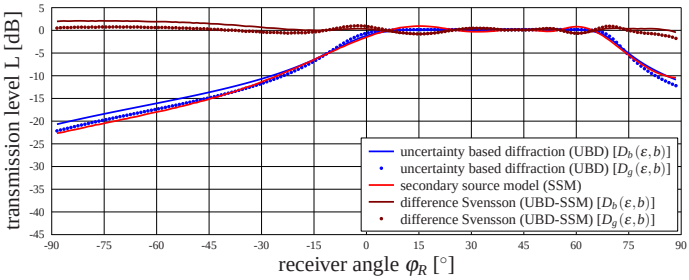

Figure 5.37.: Validation of a slit ($d = 10\lambda$) as a function of φ_R, with $r_S = 10\lambda$, $\varphi_S = -45°$ and $r_R = 10\lambda$.

For $\varphi_S = -45°$, two shadow regions exist with different transmission levels. For $\varphi_R < 0°$, transmission levels down to $-22dB$ are computed and the SSM matches the UBD_g almost perfectly. In contrast, the shadow region for $\varphi_R > 0°$ computes transmission level down to $-10dB$, but the SSM now matches the UBD_b better. As the first shadow zone exists in a wider angle range, the mean difference of the UBD_g is $+0.1dB$ in *region3* and $+0.6dB$ in case of the UBD_b. The average over the *region3* values of all source angles shows a by far better agreement of the UBD_g ($0.1dB$) with the SSM than in case of the UBD_b ($0.7dB$), but both still agree well with respect to the different diffraction theories.

5.5.1.3. Double Wedge

Finally, as a completely new investigation compared to the experiments that were carried out by Stephenson until 2009[Ste09], the validation of two subsequent wedges is discussed. Here, both wedges are parallel to the $z-axis$. The same investigations are performed as for the slit experiments, but the distance d now describes the distance between the wedges in $x-$ direction. It should be noted that the source and the receiver distances are given relative to the closest wedge (see Fig. 5.38). In case of the MDL, the transmission level is computed directly from Eqn. 5.4 with the detour of Fig. 5.2. The EDB is used to perform the SSM, where an accuracy parameter had to be introduced for higher order diffractions. In order to achieve results for this setup, the wedge length of $\Delta z = 2000m$ has to be adjusted depending on the accuracy parameter for each experiment to reduce the memory effort. Although the results are valid for a wide range of parameters, singularities are occurring for the SSM and will be mentioned.

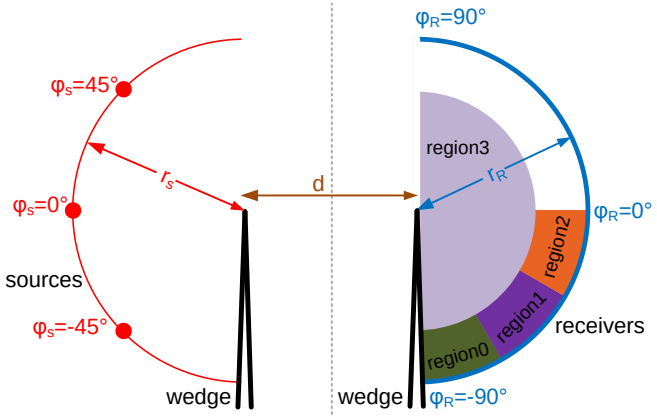

Figure 5.38.: Definition of the investigated regions of the double wedge

The reference experiment is given by an source angle of $\varphi_S = 0°$ and distances of $r_S = r_R = d = 10\lambda$. The transmission levels $L = 10 \cdot log_{10}(T)$ are shown in Fig. 5.39.

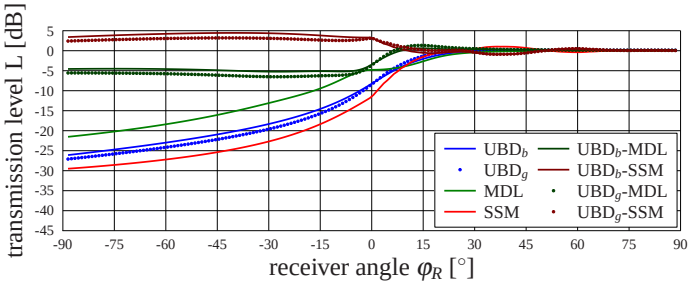

Figure 5.39.: Validation of a double wedge ($d = 10\lambda$) as a function of φ_R, with $r_S = 10\lambda$, $\varphi_S = 0°$ and $r_R = 10\lambda$.

The transmission level equals the behaviour of a single wedge qualitatively, but transmission level down to $-30dB$ are achieved. Although very good agreements in the view zone are still observed, the difference between the UBD and the reference methods increases in the shadow zone. When comparing the UBD_g with the SSM, the difference has a maximum of $+3.2dB$ at $\varphi_R = -42°$ and a minimum of $-0.9dB$ at $\varphi_R = +37°$. The minimum difference is caused by the same interference ripples as in the former experiments. Although the SSM is influenced by singularities in the region around $\varphi_S \approx 0°$, the results are accurate for the remaining angle range. In the shadow zone the UBD_g results in transmission levels of about $1dB$ below the transmission levels of UBD_b (as for the former investigations), resulting in a better match with the SSM. In the complete angle range (*region3*), the UBD_g matches the SSM about $0.5dB$ better than the UBD_b. On the other hand, the MDL computes up to $6.5dB$ greater transmission levels compared to the UBD and even $8dB$ greater transmission levels compared to the SSM. Thus, the results of the MDL are assumed to be totally wrong for double diffraction.

The parameters are varied as for the former experiments.

Changing Source Distance In this experiment, the source distance is varied within a range of $0.1\lambda < r_S < 1000\lambda$. For larger source distances $r_S > 10\lambda$, the difference between the UBD and the SSM increases slightly about $0.3dB$ in *region3* (see Tab. A.10). Nevertheless, a convergence to the far field case is observed, as the difference in-between $r_S = 100\lambda$ and $r_S = 1000\lambda$ is below $0.1dB$ except for the deep shadow zone (*region0*), where the UBD still decreases for increasing source distances. In case of decreasing source distances, however, the difference between the SSM and the UBD_g almost vanishes (see Fig. 5.40 for $r_S = 1\lambda$).

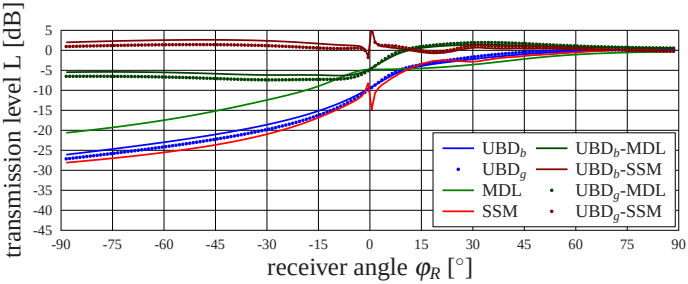

Figure 5.40.: Validation of a double wedge ($d = 10\lambda$) as a function of φ_R, with $r_S = 1\lambda$, $\varphi_S = 0°$ and $r_R = 10\lambda$.

Unfortunately, the decreasing source distance r_S increases the effect of the singularity around $\varphi_R \approx 0°$ (SSM), but the effect occurs only locally. Both the maximum difference of $+5.6dB$ at $\varphi_S = +1°$ and the minimum difference of $-1.8dB$ at $\varphi_S = -1°$ between the SSM and the UBD_g are caused by this singularity. For the remaining angle range, the UBD and the SSM fit quite well (differences below $1.0dB$), such that an average of $0.8dB$ is computed for *region3*. The UBD_b computes an average error of $1.2dB$ in the same range and the average over all source distances shows better agreement of the UBD_g ($0.8dB$) in comparison to the UBD_b ($1.3dB$).

The variation of the receiver distance behaves alike, but the average difference between the SSM and the UBD is increased by $0.5dB$ ($1.2dB$ with the UBD_g compared to $1.7dB$ with the UBD_b). All numerical values are listed in Tab. A.11.

Changing Distance Between Wedges In the following test case, the distance d is varied and the distances $r_S = r_R$ are set to 10λ. Increasing the wedge distance above the reference distance ($d > 10\lambda$) reduces the difference between the SSM and the UBD. A convergence to a far field distribution of all three models is observed – at least in the shadow region (*region0*-*region2*, see Tab. A.12). For these increased distances, a variation of the transmission level in the view zone is noticed for the first time. Here, the transmission level decreases from $0dB$ at $d = 10\lambda$ to $-6dB$ at $d = 1000\lambda$. This effect is almost identical for all three models. The physical reason for this effect is that even the sound wave propagating to the receivers in the upper view zone passes the first wedge with a short distance, such that the decreased transmission level is mainly an effect of first order diffraction. This effect is independent of the DAPDF and very smooth for the UBD and the SSM, whereas it is a hard transition at $\varphi_R \approx 0°$ in case of the MDL. For wedge distances below the reference distance ($d < 10\lambda$), the computation of diffraction becomes incomputable for the SSM (see Fig. 5.41 for $d = \frac{1}{10}$) due to the computational effort.

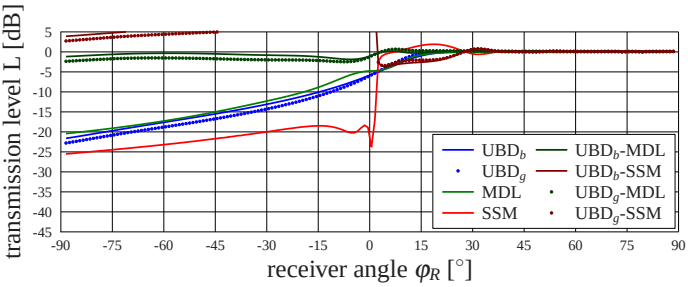

Figure 5.41.: Validation of a double wedge ($d = \frac{1}{10}\lambda$) as a function of φ_R, with $r_S = 10\lambda$, $\varphi_S = 0°$ and $r_R = 10\lambda$.

The singularity of the SSM is observed in the angle range of $-30° < \varphi_R < 30°$, $d = \frac{1}{10}$, such that the reference solution becomes doubtful for the complete angle range. Without a wave theoretical reference solution, the UBD can only be compared to the MDL, which shows good agreements for very close wedges. Although the MDL is only a very rough approximation, the results are plausible in this case, because such close wedges act almost like a single diffraction event (see Sec. 5.5.2.2). Although doubtful, the average difference over all distances in *region3* between the SSM and the UBD$_b$ is $1.5dB$ and $2.0dB$ in case of the UBD$_g$. The reader is reminded that these values are strongly influenced by the singularities of the SSM.

Changing All Distances Now, all distances $r_S = r_R = d$ are modified simultaneously. This can be reinterpreted as constant distances, but varying frequencies. The simultaneous modification of all distances allows a better adjustment of the SSM parameters, such that this reference model is valid almost for the complete distance range. For very small distances, $r_S = r_R = d = 0.1\lambda$, i.e., very low frequencies, the agreement between the SSM and the UBD is quite good for both DAPDFs, although the UBD$_b$ shows better results in *region0* ($+0.1dB$ in contrast to $-1.0dB$, see Tab. A.13). The MDL, on the other hand, yields different results as it overestimates the transmission level with about $3dB$ for $\varphi_R < 0°$ and underestimates the transmission level to the same amount for $\varphi_R > 0°$. In case of a distance of $r_S = r_R = d = 1\lambda$, the SSM matches the UBD$_g$ in both the deep shadow zone *region0* and the view zone. Only in the transition zone

around $\varphi_R \approx 0°$, the UBD computes a greater transmission level of approximately $2dB$. Larger distances result in even better agreements than the reference distance of $r_S = r_R = d = 10\lambda$ (see Fig. 5.42 for $r_S = r_S = d = 1000\lambda$).

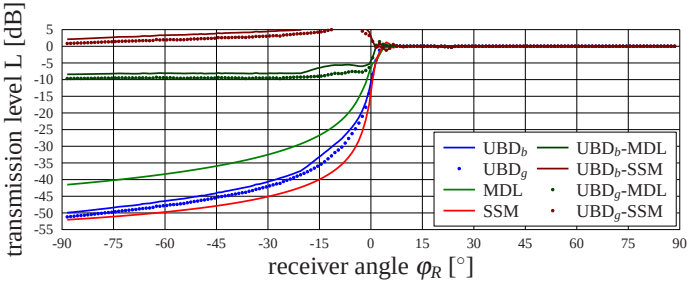

Figure 5.42.: Validation of a double wedge ($d = 1000\lambda$) as a function of φ_R, with $r_S = 1000\lambda$, $\varphi_S = 0°$ and $r_R = 1000\lambda$.

For such large distances, transmission levels down to $-52dB$ are computed with the SSM. Astonishingly, this transmission level almost matches the UBD$_g$, but also the UBD$_b$ computes transmission levels down to $-50dB$ in the deep shadow zone (*region0*). The MDL overestimates the transmission levels (only down to $-42dB$) in the same region and, thus, adds an error of up to $10dB$. Like in the experiment for the single wedge and the slit, the maximum error between the UBD and the SSM is not in the deep shadow zone (*region0*), but occurs at $\varphi_R = -6°$ where the slope of the transmission level has its maximum. The average difference over all distances between SSM and the UBD$_b$ is $1.5dB$ and $1.0dB$ in case of the UBD$_g$, respectively. However, the difference between the UBD and the MDL is $-2.3dB$ and $-2.8dB$, respectively.

Changing Source Angle The last experiment handles the variation of the source angle φ_S in steps of 15° for double diffraction. The distances are set to $r_S = r_R = d = 10\lambda$. Due to the geometrical setup, source angles in the view zone with $\varphi_S > 0°$ result in single diffraction events at the second wedge. As described in the section on the single wedge, the agreement between the SSM and the UBD$_b$ is only a little bit better than with the UBD$_g$. Thus, the more interesting case is defined by sources in the shadow zone $\varphi_S < 0°$ (see Fig. 5.43 for $\varphi_S = -45°$).

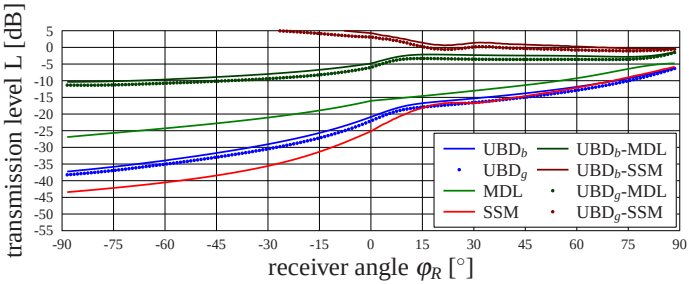

Figure 5.43.: Validation of a double wedge ($d = 10\lambda$) as a function of φ_R, with $r_S = 10\lambda$, $\varphi_S = -45°$ and $r_R = 10\lambda$.

Two regions are identified for a sound source in the shadow zone ($\varphi_S = -45°$). In case of receivers in the former view zone $\varphi_R > 0°$, single diffraction occurs which has already shown good agreements (see Sec. 5.5.1.1). Receivers in the shadow zone ($\varphi_R < 0°$) are influenced by both double diffraction and diffraction angles above $\varepsilon > 90°$. In contrast to single diffraction or the diffraction at a slit, the transition of a sound source into the shadow zone increases the difference between the SSM and the UBD even with the new DAPDF up to $5.5dB$ at $\varphi_R = -52°$ (see Tab. A.14). This difference decreases for even lower receivers slightly, such that a mean difference in *region0* of $5.3dB$ is observed. This difference is reduced to $2.4dB$ in *region3*. The average over all source rotation angles shows that the UBD_g yields significantly better results ($1.1dB$) than the UBD_b ($1.8dB$).

5.5.1.4. Discussion of the Validation of the Simple Test Cases and Choice of the Diffraction Angle Probability Density Function

The analytical comparison of the UBD with the wave theoretical reference model SSM for the single wedge, the slit and two subsequent wedges showed that in either case a convergence to a far field distribution is observed with increasing source and receiver distances. Also for close distances, acceptable agreements are noticed, where a failure of the UBD was actually expected. In general, the UBD matches the SSM in almost all test cases for the single wedge and the slit. Although the UBD is based on Kirchhoff assumptions and, thus, it is theoretically only valid for small diffraction angles, very good agreements between the SSM and the UBD are observed for the transition of the sound source even in the shadow zone for the single wedge and the slit. This is achieved by the introduction of the *projected* slit width (see Sec. 5.4). All former EDSs were not able to handle this critical section correctly. In case of double diffraction, the UBD computes greater transmission levels (up to $5dB$ in the worst case, where the absolute transmission level is in the range of $-50dB$). In all experiments the UBD proved to be a huge improvement in comparison to the MDL.

In order to choose the best-suited DAPDF, the numerical values of the single wedge, the slit and two subsequent wedges are averaged and minimum and maximum values are determined. The results are given in Tab. 5.1

		region $[dB]$				Min$[dB]$	at$[°]$	Max$[dB]$	at$[°]$
		0	1	2	3				
single	UBD_b-MDL	-1.1	-1.1	-1.4	-0.4	-7.5	-89	$+5.1$	$+89$
	UBD_b-SSM	$+0.9$	$+1.2$	$+0.6$	$+0.5$	-3.0	-89	$+7.2$	-89
	UBD_g-MDL	-2.6	-2.4	-2.2	-1.0	-11.4	-89	$+4.7$	$+89$
	UBD_g-SSM	-0.5	± 0.0	-0.2	-0.1	-4.7	-89	$+3.8$	-25
slit	UBD_b-SSM	$+1.4$	$+0.6$	± 0.0	$+0.7$	-3.4	± 89	$+5.2$	± 66
	UBD_g-SSM	$+0.3$	$+0.2$	$+0.1$	$+0.2$	-3.4	± 89	$+3.6$	± 66
cascade	UBD_b-MDL	-4.4	-4.5	-4.4	-2.2	-12.2	-80	$+2.6$	$+89$
	UBD_b-SSM	$+2.7$	$+3.6$	$+2.9$	$+1.7$	-18.1	-01	$+28.3$	$+01$
	UBD_g-MDL	-5.6	-5.8	-5.4	-2.8	-13.9	-82	$+3.0$	$+89$
	UBD_g-SSM	$+1.5$	$+2.3$	$+1.9$	$+1.1$	-18.4	-01	$+28.2$	$+01$

Table 5.1.: Average differences between different diffraction models for the single wedge, the slit and the double wedge.

The UBD_b shows in all regions and every setup better agreements with the wave theoretical reference (about $1dB$), but the choice of the DAPDF showed a minor effect than expected. However, as the UBD_b matches the SSM better, UBD_b is discarded and only UBD_g is used in the following (the index g is omitted).

5.5.2. Consistency of the Uncertainty relation Based Diffraction Module

In this section, the consistency of the UBD is discussed. In this context, consistency means that the UBD model has to fulfil the most important physical laws and has to be independent of the variation of (no physical/geometrical) parameters. The important reciprocity principle has already been investigated before (see Sec. 5.4).

Now, the fulfilment of Babinet's principle[Bab37] is discussed. Second, the convergence of double diffraction to single diffraction ($d \rightarrow 0$) is studied. As the VW is constructed by the convex sub-division and, thus, is not necessarily placed exactly on the bisecting line of the wedge, the influence of the misplacement of this VW is investigated. The studies are restricted to the distance of $r = 10\lambda$, since only the principle behaviour is of interest and the results are assumed to be applicable to other distances.

5.5.2.1. Babinet's Principle

Babinet's principle[Bab37] is basically known from optics[Hec01]. It states that the superposition of a wave propagating around a screen adds up with the wave propagating through the complementary screen to the equivalent wave without any obstacle. In this context, complementary means that the opening is replaced by a solid screen and vice versa. In addition, the impedance of the objects has to be inverted, too (hard $\leftrightarrow$ soft) [HC99], and complex sound pressures have to be added. However, as the aim of this section is to check whether the energetic UBD fulfils Babinet's principle, identical (hard) surfaces are assumed and intensities are added up.

In this work, the diffraction of a slit is combined with the diffraction around a screen (obstacle) with the same size as the slit (see Fig. 5.44).

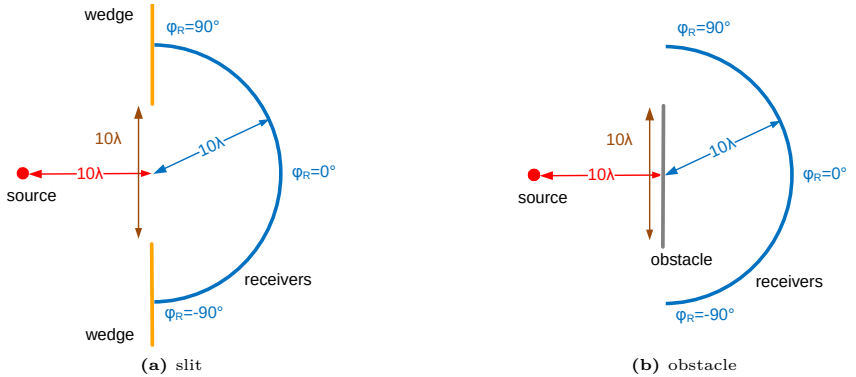

Figure 5.44.: Geometrical definitions for an investigation of Babinet's principle by superposing diffraction at a slit and diffraction around an obstacle.

The transmission level of the slit in case of the UBD can directly be computed from Eqn. 5.36 by integrating in the range of $-\frac{d}{2} < a < \frac{d}{2}$. However, in case of the screen, the integration has to be performed from $-\infty < a < -\frac{d}{2}$ and from $\frac{d}{2} < a < \infty$. In addition, the energetic sum is shown in Fig. 5.45, too.

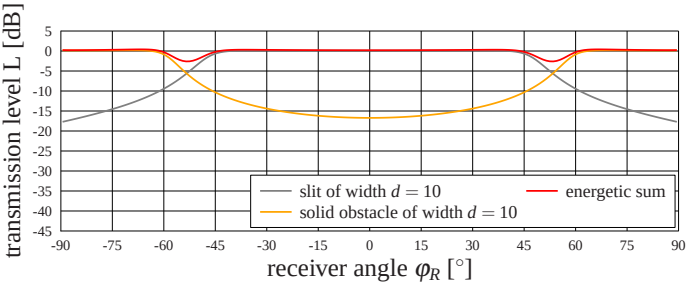

Figure 5.45.: Validation of Babinet's principle at a slit, its complementary screen and their energetic sum for the Uncertainty relation Based Diffraction.

In the view zone of the slit ($-45° < \varphi_R < 45°$) as well as in the view zone of the screen ($|\varphi_R| > 60°$) a transmission level of $L = 0dB$ is obtained solely by either the slit or the screen. The appropriate transmission level is small enough ($L < -10dB$), such that the energetic sum also fulfils the $L = 0dB$ requirement. Geometrically, the point of transition is found at $|\varphi_R| \approx 53.13°$ (see Fig. 5.31). At this point, the transmission level is computed by the UBD to $-5.6dB$ for both the slit and the obstacle. Hence, both energies add up to $-2.6dB$. Around this transition angle, the transmission level of the sum of both transmission levels converges quite linearly to the $0dB$ level in the view zones described earlier. Unfortunately, the requested transmission level of $L = 0dB$ is underestimated by the energetic sum with about $-2.6dB$ at the most. To understand this behaviour, the same experiment is performed for the SSM. In theory, the SSM fulfils Babinet's principle exactly for a single frequency, as it is a wave-based approach. In contrast to Kirchhoff, the SSM needs a well-defined wedge angle. This angle is set to 1° for both limits of slit and for the screen. The crucial point is that the diffraction modules that are applicable in GA have to be valid for a frequency range. Due to this requirement, the SSM was evaluated in octave bands in the former experiments. Assuming this octave band averaging also for the investigation of Babinet's principle, the transmission levels are computed with the SSM (see Fig. 5.46).

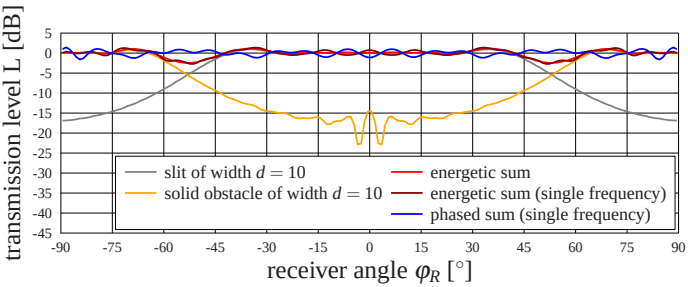

Figure 5.46.: Validation of Babinet's principle at a slit, its complementary screen and their energetic sum for the Secondary Source Model.

The SSM computes transmission levels greater than $L = 0dB$ for both the slit and the screen. The energetic sum yields the same overestimations of about $1dB$ for the diffracted energy. In the transition region, the underestimation of the UBD is repeated.

In order to exclude the effect by averaging, the SSM is computed for a *single frequency* instead of an octave band and, again, the results for the screen and the slit are added up energetically (see Fig. 5.46, *dark red*). Due to the evaluation at a single frequency, the overall behaviour of the transmission level slightly varies over the complete angle range ($\pm 1dB$), but in the transition region, the significant reduction of the transmission level still exists. Hence, the octave band averaging cannot be the reason for the underestimation of the transmission level in the transition region. In both experiments, the transmission levels were added up energetically. In case of the SSM, the phase information of the amplitude can be taken into account. Therefore, the (complex) transmission degree is added up before the transmission level is computed from the magnitude of this addition (see Fig. 5.46, *blue*). Then, the reduction of the transmission level in the transition zone is compensated almost completely and the interference effects that overestimate the transmission level are compensated as well. The insignificant variations over the complete angle range might be explained by the not exact complementary setup: The geometrical reason is that wedges are modelled in contrast to flat barriers as in the original case of Babinet. Thus, the superposition of slit and obstacle does not exactly form an infinite flat wall. Another reason is that one of the setups would have been modelled with soft instead of rigid surfaces.

The conclusion is that the discrepancy between the SSM and the UBD is mainly caused by the energetic addition of the transmission levels. However, this effect cannot be modelled by the UBD, as phase information could not be introduced at any time.

5.5.2.2. Convergence of Double Diffraction to Single Diffraction

As an analytical solution is available now for double diffraction, the convergence from double to single diffraction is investigated for the first time. In order to have a consistent diffraction module, the transmission levels of the double diffraction experiments for small wedge distances have to converge to the transmission levels of the single wedge. Mathematically speaking, Eqn. 5.50 should converge to Eqn. 5.32 for $d \to 0$. Unfortunately, this transition is not performable in an analytical way, because too many geometrical singularities occur. A geometrical investigation is presented that shows arguments for such a convergence. In addition, numerical experiments are performed.

As shown in Fig. 5.17b, the transition of $d \to 0$ does not affect the diffraction at the first VW. However, by moving the second VW in the direction of the first VW, the distance a_2 has to equal a_1, because both VWs merge to one. The numerical problem for $d \to 0$ occurs for the computation of the angle of incidence ζ_1 on the second VW. It is computed from Eqn. 5.39 (see Fig. 5.18). It is shown in Fig. 5.47 for different d.

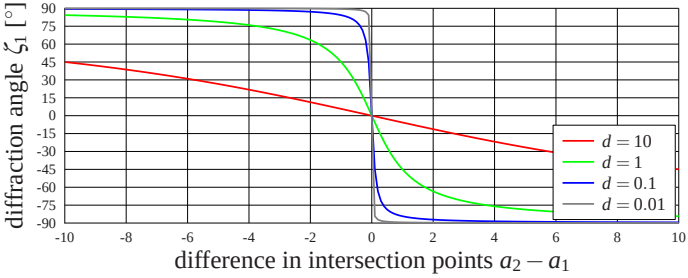

Figure 5.47.: Angle between two Virtual Walls ζ_1 for different wedge distances d as a function of the difference of intersection point $a_2 - a_1$.

For $d = 0$, the angle ζ_1 is not defined, but for infinitesimally short distances $d \to 0$, the angle ζ_1 jumps from $\zeta_1 = 90°$ at $a_2 = a_1 - \epsilon$[a)] to $\zeta_1 = -90°$ at $a_2 = a_1 + \epsilon$.

This singularity, or undefined behaviour, of the angle between those VWs makes an analytical formulation hard to define. However, as the distance d between both VWs converges to zero, the sound particles travel almost no distance in-between the VWs (in neither $x-$ nor y direction). So, the scattering and the *broadening* of the distribution of the secondary sound particles that are diffracted by the first VW, and, thus, the diffraction effect, is approximately suppressed. Hence, only the diffraction at the second VW takes place - as expected.

For a numerical investigation of the former assumption, the transmission level of the double wedge (see Sec. 5.5.1) with different d are compared directly to the transmission levels of the single diffraction. Although for double diffraction the source position and the receiver position are defined relative to the closer VW, their positions are practically the same as in the single diffraction case. For the UBD, the results are compared in Fig. 5.48.

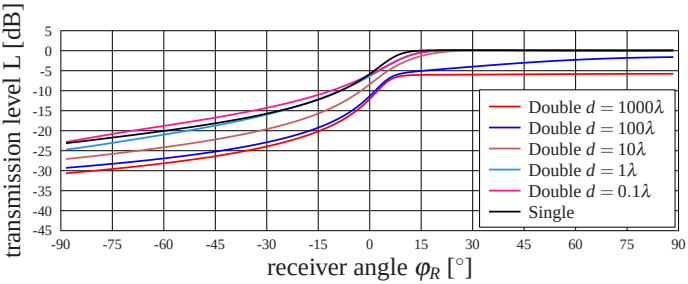

Figure 5.48.: Convergence of the transmission level from double diffraction to single diffraction for $r_S = r_R = 10\lambda$ of the Uncertainty relation Based Diffraction.

The transmission level of the UBD converges to the single diffraction experiment (*black*) above $\varphi_R > 15°$. Furthermore, in the deepest shadow zone at $\varphi_R = -89°$ the same convergence is noticed. In the shadow zone $-80° < \varphi_R < 0°$, the double diffraction converges to the single diffraction for decreasing wedge distances down to $d = 1\lambda$. For even shorter distances $d = 0.1\lambda$, the transmission level increases even further, i.e., an over-convergence of the double diffraction experiment is observed. However, this effect is $2dB$ at the most. This is better than expected, because mathematically a double diffraction is still computed even for $d = 0.1\lambda$.

This effect could be reduced by scaling the EDS by a factor that takes into account the distance from the last point of diffraction, such that the influence of the EDS is weakened. The main advantage of such a factor is that the convergence to single diffraction is achieved, as the diffraction at the second VW is disabled for $d \to 0$. This factor would, on the other hand, abandon the assumption that sound particles should be handled independently with respect to their history. That is very important for the reunification of sound particles, because sound particles might differ in another attribute (distance since last diffraction) and could not be reunified with particles with the same propagation path, but different diffraction distances. Therefore, a modified EDS should be avoided and slight differences in the convergence of double to single diffraction for the UBD should be accepted.

[a)] Here ϵ indicates an infinitesimally small positive distance

Double diffraction that is computed with the MDL, converges of course exactly to the single diffraction results (see Fig 5.49), if just the total detour is measured.

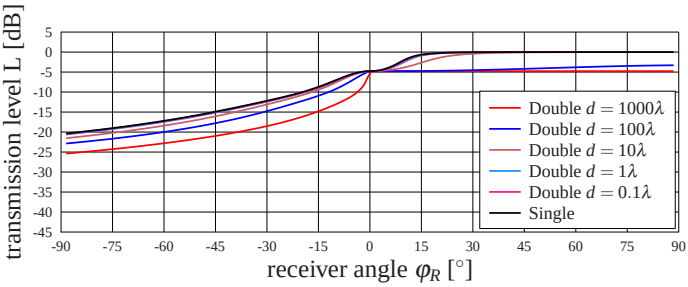

Figure 5.49.: Convergence of the transmission level from double diffraction to single diffraction for $r_S = r_R = 10\lambda$ of the Maekawa Detour Law.

Due to the simple geometry, it is clear that with decreasing d the detour converges to the single diffraction case.

Finally, the convergence of the SSM is investigated (see Fig. 5.50).

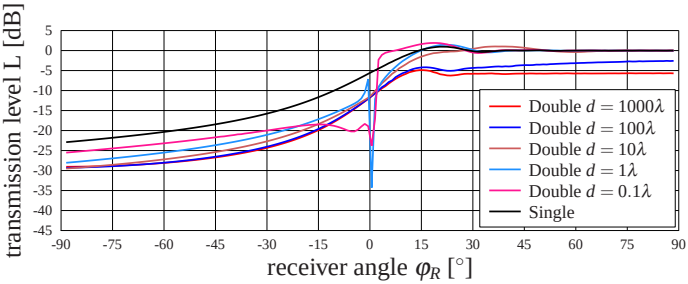

Figure 5.50.: Convergence of the transmission level from double diffraction to single diffraction for $r_S = r_R = 10\lambda$ of the Secondary Source Model.

In both the upper view and the deep shadow zone, the double diffraction case converges to the single diffraction case with decreasing d, but in contrast to the UBD, the single diffraction level is not reached for $d = 0.1\lambda$ yet $(-3dB)$. However, the results are doubtful anyway, because singularities occur in the angle range of $\varphi_R \approx 0°$ which spread at least 30° in both the shadow and the view zone. As described in the previous section about double diffraction, it is mathematically demanding to compute double diffraction for very close wedges, because of two countervailing requirements. First, the wedge has to be split up in very small parts for the numerical integration due to the very close wedge and, second, the wedge has to be of proper length due to the source and receiver distances of $r_S = r_R = 10\lambda$. Both restrictions spread for decreasing wedge distances, such that the numerical problems increase for closer wedges.

5.5.2.3. Influence of the Angle of the Orientation of a Virtual Wall

The investigations so far assumed the VW to be identical with the $yz - plane(x = 0)$. In the SPSM, however, this VW can be rotated around the diffracting wedge by convex

sub-division (see Chapter 4). This influence has to be small in order to obtain a robust model. In this section, the influence of such a rotation by an angle of γ is investigated for the single wedge case (see Fig. 5.51a).

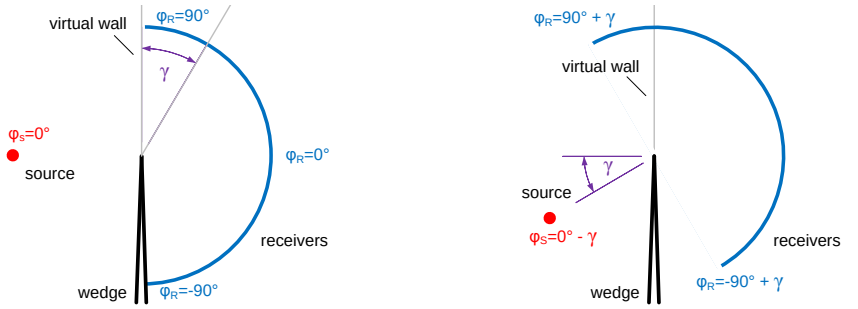

(a) rotation of a Virtual Wall by an angle of γ

(b) rotation of the complete scene by an angle of γ

Figure 5.51.: Rotation of a Virtual Wall and its complementary scenario.

This rotation yields extensive modifications for Eqn. 5.32, as all angles and distances have to be recalculated. As, on the other hand, the actual wedge does not affect the UBD, a complementary scenario is defined by rotating both the source and the receiver position (see Fig. 5.51b). Mathematically speaking, the complementary scenario is described by

$$\varphi_S \rightarrow \varphi_S - \gamma \qquad \text{and} \qquad \varphi_R \rightarrow \varphi_R + \gamma. \tag{5.70}$$

Using these modifications, Eqn. 5.32 is utilized to compute the transmission level for a rotated VW. The angle γ is rotated in steps of 30° in the range $-90° \leq \gamma \leq 90°$ as shown in Fig. 5.52a.

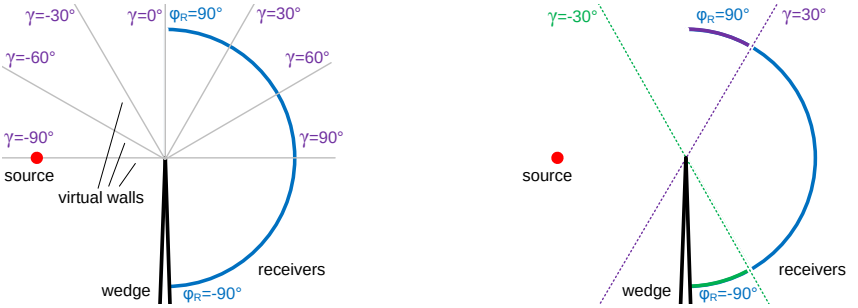

(a) investigated positions of a Virtual Wall

(b) neglected receiver positions due to geometrical restrictions

Figure 5.52.: Geometrical definitions for the rotation of a Virtual Wall

Due to the rotation of the VWs, some receivers may become invalid and cannot be computed with Eqn. 5.32. This effect differs for $\gamma < 0°$ and $\gamma > 0°$, such that both effects are discussed independently from each other.

Invalid receivers for $\gamma < 0°$ Deep in the shadow zone, receivers become invalid (see *green* receivers in Fig. 5.52b). The analytical equation of the transmission level cannot be computed, because the normalization of the diffracted energy is restricted to diffraction angles behind the VW of $|\varepsilon_2| < 90°$. Although that effect could be handled by changing to a different normalization (see Sec. 5.2.4), no energy would be transported by sound particles. For sound particles that intersect with the VW, the emitted secondary sound particles cannot reach the lower receivers, as the wedge still shadows the receivers. This problem, however, cannot occur if the space is properly subdivided into convex subspaces by means of VWs. Thus, an additional VW has to be inserted. The effect of these multiple VWs is discussed in Sec. 5.5.4.

Invalid receivers for $\gamma > 0°$ For the analytical formulation of Eqn. 5.32, receivers in the upper view zone become invalid. Some receivers rotate through the VW to the source-side of the VW (see *purple* receivers in Fig. 5.52b). This cannot be handled by the analytical equation, because no sound energy is diffracted back to the source-side of the wedge. However, this effect is only a problem of the analytical formulation. In an actual SPSM, the receivers on the source-side of the VW would detect the direct (undiffracted) sound field of the sound source yielding a transmission level of $L = 0dB$, respectively, as physically expected.

For the remaining receiver positions, the transmission level is shown in Fig. 5.53 for different rotation angles γ. The transmission level for $\gamma = 0°$ is the target function, as it was used in the former evaluations.

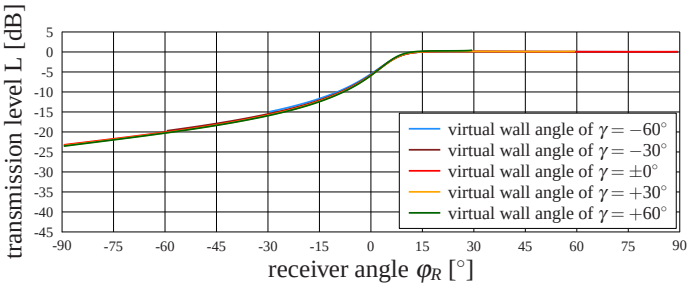

Figure 5.53.: Influence of the rotation of a Virtual Wall on diffraction using the Uncertainty relation Based Diffraction for a single wedge with $r_S = r_R = 10\lambda$.

Rotations of the VW of $\gamma = \pm 90°$ are not computable, because the sound source at $\varphi_S = 0°$ is in plane with the VW. For this geometrical setup, singularities occur in the computation of angles and distances (see Fig. 5.52b). In case of the SPSM, this could be directly explained by the absence of sound particles that could intersect with this VW. For the remaining rotation angles, good agreement ($\Delta L < 1dB$) is achieved. The experiment has also been extended to different source angles, where the same very small differences occurred and only the valid receiver positions varied (see above).

The very high robustness of the UBD is explained by the introduction of the cosine factor to the EDS (see Sec. 5.4.3.3), whereas discrepancies occurred without that modification[Ste10b]. When using this extension, the point of diffraction stays on the VW, but the decisive point is that the by-pass distance is computed as a *projected* by-pass distance that is independent of the VW position. Therefore, the position of the VW only slightly influences the transmission level.

This independence of the VW position results in a certain degree of freedom to position these VWs. An upper boundary for the rotation of the VW is not necessary.

5.5.3. Numerical Errors by the Combination of Diffraction with the Sound Particle Simulation Method

All former results have been achieved with the analytical equations for the transmission level, i.e., a fictive sound particle experiment with an infinite number of sound particles and infinitesimally small receivers. Originally, the UBD method had been derived (at least for the single wedge) for sound particle and later for beam tracing experiments[Ste04].

The analytical solution must match a sound particle experiment, before validations of the SPSM including the UBD are performed. In contrast to the analytical solution, a specified number of sound particles have to be emitted and the receivers have to be spatially extended (see Sec. 3.4). In order to fulfil this requirement, the number of receivers is reduced from 180 (in steps of 1°) to 15 receivers (in steps of 12°). To obtain an equal distribution, the centre points of the receivers are set to $\varphi_R = \{-84, -72, -60, -48, -36, -24, -12, 0, 12, 24, 36, 48, 60, 72, 84\}°$[Ste06]. The radius r_D of these receivers is defined as

$$r_D = r_R \cdot asin\left(\frac{12°}{2}\right), \tag{5.71}$$

such that receivers are tangent to each other (see Fig. 5.54).

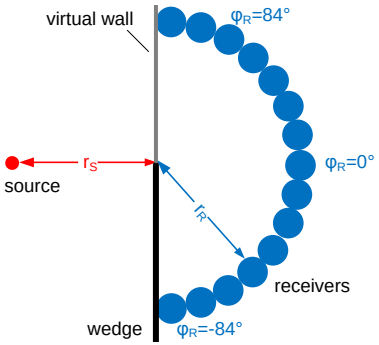

Figure 5.54.: Geometrical definitions of a sound particle diffraction experiment at a single wedge.

In this section, the numerical influences of these parameters on the UBD are discussed and a convergence of the sound particle diffraction to the analytical equation is shown.

5.5.3.1. Receiver Size

In a first investigation, a single diffraction experiment is performed for $r_S = r_R = 10\lambda$, which relates to a receiver radius (see Eqn. 5.71) of $r_D = 1.0491\lambda$. The results of the transmission level for each receiver are compared with the analytical formulation of Eqn. 5.32 and are shown in Fig. 5.55. A very large number of $N = 10000$ primary and $S = 1000$ secondary sound particles (see Sec. 5.5.3.2 and 5.5.3.3) is emitted to eliminate the numerical influence of these parameters.

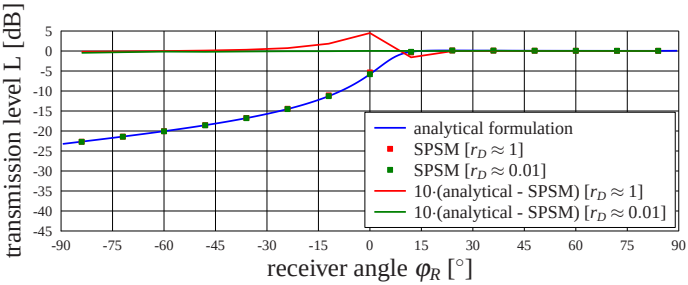

Figure 5.55.: Influence of the receiver radii r_D on diffraction at a single wedge, with $r_S = r_R = 10\lambda$.

As a first result, the transmission level computed with the SPSM (*red marker*) matches the analytical formulation (*blue*). Only a small deviation is noted ($\varphi_R = 0°$). In order to examine this effect, the difference of the analytical formulation and the SPSM is shown **multiplied by a factor of** 10 (*red*). Similar results were found earlier, but no explanation was given [Ste06]. However, the difference comes from averaging over the angle range of 12°, which has the greatest effect in regions of strongly varying transmission levels. In order to prove this assumption, the SPSM is repeated for receivers with a reduced radius by a factor of 100 (*green marker*). Then, the deviation in the transmission level (*green*) vanishes almost completely, such that, at least for very small receivers, an exact agreement between the analytical formulation and the SPSM is found. On the other hand, the differences for larger receiver sizes are still very good.

Classical ray tracing methods without weighting the detected energy with the inner crossing distance[Sch11] showed slightly greater deviations (for the UBD with the former DAPDF) compared to the SPSM proposed here, because the inner distance weighting reduced the averaging effect[SPS+12].

5.5.3.2. Number of Primary Sound Particles

The receiver size discussed above directly correlates with the necessary number of sound particles to be emitted from the sound source. Now, the influence of the number of primary sound particles N on the transmission level is investigated for a receiver radius of $r_D = 1.0491\lambda$ and a large number of secondary sound particles $S = 1000$ (for each incident sound particle). The results are presented in Fig. 5.56.

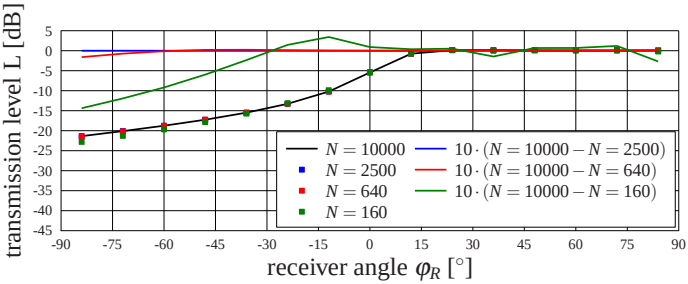

Figure 5.56.: Influence of the number of primary sound particles N on diffraction at a single wedge, with $r_S = r_R = 10\lambda$.

Besides the computed transmission levels (*markers*), the difference between the reference solution ($N = 10000$) and these simulations is shown multiplied by a factor of 10. A comparison of $N = 10000$ and $N = 2500$ shows absolutely no difference even in the difference plot, with the result that no improvement for even larger numbers is expected. Even for $N = 640$ primary sound particles, the difference is very small and only in the deepest shadow zone a difference of up to $0.1dB$ is noted. A further decrease to $N = 160$ sound particles results in an unacceptable numerical error of $1.5dB$. These occurring differences are explained as follows: the VW upon the edge is assumed to be a special kind of receiver. Using this assumption, it is clear that the accuracy of the transmission level increases with a larger number of sound particles that intersect with the VW. As a rule of thumb, Stephenson proposed a region $0 < a < 0.1\lambda$ above the wedge, where at least a few (≈ 12) sound particles have to intersect for a proper accuracy[Ste86]. To verify this empirical estimation, the number of sound particles N_0 that intersect with the VW in this region is estimated.

This number is proportional to the angle range the region is visible from the sound source

$$N_0 = N \cdot \frac{\alpha}{2\pi} = N \cdot \frac{atan\left(\frac{0.1\lambda \cdot cos(\varphi_S)}{r_S}\right)}{2\pi} \approx N \cdot \frac{1}{2\pi} \cdot \frac{0.1\lambda \cdot cos\left(\varphi_S\right)}{r_S}. \qquad (5.72)$$

For $r_S = 10\lambda$ and $N = 640$ primary sound particles, one sound particle intersects with the 0.1λ region ($N_0 \approx 1$). For less than $N = 640$ sound particles, less than one sound particle intersects with the 0.1λ region ($N_0 < 1$), such that the numerical error exceeds $1dB$. In order to verify the assumption for different frequencies, the simulation is repeated for distances of $r_S = r_R = 1\lambda$ and $r_S = r_R = 100\lambda$. The receiver radius is modified regarding Eqn. 5.71. For each combination, the absolute difference between the transmission level and the reference solution ($N = 10000$) is computed and the mean value over all receiver positions is determined. The results are given in Fig. 5.57

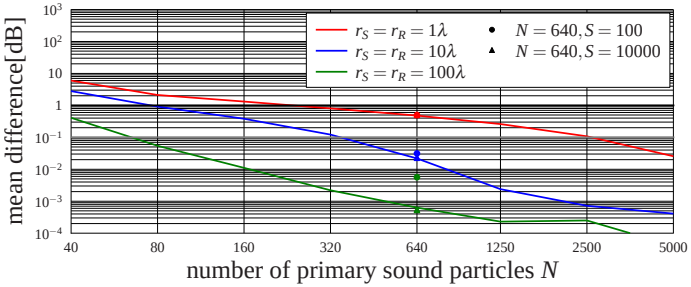

Figure 5.57.: Accuracy of the transmission level computed with the Uncertainty relation Based Diffraction for different numbers of sound particles N and distances $r_S = r_R$.

For $r_S = r_R = 10\lambda$, the *blue* curve represents the results that were already presented in Fig. 5.56. In addition, values for $S = 100$ (*circle*) and $S = 10000$ (*triangle*) are shown for $N = 640$.

The number of sound particles that intersect with the 0.1λ region is inverse proportional to the source distance r_S (see Eqn. 5.72). Assuming Stephenson's estimation to be correct, $N = 6400$ sound particles would be necessary for $r_S = r_R = 100\lambda$ and $N = 64$ sound particles for $r_S = r_R = 1\lambda$ to obtain the same accuracy. As shown in

Fig. 5.57, a mean difference of $0.02dB$ is found for $r_S = r_R = 10\lambda$ at $N = 640$. The same mean difference is found for $r_S = r_R = 100\lambda$ at $N \approx 5000$ and for $r_S = r_R = 1\lambda$ at $N \approx 100$. With respect to the rough estimation of Stephenson, the assumption that at least one sound particle has to intersect with the 0.1λ region, is confirmed. Unfortunately, for high frequencies and, thus, small wavelengths, a large number of sound particles are necessary.

5.5.3.3. Number of Secondary Sound Particles

A second parameter besides the number of primary sound particles is the number of secondary sound particles S that are emitted for every primary sound particle that intersects with the VW. For $r_S = r_R = 10\lambda$ and a very large number of primary sound particles $N = 10000$, the transmission level is computed for different S and shown in Fig. 5.58.

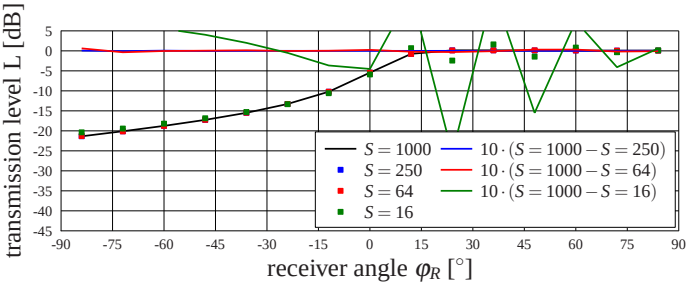

Figure 5.58.: Influence of the number of secondary sound particles S on diffraction at a single wedge, with $r_S = r_R = 10\lambda$.

In order to highlight the small differences, the differences are multiplied by a factor of 10. Both transmission levels for $S = 250$ and $S = 64$ match the reference solution ($S = 1000$) exactly ($< 0.01dB$), such that $S = 64$ is a sufficient number. For even less secondary sound particles $S = 16$, significant differences of up to $2.5dB$ are found.

This difference is explained by the restrictions of the SPSM itself. The intersection point emitting secondary sound particles can be interpreted as a secondary sound source. As the 15 receivers are tangent to each other in the whole angle range, the number of secondary sound particles that intersect with a receiver S_0 is approximately

$$S_0 \approx S \cdot \frac{1}{15}. \tag{5.73}$$

Hence, the number of sound particles that intersect with the receivers is nearly independent of the frequency. Thus, the accuracy is independent of the frequency, too. For verification, the same mean absolute difference as for the primary sound particles is shown in Fig. 5.59.

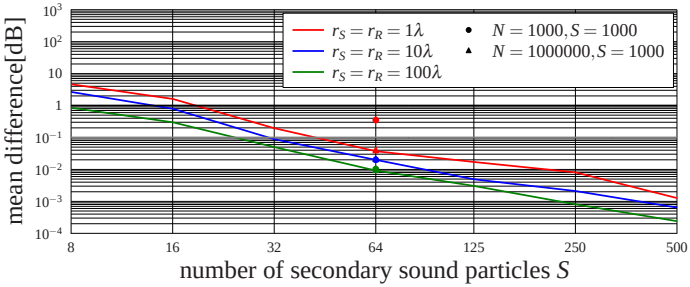

Figure 5.59.: Accuracy of the transmission level computed with the UBD for different numbers of sound particles S and distances $r_S = r_R$.

The result is explained by the Gauss law for detection[Ste14]

$$\Delta L = 10 \cdot log_{10}\left(1 + \frac{1}{\sqrt{D}}\right), \tag{5.74}$$

where D is the number of detected sound particles. In contrast to the former variations of the primary sound particles, the accuracy is nearly independent of the variation of the distances (frequencies). For an accuracy of $0.02dB$, for example, $S \approx 40$ secondary sound particles are needed for $r_S = r_R = 1\lambda$, $S \approx 64$ for $r_S = r_R = 10\lambda$ and $S \approx 110$ for $r_S = r_R = 100\lambda$. As a rule of thumb, $S = 64$ seems to be an accurate choice, as $S_0 \approx 4$ sound particles intersect with each receiver and a mean absolute difference of approximately $0.02dB$ is reached.

5.5.4. Combination of reflections of the Sound Particle Simulation Method with diffraction by the Uncertainty relation Based Diffraction Method

The combination of the UBD method with the SPSM allows a validation of the diffraction module for critical setups that could not be handled with the analytical formulation. Especially the influence of the faces forming the wedge is investigated. As a reference, the SSM is computed by the EDB.

In this section, the influence of specularly reflecting faces of the wedge is investigated by varying the opening angle of the wedge. A crucial point for the UBD (in contrast to the SSM) is the independence of the diffraction module on the wedge angle. This independence of diffraction and reflection module is wanted, as it is the advantage of the UBD. Due to the convex sub-division procedure, multiple VWs are possibly introduced, even on (almost) flat surfaces, e.g., a roof, such that this effect is discussed for both the wedge and flat surfaces. As in all these studies, again, only the general effect is of interest, the distances are restricted to $r_{S,R} = 10\lambda$. In addition, the influence of a both reflecting and a scattering surface underneath the diffracting wedge is investigated. As here also numerical values are of interest, this study is extended to other distances. In case of the UBD, the SPSM is performed with $N = 1000$ primary and $S = 200$ secondary sound particles for both scattering and diffraction, which showed up to be sufficient in the last section.

5.5.4.1. Influence of the Wedge Angle

As UBD is based on the Fraunhofer diffraction and, thus, on the Kirchhoff assumption (see Sec. 2.3.4.3), neither the shape nor the material properties of the flanking walls are taken into account.

The SSM, in contrast, takes (as a wave method) the boundary conditions into account, i.e., the effect of the wedge shape. Totally reflecting walls are assumed for the wedge's faces. The diffraction results depend on the wedge angle (see Sec. 2.3.4.2). Such an experiment has been performed by Stephenson, but only for a wedge angle of $\varphi_W = 90°$ without reflections[Ste11]. In order to quantify the effect of this wedge angle φ_W, the single wedge experiment is repeated for $r_S = r_R = 10\lambda$ and $\varphi_S = 0°$ (see Fig. 5.60)[SPS+12].

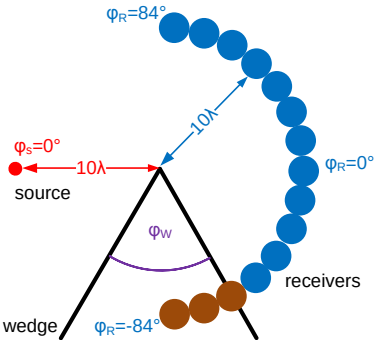

Figure 5.60.: Geometrical definitions for the investigation of the wedge angle φ_W on single diffraction.

The wedge angle is set to $\varphi_W = 1°$ in order to meet the assumptions by Kirchhoff (see Sec. 2.3.4.3). Furthermore, for these thin wedges, all receiver positions are computable. The results for different φ_W are displayed in Fig. 5.61. With increasing wedge angles, receivers in the deep shadow zone become invalid, because their position transits into the wedge (see Fig. 5.60, *brown* receivers). Hence, a computation of the transmission level is not reasonable for such cases. Due to this effect, the transmission level of the SSM is only computable for $\varphi_R < -90° + \frac{\varphi_W}{2}$. In addition to the results for different φ_W, a region of valid transmission levels is added in Fig. 5.61 that includes all possible angles φ_W and, thus, describes the available range of transmission level independent of the wedge angle.

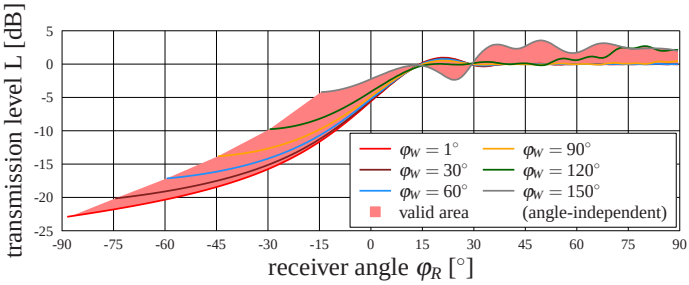

Figure 5.61.: Influence of the wedge angle φ_W on diffraction at a single wedge with the Secondary Source Model.

At $\varphi_R = 15°$ the transmission level is independent of φ_W. For even larger receiver

angles, the transmission level is approximately $0dB$ (except for the interference ripple) for all wedge angles below $\varphi_W \leq 90°$. Starting from that wedge angle, an image source becomes visible, which results in additional sound energy behind the wedge, too (see Fig. 5.62a).

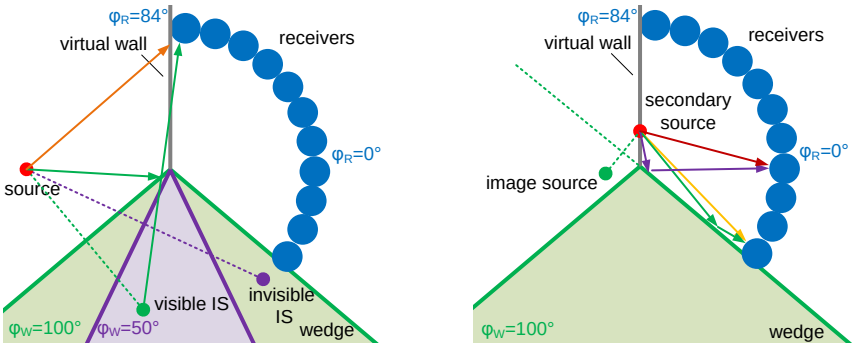

(a) An image source (or the respective reflection with sound particles) is either constructable (*green*) or not constructable (*purple*) depending on the wedge angle

(b) Different distances from either a secondary source or an image source to the receiver (direct path: *orange*, *dark red*, reflected path: *green*, *purple*)

Figure 5.62.: Visualization of different sound propagation paths from the sound source to the receivers around an edge.

The sound energy emitted by the sound source is reflected on the wedge's left face and diffracted afterwards. Adding up the diffracted sound energy of both the initial and the image source yields complicated interference effects in the view zone as shown in Fig. 5.61. Both sound sources have different distances to the receiver, such that both constructive and destructive interference effects cause significant variations of the transmission levels for different receiver positions. In total, a transmission level of up to $4dB$ occurs, but on average incoherent superposition occurs ($3dB$).

The same experiment has been performed with the SPSM and the UBD. As for the SSM, the faces of the wedge are modelled completely reflecting ($\alpha = 0.0$). The results are shown in Fig. 5.63.

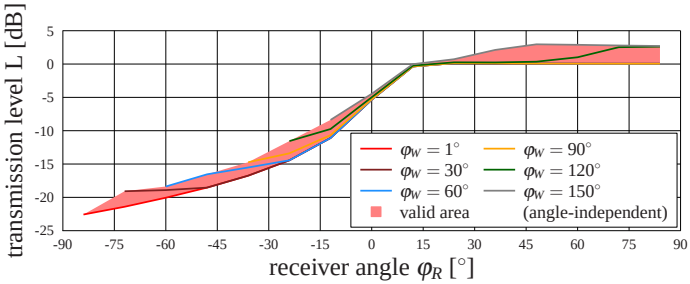

Figure 5.63.: Influence of the wedge angle φ_W on diffraction at a single wedge for the Uncertainty relation Based Diffraction.

The combination of the UBD with specular reflections yields different results than the SSM. In the shadow region, the transmission level is increasing with increasing wedge angles φ_W. In contrast to the SSM, where an increase of up to $6dB$ could be achieved, only up to $2.5dB$ are possible with the UBD. Sound particles that are diffracted into the deep shadow zone and reflected at the wedge's rear face are detected in receivers with greater angles φ_R. If these sound particles would have the same energy as the directly detected sound particles, the transmission level would be increased by $3dB$ (see Fig. 5.62b). However, sound particles in the deeper shadow zone have even less energy, such that a total increase is a bit below this upper limit. Without the consideration of phase, no greater transmission level (as for the SSM) is possible.

In the view zone $\varphi_R > 0°$, the transmission level is constantly $0dB$ for all wedge angles below $\varphi_W \leq 90°$. For larger wedge angles, the transmission level increases up to $3dB$, because sound particles that are reflected on the left face of the wedge are also reflected towards the VW. Together with the sound particles diffracted directly when emitted from the sound source, the transmission level increases up to $3dB$ at the most only for infinite, hard flanking walls. This increase is, similar to the increase in the shadow zone, slightly smaller than for the SSM.

In summary, the correctly increasing transmission level of the SSM, although not included in the UBD, is achieved by adding specular reflections on the faces of the wedge. This effect is about $2dB$ stronger for the SSM than for the UBD. Further improvement could only be achieved by applying modifications to the UBD taking the wedge angle into account and, thus, ignoring the Kirchhoff theory.

5.5.4.2. Influence of Virtual Walls Upon a Flat Surface

As the UBD is independent of the wedge angle, a crucial experiment for the UBD is the diffraction at a) a $\varphi_W = 179°$ wedge (including edge diffraction) and b) a $\varphi_W = 181°$ wedge (no edge diffraction). This effect is only problematic for the UBD, because for the SSM the diffraction impulse response vanishes for wedge angles $\varphi_S \to 180°$ automatically.

In the SPSM, the diffraction is only computed when a VW is constructed. To investigate this effect, multiple VWs are placed upon a flat surface. Physically, this makes no difference. This surface is modelled either completely absorbing ($\alpha = 1.0$) or completely reflecting ($\alpha = 0.0$). The recursive split-up of sound particles, and thus the CT, restricts the number of VW to a maximum of three as shown in Fig. 5.64. The sound source and the receivers are placed relatively to the left or the right VW, respectively.

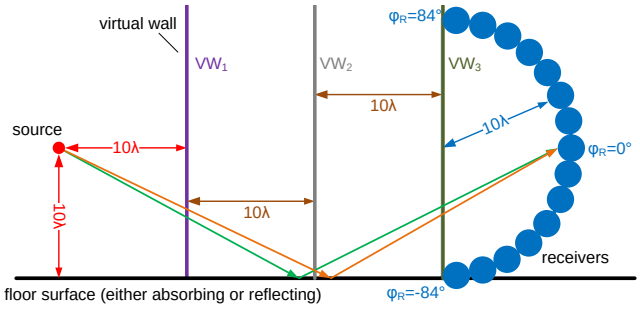

Figure 5.64.: Geometrical definitions of three Virtual Walls between the sound source and the receivers over a flat surface.

In a first attempt, the floor surface is completely absorbing and no VW is inserted. For this setup, the sound intensity at the receiver point exactly equals the free-field sound intensity, such that the transmission level is $L = 0dB$ for all receivers (see Fig. 5.65, *red*, below).

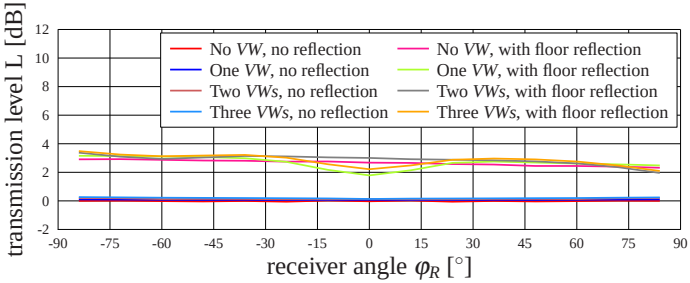

Figure 5.65.: Validation of sound propagation over a flat surface with multiple Virtual Walls.

The same experiment is repeated for one VW (VW_2), two VWs (VW_1 and VW_3) and all three VWs (VW_1, VW_2 and VW_3). In these experiments, diffraction is computed at every VW. Physically speaking, the propagating sound wave sees up to three openings one after another. In case of fully absorbing surfaces, the same results are computed whether the VWs are placed upon wedges or plane surfaces, as long as their position is identical. Although this is (up to) third order diffraction, the transmission level is quite similar ($\Delta L < 0.2dB$) to the transmission level without any VW.

This effect is explained by taking the results of the diffraction experiments into account that were performed with the analytical solution. In the view zone, the transmission level is, also for double diffraction, quite constant with $L \approx 0dB$. For receivers in the shadow zone (see Fig. 5.26, *region0* - *region2*), on the other hand, the diffraction varies very much for different setups. In the given setup (see Fig. 5.64), the edges are placed at the *foot* of the VWs, such that these regions would be underneath the floor. However, without reflections, this diffracted sound energy is totally absorbed.

Different behaviour is expected for a reflecting surface, bringing this diffracted energy back to the receivers instead of absorbing it. For a (specularly) reflecting floor without a VW, the *pink* curve is computed in Fig. 5.65. The transmission level is increased up to $3dB$ (not exactly $3dB$, because the distances of the sound source and the image source to the receivers are not identical). For receivers far above the surface, the difference in their distances increases, such that the transmission level slightly decreases for increasing receiver angles (down to $2.4dB$).

Very astonishingly, the transmission level with VWs yields only little greater transmission levels $L < 3.5dB$ in the complete angle range. Worth to be mentioned is that a small difference between the transmission level with VW and without VWs occurs for one and three VWs in the angle range $|\varphi_R| < 15°$, where the transmission level drops from $3dB$ to approximately $2dB$. As this effect is seemingly not occurring for two VWs, this effect is obviously caused by VW_2. Indeed, the specular reflection point is exactly at the *foot* position of VW_2 for the receivers around $\varphi_R \approx 0°$. In the SPSM, the sound particles responsible for the specularly reflected sound energy intersect with the floor surface in a short distance before (*green* sound particle in Fig. 5.64) or after (*orange* sound particle in Fig. 5.64) the VW. In both cases, the UBD computes diffraction for very close by-pass distances resulting in a very broad *smearing* of the sound energy

behind the VW. This smeared energy is missing at the receiver $\varphi_R \approx 0°$ and adds up partly to the remaining receivers. For the detected sound intensity and, thus, the transmission level L, a decrease at $\varphi_R \approx 0°$ and an increase for the remaining receivers is found.

The results achieved in this section can easily be extended to diffraction at a slit, where one wedge is a real wedge and the other wedge is only a flat surface (see Fig. 5.66). In this case, the diffraction at the non-physical edge is reduced by the same principles as described above.

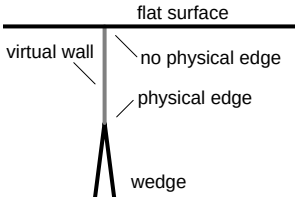

Figure 5.66.: Geometrical definitions of a Virtual Wall between a flat surface and a wedge.

In general, the experiments showed that flat surfaces are by far less problematic than expected, because receiver positions in the former shadow zone are (algorithmically) not possible and reflecting surfaces compensate the diffraction by part. Only specular reflection points exactly at the *foot* of a VW are problematic, but the transmission level only reduces about $1dB$ in a small receiver range.

5.5.4.3. Influence of Multiple Virtual Walls on a Wedge

A second possible artefact can occur from multiple VW upon a wedge due to the implemented convex sub-division. The influence of a rotation of one VW has been shown analytically. This experiment is extended for up to three VWs placed upon the same wedge as shown in Fig. 5.67.

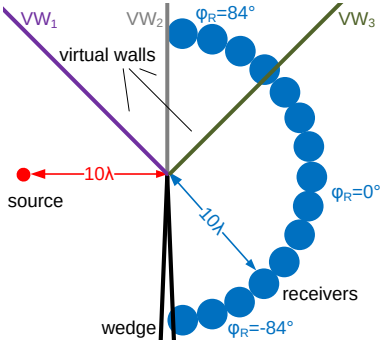

Figure 5.67.: Geometrical definitions of three Virtual Walls between source and receiver on a wedge.

The *red* curve (see Fig. 5.68) is seen as reference, because the results were confirmed earlier with both the analytical solution and the SPSM for this scenario. For the two VWs (VW_1 and VW_3), almost identical transmission levels are computed compared to the experiment with only one VW. Technically, second order diffraction is computed only for receivers with $\varphi_R < 45°$, because receivers with $\varphi_R > 45°$ are in-between the two VWs. However, the transition from single to double diffraction at $\varphi_R \approx 45°$ is very smooth. Differences of up to $1.5dB$ greater diffraction levels with two instead of one VWs occur only in the small angle range between $-30° < \varphi_R < -15°$. A reduction

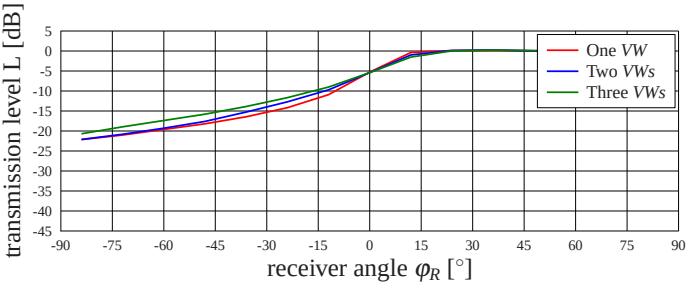

Figure 5.68.: Validation of diffraction through up to three Virtual Walls.

of the transmission level of about $1dB$ in the transition from the view into the shadow zone is found, too. Hence, a more homogeneous transition from the view to the shadow zone occurs for two VWs.

If all three VWs are used simultaneously, the effect increases even more. In the shadow zone ($\varphi_R < -15°$), the transmission level increases quite constantly up to $2.5dB$ in comparison to the setup with only one VW. Both effects are explained by the computed second or even triple diffraction, which could not result in the same transmission level as for single diffraction. However, the VWs start at the same wedge and their distance between each other is very small near the wedge. Here, most of the energy is diffracted. The positive results of the convergence from double to single diffraction for close wedges (see Fig. 5.5.2.2) and, thus, close VWs results in deviations of the transmission level up to $2.5dB$.

5.5.4.4. Ground Reflections Before and Beyond the Wedge

The final experiments in this chapter handle the influence of floor reflections in front and behind the wedge on the diffracted sound level. Therefore, the former single wedge experiment is extended by a reflecting front and rear floor (see Fig. 5.69).

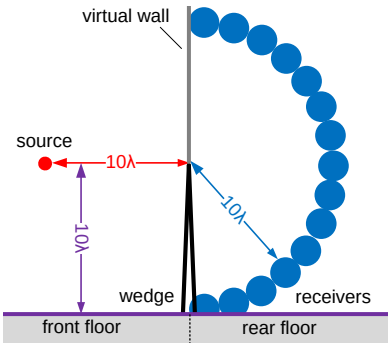

Figure 5.69.: Geometrical definitions of three Virtual Walls between source and receiver on a wedge.

Both the front and the rear floor are modified independently. The surfaces can be modelled either full absorbent ($\sigma = 0.0$, $\alpha = 1.0$), rigid ($\sigma = 0.0$, $\alpha = 0.0$) or scattering

($\sigma = 1.0$, $\alpha = 0.0$), whereas only rigid and absorbent cases are computed with the EDB. The parameters for the latter are identical to the analytical single wedge experiments. The sound source is fixed at $\varphi_S = 0°$ and the distances are restricted to $r_S = r_R = 10\lambda$ first, before they are extended to $r_S = r_R = 1\lambda$ and $r_S = r_R = 100\lambda$.

The differences between the UBD and the SSM are given in Tab. 5.2 for the different surface combinations divided into the regions known from Fig. 5.26.

			region $[dB]$				Min$[dB]$	at$[°]$	Max$[dB]$	at$[°]$
			0	1	2	3				
1λ	abso	Both	-2.0	-1.5	-1.3	-0.6	-2.1	-84	$+0.9$	$+24$
	rigid	Front	-2.3	-1.7	-1.2	-0.6	-2.4	-84	$+1.4$	$+84$
		Rear	-5.1	$+1.2$	-2.0	-0.6	-5.8	-84	$+4.8$	-48
		Both	-4.9	$+0.6$	-1.6	-0.5	-5.6	-84	$+2.7$	-48
10λ	abso	Both	± 0.0	$+0.3$	-0.3	± 0.0	-0.7	$+24$	$+0.3$	-60
	rigid	Front	± 0.0	$+0.4$	-0.2	$+0.2$	-0.7	$+24$	$+0.3$	-60
		Rear	-2.3	$+0.3$	-0.1	-0.2	-3.2	-84	$+0.6$	-36
		Both	-1.8	$+0.6$	$+0.1$	± 0.0	-2.8	-84	$+1.0$	$+72$
100λ	abso	Both	$+0.4$	$+1.3$	$+1.9$	$+0.7$	-0.1	$+48$	$+2.0$	± 00
	rigid	Front	$+0.7$	$+1.4$	$+1.9$	$+0.9$	± 0.0	$+48$	$+1.0$	± 00
		Rear	-0.5	$+1.3$	$+1.9$	$+0.6$	-1.4	-84	$+2.0$	± 00
		Both	$+0.1$	$+1.6$	$+2.0$	$+0.9$	-0.7	-84	$+2.0$	-24

Table 5.2.: Numerical comparison of transmission level L for a single wedge with reflecting floor. Besides the absorbent case, only the front floor, the rear floor or both surfaces are rigid.

Variation of the Reflectivity of Front Floor First, the front floor is modified and the rear floor is set be full absorbent. The transmission levels are shown in Fig. 5.70.

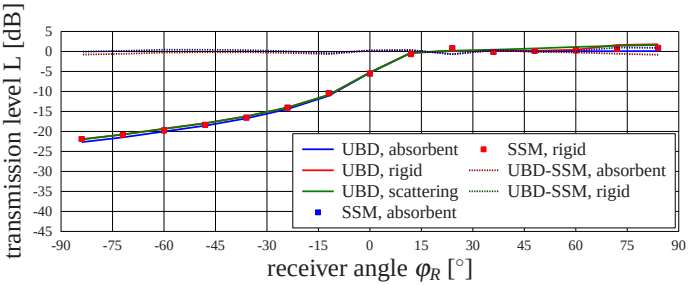

Figure 5.70.: Influence of a reflecting floor in front of wedge ($r = 10\lambda$). The rear floor is absorbent.

In case of the UBD, the reflecting floor increases the transmission level about $0.6dB$ in the shadow zone for both specularly and diffusely reflecting surfaces compared to the absorbing surfaces. This weak effect is explained by the additional sound particles that are reflected on the front floor and deliver strongly reduced energy. This reduction is caused by the greater diffraction angle of the sound particles and their increased travelled distance before they are detected by the receivers. The small difference between the specular and diffuse reflection is due to the fact that the main sound energy is diffracted close to the wedge's apex. While this region is only reachable by a few sound particles in case of a specular reflection, by far more sound particles are scattered into this direction but with reduced energy (see Fig. 5.71a).

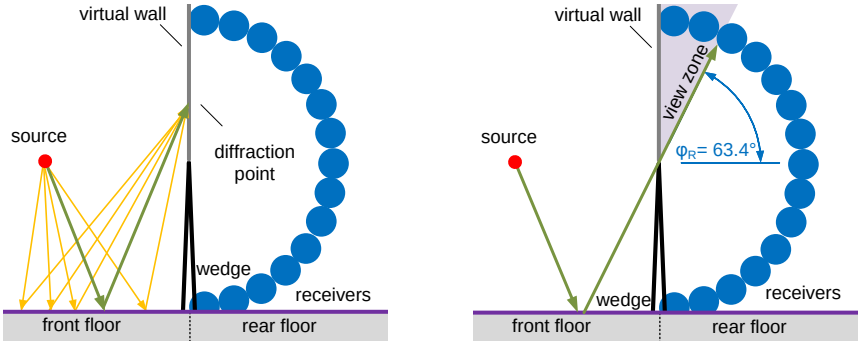

(a) sound particles reach a diffraction point either by specular (*green*) or diffuse (*orange*) reflections

(b) definition of the view zone

Figure 5.71.: Special case of reflections cause from a reflecting front floor.

Both effects seem to compensate each other. This result is perfectly confirmed by the SSM in case of the rigid surface, because the difference between both methods is almost unaffected by the insertion of a reflecting front floor ($\leq 0.1dB$, see Tab. 5.2).

In the view zone, however, reflected sound particles reach the receivers, when they are in a sufficient height above the wedge. For the given geometrical definitions, this occurs for receivers above an angle of $\varphi_R \approx 63.4°$ (see Fig. 5.71b). Upper receivers detect the reflected sound particles. Thus, the transmission level increases up to $2dB$ in case of the UBD and up to $1dB$ in case of the SSM. This difference is argued by the coherent addition assumed with SSM. The increase at $\varphi_R \approx 63.4°$ is smeared on a wider angle range in case of a scattering floor, because the reflection is smeared, too.

Variation of the Reflectivity of Rear Floor In the second experiment, the rear floor is varied and the front floor is full absorbent again (see Fig. 5.72).

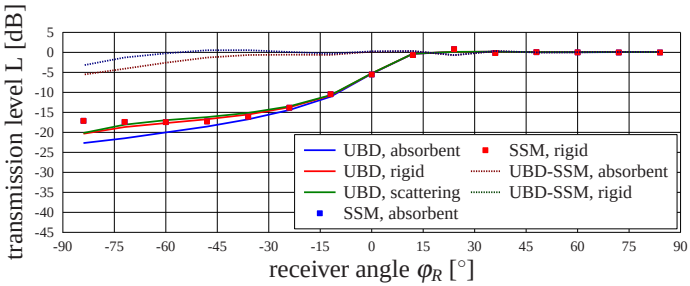

Figure 5.72.: Influence of a reflecting floor behind wedge with $r_S = r_R = 10\lambda$. The front floor is absorbent.

By a variation of the properties of the rear floor, stronger effects of the reflection on the transmission level are observed. In the whole shadow zone, the transmission level of the UBD is increased by a reflecting floor up to $3dB$. Here, the diffracted sound particles

have approximately the same diffraction angles as the sound particles that are reflected and diffracted. This effect is weakened for receivers that have a larger distance to the floor, because the diffraction angles of the reflected sound particles are greater than the diffraction angles of the directly detected sound particles. Thus, the transmission level increases more for receivers deeper in the shadow zone. This behaviour is again approved by the SSM, except for the receiver at $\varphi_R = -84°$. This receiver is doubtful, because the spatially extended receiver intersects with the reflecting surface and, thus, the detected energy is computed incorrectly.

Almost no difference of the transmission level in the view zone is noticed for neither SSM nor UBD.

Variation of the Reflectivity of Both Surfaces Finally, both surfaces in front and to the rear of the wedge are interchanged simultaneously (see Fig. 5.73).

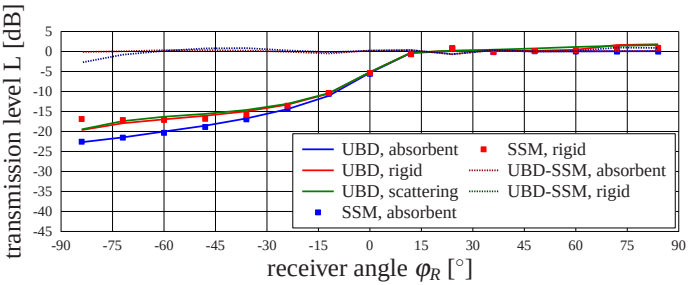

Figure 5.73.: Influence of a reflecting floor in front and behind a wedge with $r_S = r_R = 10\lambda$.

The effects of both previous investigations add up by introducing two reflecting surfaces.

Extension to Different Distances The results for $r_S = r_R = 10\lambda$ have been extended to distances of 1λ and 100λ. The numerical results are given in Tab. 5.2, too. The graphical comparisons are shown in appendix A.2.4.

For $r_S = r_R = 1\lambda$, the increased transmission level in the shadow zone is greater and more dependent on the receiver angles, as for these short distances the coherent addition yields complicated results for the SSM. Thus, the transmission level for receivers in the deep shadow zone is even greater than the transmission level for receivers in the medium shadow zone.

The results of the $r_S = r_R = 10\lambda$ experiments are confirmed by the results of $r_S = r_R = 100\lambda$.

5.6. Summary of the results of the Uncertainty relation Based Diffraction

The UBD method and module by Stephenson was presented and investigated in detail. Different detection techniques were discussed in Sec. 5.2.3. The result was that the convex sub-division was the only technique that reduced the CT and handled multiple edges at a time (see Tab. 5.3, valid (✓), not valid (✗) and by part valid (✗✓)). However, in contrast to diffraction cylinders, it detected the smallest by-pass distance only approximately.

	reduction of Computation Time	smallest by-pass distance	multiple edges at a time
tolerance region	✗	✗	✗
diffraction cylinders	✗	✓	✗
diffraction flags	✗	✗✓	✗
convex sub-division	✓	✗✓	✓

Table 5.3.: Comparison of different detection techniques.

Based on this detection technique, different normalization methods were discussed in Sec. 5.2.4. In contrast to the normalization symmetrical to the incidence direction that was proposed by Stephenson, it was shown that the normalization to the angle range behind the VW allowed diffraction into the deep shadow zone and kept the separation of sub-spaces (see Tab. 5.4). However, it still was compatible to the Kirchhoff assumptions.

	compatible to Kirchhoff assumption	diffraction in deep shadow	separation of sub-spaces
symmetrical to the incidence direction	✓	✗	✗
complete angle range	✗	✓	✗
angle range behind the Virtual Wall	✓	✓	✓

Table 5.4.: Comparison of different normalization techniques.

Based on these techniques, analytical equations for the transmission level at a single wedge and, for the first time, at a slit and the diffraction at two subsequent wedges were derived. Stephenson proposed three different EDSs (see Sec. 5.2.1), but it was shown that the UBD did not fulfil the reciprocity principle, where deviations of up to $20dB$ were observed (see Sec. 5.4). To overcome this, a new EDS was presented that fulfils the reciprocity principle for almost all combinations (see Tab. 5.5).

	mathematically derived	heuristically found	fulfils reciprocity principle
$S(a) = \frac{1}{6 \cdot a}$	✗✓	✗✓	✗
$S(a) = \frac{1}{6 \cdot a}$ for $a < 7\lambda$	✗	✓	✗
$S(a) = \frac{1}{3 \cdot a + e^{a}}$	✗	✓	✗
$S(a) = \frac{1}{6 \cdot a \cdot cos(\varepsilon_1)}$	✗✓	✗✓	✓

Table 5.5.: Comparison of different Edge Diffraction Strength.

Six of the eight investigated DAPDFs were already discarded in Sec. 5.2.2. The UBD was investigated (see Sec. 5.5.1.4) for three analytically scenarios with the remaining DAPDFs in a wide range of distances and angle parameters with the new EDS. The DAPDF $D_g(\varepsilon, b)$ yielded about $1dB$ greater transmission levels than the DAPDF $D_b(\varepsilon, b)$ in the shadow zones, which matched the wave theoretical SSM better (see Tab. 5.6).

	valid for $\varepsilon = \pm 90°$	valid for $\lvert\varepsilon\rvert > 90°$	simple to compute	matches SSM
$D_a\,(\varepsilon, b)$	✔	✔	✗	
$D_b\,(\varepsilon, b)$	✔	✔	✔	✗✔
$D_c\,(\varepsilon, b)$	✗	✗	✔	
$D_d\,(\varepsilon, b)$	✔	✗	✔	
$D_e\,(\varepsilon, b)$	✔	✗	✔	
$D_f\,(\varepsilon, b)$	✗	✗	✔	
$D_g\,(\varepsilon, b)$	✔	✔	✔	✔
$D_h\,(\varepsilon, b)$	✔	✗	✗✔	

Table 5.6.: Comparison of different Diffraction Angle Probability Density Function.

Sufficient agreements were found for almost all setups with diffraction at a single wedge or a slit, also the results of double diffraction showed acceptable results for many combinations. A variation of the source angle was investigated and showed very good results.

The investigation of the consistency of the UBD (see Sec. 5.5.2) revealed that the double diffraction converged at least approximately to the single diffraction for close wedges and that Babinet's principle was fulfilled within the potential of an energetic model. Even more, the influence of rotated VWs was proven to be very small, which is a good argument against the arbitrariness of the UBD (see Tab. 5.7).

	checked with analytical formula	checked with sound particle experiment
Babinet's principle	✗✔	
convergence of double to single diffraction ($d \to 0$)	✗✔	
influence of a rotated Virtual Wall	✔	
influence of the wedge angle		✗✔
influence of multiple Virtual Walls		✔
influence of reflecting surfaces		✔

Table 5.7.: Results of different numerical experiments.

After it was proven that the analytical equations matched the sound particle experiments (see Sec. 5.5.3), it was shown that the influence of the wedge angle is handled by reflections automatically. Finally, the UBD diffraction module turned out to be very robust with respect to the number of VWs, even for flat surfaces (see Sec. 5.5.4).

6. Sound Energy Reunification

The introduction of diffraction into Geometrical Acoustic (GA) simulation methods is performed (like scattering) by introducing secondary sound particles. The recursive split-up of sound particles causes an exponential increase of their number and, thus, the Computation Time (CT). For both the Sound Particle Simulation Method (SPSM) and Beam Tracing (BT), this can only be compensated by the reunification of the sound particles or beams, respectively. To achieve this reunification, a solution is aimed at that is based on the GA simulation methods handling specular reflections and adds only the reunification effect of the Acoustic Radiosity method.

Stephenson published Quantized Pyramidal Beam Tracing (QPBT)[Ste96, Ste04] as a combination of BT (and partially the Image Source method) with the Acoustic Radiosity and later Sound Particle Radiosity (SPR)[Ste01, Ste03b] as a combination of the SPSM with the Acoustic Radiosity.

Both methods are described by Stephenson in detail, but due to a lack of implementation, some important misassumptions have not been realized so far. To explain these misassumptions, both methods have to be described in detail and modified by part for a concrete implementation. Although the reunification method within SPR and QPBT is different, the algorithmic core of both methods is practically identical. Sound particles and beams are named as *sound energy carriers* in the following, although beams carry physically a sound power.

In this chapter, after a short summary of the related work, the idea of reunification is introduced and the SPR method as well as QPBT allowing the reunification of sound energy carriers are presented. This presentation order is preferred in contrast to the historical order, because SPR is geometrically simpler.

Both methods are discussed and implemented for the first time, such that both implementations are comparable. They are compared qualitatively to find the preferable reunification technique. The resulting method is analysed with respect to the efficiency and the numerical errors, and a discussion of further optimizations is presented.

6.1. Related Work

The idea to reunify sound energy is covered by the Acoustic Radiosity (see Sec. 3.6)[Mil84] in acoustics. This method is implemented, e.g., by Nosal et al. [NHA04]. Although, in principle, the Acoustic Radiosity method is only capable of completely diffuse reflections, Christensen presented the wavelet radiance method[CSDS94] for optics, which is capable of specular reflections. For acoustics, Siltanen et al. present the Acoustic Radiance Transfer method[SLKS07], which adds specular reflections to the diffuse reflections. Another approach by Dalenbäck used in CATT Acoustics[CAT] is to add diffuse reflections by a multi-pass procedure.

Furthermore, Lewers combines the Acoustic Radiosity with BT[Lew93] to add specular reflections in the first part of the impulse response. As this method handles both simulation methods one after each other (for first and late reflections), it is not considered here. Another approach to combine specular with diffuse reflections is presented by Korany[KBA01], but he has to neglect specular reflections after a certain order, too.

However, the Acoustic Radiance Transfer method as well as the method of Dalenbäck are briefly described.

6.1.1. Acoustic Radiance Transfer Method

Based on the room acoustic rendering equation[SLKS07], an Acoustic Radiance Transfer method[SLS09] is proposed that replaces Lambert's diffuse reflections by directional diffuse reflections[SLS10]. The main idea of this method is to divide the circumference of the scene into huge patches and the energy exchange factors between these patches are determined. These form factors make use of the bi-directional reflectance distribution functions (BRDF)[PSS+12]. As in the classical Acoustic Radiosity method, the energy is propagated in-between these patches without taking the receivers into account. In a second phase, the patches reemit the *radiance* for all receivers. Thus, this method is applicable efficiently for auralization purposes, because the *radiance* remains constant during a translation of the receivers. This method is capable of diffraction of first order[SL08] using the Biot-Tolstoy-Medwin theory.

As this method is based on the Acoustic Radiosity method, specular reflections are added to the energy exchange factors of diffuse reflections, on the contrary to an aspired equal weighting of specular and diffuse reflections.

6.1.2. Dalenbäck's Method

The method of Dalenbäck is divided into two phases, too[Dal95]. In the first phase, a cone tracing algorithm, as a variant of ray tracing is performed in the complete scene. At each wall interaction, the diffusely reflected energy of the cone is stored at the surface and not traced further, first. After a complete simulation over multiple (specular) reflections is performed, the stored energies for diffuse reflections are processed in the second phase. They are traced regarding Lambert's law and, again, stored in the intersected walls. This is repeated several times, but the accuracy is reduced with each pass.

This method already realizes important theories for the reunification of sound, but Stephenson assumes QPBT to be even more efficient and accurate[Ste04]. This assumption is investigated in this chapter by implementing the algorithm for the first time.

6.2. Reunification of Sound Energy Carriers

The CT of GA simulation methods without split-up of sound energy carriers is proportional to the number of computed reflections. For the application of the SPSM or BT to practical setups, both diffraction and scattering have to be added yielding an exponential growth of the number of sound energy carriers. This CT can be reduced by different acceleration techniques (see Chapter 4), but the exponential behaviour cannot be compensated. In this section, first this exponential growth is discussed by abstracting the sound propagation to the growth of a directed graph. Based on this abstraction, the two requirements to reunify sound energy carriers are analysed:

- discretization: the continuous description of a sound energy carrier's propagation path has to be discretized to allow reunification. In contrast to the first publications[Ste96, Ste01, Ste03b, Ste04], this effect called *discretization* instead of *quantization*. For simplification, the discretization of a sound energy carries is defined as the discretization of its sound propagation path.

- sequence: the processing order of sound energy carriers has to be adjusted for reunification (called *Logistics* by Stephenson).

Both requirements are presented one after another. In the following, the reunification of sound energy carriers and their energies is used synonymously.

6.2.1. Exponential Growth of Sound Energy Carriers

In order to investigate the effects of exponential growth and reunification, the SPSM is abstracted to a directed graph (tree)[Ste04]. With this abstraction, the geometrical structure of the room can be neglected. Without loss of generality, the investigation is restricted to a convex room, because complex rooms can be composed of these convex rooms (see Chapter 4). In order to create the tree structure, the surface of the room is projected to the $c-axis$ (see Fig. 6.1a), such that each intersection point on the surface is mapped to $0 < c < C$, where C is the circumference of the room.

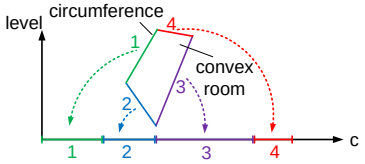

(a) projection of the surface of a convex room to the $c-axis$. A different colour is assigned to each wall (*green*, *blue*, *purple* and *red*)

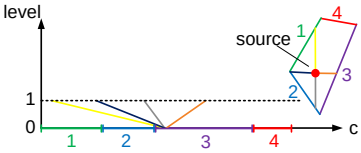

(b) 4 sound energy carriers (*yellow*, *dark blue*, *gray* and *orange*) emitted from a sound source. They start at level 0 (random $c-value$) and end at level 1 at the $c-value$ representing their intersection point on the surface.

Figure 6.1.: Illustration of sound propagation in a tree-like data structure. The lower $axis$ represents the surface position.

On the second $axis$, the level of reflections or diffractions is displayed. Starting from the sound source (level 0), the propagation to the next wall intersection is shown by a connection to the $c-value$ that represents the intersection point at level 1 (see Fig. 6.1b). The sound propagation of one reflection order is completed, when all sound energy carriers have reached the next level.

For the general discussion of the tree structure, two different terms are introduced which are very similar, but it is very important to distinguish between them:

- iteration: the transition of one sound energy carrier to the next level and
- order: the transition of all sound energy carriers to the next level.

Without split-up, the number of nodes and, thus, the number of sound energy carriers per level is constant as shown in Fig. 6.2a. For one additional sound energy carrier on each reflection ($S = 1$, i.e., a split-up into 2 sound energy carriers), the exponential growth becomes visible in Fig. 6.2b. The result is an explosion of CT.

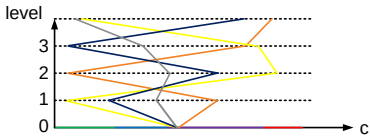

(a) four sound energy carries without split-up

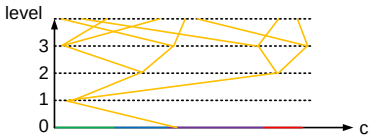

(b) one sound energy carrier with split-up into two sound energy carriers ($S = 1$, binary tree)

Figure 6.2.: Traces of the abstracted sound propagation up to $4th$ order between four walls.

Assuming N primary sound energy carriers and a split-up of S additional sound energy carriers, the number of sound energy carriers N_{SEC} existing solely for order o reads

$$N_{SEC}(o) = N \cdot (1+S)^o . \tag{6.1}$$

6.2.2. Sound Energy Carrier Logistics

In order to reunify sound energy carriers, the moment of reunification has to be specified first. In case of QPBT, Stephenson assumes a reunification in the image source space, whereas for SPR a reunification of sound particles is plausible when they intersect with the room surface, because this is the only time when sound energy particles change their direction or split up. Any other time of reunification would be less efficient, because the sound energy carriers that could have been reunified travelled on the same sound propagation path since their last wall intersection. For Stephenson, a continuous search for similar sound energy carriers would exceed the CT of the actual sound simulation by far[Ste04].

Algorithmically, sound energy carriers must *wait* at the position where they should be reunified, until all sound energy carriers have reached this position. If such a sound energy carrier is traced further before all other sound energy carriers reached that point, at least one reunification is skipped. This cannot be achieved with the recursive processing order of BT and SPSM.

This is shown by the abstraction of sound propagation paths to the growth of the tree of Fig. 6.2. By splitting up each sound energy carrier into two sound energy carriers at each intersection, an equivalent tree growth as shown in Fig. 6.3 occurs.

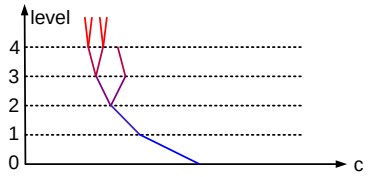

(a) recursive: the left most branch reaches the highest level before any branch to the right can grow

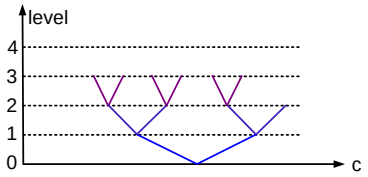

(b) parallel: all branches have to reach a certain level before any branch can start to grow to the next level

Figure 6.3.: Snapshot of a tree after 12 branches are grown, if each branch splits up into two branches.

For reunifications, a parallel growth as shown in Fig. 6.3b is aspired as described above. For the processing order of sound energy carriers, this means that all sound energy carriers have to reach a certain reflection order, before the first sound energy carrier is allowed to be propagated further.

This processing order is achieved by a completely new frame algorithm for the computation of sound propagation. The realization of this processing order is presented in Sec. 6.3.1.

6.2.3. Discretization of Sound Energy Carriers

For a reunification of sound energy carriers it is necessary that they propagate at least similarly. The data set of a sound energy carrier is defined when a sound energy carrier intersects with a wall by

a) Position: intersection point on the surface. In case of BT, this intersection point is extended to an intersecting region due to the spatial extension of a beam.

b) Direction: direction of incidence on the surface. This can be substituted by the emission point of the sound energy carrier.

c) Time: the time the sound energy carrier intersects with the position (see *a*))

in addition to the carried energy. Consequently, a discretization of a sound energy carrier is defined as a discretization of these three parameters. The actual energy remains continuous. Slight differences have to be tolerated in all three parameters by discretization.

If all these discretized parameters are identical for two sound energy carriers, their energies can be added up into only one sound energy carrier. This is defined as reunification of two sound energy carriers in the following.

6.3. Sound Particle Radiosity

To allow the reunification of sound particles, the SPSM has been extended by Stephenson to the SPR[Ste01, Ste03b] method (later investigations: [PS10a, PS11b]). After investigating the Acoustic Radiosity method, Stephenson came up with the core idea to reunify sound particles on discrete points on the surface.

A Reunification Matrix (RUM) had already been introduced by Stephenson[Ste96] (for both QPBT and SPR) to allow a *parallel* processing of the sound particles – the sound particle logistics. Thus, it is only shortly repeated. Then the discretization of sound particles as a specialization of sound energy carriers is presented and a complete algorithm of the SPR is derived for the first time.

6.3.1. Reunification Matrix

The RUM is proposed to temporarily store sound particles and extract them when needed. The RUM has to be understood as a multi-dimensional storage of energy, where the parameters of the sound particles (position, direction and impact time, see Sec. 6.2.3) are encoded in the position of the energy in the RUM first. The propagation information of a sound particle is defined by the three conditions that were described above. One dimension is reserved for each of the three geometrical identifiers of the sound particle (starting point, end point and intersection time on the surface). In total, a number of k^2 combinations is theoretically possibly, where k is the maximum number of discrete starting and end points. The index of the starting point and the index of the end point can be mapped to such a combined index and vice versa. Multiple intersection times are distinguished by discrete time values. In total, a RUM as shown in Fig. 6.4 is created.

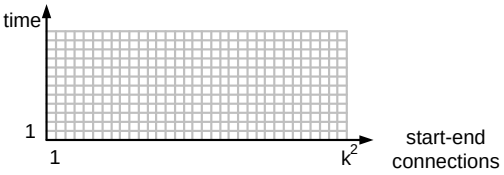

Figure 6.4.: Definition of an empty Reunification Matrix with start-end connections on the $x-axis$, and time on the $y-axis$.

Any non-zero entry in the RUM represents the energy of a sound particle that starts at a discrete position on the circumference on the wall in the direction of another intersection point ($k^2 - axis$) at a given time.

It should be noted that in case of the simulation of multiple frequency bands, each matrix element stores not only one energy but one energy for each frequency band.

6.3.2. Discretization of Sound Particles

In order to create the discretization of sound particles, the three parameters of a sound energy carrier (see Sec. 6.2.3) have to be discretized. This is shown for sound particles in Fig. 6.5.

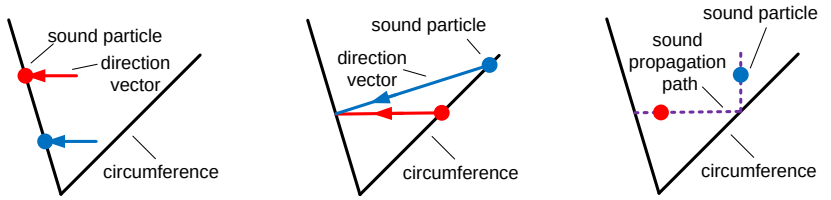

(a) position: intersection point

(b) direction: direction of incidence or emission point

(c) impact time

Figure 6.5.: Three parameters describe the sound propagation path of a sound particle. Two identical sound particles are shown only differing in the current parameter.

To discretize the first two parameters, the circumference of the room is divided into small patches, similar to the Acoustic Radiosity method. These patches are small wall elements, whose centre is used as unified intersection point. By these patches, intersections of the sound particle's starting point and end point with the circumference are mapped to a patch number. In addition, the time is discretized in time elements Δt, whose traveling distance $c \cdot \Delta t$ is defined proportional to the length of a patch.

In total, *two* discretizations have to be made to discretize *three* parameters:

1. intersection point: patches (patch number)
2. emission point (or direction): patches (patch number)
3. time: time intervals t_Q (time interval number)

A discretized sound particle is completely described by these three numbers, as the complete sound propagation path can be reconstructed from them.

6.3.2.1. Discretization of Intersection Points

The sub-division of the circumference into small elements is known, i.e., from the Acoustic Radiosity method (see Sec. 3.6). The average patch length l_P (to be fitted for each wall) is a simulation parameter and is defined by the user. An input parameter f_P describes the average ratio of the patch length l_P relative to the Mean Free Path Length (MFPL) $\bar{l}$[Kos60]. This value is preferred over an absolute value to make the number of patches independent of the size of the room. An alternative would be to define the patch length relative to the wavelength λ as recommended by the diffraction

theory. However, the wavelength has no influence on the geometrical propagation of sound particles for the used diffraction module, such that it is not used here.

As not every wall can be split up into patches of exactly the same length l_P, it has to be adjusted for each wall. Therefore, l_P is reduced until the patches match the length of the wall. The number of patches for the current wall k_W is computed by rounding up the ratio of the wall length l_W and the patch length l_P to the next whole number[a)]

$$k_W = \left\lceil \frac{l_W}{l_P} \right\rceil = \left\lceil \frac{l_W}{\bar{l} \cdot f_P} \right\rceil . \tag{6.2}$$

The k_W patches are equally distributed on the wall. The continuous intersection point of the sound particle with the circumference is mapped to a Patch Identification Number (patchID). The exact intersection point is lost, such that the centre of the patch is used as new end point of the sound particle (see Fig. 6.6a).

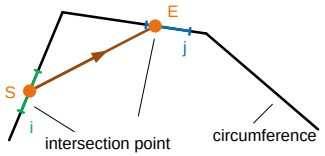

(a) sound particle: the end point E is computed by the intersection test with the circumference

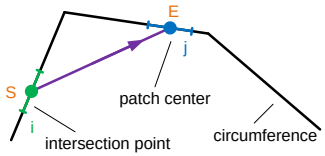

(b) discretized sound particle: the end point E is translated to the centre of the patch with number j. The direction vector (*purple*) is reconstructed from these numbers

Figure 6.6.: Comparison of sound particle and discretized sound particle.

In other words, the discretization of the intersection point is interpreted as an adjustment to the centre of the intersected patch. In order to reconstruct the actual sound particle's propagation path, both intersection and emission point are reconstructed by the centres of the patches as shown in Fig. 6.6b. This is needed to remain compatible with the former SPSM routines of Sec. 3.4.

6.3.2.2. Discretization of Time

In a next step, the impact time of a sound particle with the patch has to be discretized, too. To do so, the time is discretized in intervals of t_Q. The latest possible intersection time of a sound particle on the circumference is given by the total length of the echogram T_{Max} (see Sec. 2.4.2), since T_{Max} is an abort criterion for the SPSM. The length of the time intervals t_Q is not necessarily identical to the time intervals of the echogram.

In a first attempt, the time interval t_Q is defined as the time that a sound particle needs to travel the distance of a patch length $t_Q = l_P/c$, where c is the speed of sound. A Time Identification Number (timeID) is assigned to each interval. Thus, only one discretization parameter is used as the discretization of the sound particle's intersection time scales linearly with the patch length.

6.3.3. Main Algorithm

In the following, the main algorithm of the SPR is presented. The former concepts are already published by Stephenson, but the main algorithm here is different.

[a)] $\lceil x \rceil$ is the ceil function yielding the smallest next integer

As the actual sound propagation path is reconstructed from the three IDs, the exact same algorithm is used to trace the sound particle as in the SPSM (see Sec. 3.4).

The RUM is the core of the SPR algorithm. To include the RUM into the SPR, the algorithm is separated into two phases. In the first phase, the RUM is filled with the initial data and in a second phase the simulation is performed on the RUM.

In the initialization phase of the SPR, both main loops (see List. 3.4) of the SPSM are used to fill the RUM. For each sound particle, the first intersection point with the circumference is determined and the intersection point as well as the emission point are discretized to their unique patchIDs. It should be noted that a special patchID for the source position is used. With the timeID of the impact time on the wall, the energy is stored in the RUM at the position given by the three discretized IDs (see List. 6.1, compare List. 3.4). Actually, no acoustic computations are performed in this phase.

```
function soundParticleRadiosityInitialization()
for (all sources)
  for (all sound particles)
    findWallIntersection();  // use convex shape, see Sec. 3.4.2
    discretizeSoundParticle(); // compute unique IDs
    addSoundParticleToRum(); // store energy in RUM
```

Listing 6.1: Pseudocode for the initialization of the Sound Particle Radiosity.

In the second phase, the initially filled RUM is processed until no unprocessed element remains. Therefore, a sound particle is extracted from the RUM. The address of the element in the RUM is used to reconstruct the three discretized parameters (starting and end patchIDs as well as the timeID), although only the sound particle's energy is stored in the RUM. In case of a simulation of multiple frequency bands simultaneously, all energies from the specified element are extracted. From these IDs, the sound propagation path is reconstructed (with the centre of the patches).

Each of these extracted sound particles is processed for one iteration. The recursive call after the reflection and split-up (see List. 5.1) is replaced by the storage of the sound particle back in the RUM. Therefore, the three parameters of the sound particles have to be discretized again to find the position of the energy in the RUM (see List. 6.2).

Discretized sound particles that are placed back into the RUM are either placed on an empty or an already used element. In case of an occupied element, the energy of the sound particle is added to the already present energy and, hence, the sound particles represented by these energies are reunified. An additional advantage is that even sound particles of different sound sources (even with time delay) can be reunified with this procedure, because sound particles are only defined by geometrical definitions and their energy.

In addition to the abort criteria of the SPSM, the maximum propagation time is restricted to the maximum number of possible timeIDs and, thus, the size of the RUM. This restriction is implemented by ignoring the sound particles stored in the RUM for greater time values. To save memory, Stephenson proposed a cyclic usage of the RUM (see Sec. 6.6.1).

As described in Sec. 6.2.2, the optimal choice for the processing order is always *the oldest sound particle first* (lowest in the RUM). This processing order guarantees that the cleared matrix element is not reachable for any other incident sound particle yet to process. If multiple elements are set with the same time index, an arbitrary element of them is chosen. This is not problematic for the reunification, as long as it is assured that a sound particle travels at least the distance of one time element to avoid singularities. The algorithm is summarized in List. 6.2 and acoustical identical to List. 5.1.

```
function soundParticleRadiosity()
while(numberOfElementsInRUM>0)
  getAnyOldestSoundParticleFromRum();
  traceDiscretizedSoundParticle(); // iteration in the SPSM

function traceDiscretizedSoundParticle()
deDiscretizeSoundParticle(); // reconstruct propagation path
findWallIntersection();  // use convex shape, see Sec. 3.4.2
detectSoundParticle(); // either single or grid, see Sec. 3.4.4
energy = energy  * exp(-m * r); // see Eqn. 3.11, only air
if(isVirtual(intersectedWall))
  for (all secondary sound particles) // split-up in S
    float newEnergy = energy * diffractionRatio(); // see Eqn. 5.19
    v = computeDiffractedDirection(); // see Eqn. 5.18
    if(newEnergy > energyThreshold) // see Eqn. 3.26
      discretizeSoundParticle(); // compute unique IDs
      addSoundParticleToRum(); // former recursive call
else
  energy = energy * (1 - alpha) // see Eqn. 3.11, only alpha
  for (all secondary sound particles) // split-up in S + 1
    if(i==0) // specular reflection
      float newEnergy = energy * (1 - sigma); // see Eqn. 3.13
      v = v - 2 (v * n) * n // see Eqn. 3.12
    else
      float newEnergy = energy * scatteringRatio(); // see Eqn. 3.16
      v = computeScatteredDirection(); // see Eqn. 3.15
    if(newEnergy > energyThreshold) // see Eqn. 3.26
      discretizeSoundParticle(); // compute unique IDs
      addSoundParticleToRum(); // former recursive call
```

Listing 6.2: Pseudocode for the Sound Particle Radiosity.

6.3.4. Example

In order to understand the SPR, the algorithm is described for an example in Fig. 6.7.

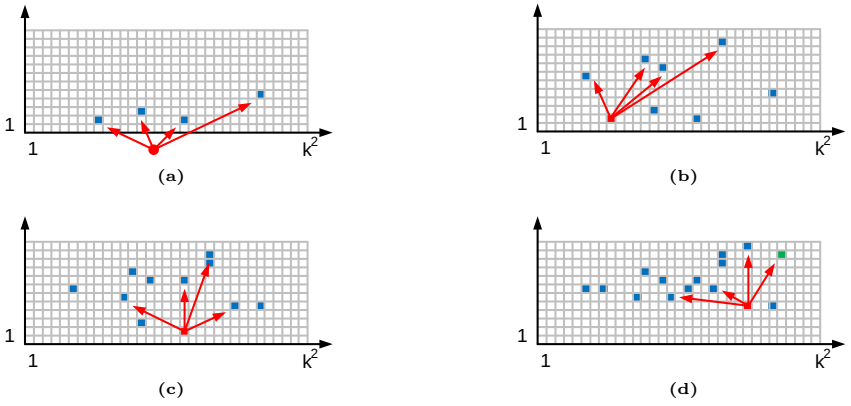

Figure 6.7.: Example of processing the Reunification Matrix. Occupied matrix elements are shown in *blue* and reunified matrix elements in *green*.

In the initial step, the sound particles are emitted from the sound source and sound particle energies are stored in the RUM (see Fig. 6.7a). In the actual simulation, the *oldest* sound particle is removed from the RUM and traced through the scene by means of the SPSM. During this simulation, four new sound particles are created and, thus, their energy is assigned to four new entries in the RUM (see Fig. 6.7b, 6.7c). Due to the increased density of occupied matrix elements, energies are added to already used elements in the RUM (see Fig.6.7d) - this is the desired reunification effect.

6.4. Quantized Pyramidal Beam Tracing

The combination of the SPSM with the Acoustic Radiosity method to the SPR allows the reunification of sound particles and, thus, a compensation of the exponential growth of the CT. However, Stephenson proposed QPBT combining BT with the Acoustic Radiosity method, because BT seems to be a more accurate and efficient simulation technique[Ste96, Ste04]. Stephenson's motivation for QPBT has been the combination of BT with both diffuse reflections and diffractions.

Unfortunately, many of the assumptions yielding these conclusion are questionable, such that a detailed comparison of SPR and QPBT is aimed at. Therefore, first Stephenson's concept of QPBT has to be specified to an exact algorithm. QPBT uses a similar algorithmic reunification technique as the SPR, such that the RUM is inherited directly from the SPR. First, the more complex discretization of beams in contrast to sound particles is presented. In the following, the complete algorithm is described based on the SPR algorithm (by part based on Stephenson's descriptions). The actual sound propagation algorithm is very similar to the unquantized BT (see Sec. 3.5).

6.4.1. Discretization of Beams

The discretization of beams is more complicated than the discretization of sound particles due to the more complicated geometrical structure of the sound energy carrier. The three parameters of a sound energy carrier (see Sec. 6.2.3) are depicted in Fig. 6.8 for a beam.

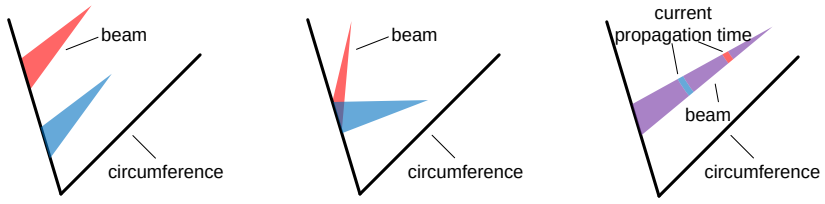

(a) position: intersection area

(b) direction: emission point (image source position)

(c) impact time

Figure 6.8.: Three parameters describe the sound propagation path of a beam. Two identical beams are shown only differing in the current parameter.

In contrast to the point-shaped intersection point of a sound particle, a beam intersects with a whole area. This area is actually a *length* in $2D$ and is discretized by patches. This definition is different from the definition of Stephenson, who discretizes solid angles instead of intersected areas. The starting point, however, has to be handled by a different type of discretization, because the emission point of a beam is not

restricted to the circumference of the scene (different solutions are discussed in Sec. 6.4.1.2). The time when a beam intersects with a patch has to be discretized, too. In total, *three* instead of *two* types of discretizations (as with the SPR) have to be performed in case of QPBT:

1. intersection area: patches (patch number)

2. emission point: position of image source (still to define)

3. time: time intervals t_Q (time interval number)

The beam has to be completely described by these three discretized parameters, as they must be sufficient to reconstruct the sound propagation path.

6.4.1.1. Discretization of Intersection Area (Including Power Interpolation)

In contrast to the SPR, where the sound particles intersection point is discretized to the centre of the patch that it intersects with, the beam has a spatial extension when it intersects with the circumference (see Fig. 6.9a). Due to the discretization of a beam's intersection area to a patch, a patch can only be intersected completely or not intersected at all. In this work, all (even partly) intersected patches are defined as intersected completely. This extension does only affect the outer most patches that are intersected by the incident beam (see Fig. 6.9b).

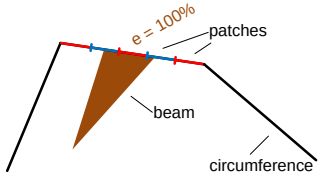

(a) beam: the beam intersects with the circumference over an area hitting different patches

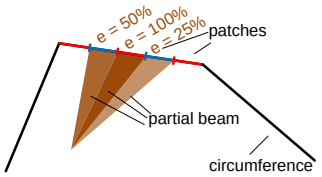

(b) discretized beam: the beam is split up into one beam for each intersected patch. Due to the restriction to patchIDs, every patch is per definition covered completely.

Figure 6.9.: Comparison of beam and discretized beam.

The most important criterion of GA is the energy conservation. As beams represent a sound power, this sound power has to remain constant. By extending the cross-section of the beam, the solid opening angle of the beam is extended, too. In case of a constant sound power density per angle within the beam, the sound power represented by the beam would be increased. If a patch is intersected on a length l by a beam, this intersection area is extended to the patch length l_P and, thus, increased by a factor of l_P/l. This extension is compensated by reducing the sound power density of the beam proportionally to the increased intersection area $p' = p \cdot l/l_P$. Beams that almost completely intersect with patches ($l \approx l_P$) are almost unaffected, whereas beams that intersect with patches on a small length $l \ll l_P$ are extend widely. The sound power density of the latter is reduced drastically (see Fig. 6.9b). Hence, the energy conservation criterion is fulfilled. This modification of the beam is summarized in List. 6.3.

```
function reshapeBeam()
// reduce power density
float l = computeIntersectedLength();
float newPowerDensity = powerDensity * l / patchLength
// extend beam direction vectors to patch limits
Vec firstBeamIntersection = patchStartingPoint;
Vec secondBeamIntersection = patchEndPoint;
```

Listing 6.3: Pseudocode for reshaping a beam to a patch.

6.4.1.2. Discretization of the Emission Points

The discretization of the starting point of a beam differs from the discretization of a sound particle's emission point significantly. While the position of a sound particle's starting point is restricted to the circumference of the scene, the starting point of a beam can be freely placed in the whole scene. The position of the starting point of a beam equals the position of the image source (see Sec. 3.3) and is used in this section synonymously during the mirroring to higher orders. The image sources translate away from the initial source (*image source space*, see Fig. 3.4).

This illustration of the image source indicates that the radius of the image source shell equals c times the arrival time at the original source. For both scattering and diffraction, secondary sources have to be constructed at the position of the scattering/diffraction event. Thus, the beam's propagation time (times c) is larger than the distance of the image source (of the secondary sources) to the initial source.

Stephenson [Ste04] proposes a discretization of the concentric *image source space* with the initial source as origin. However, the distance between the image source and the **initial source** does not represent the propagation time of a beam, because the propagation time of a beam is defined by the distance between the image source and the **receiver**. Furthermore, this discretization prohibits the reunification of beams of different sound sources, because each sound source (including secondary sources) requires an own coordinate system. Both facts prevent an efficient usage of this discretization.

In order to get a discretization that represents a beam's propagation time, Stephenson proposed a spherical coordinate system centred to the receiver[Ste04] (see Fig. 6.10).

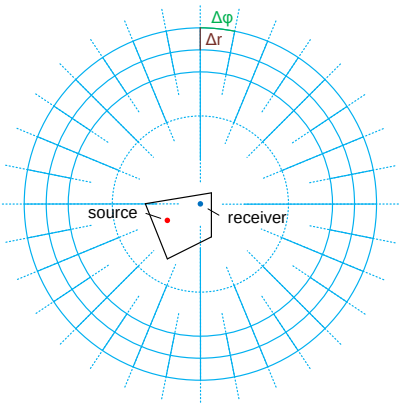

Figure 6.10.: Discretization of the image source space by spherical coordinates that are concentric with the sound receiver (after Stephenson[Ste04]).

Using this definition, the average radius r of a shell equals the distance (rounded by Δr) between the image source and the receiver (which is proportional to the propagation time of a beam). Beams in the innermost shell represent the beams with the smallest propagation time to the receiver and are to be computed first. As an advantage, beams originating from other original sources can be reunified as this coordinate system is independent of the image source position. On the other hand, the discretization is dependent on the receiver position, such that only one receiver can be used. In case of many receivers (e.g., if noise maps have to be computed), the procedure has to be repeated for each receiver position.

To retrieve a coordinate system independent of the source position as well as the receiver position, the plausible selection is a Cartesian coordinate system, because no centre is needed (see Fig. 6.11).

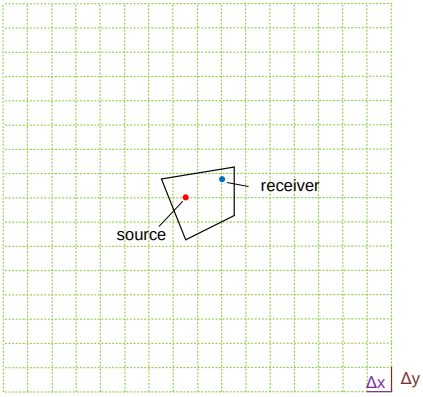

Figure 6.11.: Discretization of the image source space by Cartesian coordinates.

The Cartesian coordinate system is a compromise solution, as neither the source position nor the receiver position influence the coordinate system. Thus, a reunification of beams is possible that were emitted by different sound sources and are detected by different receivers. Although it is a huge advance of the coordinate system, the grid dimensions Δx and Δy cannot be adjusted to different distances. The result are equally sized grid elements, whereas the size of these elements grew for larger distances with the former spherical coordinates. Even more, it was possible to construct distance dependent intervals $\Delta r = f(r)$ with the polar coordinate systems, which is not possible in Cartesian coordinates. The equally sized grid elements are either too large in the near field (where the position of the image source is important) or too small in the far field (resulting in extreme memory usage).

All the former coordinate systems assume that the distance and, thus, the time between the image source and the receiver is the relevant value for reunification. However, Stephenson found[Ste04] (in contrast to [Ste03a]) that the intersection time of the beam at the circumference of the wall (patch) is rather relevant than at the receiver.

Obviously, none of the presented coordinate systems is an optimum choice, as at least one elementary requirement is not fulfilled. Based on these requirements, a new coordinate system is found. This coordinate system is defined in spherical coordinates and concentric with the patch that is aimed at by the beam (see Fig. 6.12).

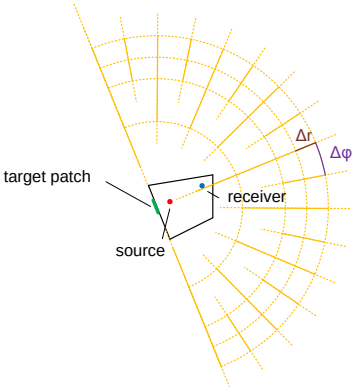

Figure 6.12.: Discretization of the image source space by spherical coordinates that are concentric with the target patch.

This coordinate system is independent of the source position and allows the reunification of beams that belong to different sound sources. As the coordinate system is also independent of the receiver position, the distance between the image source and the patch is proportional to the propagation time of a beam to a patch. Thus, the *age* of a beam (since the last secondary source) is proportional to the radius of the coordinate system. Finally, this coordinate system reduces the memory requirement by half in comparison to the former spherical coordinates, because a beam can only intersect with a patch *from inside*. In a first attempt, these coordinate systems seem to be very inefficient, because a different coordinate system for each patch has to be constructed and the number of these patches exceeds the number of sound sources or receivers by far. Together with the discretization of the intersection area, however, beams are already distinguished by the patches they aim at. Thus, no additional differentiation is introduced by using this coordinate system. In summary, the spherical coordinate system that is concentric with the target patch allows an efficient reunification of beams.

First, the distance of the beam's starting point to the centre of the patch is (in a first attempt) divided into equally sized elements. The size of the elements is defined as the patch length $\Delta r = l_P$ and a Distance Identification Number (distanceID) is assigned. Second, the angle of incidence of the beam (relative to the surface normal of the patch) is also split into equally sized elements. The number of these elements is as a first proposal set equal to the patch length per MFPL $f_P = \Delta\varphi/\pi$. The size of both elements is first based on the idea to end up with only one discretization parameter f_P.

Finally, *four* parameters need to be discretized for a beam in total:

1. intersection area: patches (patch number)
2. emission point:
   a) distance (distance number)
   b) angle (angle number)
3. time: time intervals t_Q (time interval number)

The propagation time of the beam without any secondary source, i.e., without diffraction or scattering, is proportional to the distance between the image source position and the patch (see Fig. 6.13a).

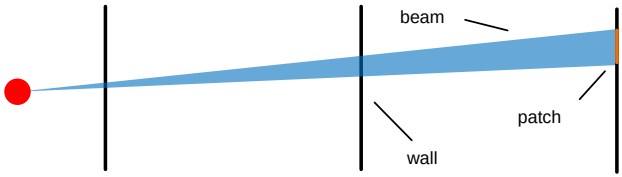

(a) without secondary sources

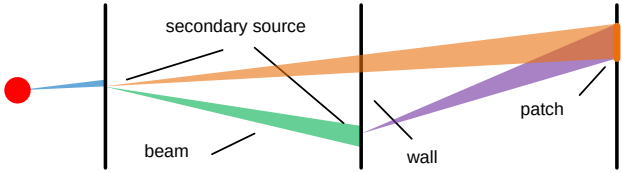

(b) with secondary sources

Figure 6.13.: Comparison of propagation time and image source distance of one beam between three walls.

Whenever such a secondary source is constructed, both values are not connected to each other anymore (see Fig. 6.13b). The arrival time of the *purple* and the *orange* beam is almost identical, whereas the distance of the secondary source to the intersected wall is significantly smaller for the *purple* beam. In case of SPR, the number of secondary sources (split-ups) between the sound source and the patch has no influence on the geometrical shape of a sound particle, whereas the beam shape (opening angle) is strongly influenced. In other words, the geometrical starting point can only be the one that intersected with the *last* wall for the SPR.

6.4.1.3. Discretization of Time

The discretization of the time when a beam impacts a patch is performed in the same way as the discretization of a sound particle's impact time. The relevant time is the time when the beam intersects with the patch centre. Time elements with the size of $t_Q = l_P/c$ are used.

6.4.2. Main Algorithm

The algorithm of BT has to be modified in the same way as the SPSM to achieve a reunification by QPBT. The recursive calls of BT (see Sec. 3.5.6) have to be replaced by iterative processing based on the RUM.

This RUM-based process is mainly identical to that of sound particles, as only energies are stored for given IDs. However, as described in the previous section, four instead of three discretization parameters are necessary to describe a discretized beam completely. Therefore, the RUM for QPBT is a four dimensional matrix in comparison to a three dimensional matrix in case of the SPR. By using this extended RUM, the same two phases have to be performed for QPBT as for the SPR. In the first initialization phase, the initial beams are stored in the RUM before, in the second phase, this RUM is processed.

In the first phase, the two outer loops of BT that handle all sound sources and all walls of the current room (see List. 3.5) are used in QPBT. The two edge vectors of those beams (in $3D$: pyramidal) are created and describe the spatial extension of the

beams, but, in contrast to unquantized BT, these beams directly aim at all patches (as described in Sec. 6.4.1.1). These partial beams are discretized in all four dimensions by determining their regarding IDs for each dimension. Finally, the sound power of all those discretized beams is stored in the RUM at the position specified by those IDs (see List. 6.4). As in the SPR, no acoustic computation is performed in the first phase.

```
function QuantizedPyramidalBeamTracingInitialization()
for (all sources)
  for (all walls)
    createBeamDirectionVectors(); // see Eqn. 3.27
    for (all patches)
      createPartialBeam(); // edge vectors to patch
      discretizeBeam(); // compute unique IDs
      addBeamToRum(); // store power in RUM
```

Listing 6.4: Pseudocode for the initialization of Quantized Pyramidal Beam Tracing.

The second phase of QPBT processes the RUM exactly like in the SPR. The beam with the smallest time travelled yet is taken out of the RUM. This beam is traced by a modified version of the BT iteration procedure. This processing is ended whenever no element remains in the RUM (see List. 6.5, compare List. 3.5).

During the iteration of a discretized beam, the beam's propagation path is reconstructed by the four IDs. Similar to the SPR, the actual propagation routines are only slightly modified compared to their undiscretized version (see Sec. 3.5). One difference is that the beams have to be de-discretized (reconstructing the actual sound propagation path) before they are propagated through the geometrical scene. In addition, the beam has to be split up again according to all patches of the intersected wall as in phase one after the beam is propagated to the next wall (including a possible split-up due to multiple intersected walls (see Sec. 3.5.2)). After this second split-up, the beams are discretized and their power (for multiple frequency bands: powers) are stored in the RUM at the position given by these IDs (see List. 6.5).

```
function QuatizedPyramidalBeamTracing()
while(numberOfElementsInRUM>0)
  getAnyOldestBeamFromRum();
  traceDiscretizedBeam(); // iteration in the BT

function traceDiscretizedBeam()
deDiscretizeBeam(); // reconstruct propagation path
detectBeam(); // either single or grid, see Sec. 3.5.4
float newPower = power * (1 - alpha) * exp(-m * r); // Eqn. 3.11
v1 = v1 - 2 (v1 * n) * n // see Eqn. 3.12
v2 = v2 - 2 (v2 * n) * n // see Eqn. 3.12
switch(v1,v2) // ensure counter-clockwise

findWallIntersections(); // use convex shape 2x, see Sec. 3.4.2
for (all intersected walls)
  createPartialBeamDirectionVectors();  // see Eqn. 3.28
  for (all intersected patches)
    createPartialBeam(); // edge vectors to patch
    reshapeBeam(); // see List. 6.3
    discretizeBeam(); // compute unique IDs
    if(newPower > powerThreshold AND aMin > aDelta) //Eqn.3.26,3.30
      addBeamToRum(); // store power in RUM
```

Listing 6.5: Pseudocode for Quantized Pyramidal Beam Tracing.

6.5. Determination of the Preferred Simulation Technique

So far two different $2D$-GA simulation methods allowing reunification have been presented. A common feature of both techniques is the compensation of a split-up of the sound energy carriers by diffraction or scattering. Stephenson proposed in his work[Ste04] that BT is much more efficient than the SPSM and should, therefore, be the preferred simulation technique to be extended by reunification. As a second aspect, he states that reunification is more intuitive by beams instead of sound particles as the spatial overlap is utilized. The latter has been disproved already as an implementation of the SPR (where sound particles are reunified) has been presented. In order to find the most efficient algorithm, the author investigated[PS10c] first the SPSM and BT in detail. In this investigation, a statistical estimation of the CT for both the SPSM and BT was found as a function of the number of initially emitted sound energy carriers and a given maximum reflection order. As BT is exact within GA, a maximum error of the SPSM was defined. Thus, the number of sound particles to emit was given by the wanted accuracy. The former assumption that BT is always more efficient than the SPSM because many sound particles have to travel in a beam for the same accuracy, was disproved[PS10c]. Three different requirements of accuracy were distinguished:

1. Accuracy of the overall sound intensity: if the temporal resolution of the sound intensity is not of interest (as for the creation of level maps), the SPSM is more efficient for a reflection order greater than 10. Then, the relative error is below $0.5dB$.

2. Accuracy in a certain time interval: if the temporal resolution of the sound intensity is important (as for the determination of room acoustical parameters), it strongly depends on the number of reflections whether to prefer BT or the SPSM. In case of a relative error of $1dB$ in an interval of $25ms$, the SPSM is more efficient for reflection orders above typically 10.

3. Accuracy of intensity of a selected sound energy propagation path or image source: in this case, BT is always the method of choice, although it is doubtful whether this requirement occurs in practical cases.

Now, in case of the discretized simulation methods SPR and QPBT, the accuracy and the computational effort of the discretized simulation methods SPR and QPBT are compared and a decision is carried out which method to use[PS11c].

6.5.1. Accuracy

The main advantage of BT is the exact result of the received sound energy. The spatially extended beams allow an exact detection of all image sources and the point-shaped receivers detect the correct energy (see Sec. 3.5.4). However, due to discretization, the beam is modified, a divergence of its shape occurs and wrong image sources might be detected. In the following, both inaccuracies are checked, one after another.

6.5.1.1. Divergence of Energy

Due to the principle of QPBT, the discretized beams can intersect with patches only completely by definition (see Sec. 6.4.1.1). To analyse the effect of this interpolation, the propagation of a single beam is investigated. A beam is reflected in the actual simulation at each intersected wall and passed on to the next one (see Fig. 6.14a). For the sake of simplification, the reflection is left out, such that the walls are placed one after another (see Fig. 6.14b).

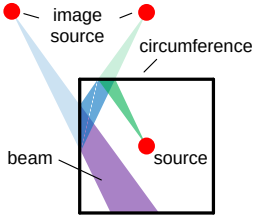

(a) real scene

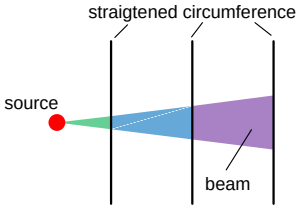

(b) equivalent, straightened scene

Figure 6.14.: The sound propagation path of a beam that is reflected twice can be straightened by placing the reflecting walls one after another.

By this simplification, the *smearing* of power by discretization and interpolation is illustrated. Without discretization, the power density of the beam is constantly 100% within the exact range of the beam. The split-up of the beam to partial beams assures a constant sound power (besides absorption, which is excluded in this investigation), but the extension of the beam width causes a modification of the sound power density (per angle) such that the energy conservation criterion is fulfilled. This reduced sound power density (on a wider range) is shown in Fig. 6.15a).

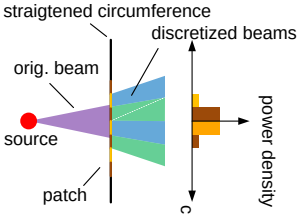

(a) with discretization (the power density of the outer two beams is interpolated)

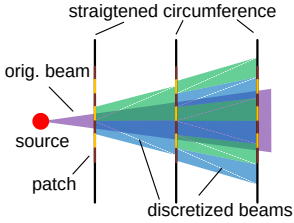

(b) divergence of a beam by discretization.

Figure 6.15.: Smearing of the power density by the first interpolation.

Although the power density is plotted against the length of the circumference, c, this is approximately proportional to the beam angle, because the opening angle is always very small ($\alpha \lesssim c$). The crucial point is that the divergence of the power transported by the beam and its *children* cumulates at each interpolation, because there is no chance that power re-concentrates again. Stephenson wrongly assumed that the interpolation errors cancel each other by part. In principle this widening is shown in Fig. 6.15b for beams with a reflection order of up to three (two interpolations) in *green* and *blue* beams, whereas the undiscretized beam is shown in *purple*. The sharp edge of a beam *smears* by discretization from an exact assignment to an uncertain assignment of receivers to the beams or image source, respectively. Thus, the uncertainty is a loss of accuracy of QPBT in contrast to BT, as the power propagates in a wider angle range by discretization. Still, a single impulse in the echogram is achieved, but it is not sure anymore that the energy is correct or there is even a sound propagation path for the detected impulse without discretization.

To quantify this effect, a numerical simulation was performed. Therefore, the walls were placed in a distance of a MFPL $\bar{l}$ and the sound source was placed half a MFPL in front of the first wall. The size of the patches was varied in a range of $1/10 < f_P = l_P/\bar{l} < 1/200$, as no absolute distances are relevant for this investigation. Beams that intersect with a wall were split up into partial beams. The beams that intersected with a patch only by part were interpolated as described in Sec. 6.4.1.1. Besides the computation of the power density distribution of the beams over the last wall, the discretized beams are shown in Fig. 6.16. The brightness of each beam is proportional to the power density that the beam carries, such that the *smearing* of energy is recognized in the propagation, too. For overlapping beams, the brightness is added up.

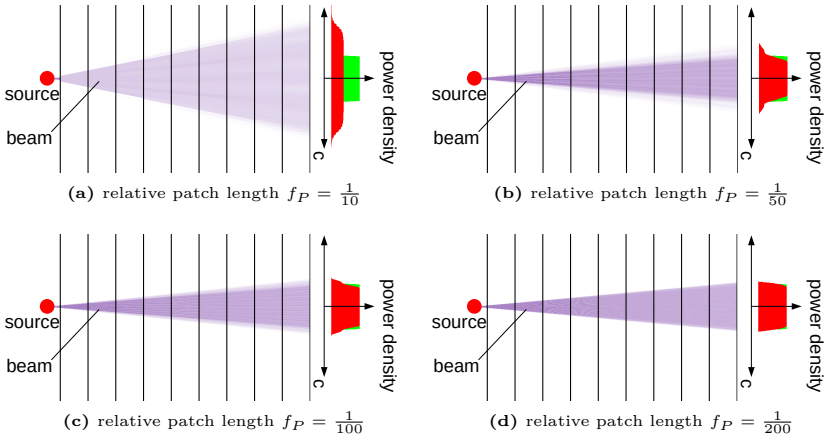

(a) relative patch length $f_P = \frac{1}{10}$ **(b)** relative patch length $f_P = \frac{1}{50}$

(c) relative patch length $f_P = \frac{1}{100}$ **(d)** relative patch length $f_P = \frac{1}{200}$

Figure 6.16.: Investigation of beam widening at reflection order 10 and $\varphi = 10°$ for Beam Tracing (*green*) and Quantized Pyramidal Beam Tracing (*red*). For visualization, the brightness is proportional to the power density of the discretized beam.

As expected, the *smearing* of power density strongly depends on the patch size. For very large patches ($f_P = 1/10$), the power density is completely *smeared* after only 10 interpolations. Even in the centre of the former beam, the power density is reduced to 50%. In case of smaller patches ($1/50 \leq f_P \leq 1/100$), the power density in the centre of the patch remains at 100%, but at the limits of the former beam still a *smearing* of power density is observed. For the smallest considered patches ($f_P = 1/200$), the widening of the beam almost vanishes. The final beam width $d\,(i)$ after $i = 10$ interpolations is shown in Fig. 6.17 for an opening angle of $\varphi = 10°$ (*solid*) and $\varphi = 2.5°$ (*dotted*).

The energy conservation, a crucial criterion of all GA simulation methods, is fulfilled, as the power (integral over the beam's power density, surface below graphs in Fig. 6.17) is constant for an opening angle of $\varphi = 10°$ as well as for $\varphi = 2.5°$. The width of the beam d strongly depends on the initial beam opening angle φ and the reflection order i. In addition, the beam width is proportional to the MFPL $\bar{l}$, but the overall behaviour is independent of the absolute sizes. In general, a plateau of power density in the centre of the beam (for not too large patches) exists with a power density of 100%. A reasonable value to quantify the widening is the difference between the beam width

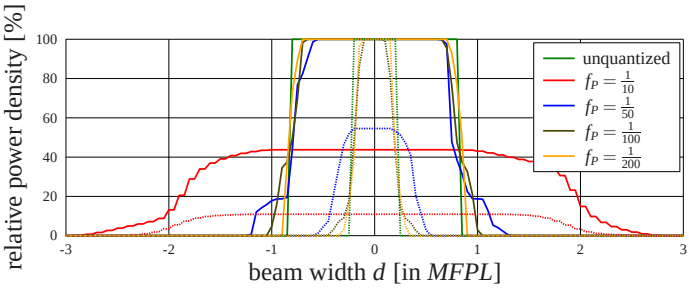

Figure 6.17.: Comparison of beam widening for different patch sizes f_P and different initial beam angles (*solid*: $\varphi = 10°$,*dotted*: $\varphi = 2.5°$) after 10 reflections.

with discretization $d_{discretized}$ and the beam width without discretization $d_{initial}$

$$\Delta d = d_{discretized} - d_{initial}. \tag{6.3}$$

Numerical investigations showed that the beam widening Δd is quite independent of the initial beam's opening angle. In other words, the widening effect is more important for narrower than for wider beams.

To discuss the behaviour of the beam widening with respect to the reflection order i, it is shown in Fig. 6.18 for different reflection orders and a patch length of $f_P = 1/10$ (*solid*) and $f_P = 1/100$ (*dotted*). To mask the effect that the beam itself widens out with each reflection order proportional to the reflection order i, the opening angle itself φ is adjusted by a factor of $1/i$ for each reflection order. Thus, the undiscretized beam width is constant.

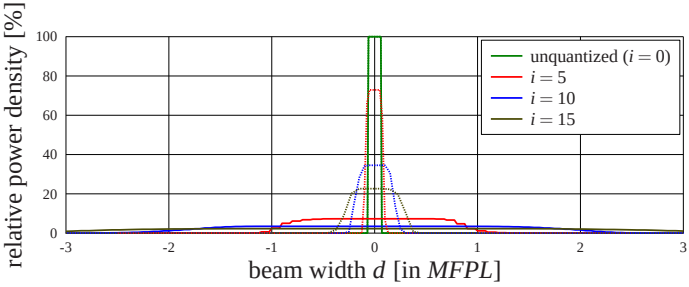

Figure 6.18.: Comparison of beam widening for different reflection orders i and different patch sizes (*solid*:$f_P = \frac{1}{10}$, *dotted*:$f_P = \frac{1}{100}$). The initial beam angle is adjusted for each reflection order, such that the width (without widening) would be constant.

The assumption that the beam widening increases is proven again. In the case of $f_P = 1/10$, the beam is smeared almost completely even after 5 interpolations, whereas the shape is kept better for $f_P = 1/100$. But even in case of $f_P = 1/100$, the beam is *smeared* to its triple width after 15 reflections. Investigations for more cases revealed that the widening increases proportionally with the reflection order. The beam widening is even worse in an actual simulation. While the beam widening increases linearly (even for a constant width of the undiscretized beam) with the reflection order, the reference

width of an initial beam even decreases with the reflection order. Thus, the beam widening is even stronger for the actual simulation of QPBT.

In contrast, only the starting point and the end point are discretized to the centre of the patches in case of the SPR. However, the error in propagation direction does not cumulate as for QPBT, because the energy flow is restricted to thin lines instead of extended beams. In contrast to QPBT, where only the beams widen out, sound particles are shifted to the inside with the same probability, too (see Fig. 6.19). In addition, no energy modification as in QPBT is necessary for the SPR.

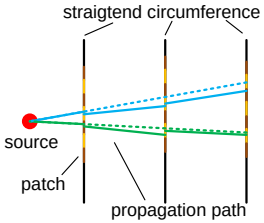

Figure 6.19.: Divergence of sound particles by discretization.

6.5.1.2. Detection Of Wrong Image Sources

The point-shaped receivers cause problems for the discretization. To investigate this, a single beam is used that intersects with a wall. It is a generalization of a higher order beam. This beam is split up into one partial beam for each patch (see Fig. 6.20a).

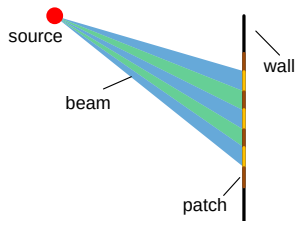

(a) one partial beam for each patch

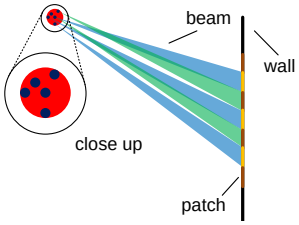

(b) translation of a beam's starting points (image source position)

Figure 6.20.: Discretization of a beam in Quantized Pyramidal Beam Tracing.

This split-up alone does not affect the detected sound energy. But, in order to store the beam power in the RUM, a discretization of the starting point has to be performed in a local coordinate system of each patch (see Fig. 6.12). By discretizing the angle and the radius, the starting points are translated relative to each other (see Fig. 6.20b). The translation of the starting point results together with the constant intersection area in two regions: a) no beam is present anymore and b) beams overlap each other (see Fig. 6.20b). This causes significant errors in the detected sound intensity, as either no energy or double energy is detected by different receivers. To demonstrate this, the sound intensity within a receiver grid is determined (see Fig. 6.21a). While without discretization the shape of the beam is noticeable in the intensity map (see Fig. 6.21b) and a homogeneous distribution is achieved, drastical errors occur through discretization. An error of 100% ($3dB$, *red*) is gained when the same image source is detected twice. This effect is caused by the coverage of receivers by multiple beams (see Fig. 6.21c). Another effect is the separation of beams forming a region uncovered by any beam. Receivers placed in these regions detect no energy (*white*). Hence, the homogeneous distribution without discretization is disturbed by receivers with double and no energy. Such errors are unacceptable for any simulation method, especially as they occur at any wall intersection.

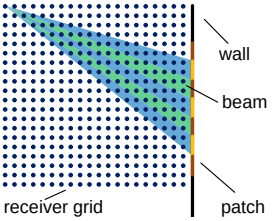

(a) receiver grid with beams without discretization

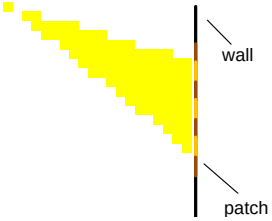

(b) intensity distribution without discretization

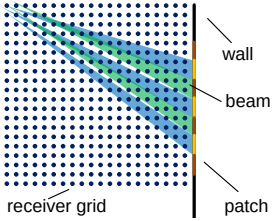

(c) receiver grid with beams with discretization

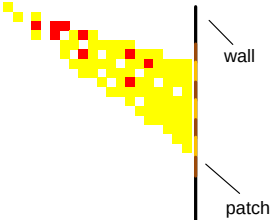

(d) intensity distribution with discretization

Figure 6.21.: Influence of discretization on an intensity map of a single beam.

In case of the SPR, the discretization causes similar translations of the sound particles. Principally, similar effects in the intensity maps are conceivable. But, in contrast to BT, the receivers instead of the sound energy carriers are spatially extended. The spatial extension averages over a small area automatically. This averaging is actually the reason for the inaccuracies of the SPSM in contrast to BT. Whenever a sound particle is translated slightly, the energy detection is not changed totally (*yes* or *no*) as for BT, but the inner crossing distance, and thus the detected energy, is varied slightly. Sound particles that already intersect with a receiver close to the boundary, i.e., a small inner distance, might be excluded from a detection by the translation, but the energy weighting keeps the error small (see Fig 6.22).

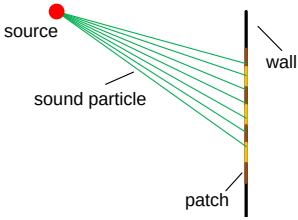

(a) one sound particle for each patch

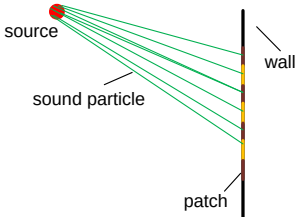

(b) translation of a sound particle's the starting and end points to the patch centres

Figure 6.22.: Discretization of a sound particle in the Sound Particle Radiosity.

By the discretization of beams, the benefit of the *exact* method is destroyed anyway. Hence, no additional inaccuracy occurs in the SPR by the detection of wrong image sources. In other words, this effect is by part already included in the SPSM.

6.5.2. Computational Complexity

The computational complexity of QPBT and the SPR is separated into two investigations. The frame algorithm of both methods (RUM logistics) is identical, but one of the differences is found in the initialization phase. For both methods, the number of initially traced sound energy carriers is one condition. Another one is the overall memory effort, which is given by the RUM.

6.5.2.1. Number of Initial Sound Energy Carriers

In case of the undiscretized version of the SPSM and BT, it is obvious that the number of primary beams is far below the number of primary sound particles, because many sound particles have to travel in a beam to achieve the same accuracy for this dedicated sound propagation path. For a rectangular room ($n = 4$), one beam per wall is emitted, whereas a huge number of sound particles has to be emitted ($N \gg n$) (see Fig. 6.23). These more efficient beams result in even higher accuracies.

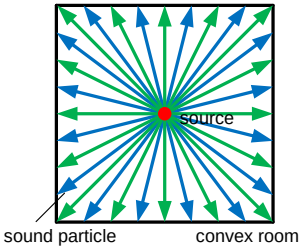

(a) Sound Particle Simulation Method

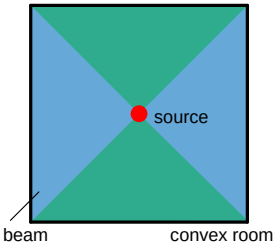

(b) Beam Tracing

Figure 6.23.: Initial number of sound energy carriers without discretization.

However, after the discretization (with the same parameter f_P), one sound energy carrier, either beam or sound particle, has to be created for each patch (see Fig. 6.24).

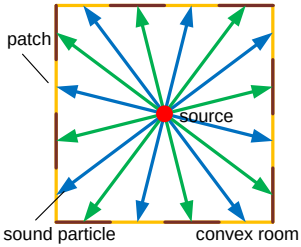

(a) Sound Particle Radiosity

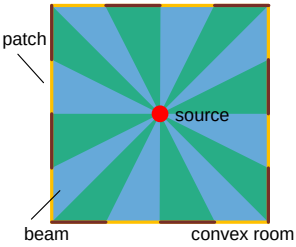

(b) Quantized Pyramidal Beam Tracing

Figure 6.24.: Initial number of sound energy carriers with discretization.

In a room with k patches, k sound energy carriers have to be emitted initially for the SPR as well as for QPBT. Without a split-up due to scattering or diffraction, the number of sound particles keeps constant $N = k$, whereas the number of beams increases quadratically (in $2D$) with the reflection order[PS10c]. So, in contrast to the unquantized version, the number of initially emitted sound particles equals the number of beams, such that the SPR is always faster than QPBT due to the even **reduced** number of sound energy carriers. This might cause different accuracies, but the former section showed that the inaccuracies of QPBT are even higher with the same parameter f_P than with the SPR.

6.5.2.2. Memory Usage

The SPR as well as QPBT feature exactly the same frame algorithm. The RUM is processed until no sound energy carrier remains. As pointed out in the previous section, the number of sound energy carriers that are initially stored in the RUM is identical for both simulation methods. However, it will be shown that the necessary size of the RUM differs drastically between the SPR and QPBT. In case of the SPR, a sound particle is discretized by three parameters (see Sec. 6.3.2). In a convex room, the overall circumference C_R is divided into k_P patches of length $l_P = f_P \cdot \bar{l}$ in analogy to Eqn. 6.2 to

$$k_P = \left\lceil \frac{C_R}{l_P} \right\rceil = \left\lceil \frac{C_R}{\bar{l} \cdot f_P} \right\rceil \approx \frac{C_R}{\bar{l} \cdot f_P}. \tag{6.4}$$

The time of intersection is discretized by time intervals t_Q, such that the number of time elements k_T reads

$$k_T = \left\lceil \frac{T_{Max}}{t_Q} \right\rceil = \left\lceil \frac{c \cdot T_{Max}}{l_P} \right\rceil = \left\lceil \frac{c \cdot T_{Max}}{\bar{l} \cdot f_P} \right\rceil \approx \frac{c \cdot T_{Max}}{\bar{l} \cdot f_P}. \tag{6.5}$$

In total, the number of matrix elements K_{RUM} for the SPR is given by the multiplication of the number of starting points, the number of end points and the number of time slots

$$K_{RUM} = k_P \cdot k_P \cdot k_T \approx \frac{c \cdot T_{Max} \cdot C_R^2}{\bar{l}^3} \frac{1}{f_P^3}. \tag{6.6}$$

Besides some geometrical constants (*left*), the size of the RUM increases with the inverse patch size to the power of three. For example, a reduction of the patch size by a factor of two increases the memory effort by a factor of eight. For high accuracies, the RUM becomes very huge, which turns out to be a crucial point of the SPR.

In QPBT, even four discretization parameters are needed to describe a beam completely (see Sec. 6.4.1). While the intersection area is described by the number of patches k_P and the time by k_T elements, the emission point is described by both distance and angle and, thus, k_E possible values (see Fig. 6.12). With the maximum distance r_{Max}, k_E is estimated by

$$k_E = \left\lceil \frac{r_{Max}}{\Delta r} \frac{\pi}{\Delta \varphi} \right\rceil = \left\lceil \frac{r_{Max}}{l_P} \frac{\pi}{f_P \cdot \pi} \right\rceil = \left\lceil \frac{r_{Max}}{\bar{l}} \frac{1}{f_P^2} \right\rceil \approx \frac{r_{Max}}{\bar{l}} \frac{1}{f_P^2}. \tag{6.7}$$

In summary, K_{RUM} for QPBT is computed by the multiplication of the number of starting points, the number of intersection areas and number of time interval to

$$K_{RUM} = k_E \cdot k_P \cdot k_T \approx \frac{r_{Max} \cdot C_R \cdot c \cdot T_{Max}}{\bar{l}^3} \frac{1}{f_P^4}. \tag{6.8}$$

The size of the RUM increases with the inverse patch size to the power of four. Thus, the memory effort of the SPR is even higher than for QPBT.

6.5.2.3. Evaluation of Computed Noise Maps

Despite the problems of QPBT, the simulation method has been implemented. Due to the huge memory effort, only simple scenarios are computable. The main differences are expected rather in the spatial than in the temporal resolution. Thus, intensity maps instead of echograms are investigated. These are considered in three test cases.

Free Field The first and most simple case is the sound propagation in free-field, i.e., without any reflections.

This is approximated by a rectangular room ($20m$ times $20m$) with totally absorbent walls ($\alpha = 1.0$) and a receiver grid with $w_{grid} = 0.25m$ (see Fig. 6.25). A sound source with $P' = 1W/m$ is positioned at the centre of the room. A BT simulation is used for the reference sound intensity level map (see Fig. 6.26a). The discretization size of the reunification techniques is set to $f_P = 1/100$. A number of $N = 100000$ sound particles is chosen in case of SPR to exclude this parameter as source of numerical errors. The results of those simulations are given in Fig. 6.26b and 6.26c. In addition, the absolute value of the difference of the intensity levels computed with the reunification techniques to the reference levels (BT) are added (see Fig. 6.26d and 6.26e).

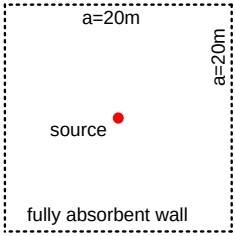

Figure 6.25.: Geometrical definitions of the free field.

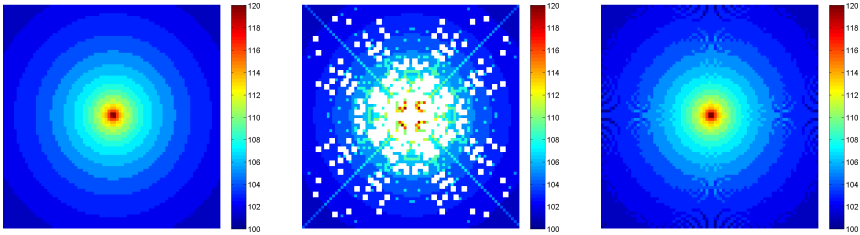

(a) Beam Tracing **(b)** Quantized Pyramidal Beam Tracing **(c)** Sound Particle Radiosity

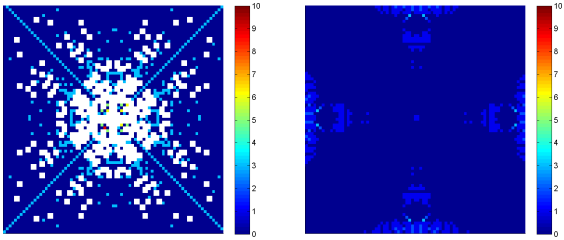

(d) $|QPBT - BT|$ **(e)** $|SPR - BT|$

Figure 6.26.: Intensity maps (in dB) of Beam Tracing, Sound Particle Radiosity and Quantized Pyramidal Beam Tracing in free field.

While in case of the SPR a maximum of $3dB$ occurs at the most for only 8 receiver points, differences of up to $10dB$ occur in case of the QPBT. Additionally, many

receivers detect no energy, which is a theoretical error of ∞dB. Both effects are caused by the detection of wrong image sources. A mean value of the difference is computed to $0.1dB$ for the SPR, whereas no value is computable for QPBT due to the infinite values. To achieve a numerical value, the infinite errors are replaced by an error of only $3dB$ with the result of an average error of $0.5dB$. This value describes only qualitatively that, even if the neglected receivers are weighted only by an error of $3dB$, QPBT yields five times worse results than the SPR. Thus, QPBT is even for the free-field case more inaccurate (and anyway more inefficient) than the SPR.

Convex Room The same investigation is carried out for a closed rectangular room. In the same setup as above (see Fig. 6.25), an absorption degree $\alpha = 0.5$ is applied to each wall. Sound particles and beams are traced until an energy loss of $-60dB$ (approximately 20 reflections). The other parameters remain the same. The intensity level maps are shown in Fig. 6.27.

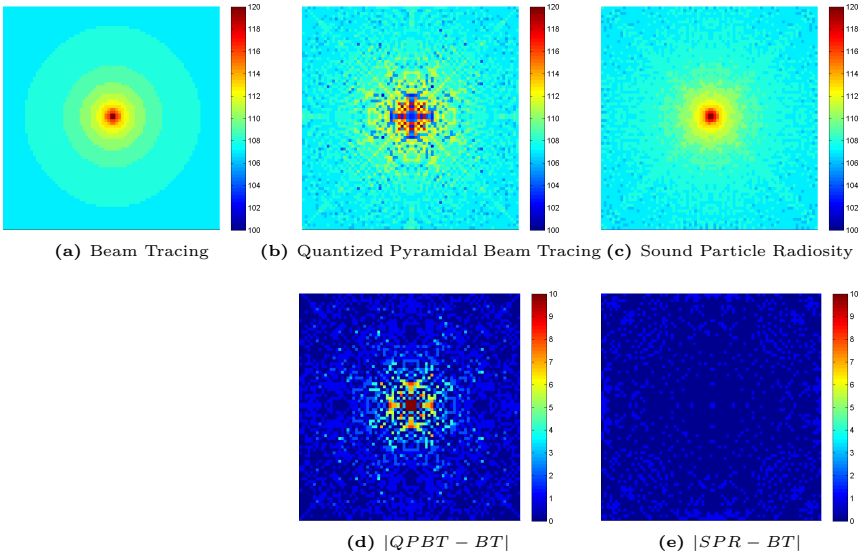

(a) Beam Tracing **(b)** Quantized Pyramidal Beam Tracing **(c)** Sound Particle Radiosity

(d) $|QPBT - BT|$ **(e)** $|SPR - BT|$

Figure 6.27.: Intensity maps (in dB) of Beam Tracing, Sound Particle Radiosity and Quantized Pyramidal Beam Tracing in a rectangular room.

In contrast to the former investigation, the sound intensity level is increased due to the wall reflections. Both the SPR and QPBT seem to result in very inaccurate simulation results, because the reference level, which is cylindrical symmetrical, can only be conjectured even for the SPR. However, the difference in the intensity levels reveals that the differences in case of the SPR are evenly distributed and $1.5dB$ at the most, whereas this difference is $16.9dB$ at the most in case of QPBT. The average error in the intensity maps is smaller for the SPR ($0.3dB$) than for QPBT ($0.8dB$), but not as significant as the maximum differences (as the latter are in a minority). The difference maps show that the SPR is again much more accurate than QPBT.

Two Rooms that are connected by a Virtual Wall Now, a slightly extended setup is chosen to investigate the influence of a Virtual Wall (VW), too.

Therefore, two of the rooms that were used in the previous sections are placed beside each other (see Fig. 6.28). The connecting wall of both rooms is replaced by a VW. Furthermore, the remaining walls are defined as fully absorbent ($\alpha = 1.0$), such that again a free-field result is achieved. As diffraction is not implemented in QPBT, the sound particle diffraction module is deactivated, too. The sound source is placed at the centre of the left room. Due to the increased sound propagation environment, the receiver grid is adjusted to $w_{grid} = 0.5m$ instead of $w_{grid} = 0.25m$ as in the previous experiments. The results are shown in Fig. 6.29.

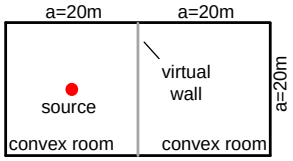

Figure 6.28.: Geometrical definitions of coupled rooms.

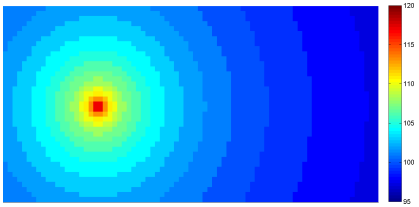

(a) Beam Tracing

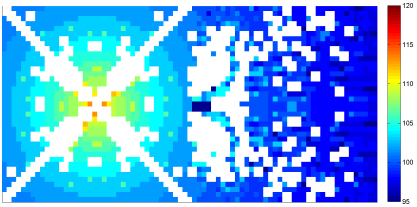

(b) Quantized Pyramidal Beam Tracing

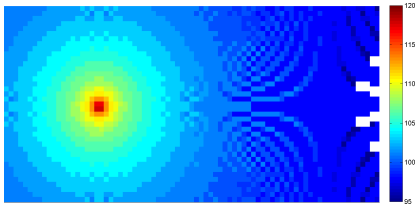

(c) Sound Particle Radiosity

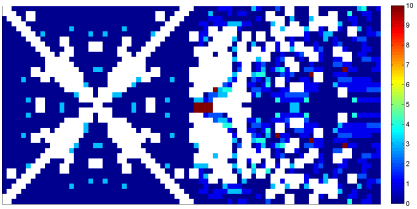

(d) $|QPBT - BT|$

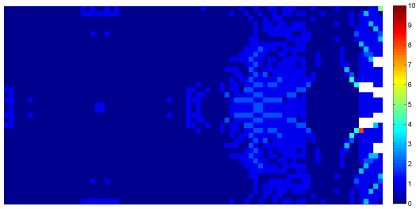

(e) $|SPR - BT|$

Figure 6.29.: Intensity maps of Beam Tracing, Sound Particle Radiosity and Quantized Pyramidal Beam Tracing in two coupled rooms.

This time, QPBT and the SPR result in receivers with no detected energy (*white spaces*), but their number is greater in the case of QPBT. It has to be noticed that the detection of wrong image sources in the case of QPBT does not only occur for the first

reflection: it is even worse after the first reflection (which corresponds to an equivalent transmission at the VW). This effect is very strong at the diagonal of the source-related subspace, because the receivers lie exactly on one of the beam's edge vectors. Thus, a minimal translation is enough here to cause such dropouts. The maximum error (neglecting the receivers without any energy) is $12.4dB$ for QPBT and $7.9dB$ for SPR. To achieve more accurate results in both cases, either the discretization parameter f_P has to be decreased or the receiver size has to be increased. The average error (replacing ∞dB by $3dB$ again) shows that the SPR is more than twice as accurate ($0.3dB$) than QPBT ($0.8dB$).

6.5.3. Choice of the Optimal Reunification Technique

The reunification techniques SPR and QPBT have been compared qualitatively with respect to their computational effort and their accuracy. In total, four arguments have been found, which reveal that the SPR is more efficient and, quite astonishing, more accurate than QPBT. These are

1. in QPBT, propagating beams are influenced by cumulating interpolation errors (*smearing* of energy),
2. correct image sources are neglected or double detected image sources are possible with QPBT,
3. there are not less beams than sound particles with discretization and
4. the memory requirement of QPBT is significantly higher than with the SPR.

With respect to these four arguments, which have been proven by numerical experiments, QPBT is abandoned. The computational effort and the accuracy of the SPR are investigated quantitatively in the next sections.

6.6. Efficiency of Sound Particle Radiosity

As shown in the previous section, the SPR has less computational complexity than QPBT, but a quantitative estimation of the efficiency is aimed at, too. To determine the efficiency, two contrary conditions have to be taken into account. On the one hand, the storage of sound particles in the RUM causes additional computational effort, whereas, on the other hand, the reunification of sound particles reduces the computational effort. Thus, the reunification rate is the main parameter that describes the efficiency of the SPR and is derived analytically. Furthermore, the CT of the SPR is investigated to determine the computational effort of reunification.

6.6.1. Statistical Analysis of the Reunification Rate

To statistically investigate the benefit of reunification, first the reunification rate has to be defined. Besides the split-up S, the main parameter for this is the size of the RUM (a formula calculating the size of the RUM was already presented in Sec. 6.5.2.2).

In this thesis, all matrix elements with the same time index are defined as *row*, whereas all matrix elements with the same start-end combination are defined as *column*.

The size of the RUM is decreased essentially by *recycling* the RUM by processing *the oldest sound particle first*[Ste04]. As sound particles travel only up to a maximum free path length l_{Max} between two walls, Stephenson postulated that only *rows* in a time range of l_{Max}/c have to be stored in the RUM. Thus, a cyclic buffer is used (see Fig. 6.30).

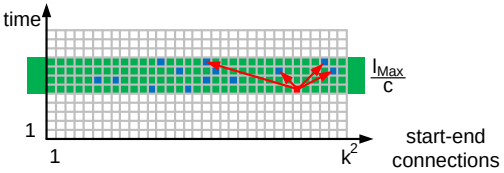

Figure 6.30.: Restriction of Reunification Matrix to the maximum time interval a sound particle travels due to the maximum free path length l_{Max}.

Based on this reduced RUM, Stephenson estimated a degree of occupation Φ_{RUM}. This degree of occupation equals statistically the reunification rate as it describes the probability to hit an already occupied element. Stephenson observed the RUM only after *many* reflections assuming a diffuse sound field (homogeneously and equiprobable, see Sec. 4.3.2), such that a steady state is approximately reached. In a diffuse sound field, the RUM is occupied homogeneously. Every patch is intersected from every direction at least one time during the cycle of $t = l_{Max}/c$. Stephenson concluded that the complete energy is distributed over a time range regarding the mean free patch length MFPL $\bar{l}$, although a time range of l_{Max} is processed. From that he computed an average degree of occupation

$$\Phi_{RUM} = \frac{\bar{l}}{l_{Max}}. \tag{6.9}$$

However, this derivation by Stephenson seems to be only an estimation of the relative number of (at least by part) occupied *rows* in the RUM. A more descriptive term is the degree of occupied elements in the RUM, which takes the occupation of each *row* into account. Stephenson's crucial misassumption was to assume that all *rows* are completely occupied, i.e., the sound propagation acts exactly like in the Acoustic Radiosity method, where the matrix of energy exchange coefficients $K_{i,j}$ is fully occupied. This assumption is only valid in a convex room for $S \approx k$, i.e., each patch emits energy in as many directions as patches exist whenever a sound particle intersects with a wall. Typically, values of S are significantly smaller. Thus, Stephenson's conclusion[Ste04] that the degree of occupation and, hence, the reunification rate is typically $\Phi_{RUM} > 0.1$ is not correct for the presented method.

To find a correct characterization of the occupation rate Φ_{RUM}, the simulation is carried out statistically. Similar to the investigation of the speed-up by convex subdivision, the smallest considered interval is an iteration i of one sound particle between two walls. Due to the functional principle of the SPR, the number of simultaneously propagating sound particles equals the number of occupied elements N_{RUM}. This number varies with the number of performed sound particle iterations, such that $N_{RUM}(i)$ denotes the number of occupied matrix elements after i computed sound particle iterations. However, these iterations are of minor practical relevance. More important is the description of the number of occupied matrix elements $N_{RUM}(o)$ as a function of the reflection order o. In this context, the term reflection includes specular reflections, diffuse reflections and diffractions. Finally, the reunification rate is defined as the ratio of occupied matrix elements to the number of available matrix elements K_{RUM}.

In summary, the parameters are:

- K_{RUM} : number of available matrix elements
- N_{RUM} : number of occupied matrix elements
- Φ_{RUM} : degree of occupation $\frac{N_{RUM}}{K_{RUM}}$
- N : number of emitted sound particles (by all sound sources)
- i : counter of single iterations
- o : reflection order (including scattering and diffraction)

6.6.1.1. Behaviour Without Reunification

To investigate the behaviour of the SPR without reunification[PS10a], the probability of reunification is set to 0. In other words, the number of available matrix elements converges to infinity ($K_{RUM} \to \infty$).

During one iteration i, one sound particle is taken out of the RUM and, after the actual propagation, $S+1$ sound particles are stored in the RUM

$$N_{RUM}(i+1) = N_{RUM}(i) - 1 + (S+1). \tag{6.10}$$

The conversion of the recursive equation to an explicit equation yields

$$N_{RUM}(i) = N_{RUM}(i=0) + i \cdot S = N + i \cdot S. \tag{6.11}$$

Thus, the number of occupied matrix elements linearly increases with every computed iteration i (except for $S = 0$, i.e., without scattering or diffraction, where the number remains constant). $N_{RUM}(i)$ is shown in Fig. 6.31 for different S and $N = 1000$ (*dotted* lines).

The determination of the number of occupied matrix elements after o reflections, $N_{RUM}(o)$, is more complicated. Mathematically speaking, a number of $\Delta i(o+1)$ iterations have to be performed to find the number of occupied matrix elements after $o+1$ reflections $N_{RUM}(o+1)$. The computation of one reflection order requires the computation of all currently propagating sound particles. Thus, all sound particles of the previous order $N_{RUM}(o)$ have to be handled once

$$\Delta i(o+1) = N_{RUM}(o). \tag{6.12}$$

The handling of the reflection order o is finished whenever $\Delta i(o+1)$ iterations are computed. Fortunately, Eqn. 6.11 already describes the number of occupied matrix elements when i iterations are computed, based on a starting value of $N_{RUM}(i=0)$. With a starting value of $N_{RUM}(o)$ occupied matrix elements and the substitutions

$$\begin{aligned} i &\to \Delta i(o+1) = N_{RUM}(o) \\ N_{RUM}(i=0) &\to N_{RUM}(o) \\ N_{RUM}(i) &\to N_{RUM}(o+1), \end{aligned} \tag{6.13}$$

Eqn. 6.11 can be analogously used to describe the whole procedure as a function of the number of reflections (instead of iterations)

$$N_{RUM}(o+1) = N_{RUM}(o) + \Delta i(o+1) \cdot S = (S+1) \cdot N_{RUM}(o). \tag{6.14}$$

This recursive equation is converted to an implicit equation using the geometric series

$$N_{RUM}(o) = N_{RUM}(o=0) \cdot (S+1)^o = N \cdot (S+1)^o . \tag{6.15}$$

This matches exactly (as already estimated in Eqn. 6.1) an exponential increase.

The number of occupied matrix elements increases exponentially with the reflection order o (see Fig. 6.32, *dotted* lines, note the logarithmic $y-scale$), whereas it increases only linearly with the number of computed iterations i.

6.6.1.2. Behaviour With Reunification

In the case of reunification, a certain probability $0 < p_r < 1$ to hit an already occupied matrix element is introduced. Consequently, the probability to hit an empty matrix element is $(1-p_r)$. Thus, only $(S+1) \cdot (1-p_r)$ new elements will be occupied.

So, in analogy to Eqn. 6.10, the number of occupied matrix elements is written as

$$N_{RUM}(i+1) = N_{RUM}(i) - 1 + (S+1) \cdot (1-p_r) . \tag{6.16}$$

Although the reunification probability p_r is dependent on the geometrical scene, p_r has to be abstracted for statistical analysis. Therefore, a diffuse sound field is assumed.

Assigning the assumption of a diffuse sound field to the reunification probability, the probability is independent of the actual position in the geometrical scene and, thus, in the RUM. It follows from the equiprobable distribution

$$p_r = \frac{N_{RUM}(i)}{K_{RUM}} = \Phi_{RUM}, \tag{6.17}$$

such that Eqn. 6.16 reads

$$\begin{aligned} N_{RUM}(i+1) &= N_{RUM}(i) - 1 + (S+1) \cdot \left(1 - \frac{N_{RUM}(i)}{K_{RUM}}\right) \\ &= q \cdot N_{RUM}(i) + S \end{aligned} \tag{6.18}$$

with

$$q = 1 - \frac{S+1}{K_{RUM}} . \tag{6.19}$$

The recursive equation is converted into an implicit equation

$$\begin{aligned} N_{RUM}(i) &= N_{RUM}(i=0) \cdot q^i + S \cdot \frac{1-q^i}{1-q} \\ &= N \cdot q^i + S \cdot \frac{1-q^i}{1-q} . \end{aligned} \tag{6.20}$$

The behaviour of the number of occupied matrix elements with reunification (see Eqn. 6.20) for $K = 10000$ available matrix elements is shown in Fig. 6.31 and compared with the case without reunification (see Eqn. 6.11).

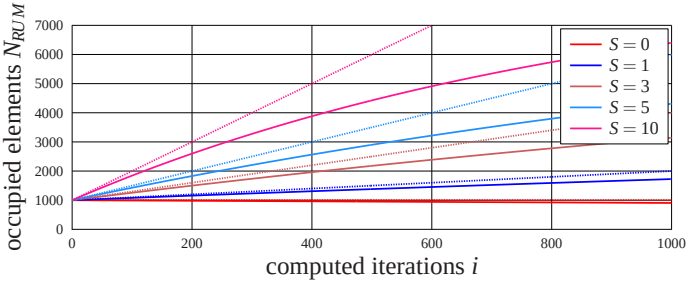

Figure 6.31.: Number of occupied elements $N_{RUM}(i)$ for different split-up values S, as a function of the computed iterations i (*dotted*: without reunification, *solid*: with reunification).

Without split-up ($S = 0$), where the number of occupied matrix elements remains constant without reunification, a slight decrease is noticed if reunification is applied. Sound particles are never split-up, but there is a slight chance to reunify. In this case, the reunification effect (difference between *solid* and *dotted* line) is so small that the SPR becomes very inefficient. However, for great split-up values $S = 10$, the number of sound particles increases with the number of computed iterations i. With reunification, the number of occupied matrix elements and, thus, simultaneously existing sound particles, is below the case without reunification. This reduced linear increase indicates the convergence of $N_{RUM}(i)$ to an upper boundary. This upper boundary exists, because $N_{RUM}(i) = K_{RUM}$ matrix elements are occupied at the most.

More meaningful is the number of occupied elements as a function of the reflection order o. With the same substitutions as in Eqn. 6.13, Eqn. 6.20 yields for $N_{RUM}(o)$

$$N_{RUM}(o+1) = N_{RUM}(o) \cdot q^{N_{RUM}(o)} + S \cdot \frac{1 - q^{N_{RUM}(o)}}{1 - q}. \tag{6.21}$$

This recursive equation is not easily convertible to an implicit equation, but it is evaluated numerically. The result is shown in Fig. 6.32 for $K = 10000$ and different split-up values S (the *dotted* lines indicate the case without reunification).

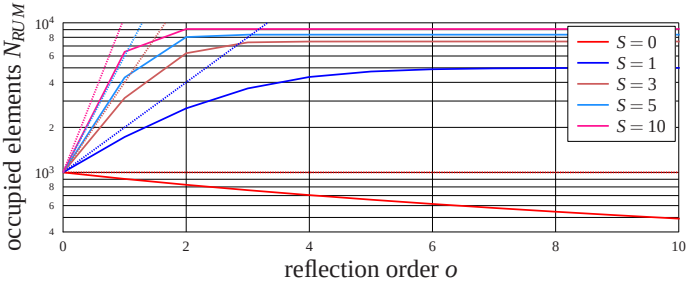

Figure 6.32.: Number of occupied elements $N_{RUM}(o)$ for different split-up values S, as a function of the reflection order o (*dotted*: without reunification, *solid*: with reunification).

For very small reflection orders, $N_{RUM}(o)$ follows the exponential increase without reunification, but converges fast to a constant upper boundary. The higher the split-up

value S is, the faster is this upper boundary reached. Only for $S = 1$, a smaller upper boundary is observed, and for $S = 0$ the number of occupied elements even decreases in comparison to the number of initially emitted sound particles. To determine the upper boundary, the same comparison is shown in Fig. 6.33 for $S = 1$, but different numbers of available matrix elements K.

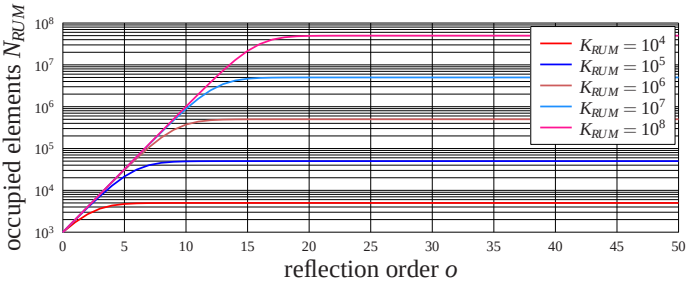

Figure 6.33.: Number of occupied elements $N_{RUM}(o)$ for different matrix sizes K_{RUM} and a split-up values of $S = 1$, as a function of the reflection order o.

The exponential increase (note the logarithmic $y - scale$) converges quite fast to a constant upper boundary. The upper boundary strongly depends on the number of available matrix elements K_{RUM}. This boundary is computed analytically, with

$$\lim_{o\to\infty} N_{RUM}(o) = \frac{S}{S+1} \cdot K_{RUM}. \tag{6.22}$$

Here, the number of occupied matrix elements is only depended on the split-up value S and the number of available matrix elements K, whereas the occupation degree $\Phi_{RUM} = \frac{N_{RUM}}{K_{RUM}} = \frac{S}{S+1}$ is only dependent on the split-up value S. Both are independent of the number of primary emitted sound particles N. Astonishingly, N_{RUM} never converges to a full occupation $\Phi_{RUM} = 1$. The steady state value is approximately reached after a different number of reflections o depending on the split-up S and the size of the RUM. Starting from this crucial reflection order, the exponential increase of sound particles is prevented, and the CT increases only linearly with the reflection order. This convergence has been proposed by Stephenson (at least qualitatively) for QPBT and the SPR. The presented equations are used to determine the reflection orders of convergence now quantitatively, too. The result is validated by a comparison with a simulation.

6.6.1.3. Comparison with Numerical Simulation

To verify the estimated reunification rate, a SPR simulation is performed in a rectangular room with a wall length of $a = 10m$ for all four walls (see Fig. 6.34). The scattering degree is set to $\sigma = 0.5$ and absorption is disabled ($\alpha = 0.0$). Sound particles are only aborted after a certain number of reflections, such that no sound particles are aborted within the investigated iterations.

The number of available matrix elements is computed by Eqn. 6.6, where T_{Max} is replaced by l_{Max}/c due to the cyclic buffer to

$$K_{RUM} = \frac{c \cdot \frac{l_{Max}}{c} \cdot C_R^2}{\bar{l}^3} \frac{1}{f_P^3} = \frac{\sqrt{2} \cdot a \cdot (4 \cdot a)^2}{\left(a \cdot \frac{\pi}{4}\right)^3} \frac{1}{f_P^3} \approx \frac{47}{f_P^3}. \tag{6.23}$$

The discretization parameter is set to $f_P = 1/100$, such that the reunification matrix consists of $K \approx 47.000.000.000$ matrix elements. In the special case of a rectangular room, the number of available patch-patch-combinations reduces by a factor of 3/4, because sound particles cannot intersect with the wall from where they were emitted. Thus, $K = 35.000.000.000$ is assumed. A SPR simulation has been performed with a split-up value of $S = 25$ and $N = 1000$ primary sound particles. The number of occupied matrix elements is counted after each iteration and compared with the estimation of Eqn. 6.20 in Fig. 6.35.

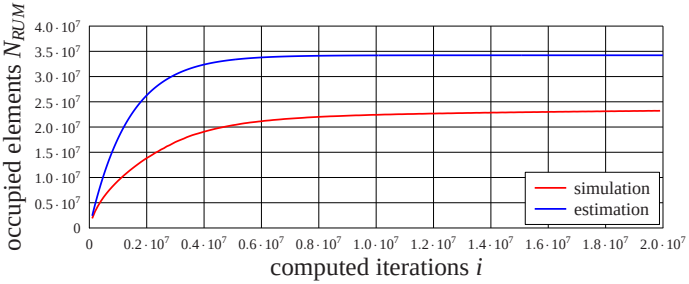

Figure 6.35.: Validation of estimated number of occupied matrix elements (see Eqn. 6.20) N_{RUM} (i) as a function of the computed iterations i by a simulation in a rectangular room. The walls are of $a = 10m$ length, $N = 1000$ sound particles are emitted and split up into $S = 25$ secondary sound particles.

Both graphs behave qualitatively similar, but the estimated maximum number of occupied elements is approximately 40% above the simulated value. This is explained by the assumption of a diffuse sound field that is (as expected) not fulfilled here. In a rectangular room with mainly diffuse reflections is the probability to intersect with an opposite wall higher than the probability to intersect with a neighbouring wall, because the projected surface of the latter is smaller (*cosine* law). Thus, regions in the RUM exist, where sound particles propagate more probable and, on the contrary, regions exist with lower density. The result of this uneven distribution is that the effective reunification rate is higher, such that the total amount of sound particles that propagate simultaneously is reduced. Consequently, N_{RUM} behaves, as if the total amount of available matrix elements is reduced. As a uniform distribution is the *worst case*, the estimated N_{RUM} is interpreted as an upper boundary for every geometrical scene, but all N_{RUM} elements must - for safety - be made accessible. The general behaviour of the occupied matrix elements as a function of the number of iterations is confirmed.

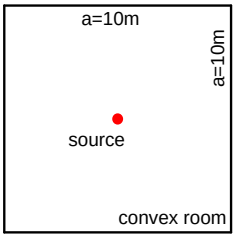

Figure 6.34.: Geometrical definitions for the test of the reunification rate.

6.6.2. Computation Time

For the comparison of the CT of the SPR (with reunification) and the CT of the SPSM (without reunification), the same simulation parameters have to be defined for both simulation methods. The same rectangular room as in the previous investigation is

used (see Fig. 6.34) with $N = 1000$ primary sound particles and a split-up of $S = 25$. As abort criterion, an energy threshold $e_{Threshold}$ is computed from the maximum reflection order (see Sec. 3.4.5, Eqn. 3.26). With a constant wall absorption $\alpha = 0.5$ and without air attenuation ($m = 0$), the energy threshold reads for a given effective reflection order o_{Max}

$$e_{Threshold} = \left(\frac{1-\overline{\alpha}}{1+S}\right)^{o_{Max}} = \left(\frac{0.5}{26}\right)^{o_{Max}} \approx (0.02)^{o_{Max}} . \tag{6.24}$$

The CTs of the SPR and the SPSM are measured and compared in Fig. 6.36.

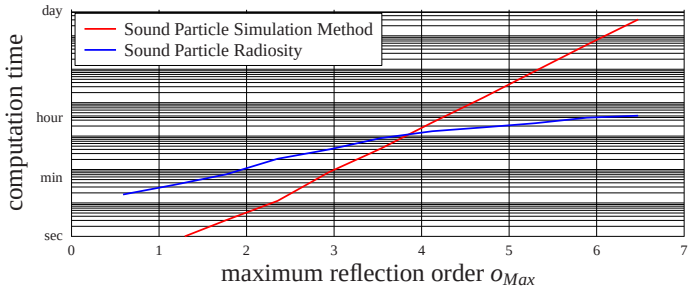

Figure 6.36.: Comparison of Computation Time of Sound Particle Radiosity and Sound Particle Simulation Method in a rectangular room. The energy threshold is defined, such that a simulation up to an effective reflection order is computed.

The CT of the SPSM increases exponentially, as expected, with the reflection order (note the logarithmic $y - scale$). The CT of the SPR increases slower than the linear increase (in logarithmic scale) of the SPSM. Both CTs match each other at approximately $o_{Max} = 4$. For higher reflection orders, in this setup, the SPR is faster than the SPSM. Unfortunately, the SPSM is still faster for simulations up to a lower reflection order. For only one reflection, the SPSM computes less than a second, whereas the SPR already has a CT of approximately one minute. The reason for this behaviour is the additional computational effort to access the RUM (see Fig. 6.36, a measurement uncertainty due to small time intervals is indicated in *green*).

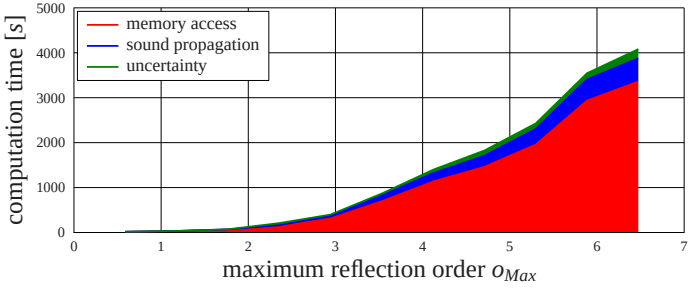

Figure 6.37.: Composition of Sound Particle Radiosity's Computation Time into memory usage and sound propagation.

The CT of the SPR is mainly based on the memory usage, since the actual propagation of a sound particle is very simple (see Sec. 4.3). In this example, this *search overhead*

is approximately 6 times higher than the CT of the sound propagation. This causes the inefficiency of the SPR below that reflection order. However, the SPR is designed for higher order reflections including diffraction and scattering.

Furthermore, the current implementation of SPR is only a prototype implementation, and a reduction of the search overhead is expected by optimizing the memory usage.

6.7. Numerical Errors of the Sound Particle Radiosity

The discretization of sound particle intersection points to the centre of the patches causes errors (described already qualitatively in comparison with the errors of QPBT in Sec. 6.5.1). In this section, these numerical errors are described quantitatively. The SPSM is chosen as reference solution. A number of $N = 1.000.000$ sound particles are emitted to suppress the numerical error ($< 0.1dB$) by this parameter.

The main discretization parameter is the patch size given by f_P. First of all, the influence of this patch size on the echogram is discussed without taking scattering and diffraction into account. In a second experiment, scattering is added and the results are discussed with respect to the echogram, too. Finally, the influence of the discretization to the intensity maps that are computed with diffraction is presented.

6.7.1. Influence of the Patch Size on Numerical Errors

The influence of the patch size to the results of the computed echogram is investigated with respect to three attributes. For city acoustics, where intensity maps are important, the overall sound intensity is computed and the error is defined relative to the result of the SPSM. For room acoustical simulations, however, the temporal behaviour of the echogram is important for the computation of the room acoustical parameters. Therefore, the relative error of the intensity in each time slot is computed and an average over those values is determined. Finally, the relative error in the reverberation time, as representative of these room acoustical parameters, is identified.

The geometrical scene is defined once more by a rectangular room with walls of length $a = 10m$. The sound source and the receiver are placed in a height of $5m$ above the floor and in a distance of $5m$ between each other (see Fig. 6.38). The receiver radius is set to $r_D = 1m$. The maximum simulation time and, thus, the length of the echogram, is set to $T_{Max} = 0.1s$ to inspect the single reflections. The time slots of the echogram are set to $\Delta t = 0.1ms$. The absorption degree is constantly $\alpha = 0.5$ and scattering is disabled ($\sigma = 0.0$, $S = 0$) on all four walls. The SPR simulation has been performed for patch sizes given by discretization parameters from $f_P = 1/10$ to $f_P = 1/200$. The echograms of those simulations are presented in Fig. 6.39. As a reference, the result of SPSM is shown, too.

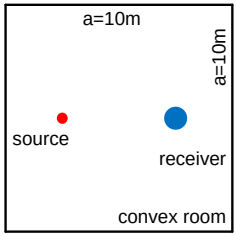

Figure 6.38.: Geometrical definitions for the investigation of discretization errors.

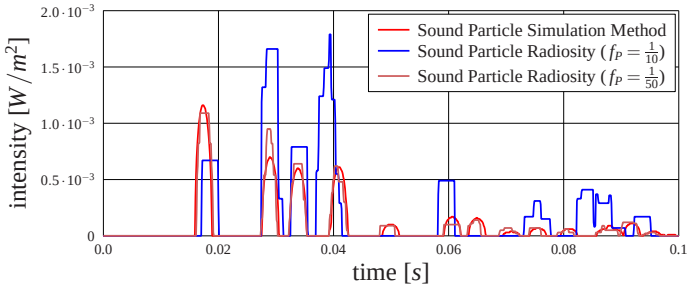

(a) $f_P = \frac{1}{10}, f_P = \frac{1}{50}$

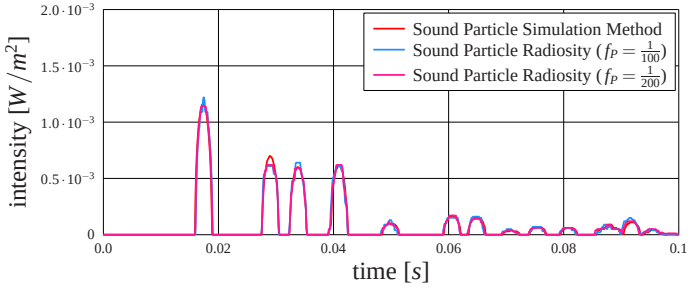

(b) $f_P = \frac{1}{100}, f_P = \frac{1}{200}$

Figure 6.39.: Echograms in a rectangular room for different discretization parameters f_P computed with the Sound Particle Radiosity and the Sound Particle Simulation Method as reference.

The results of the SPR with $f_P = 1/200$ are quite identical to use of the SPSM, whereas $f_P = 1/10$ results in a different echogram. The relative errors of the overall intensity, the time interval and the reverberation time are shown in Fig. 6.40 for different values of f_P.

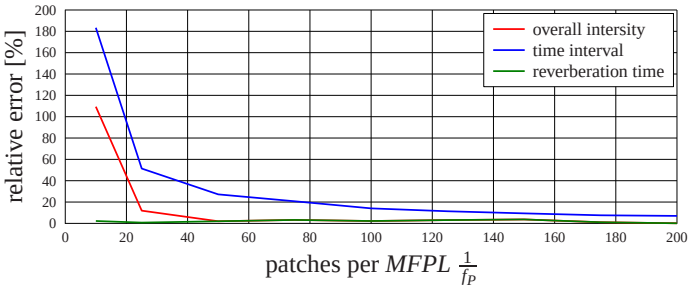

Figure 6.40.: Relative error in an echogram for different discretization values f_P.

Although the echograms are very different, the relative error of the reverberation time is almost independent of the discretization parameter. This result is caused by

the fact that the reverberation time is only a measure of the average energy loss over time. Although the sound particle propagation path is shifted to a huge extent by an insufficient discretization, the average energy loss per time is constant, especially for a homogeneous distribution of absorption. Even for very large patches, the reverberation time is constructed by different sampling points, but the slope is quite similar. In total, the reverberation time is robust with respect to the discretization.

On the contrary, the error in the overall intensity varies with the discretization parameter f_P. For $f_P = 1/10$, the relative error is approximately 100% and decreases with smaller patches ($< 5\%$ for $f_P < 1/50$). The large error for $f_P = 1/10$ is caused by the receiver size, because less than one sound particle intersects with the receiver with this rough discretization statistically.

A similar effect is found for the error in time intervals. It is extreme (180%) for $f_P = 1/10$ and decreases for smaller patches (10% for $f_P = 1/200$). The relative error in the time interval is greater than the error of the overall intensity for all patch sizes. This is explained by looking at the echograms: While in case of moderate values $f_P = 1/50$, the overall intensity is quite accurate, single (wrong) peaks lead to large temporal errors. These *steps* in the echogram start to vanish for $f_P \geq 1/100$.

The same experiments have been performed for different maximum echogram time ranges of T_{Max}. All three errors are almost not affected by this variation. In case of the reverberation time and the overall intensity, this effect is explained by the fact that intensities for small time indices are most important for the determination of those parameters. But the error in the time interval is almost constant. Hence, the accumulation of errors as in QPBT is precluded also numerically for the SPR.

The relative errors are practically independent of the number of emitted sound particles N, as long as a sufficient number of sound particles intersect with the patch during the initialization process. Whenever at least 20 sound particles intersect with a patch on average, no further increase of accuracy is observed.

6.7.2. Influence of the Discretization on the Simulation of Scattering

In a second experiment, the effect of the discretization on a simulation including scattering is investigated. A scattering coefficient of $\sigma = 0.5$ is applied to all surfaces (see Fig. 6.38) and each sound particle is split up into S diffusely reflected sound particles in addition to the specular reflected sound particle. To achieve moderate CTs, the sound propagation is aborted after an energy loss of $-60dB$. The discretization parameter is fixed to $f_P = 1/100$ in this investigation. The echogram of a simulation with a split-up value of $S = 10$ is shown in Fig. 6.41.

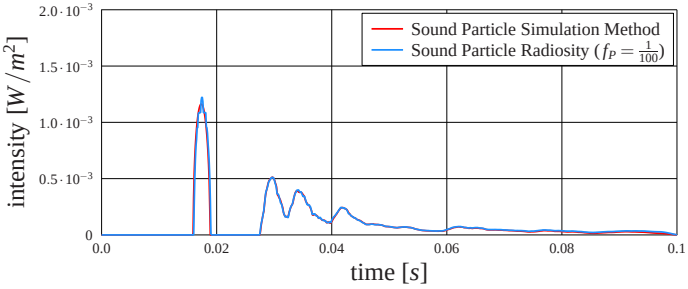

Figure 6.41.: Echograms in a rectangular room for $S = 10$ and $f_P = \frac{1}{100}$ computed with the Sound Particle Radiosity and the Sound Particle Simulation Method.

The echograms of the SPR and the SPSM agree quite well in the complete time range. Based on these computations, the same three relative errors as described above are determined for different split-up values S. The results are shown in Fig. 6.42.

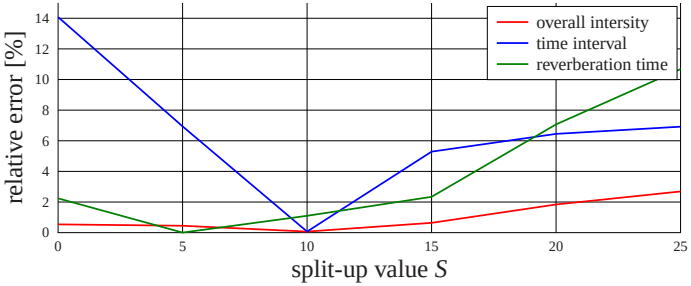

Figure 6.42.: Relative error in an echogram for different split-up values S and a discretization value of $f_P = \frac{1}{100}$.

The relative error of the reverberation time as well as the relative error of the overall sound intensity increases with increasing split-up values. While almost no relative error occurs for $S = 5$ ($< 1\%$), errors up to 10% occur in simulations with $S = 25$. The relative error in the time interval behaves similarly for $S > 10$. Unreasonable results below $S = 10$ are explained by many empty time intervals for low split-up values. Thus, a reduced number of time intervals is taken into account and the relative error is not directly comparable with the error of other split-up values.

The described effect seems to prevent an efficient simulation by the SPR, because the aim of the SPR is the simulation of scattering (and diffraction). Therefore, the occurring error is investigated in more detail. In order to determine the effect of increasing errors for greater split-up values S, the echogram of a simulation with $S = 25$ is shown in Fig. 6.43. To clarify the effect, the energy is plotted logarithmically.

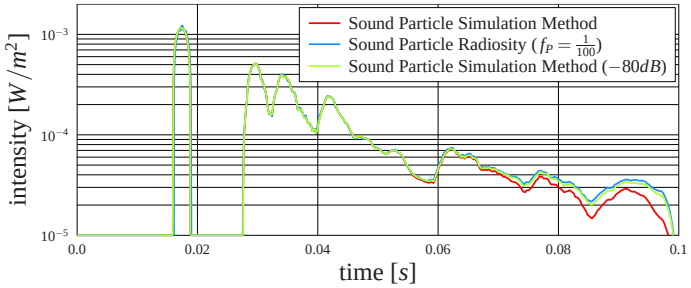

Figure 6.43.: Echograms in rectangular room for a split-up value $S = 25$ and $f_P = \frac{1}{100}$ computed with the Sound Particle Radiosity and the Sound Particle Simulation Method (note: logarithmic $y - scale$).

A comparison of the SPR with the SPSM reveals that the difference in-between both methods occurs in the later part of the echogram. More energy is detected by the SPR. The errors in the overall sound intensity, the temporal errors and even the errors in the reverberation time are explainable by this increased energy in the late part of the

echogram. Although the reverberation time seems to be quite robust with respect to the patch size f_P, the influence of the split-up value S is strongest for the reverberation time. The difference is explained by the energetic abort criterion, although it was identical for both simulation techniques.

For the given setup, an energetic abort criterion of $-60dB$ seems to be sufficient, because approximately 20 reflections are handled with an average absorption degree of $\alpha = 0.5$. But with a split-up in $S = 25$ sound particles, only 4 reflections are handled according to Eqn. 3.26. Even for an abort criterion of $-60dB$, the tracing of sound particles is aborted before they reach the maximum time of $0.1s$. Nevertheless, the same effect occurs with the SPR, such that no difference is expected in the first attempt. In the case without reunification, the tracing of sound particles below the energy threshold is directly aborted. On the other hand, in the case of reunification, multiple sound particles (each with energy below the energy threshold) might be reunified, such that the total amount of energy is above the energy threshold. As a result of this reunification, the reunified sound particle is propagated at least one more reflection. Hence, the echogram that is computed with the SPR is more accurate than in case of the SPSM. This is verified by the simulation of the SPSM with a reduced abort criterion of $-80dB$ as also shown in Fig. 6.43. The increase of the SPR in the late part of the echogram is confirmed by this simulation. The difference between the SPSM and the SPR increases, but this is rather a result of a wrong abortion criterion than an error of the SPR.

6.7.3. Influence of the Discretization on the Simulation of Diffraction

The computation of diffraction with the SPR is influenced by numerical errors, too. In case of diffraction, the spatial behaviour of those numerical errors is more important than the temporal behaviour[PS11a]. In contrast to the investigations of Chapter 5, all units are now in real distances (m) instead of relative wavelengths (λ). However, the simulation has been performed for 10 octave bands from $f = 31.5Hz$ to $f = 16.000Hz$ simultaneously. Due to the functional principle of the SPR, all sound particles are discretized by shifting their intersection points to the patch centres before they are diffracted or detected. In contrast to the former investigations in this chapter, a dependency of the wavelength λ, and thus the frequency f, is expected, because of the specification to diffract at least a few sound particles in a region of $d = 0.1\lambda$ above the wedge (see Sec. 5.5.3.2). This region is in the range of $0.002m(16.000Hz) < d < 1.092m(31.5Hz)$. In order to achieve a reference solution, the simulation has been repeated by the SPSM (i.e., without discretization) with the same parameters.

The simulations have been performed in a rectangular room of $a = 20m$ width in each dimension. A single wedge of $\frac{a}{2} = 10m$ height is placed at the centre of the floor, $x = \frac{a}{2}$, and is extended to the ceiling by a VW (see Fig. 6.44). The sound source is positioned at the centre of the room to the left of the wedge. No specified receiver position is needed, because the sound intensity maps are computed for a receiver grid. This grid has the dimensions of $w_{grid} = 0.1m$ ($200 \cdot 200$ receivers). All surfaces (including the wedge) are completely absorbent ($\alpha = 1.0$) in order to focus on the effect of diffraction (compare setup of Stephenson's investigations[SS07]). A number of $N = 500.000$ primary sound particles are emitted and split up into $S = 200$ sound particles at each diffraction event. Both values

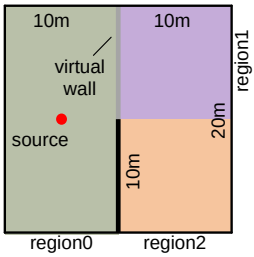

Figure 6.44.: Geometrical setup for the investigation of diffraction.

are great enough to neglect their influence (see Sec. 5.5.3.2, 5.5.3.3). The Diffraction Angle Probability Density Function (DAPDF) $D_g(\varepsilon, b)$ (see Eqn. 5.15) and the Edge Diffraction Strength (EDS) with the *projected* slit width (Sec. 5.4.3.3) are used.

The sound field is computed by the SPR for $f_P = 1/20$, $f_P = 1/50$ and $f_P = 1/100$. With a MFPL of $\bar{l} = 4\pi \approx 12.5m$, these parameters correspond to an absolute patch size of $l_P \approx 0.625m (f_P = 1/20)$, $l_P \approx 0.25m (f_P = 1/50)$ and $l_P \approx 0.125m (f_P = 1/100)$.

For $f = 500Hz$, the value of d computes to $d \approx 0.07m$, such that no accurate results are expected below $f_P = 1/100$. The results are shown in Fig. 6.45 together with the reference solution of the SPSM. In addition, the absolute difference of the intensity levels by the SPR is shown relative to the intensity maps by the SPSM. The plots for the remaining frequencies are collected in appendix A.2.6.

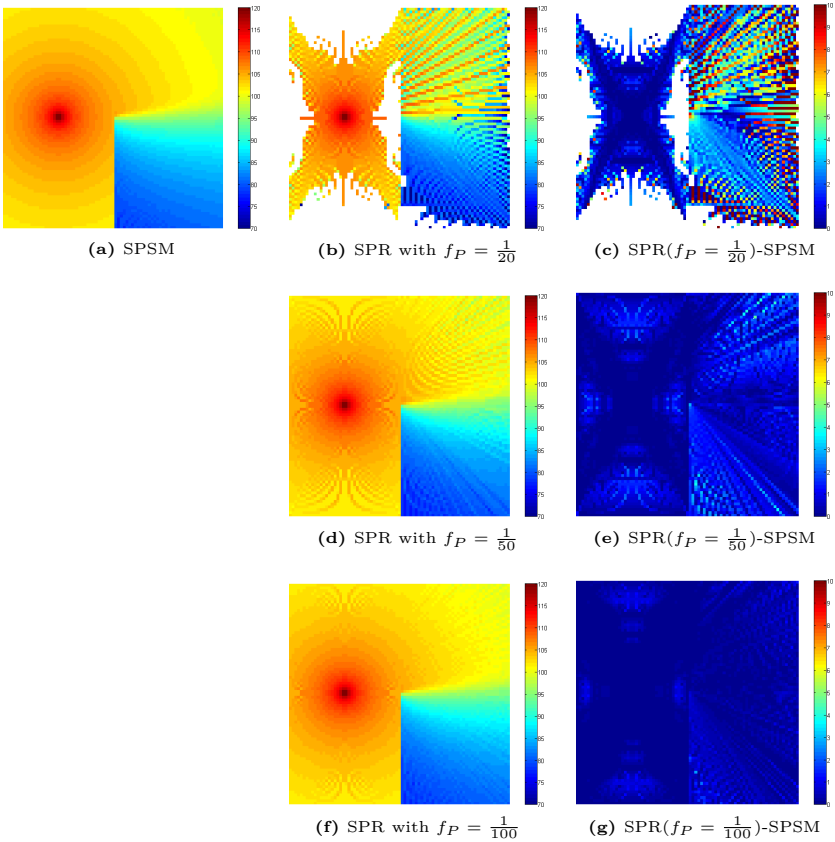

(a) SPSM **(b)** SPR with $f_P = \frac{1}{20}$ **(c)** SPR($f_P = \frac{1}{20}$)-SPSM

(d) SPR with $f_P = \frac{1}{50}$ **(e)** SPR($f_P = \frac{1}{50}$)-SPSM

(f) SPR with $f_P = \frac{1}{100}$ **(g)** SPR($f_P = \frac{1}{100}$)-SPSM

Figure 6.45.: The influence of the applied discretization in Sound Particle Radiosity on diffraction simulation compared with the Sound Particle Simulation Method for $f = 500Hz$.

The investigation of the numerical errors in the intensity maps is divided into three regions (see Fig. 6.44):

- *region0*: source-side (direct zone)
- *region1*: upper right (view zone)
- *region2*: lower right (shadow zone)

region0 No diffraction is computed, such that the intensity maps are completely identical for all frequencies (see appendix A.2.6). The sound intensity map reproduces the direct sound in case of the SPSM exactly. In case of the SPR (with discretization), sufficient results occur for $f_P = 1/50$ and $f_P = 1/100$. For smaller patches $l_P \approx 0.625m (f_P = 1/20)$, the size of the patches is larger than the receiver size, $w_{grid} = 0.1m$, such that the discretization of the sound particles to the patch centres results in receivers, which are not intersected by any sound particle. Even for $l_P \approx 0.25m (f_P = 1/50)$, this effect causes inaccuracies near the surfaces (see Sec. 6.5.2.3). This can be compensated by smaller patches or larger receivers.

region1 The same effect as in *region0* is noticed for $f = 16kHz$ (see appendix A.2.6). For this high frequency, the diffraction effect is very small, such that the sound particles are only transmitted through the VW. Thus, single (discretized) sound propagation paths are observable in case of too large patches. This effect decreases for lower frequencies, because the diffraction *smears* the energy among many secondary sound particles. They cover the receivers more homogeneous, such that for $f = 31.5Hz$ this effect is only hardly noticeable anymore.

region2 The error is more evenly distributed among all receiver points for almost all frequencies and patch sizes. The mean value increases significantly with the frequency (decreasing wavelength) due to the effect of a decreasing value of d. This effect can be reduced by decreasing patch sizes by the same argument.

To describe the discretization error on diffraction quantitatively, the average over the absolute difference of the intensity maps for all frequency bands (relative to the respective SPSM) is investigated only in *region2*. To achieve more generalizable results, this difference is shown in Fig. 6.46 as a function of the relative patch length per wavelength l_P/λ .

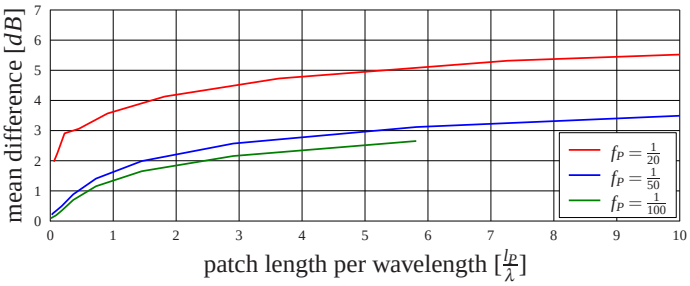

Figure 6.46.: Mean errors of the intensity maps in the shadow region computed with the Sound Particle Radiosity for different discretization parameters f_P as a function of the relative patch length l_P/λ.

The average error in simulations with $f_P = 1/100$ and $f_P = 1/50$ yield quite similar results for the same relative patch length l_P/λ. For $f_P = 1/20$, the numerical error of the receivers that detect no energy influences the average error too strong to extrapolate more information in that case. However, the behaviour is quite similar to both other functions, besides an offset of about $2dB$. For $f_P = 1/100$ and $f_P = 1/50$, the average error increases for larger patches, such that the effect of a wavelength dependent parameter d is proven.

As this effect is caused only by the patches on the VW, different discretization parameters for solid walls and VW could be introduced, such that a higher resolution is achieved for the VW. Furthermore, smaller patches near the edges and, thus, an unregular discretization of the surface, might be used to increase the accuracy.

6.8. Further Optimizations

As described in this chapter so far, the SPR is a very efficient simulation technique to simulate higher order diffractions and reflections, but the main problem of the SPR is the memory usage (see Sec. 6.5.2.2). Therefore, both the reduction of the memory requirement and the extension of the available memory are discussed briefly. Additionally, a technique to reduce the CT by computing identical sound propagation paths only once is introduced.

6.8.1. Elimination of Unused Reunification Matrix elements

The size of the RUM is the main bottleneck of the SPR, because it increases rapidly for higher accuracy. One solution to reduce the memory requirement of the RUM is to ignore matrix elements that are never used (see Fig. 6.47).

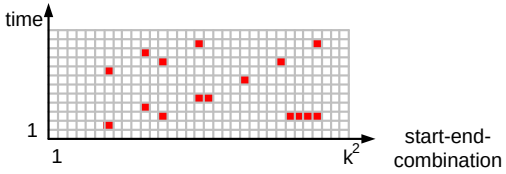

Figure 6.47.: Unused matrix elements of the Reunification Matrix. Unused elements are marked in *red*.

Candidates for those elements are, e.g., patch-patch combinations of the same surface, as sound particles can never start and end at the same surface. In addition, depending on the simulation parameters like the patch size f_P and the split-up degree S, invalid patch-patch combinations might occur. In either case, a mapping of theoretically possible matrix elements to geometrically reachable matrix elements is needed, which increases the memory requirement, but might be worth using.

6.8.2. Parallelization on a Computation Cluster

For more complex scenarios higher memory storage is needed, such that an extension to computer clusters is required[PWS13]. For an efficient usage, the RUM has to be divided into one RUM for each computer. These smaller RUMs reduce the memory requirement for each computer, although the total memory requirement remains constant. The bottleneck of these computation clusters is the communication between distributed

cluster nodes. Therefore, a good decomposition of the RUM is achieved by reducing the overall communication amount. To find an optimum decomposition, a graph of possible communications between matrix elements is needed. In this graph model, each *row* of the RUM (patch-patch-combination, see Sec. 6.6.1) is represented by a node and a possible communication between these nodes is indicated by an edge between them (see Fig. 6.48). An edgecut between nodes of different computers is equivalent to a communication between different nodes. The number of such edgecuts in that graph indicates the amount of computational overhead. For an example of eight matrix elements, two different decompositions are shown in Fig. 6.48.

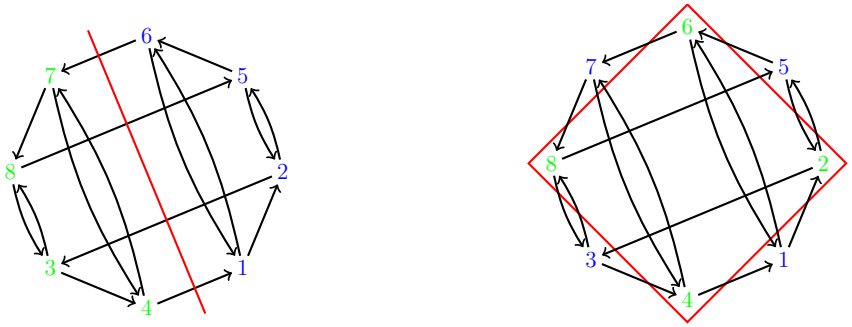

(a) 4 edgecuts **(b)** 16 edgecuts

Figure 6.48.: Two decompositions of eight matrix elements in a graph model.

Obviously, good and bad decompositions exist (in Fig. 6.48a:4, in Fig. 6.48b:16). From an algorithmical point of view, one solution to find a good decomposition is to investigate the communication between matrix elements [Win12]. From a physical point of view, however, geometrical information, e.g., the increased communication between parallel walls due to flutter echoes or the almost independent sound propagation of sound particles in distant sub-spaces, can be used.

6.8.3. Tracing of Sound Particles Simultaneously

In case of the SPR, the reunification rate and, thus, the efficiency can be increased by propagating multiple sound particles simultaneously. Due to the definition of the RUM, sound particles that are represented by one column (different absolute running times from the sound source) have the same sound propagation path (see Fig. 6.49).

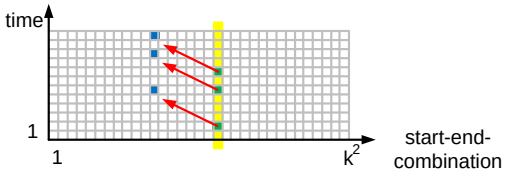

Figure 6.49.: Tracing sound particles with the same propagation path simultaneously. Matrix elements of sound particles with the same sound propagation patch are indicated in *yellow*.

As their sound propagation path (except the propagation time) is completely identical, the geometrical intersection test with the scene and the receivers has to be performed only once. Unfortunately, this method increases the overall memory effort, because sound particles are traced that do not fulfil the *oldest sound particle first* requirement, such that the cyclic RUM is increased in size.

6.9. Summary of Sound Energy Reunification

The reunification of sound energy carriers was presented for sound particles as well as for beams. Both reunification techniques were published by Stephenson before, but only theoretically without using any concrete implementation. Thus, details had to be worked out for both methods. A crucial question in the case of QPBT was the choice of the coordinate system, in which the starting points of beams were reunified. It was shown (see Sec. 6.4.1.2) that none of the former coordinate systems, i.e., a) a receiver concentric spherical coordinate system, b) a sound source concentric spherical coordinate system and c) the Cartesian coordinate system, were usable, such that a patch-related spherical coordinate system was introduced (see Tab. 6.1).

	radius proportional to propagation time	multiple sources	multiple receivers	adjustable grid size
sound source concentric spherical coordinates	✗	✗	✓	✓
receiver concentric spherical coordinates	✓	✓	✗	✓
Cartesian coordinates	✗	✓	✓	✗
patch concentric spherical coordinates	✗✓	✓	✓	✓

Table 6.1.: Comparison of different coordinate systems for the discretization of a beam's starting point in case of Quantized Pyramidal Beam Tracing.

Concrete implementations for the SPR and, using the new coordinate system, QPBT were presented for the first time (in $2D$). A detailed statistical comparison of both methods was performed and it was shown that the SPR was both more efficient and even more accurate than QPBT (see Sec. 6.5). Actually, QPBT failed totally. Four arguments were presented to prove this statement (see Tab. 6.2).

	Sound Particle Radiosity	Quantized Pyramidal Beam Tracing
errors do **not** cumulate	✓	✗
no detection of wrong paths	✗✓	✗
fewer number of sound energy carriers	✓	✗
lower memory usage	✓	✗

Table 6.2.: Comparison of both reunification techniques.

The statistical analysis was confirmed by numerical experiments, too.

For the preferred SPR, the efficiency was discussed resulting in a quantitative description of the reunification rate and an estimation of the required memory (see Sec.

6.6). This estimation contradicted to Stephenson's former estimation and the respective misassumptions were pointed out. It was shown analytically and numerically that the SPR prevented the exponential increase of the SPSM due to the split-up of sound particles (see Tab. 6.3).

	Sound Particle Radiosity	Sound Particle Simulation Method
prevents exponential increase of particles	✔	✗

Table 6.3.: Comparison of the increase of sound energy carriers.

It was shown that in non-diffuse sound fields, the RUM was occupied inhomogeneously, too. Thus, a higher effective reunification rate was observed. Although the memory requirement for the SPR was reduced compared to the case of QPBT, a very large amount of memory was still needed to obtain accurate results. To overcome this issue, an extension for computation clusters was presented.

Finally, the numerical errors that came from the discretization of sound particles were investigated for a) a simulation without scattering and diffraction, b) a simulation with scattering and c) a simulation with diffraction (see Sec. 6.7). The result was that the relative error in the reverberation time was almost independent of the discretization parameter f_P, whereas the relative error in the overall sound intensity and the relative error in a time interval decreased with smaller values of f_P. However, all three errors were almost independent of the maximum simulation time and the number of primary and secondary sound particles, as long as at least a few sound particles intersected with a patch (see Tab. 6.4).

	reverberation time	overall sound intensity	sound intensity in a time interval
independent of discretization parameter	✔	✗	✗
independent of maximum simulation time	✔	✔	✔
independent of number of sound particles	✔	✔	✔

Table 6.4.: Comparison of different coordinate systems for the discretization of a beam's starting point.

However, the patch size has to be adjusted for the given geometrical scene, the frequency and the desired accuracy of the results, but good results were achieved with a sufficient number of patches.

7. Transition to Three Dimensions

The former investigations of the convex sub-division, diffraction and the reunification of sound particles were restricted to $2D$ in order to discuss the principle effects with simplified geometrical considerations. However, real world scenarios are three dimensional problems, and some $2D$ test cases are only a special case of $3D$ scenarios (e.g., with vertical walls).

The analytical and statistical considerations of the chapters 4 – 6 are directly applicable to $3D$ (at least qualitatively), such that a detailed statistical analysis is left out in $3D$. The conclusions made in $2D$ with respect to an optimum diffraction module as well as the optimal reunification technique are *only* applied here (this is justified, as edge diffraction is mainly a $2D$ effect). A convex sub-division of a $3D$ environment has to be performed, before the Sound Particle Radiosity (SPR) is extended to $3D$. Finally, the diffraction module is extended to $3D$.

7.1. Convex Sub-Division

In analogy to the Geometrical Acoustic (GA) simulation methods in $2D$ (see chapter 3), a sub-division of the geometrical scene into convex subspaces (see chapter 4) is required in $3D$, too. The aim of this technique is again to achieve a sub-division into convex subspaces, such that the Computation Time (CT) is reduced and sound particles are automatically detected when they pass through a Virtual Wall (VW).

Unfortunately, the convex sub-division technique that was presented earlier (see Sec. 4.2) turned out to be by far more complicated in $3D$ than in $2D$, such that only the idea is presented in this section – the actual implementation has not been carried out yet. As a preliminary solution, an automatic sub-division based on Delaunay-triangulation[Si08] is then introduced, which results in a sub-division into convex tetrahedra. However, the resulting sub-division is not optimal for the application of the diffraction algorithms that were introduced earlier. But, with both methods, a subdivided scene can be assumed for the SPR method in $3D$. As an alternative, the user can sub-divide the scene manually and use it as input for the SPR. This section concludes with a short discussion of the speed-up in $3D$ (valid not only for the SPR, but for the Sound Particle Simulation Method (SPSM), too).

7.1.1. Convex Sub-Division Optimized for the Detection of Diffraction

The idea is to extend the method of convex sub-division from $2D$ (bisecting lines, see Sec. 4.2) to $3D$. Although the approach is not implemented yet, the idea is presented by the example of a simple geometrical scene as shown in Fig. 7.1a. In this scene, a single rectangular house (*brown* cube) is placed upon a single floor (*green* plane). Furthermore, five totally absorbent surfaces are added to create a closed polyhedron, which are not shown. However, the boundary edges of these surfaces are shown (*gray* lines).

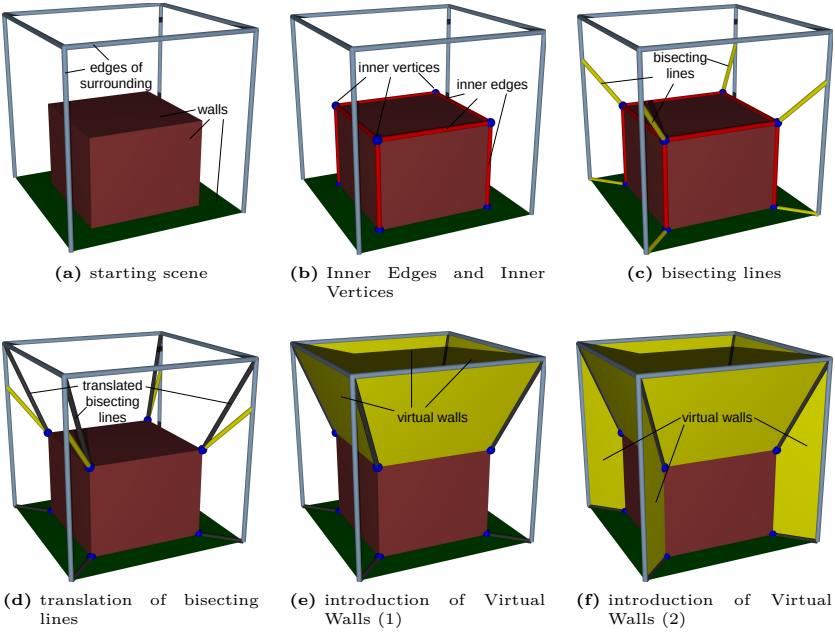

(a) starting scene

(b) Inner Edges and Inner Vertices

(c) bisecting lines

(d) translation of bisecting lines

(e) introduction of Virtual Walls (1)

(f) introduction of Virtual Walls (2)

Figure 7.1.: Extension of the convex sub-division to $3D$.

Inner Edges (IEs) have to be identified (by some vector operations) first between surfaces (which are lines instead of points as in $2D$). These are shown in Fig. 7.1b (*red* lines). Due to the higher dimension of the IEs, Inner Vertices (IVs) (*blue* spheres) are the intersection points of these IEs. Furthermore, the starting points and the end points of the IEs, which are not connected to other IEs, are defined as IVs, too.

Now, the bisecting lines of the IVs have to be constructed. To compute them, only the flanking walls of the IVs are taken into account (see Fig. 7.1c, *yellow* lines). The bisecting lines can either be inside a surface (lower IVs in Fig. 7.1c) or traversing the space (upper IVs in Fig. 7.1c). The intersection points of these bisecting lines with the scene can be computed by intersection tests.

As the intersection points of the bisecting lines with the other room surfaces introduce, in general, additional vertices to the scene, a translation to an already existing vertex of the intersected surface is carried out. Like in the $2D$ case, the vertex is chosen that adds the smallest change of angle compared to the bisecting line (see Fig. 7.1d, *gray* lines).

In a final step, VWs are introduced in-between the translated bisecting lines (see Fig. 7.1e, 7.1f, *yellow* planes). These VWs are often close to the bisecting planes on the IEs. In some cases, however, the bisecting lines spanning the VW are not *in plane*, such that the introduced VW has to be superimposed by multiple VWs. This implies a more complicated algorithm, which has to be worked out. Stephenson roughly proposed a $3D$ convex sub-division[Ste03a] based on the idea in Sec. 4.1.4, but the same disadvantages are valid for $3D$, too.

Although not implement yet, the convergence of this algorithm is obvious, because

in each step one IE is removed. Hence, the scene is convex when neither IVs nor IEs remain.

7.1.2. Convex Sub-Division Based on the Delaunay-Triangulation

As the presented sub-division technique is not implemented yet, an alternative is used to test the SPR (besides a manual sub-division). As an example, the boundary conforming Delaunay mesh generation[Si08] is chosen. This theory is mainly used for the generation of meshes to solve differential equations of, e.g., finite element methods. The result is a sub-division into a huge number of tetrahedra, i.e., convex volumes in $3D$ described by exactly four vertices and four planes. No additional vertices are introduced into the scene, but the simple form of the volume requires a huge number of convex sub-spaces and, thus, a huge amount of VWs. To create these meshes, the freely available library *TetGen*[Si11] is used in this work to perform these sub-divisions (see Fig. 7.2).

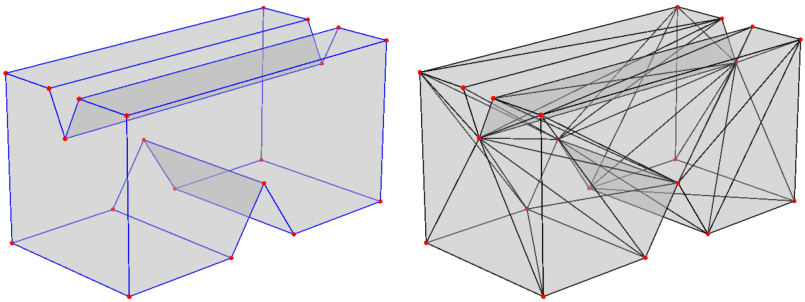

(a) initial setup with 20 vertices and 12 surfaces

(b) 29 sub-spaces with still 20 vertices

Figure 7.2.: Convex sub-division by *TetGen* (after [Si08]).

Although all scenes are computable by this library, the first method should be preferred in later implementations, as it is optimized for the detection of diffraction and the number of VWs is reduced.

7.1.3. Applicability of the Speed-Up

In Sec. 4.3 it has been shown that the CT of the SPSM with convex sub-division is independent of the number of walls or vertices of the scene, but dependent on a shape factor q (see Eqn. 4.9). The same considerations are made in $3D$ with the Mean Free Path Lengths (MFPLs) [Kos60] of $4 \cdot \frac{V}{S}$ in $3D$ instead of $\pi \cdot \frac{S}{C}$ in the $2D$ case. The overall surface S of the scene with volume V is extended by the surface of the VWs S_{VW}, such that the shape factor q reads

$$\frac{l_{nc}}{l_c} = \frac{4 \cdot \frac{V}{S}}{4 \cdot \frac{V}{S+S_{VW}}} = 1 + \frac{S_{VW}}{S}. \tag{7.1}$$

Regarding Eqn. 7.1 instead of Eqn. 4.7, it is clear that the sub-division by the tetrahedra is not perfect, because the surface of the additional walls S_{VW} is very large.

7.2. Sound Particle Radiosity

The algorithm of the SPR method in $3D$ is similar to the $2D$ case. Especially the core of the SPR, namely the Reunification Matrix (RUM), stays completely unchanged. As the processing of the RUM remains unaffected, the investigations of the reunification probability (see Sec. 6.6.1) are directly applicable to $3D$. Thus, only the geometrical computations of the sound propagation between two surfaces that are based on the SPSM, have to be modified. Even the algorithms of List. 6.1 and List. 6.2 are valid.

The emission of sound particles as well as the computation of the wall intersection points are mostly known. In the following, the split-up of sound particles and the discretization of the surface into patches are described in more detail. Furthermore, the detection of sound particles by weighting the inner crossing distance is extended to $3D$.

7.2.1. Emission of Sound Particles

For both the SPSM and ray tracing techniques, an omnidirectional emission of sound particles from a source point is a problem, because the sphere cannot be subdivided in equally sized and shaped surface elements except for the platonic bodies. This can be handled either by a deterministic or a stochastic model. Stephenson presented a combination of both models[Ste85]. The complexity to construct the direction vectors is in the same order of magnitude in $2D$ and in $3D$[Mar72] in case of a stochastic model.

However, in this work, a deterministic SPR is aimed at, such that no random numbers are used to compute the distribution of sound particles. The reason is that the same distribution is used for the emission of secondary sound particles by the split-up of sound particles of both scattering and diffraction. The problem is that not only N direction vectors for each such particle have to generated but the solid angle ranges have to be described analytically, too. For this purpose, the recursive zonal sphere partitioning[Leo07a] yields a sub-division of the unit sphere into N equally sized (not shaped) solid angle ranges (see Fig. 7.3).

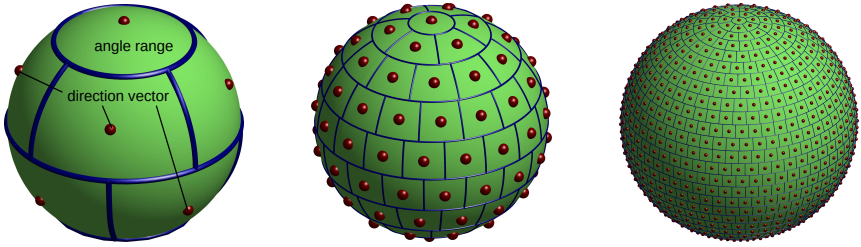

(a) $N = 10$ **(b)** $N = 100$ **(c)** $N = 1000$

Figure 7.3.: recursive zonal sphere partitioning for different N. The *green* surfaces define the angles ranges to the respective direction vector in *red* (after [Leo07a]).

These solid angle ranges are defined in spherical coordinates, where the region of each sound particle i around its direction vector v_i is defined within

$$\begin{aligned} \vartheta_{Min,i} &< \vartheta < \vartheta_{Max,i} \text{ and} \\ \varphi_{Min,i} &< \varphi < \varphi_{Max,i}, \end{aligned} \tag{7.2}$$

such that the whole solid angle reads

$$\int_{\varphi_{Min,i}}^{\varphi_{Max,i}} \int_{\vartheta_{Min,i}}^{\vartheta_{Max,i}} d\Omega = \Delta\Omega \approx \frac{4\pi}{N}. \tag{7.3}$$

Both the angle ranges and the direction vectors are computed by the *EQSP Toolbox*[Leo07b].

Although this distribution is not optimum with respect to the shape of the solid angle ranges, the benefit of well defined, orthogonal integration boundaries compensates this disadvantage, since Eqn. 7.3 has to be solved for different distributions in case of scattering or diffraction later.

7.2.2. Wall Intersection Test

To find the valid intersection point of a sound particle with the geometrical scene, four criteria have to be tested in general (see Fig. 3.6). Due to the restriction to convex subspaces by the convex sub-division, only two of these criteria have to be verified to determine the valid intersection point.

As the *point-in-polygon* test is much more complex in $3D$, the closest intersection point instead of the *point-in-polygon* is computed in addition to the test whether the polygon is intersected from the inside.

The distance of the sound particle to the surface in direction of propagation is determined by the Hesse normal form. It is valid for any point $\vec{x}$ in the plane, whenever $\vec{P}$ is an arbitrary point within the surface

$$\left[\vec{x} - \vec{P}\right] \circ \vec{n} = 0. \tag{7.4}$$

The distance d from the sound particle's starting point $\vec{S}$ to the intersection point $\vec{I}$ is found (assuming all direction vectors are in unit length) by solving

$$\left[\left(\vec{S} + d \cdot \vec{v}\right) - \vec{P}\right] \circ \vec{n} = 0. \tag{7.5}$$

The intersection point $\vec{I}$ is computed by

$$\vec{I} = \vec{S} + d \cdot \vec{v}. \tag{7.6}$$

The distances to all walls of the convex room, which are intersected from the inside, are computed, and the intersection point with the minimum distance is chosen as valid intersection point (see List. 7.1).

```
Vec I // container for intersection
float dMin = 1000.000f; //initialize distance with large value
for (all walls)
  I = findCurrentIntersection(); // see Eqn. 7.7,7.8
  if(n * a > 0) // see Eqn. 3.7
    if(d < dMin) //see Eqn. 3.10
      IMin = I;
      dMin = d;
```

Listing 7.1: Pseudocode for the determination of a wall intersection.

7.2.3. Wall Interaction

To determine the interaction of a sound particle with a wall, it has to be distinguished between a real wall and a VW. In case of a real wall, the sound particle is split-up due to scattering (for the scattering coefficient $\sigma > 0$, see Sec. 2.3.3), whereas the sound particle is split up due to diffraction in case of a VW.

In either case, a number of S equally distributed sound particles is emitted. Their direction vectors are independent of the angle of incidence and, thus, computed by the same principle as the emission of primary sound particles. However, the direction vectors are distributed only on a half sphere with $0 < \vartheta < \pi/2$.

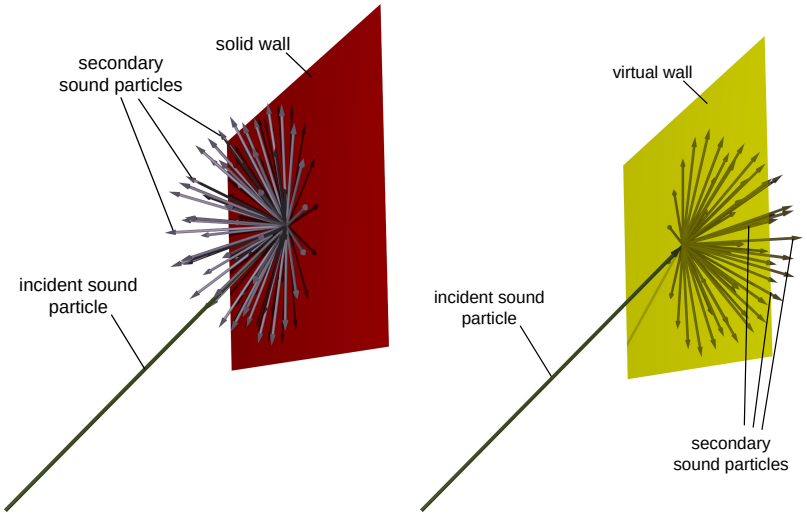

(a) scattering (solid wall) **(b)** diffraction (Virtual Wall)

Figure 7.4.: Split-up of sound particles in equally distributed secondary sound particles.

Scattering The coordinate system of the half sphere is chosen, such that the direction vectors point into the convex room and the origin is equal to the intersection point (see Fig. 7.4a). The boundaries ϑ_{Min},ϑ_{Max},φ_{Min},φ_{Max} of each angle range i are defined in the same (rotated) coordinate system, where the centre vector points in direction of the inverse surface normal. The relative energy e_i of each secondary sound particle with index i reads with air attenuation m, the absorption degree α and the travel distance since last intersection r (compare Eqn. 2.22, 3.16 and 7.3)

$$e_i = e^{-mr} \cdot (1-\alpha) \cdot \sigma \int_{\varphi_{Min}}^{\varphi_{Max}} \int_{\vartheta_{Min}}^{\vartheta_{Max}} \frac{cos(\vartheta)}{\pi} d\Omega. \tag{7.7}$$

In addition to the S secondary sound particles, a sound particle with the specularly reflected energy is emitted in the specularly reflected direction with an energy amount of

$$e_0 = e^{-mr} \cdot (1-\alpha) \cdot (1-\sigma). \tag{7.8}$$

Diffraction When a VW is intersected, the sound particles are transmitted through the VW (see Fig. 7.4b).

The determination of each sound particle's relative energy is computed similar to Eqn. 7.7 (compare Eqn. 5.19) by an integration over the solid angle the sound particles represents

$$e_i = e^{-mr} \cdot \int_{\varphi_{Min}}^{\varphi_{Max}} \int_{\vartheta_{Min}}^{\vartheta_{Max}} D^* \left(S_{AP}, \vec{I}, \Omega_1, \Omega\right) d\Omega, \tag{7.9}$$

where $D^* \left(S_{AP}, \vec{I}, \Omega_1, \Omega\right)$ is the $3D$-Diffraction Angle Probability Density Function (DAPDF), i.e., the Diffraction Angle Probability Function (DAPF) derived by the solid angle

$$D^* \left(S_{AP}, \vec{I}, \Omega_1, \Omega\right) = \frac{\partial DAPF}{\partial \Omega}. \tag{7.10}$$

In general, it depends on the aperture S_{AP}, the intersection point $\vec{I}$, the direction of incidence Ω_1 and the outgoing direction Ω (each consisting of a polar and an azimuth angle). This $3D$-DAPDF is derived in Sec. 7.3.

7.2.4. Discretization of the Surface into Patches

The discretization of any wall into patches can be handled in different ways. One attempt is to perform a triangulation of the wall into triangles by a refined Delaunay triangulation[She96] (see Fig. 7.5a). An efficient version is Triangle[She05].

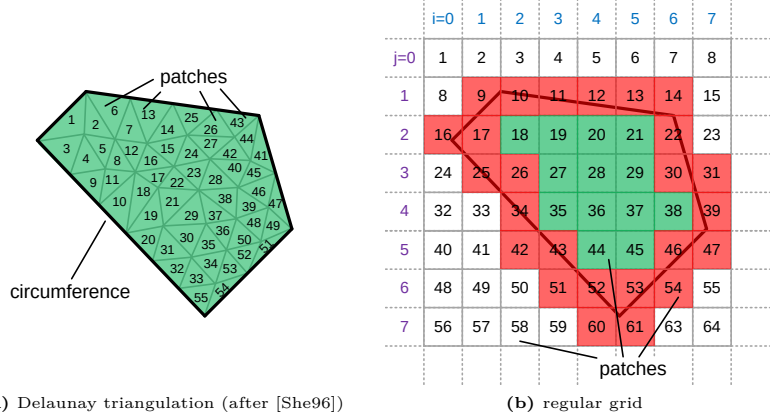

(a) Delaunay triangulation (after [She96]) **(b)** regular grid

Figure 7.5.: Different techniques defining patches on a surface.

This approach describes the split-up of the surface in equally sized triangles, such that the complete surface is covered without overlap. For the discretization, the triangular patches are numbered linearly. Although this concept fits any arbitrary surface exactly, the computation of a Patch Identification Number (patchID) is very complicated. The dediscretization, i.e., the computation of each triangle centre from the respective patchID, is complex, too. Thus, a more simplified method is used in this work.

This simplification is achieved by placing a linear grid to discretize the surface in a pre-defined, arbitrary $2D$ wall coordinate system (see Fig. 7.5b). In the example above, a grid of $8x8$ patches is constructed to cover the complete surface. The computation of the patchID is performed by using the same linear numbering technique as in $2D$ for both indices i and j (see Sec. 6.3.2.1). Both are combined to a single number as shown in Fig. 7.5b. Defining the surface of these patches as $l_P \cdot l_P$, the simulation parameter $f_P = l_P/\overline{l}$ describes the size of a patch in one dimension. Due to the simple technique, three different patch types exist that have to be handled differently.

Completely covered patches (*green*) The first group of patches is completely covered by the surface. Every intersection point can be directly converted to a patchID and this patchID is dediscretized to the patch's centre $[(i + 0.5) \cdot l_P, (j + 0.5) \cdot l_P]$.

Partly covered patches (*red*) The discretization of the intersection points on these patches is equal to the discretization of the completely covered patch. However, intersection points outside the surface are geometrically not possible, such that the centre of the patch (where the intersection point has to be shifted to) is adjusted to the centre of gravity of the remaining patch surface. The patch surface of these patches is smaller. In an actual simulation, theses patches are a minor part of all patches. Thus, the additional computational effort to adjust the intersection point during simulation is neglectable compared to the effort by Delaunay triangulation.

Not covered patches (*white*) In general, some patches are completely outside the wall. The discretization of intersection points is not needed, because no intersection point outside the wall can occur. The geometrical simulation is independent of these patches, but a huge number of unreachable patches in the RUM cause an increased CT. Thus, a mapping is used to skip these patches.

7.2.5. Detection

The spatially extended receivers are volume detectors with volume V_D instead of surface detectors in $2D$. Thus, the energy density is given by the detected energy E_D per volume

$$I = c \cdot w = c \cdot \frac{E_D}{V_D}. \tag{7.11}$$

With the inner crossing distance of a sound particle within a volume of the detector w_i, the sound particle detection formula reads (with the same derivation as in Sec. 3.4.4)

$$I = \frac{P}{N \cdot V_D} \sum_{i=1}^{N_0} e_i \cdot w_i, \tag{7.12}$$

where P is the sound power, N and N_0 the number of emitted or detected sound particles, respectively.

Like in $2D$, the detected sound intensity is independent of the shape of the detector. Spherical detectors are used, whenever a moderate number of receivers are used. The inner crossing distances are shown in Fig. 3.7. Cubical receivers are used when the area of interest is an array or a matrix (see Fig. 3.9).

7.3. Uncertainty relation Based Diffraction

The Uncertainty relation Based Diffraction (UBD) module is based on the Fraunhofer diffraction at a slit as well as the uncertainty relation. Both physical principles are valid, of course, in $3D$, such that the extension of the UBD to $3D$ is conducted consequently.

The main goal of a UBD module in $3D$ is that the module has to be applicable to apertures of arbitrary shape instead of only a slit, like in $2D$. Also its results in a $2D$ cross-section should be identical to the former $2D$ experiments, as these were interpreted as a specialization of diffraction in three dimensions.

In this section, different concepts on extending the UBD to $3D$ are discussed. The actual $3D$-DAPDF is derived analytically based on the preferred concept. Then, an analytical formulation of the transmission level by diffraction through an arbitrarily shaped aperture is derived based on a fictive SPSM (without discretization). The extension of the $2D$-DAPDF to $3D$ is a crucial point, because different definitions of the $3D$-DAPDF are possible, such that conversions are derived. This aspect is discussed in more detail. A validation of the $3D$-UBD is achieved by evaluating the analytical equation for the former $2D$ experiments to ensure compatibility. Some extended $3D$ scenarios are validated by the wave theoretical Secondary Source Model (SSM). Due to a lack of a full implementation of this diffraction module in the SPSM, the influence of reflections or the discretization cannot be discussed yet.

7.3.1. Concepts of 3D diffraction

In this work, the diffraction in $3D$ is defined as the diffraction through an (arbitrarily shaped, but polygonal) opening in a wall. This opening is represented by a VW. This definition correspondents to the derivation of the UBD by Fraunhofer diffraction through an aperture. However, the second basis of the UBD is the uncertainty relation. Even in $2D$, the discussion of the reciprocity principle showed that the definition of the uncertainty in *position* (i.e., the by-pass distance a) is questionable. This definition becomes even more arguable as the $3D$-DAPDF is a function of two dimensions. Thus, the definition of uncertainty or, in other words, the definition of the Edge Diffraction Strength (EDS) is discussed.

Six concepts are briefly presented, of which the last is proposed by Stephenson[SS07]. Due to the convex sub-division, it is assured that the apertures are convex, too. As the UBD is applied to sound particle diffraction, the diffraction of a single sound particle is observed that intersects with the opening at an arbitrary position. Of course, the final transmission level is the superposition of all sound particles that intersect with the aperture. The aperture is, so to say, *sampled* by the SPSM (as in $2D$ a line above the wedge).

7.3.1.1. Whole Circumference

The first concept is to take the complete circumference of the opening into account. The idea is shown for an arbitrary opening with $n = 7$ vertices in Fig. 7.6. An intersection point of the current sound particle is marked in *red*.

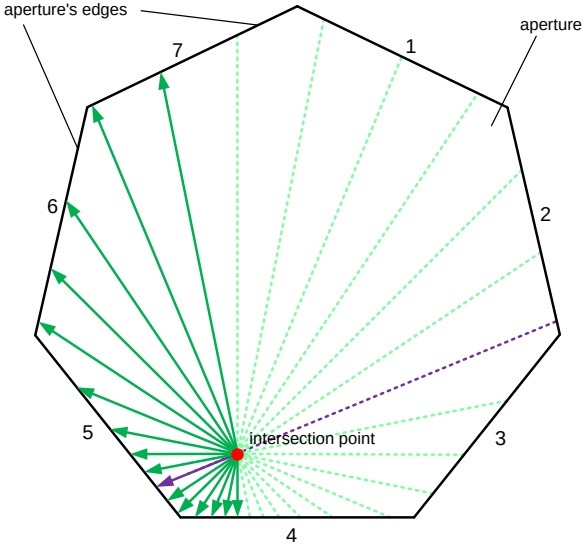

Figure 7.6.: Sampling of the aperture's circumference in steps of constant angle.

In this concept, the aperture itself is sampled for each sound particle that intersects with the aperture. Therefore, a number of cross-sections h is defined that start from the intersection point (*red*) in equally distributed angles $\Delta\alpha = \pi/h$. For each cross-section h ($h = 16$ in Fig. 7.6), their intersection points with the aperture's edges are determined. Since both distances to the aperture on this line, e.g., the *purple* line, are taken into account, only half of the angles are considered. The EDS is computed for every cross-section independently, such that h EDSs (uncertainties) are derived in total. These EDSs are defined in the current direction (*green* ray). On this line, e.g., the *purple* line, both distances to the aperture are taken into account, such that actually the EDS of a slit is computed (see Eqn. 5.34) for each line. Corresponding to these lines, a plane is constructed perpendicular to the surface for each cross-section. The angle of incidence ε_1 inside each plane is considered to independently compute a $2D$-DAPDF for each cross-section, such that the results of this concept is a number of h $2D$-DAPDFs. The $2D$-DAPDFs are superposed in a three dimensional space by a projection of each $2D$-DAPDF into the respective plane that belongs to the EDS. The transition to an infinite number of cross-sections $h \to \infty$ results in a homogeneous distribution of the $3D$-DAPDF.

The benefit of this concept is that the exact same EDSs as in $2D$ are used and the simultaneous diffraction at multiple edges is handled. Furthermore, the convergence for a circular aperture (a polygon with an infinite number of vertices) is possible.

On the other hand, the accordance to the $2D$ diffraction is doubtful, because sound particles passing by a single edge are diffracted in all directions. Besides this disadvantage, the CT of this concept is very high, because an integral over the complete aperture has to be performed for each diffracted sound particle. It is hard to estimate, which number of cross-sections h is sufficient.

As this concept cannot result in an efficient simulation, it is discarded.

7.3.1.2. Edges of Circumference

In order to reduce the computational effort of the former concept, the number of cross-sections h is reduced to the number of vertices n and, thus, edges, of the aperture (see Fig. 7.7). A physical reason for this concept is that the uncertainty is given by the distance to the edge, which is handled explicitly for each edge. This distance is constant for the whole edge.

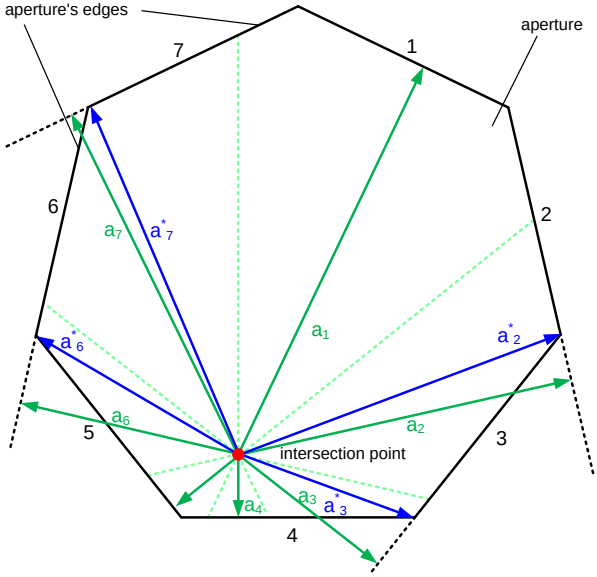

Figure 7.7.: Sampling all edges of the aperture's circumference.

The computation of the $3D$-DAPDF is similar to the former concept, but the number of cross-sections h is reduced ($h = n = 7$ in Fig. 7.7). For each edge of the aperture, an EDS is constructed including both the distance to the current edge and the distance in opposite direction to maintain compatibility with the $2D$ approach. A superposition of the $2D$-DAPDFs, which are computed from these EDSs, yields the $3D$-DAPDF.

The main benefit of this concept is that the compatibility to $2D$ is given, because in case of the respective cross-section, the resulting $3D$-DAPDF is identical to the former $2D$ DAPDF. Another benefit is that the CT is reduced, because the number of dimensions is restricted to the number of edges of the aperture.

However, the consideration of the opposite by-pass distance can be questioned, because more complicated cases can occur. Whenever two edges of the aperture are exactly parallel, two interpolation planes collapse to one, whereas they are independent interpolation planes for the $3D$-DAPDF if they differ by an infinitesimally small angle. A second critical case is when the point of the closest distance between the edge and the intersection point is not within the circumference of the aperture (see intersections with *dotted black* lines in Fig. 7.7). In these cases, two closest distances, e.g., a_6 (the closest

distance to the infinite line) or a_6^* (the distance of the closest vertex), are possible and even the plane might be constructed with either the *blue* or the *green* ray in Fig. 7.7. The major disadvantage of this concept is revealed by very small edges of the aperture. Any edge, however small it is, adds an interpolation plane by an own $2D$-DAPDF to the construction of the $3D$-DAPDF. If the edge is removed from the aperture (as a thinking experiment), the interpolation plane with this edge vanishes, such that the $3D$-DAPDF behaves differently. Due to these physical discrepancies, the advantages cannot be compensated. Hence, this concept is discarded, too.

7.3.1.3. Closest Edge

From a computational point of view, the simplest concept is to take only the closest edge of the aperture into account. This was proposed by Heinisch[HC71] for optical ray diffraction[FGH99], where it is justified since the aperture is large compared to the wavelength λ. This photon diffraction model is based on Gaussian functions, but very good agreements with the diffraction pattern at a circular aperture were found.

The concept to use only the closest edge is depicted in Fig. 7.8.

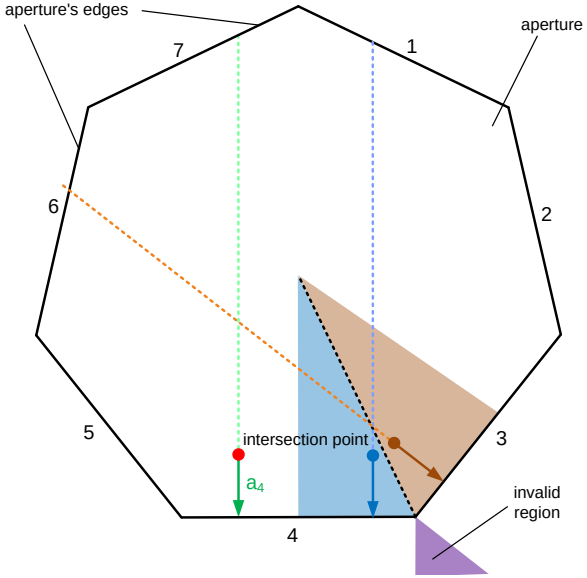

Figure 7.8.: Considering only the closest edge between the intersection point and the aperture's circumference.

When only the closest edge is taken into account, the EDS and $3D$-DAPDF can be computed as in the $2D$ case. The result of this concept is still a $2D$ DAPDF (in direction of the closest edge) and, hence, sound particles are diffracted in a plane. Nevertheless, it is possible to take the opposite distance into account, but this is not consequent with respect to the consideration of only the closest edge[a)].

[a)] For self-consistency with the slit experiment, Stephenson found the constant in Eqn. 5.10 to be 4 instead of 6 if only one edge is considered[Ste08]

As in the previous concept, it is highly probable that this concept ends up with the same results as in $2D$, because this time even more similarities with the $2D$-diffraction are noted. Furthermore, the CT is not only reduced by the fast computation of the by-pass distance but also by the emission of secondary sound particles only in a plane.

The disadvantage of this concept is, however, caused by exactly this emission of secondary sound particles in a plane. When considering not only one but all sound particles that intersect with the aperture, sound particles are diffracted in as many planes as the aperture has edges. Discontinuities occur for sound particles, which are close to two edges. As shown in Fig. 7.8, sound particles that intersect the *blue* surface are diffracted in the *blue* direction, whereas sound particles that intersect with the *brown* surface are diffracted in the *brown* direction. No sound particles are diffracted in direction of the *purple* region. Thus, no energy is detected at any chance in this region. The good results for diffraction around a circular disc [FGH99] can therefore only be explained by the complete disappearance of these regions for $n \to \infty$. For a smaller number of vertices, however, strong discontinuities occur and prevent a steady sound distribution.

As this is a decisive factor, this concept is abandoned, too.

7.3.1.4. Closest and Perpendicular Edge

To avoid the region with no diffracted energy that appeared in the previous concept, additional diffraction in the direction perpendicular to that direction is performed (two uncertainties, see Fig. 7.9).

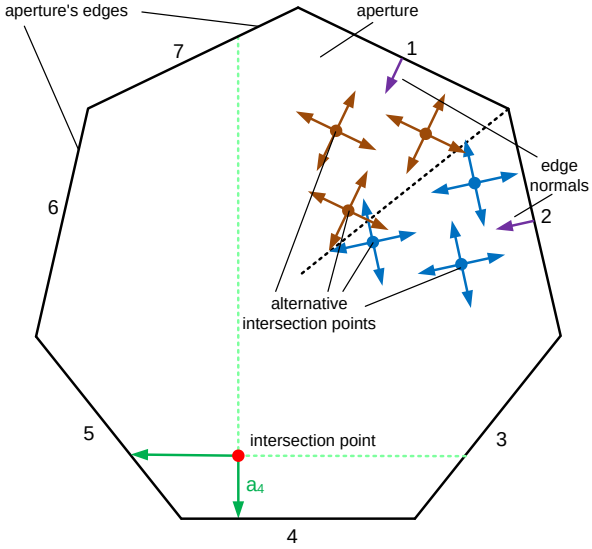

Figure 7.9.: Considering only the closest edge (here: distance a_4) and the perpendicular axis.

By this definition, the resulting $3D$-DAPDF for one sound particle diffracts sound

particles into the complete space instead of in a single plane. This $3D$-DAPDF is composed by the superposition of two $2D$-DAPDFs. In contrast to the former concepts, the interpolation with this concept is by far simpler, because both diffraction planes are perpendicular to each other and there are only two instead of h or n planes.

The advantages of this concept are that the EDSs as well as the $2D$-DAPDFs are equal to the $2D$ diffraction case, and the CT is reduced due the computation of only two $2D$-DAPDFs. Furthermore, the discontinuities of the former concept are compensated.

However, still boundaries exist at which the coordinate systems are rotated (see Fig. 7.9, difference between *blue* and *brown* coordinate systems), such that singularities are possible.

Nevertheless, this is the most preferable concept and is used first, but a variation of this concept is presented in the following.

7.3.1.5. Arbitrary and Perpendicular Edge

This concept in quite identical to the former concept, but the perpendicular coordinate system is independent of the aperture and the sound particle's intersection point, respectively (see Fig. 7.10).

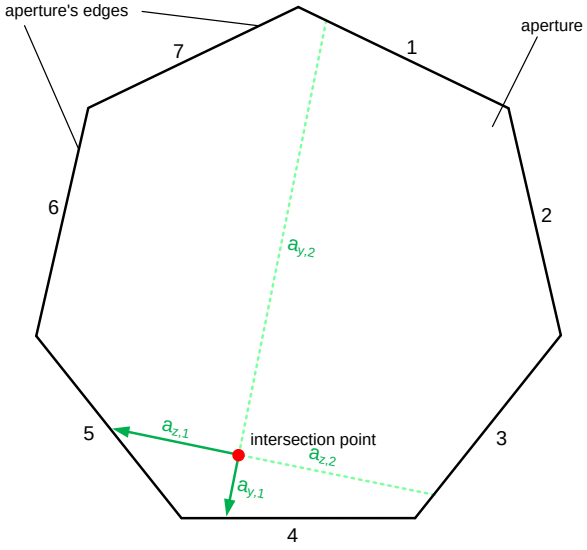

Figure 7.10.: Considering two arbitrary, but perpendicular axes.

In contrast to the previous concept, the by-pass distance is defined as closest distance ($a_{y,1}$ in Fig. 7.10) in an arbitrary direction. The perpendicular direction is computed as before including the perpendicular distance ($a_{z,1}$ in Fig. 7.10). Both concepts are identical for a rectangular aperture, whenever the arbitrary coordinate system is along the axes of the rectangle.

This concept is even simpler and the last mentioned disadvantage of the different coordinate system vanishes.

But, due to this arbitrary coordinate system, the computed distances are not the closest distances anymore (the relation to the *uncertainty* is doubtful). This might introduce large errors in contrast to the former, more physical definition. However, it will be shown in Sec. 7.3.5.2 that these errors are smaller than expected.

7.3.1.6. Vectorial Addition of Edge Diffraction Strengths

A basic idea of Stephenson[Ste85, SS07] is that the EDS is a vector (like the attractive force of electrons). The last concept is based on the idea (already described in Sec. 5.2.1) to add up the EDSs of different edges. Therefore, each edge is taken into account as shown in Fig. 7.11.

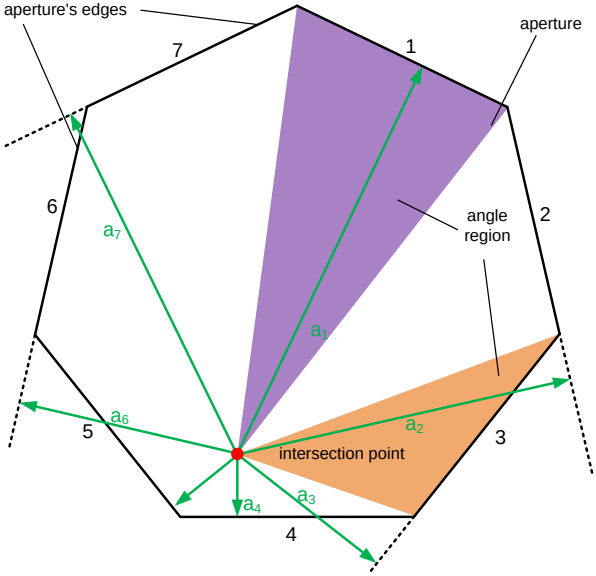

Figure 7.11.: Adding Edge Diffraction Strengths of each edge vectorially.

The idea is to compute a scalar EDS for each edge like in $2D$ and multiply these EDSs with the direction vector pointing from the intersection point to the current edge. These vectorial EDSs are added up and the result is a single EDS including an averaged direction. The physical reason for this is to add the *attractions* of each wedge. A variant of this concept is to weight each vectorial EDS with the angle of the edge that is visible from the intersection point (e.g., *purple* and *orange* area in Fig. 7.11.) The resulting EDS is used to create a $2D$-DAPDF as in concept 7.3.1.3, which is applied in a plane constructed by the direction of added EDS and the surface normal.

With both variants, the invalid regions of concept 7.3.1.3 are compensated and a low computational effort is achieved, but the main problem of concept 7.3.1.2 remains, i.e., the partial EDS of one edge might not point to the actual edge (the direction a_3 in Fig. 7.11 is outside the *orange* angle region). A more critical problem of this concept is that the EDS of a rectangular aperture that is intersected in the centre results in an EDS of 0, because the partial EDSs compensate each other due to the symmetrical

setup. In case of a single wedge, the introduction of an additional edge in opposite direction would **reduce** the EDS instead of increasing it like in the $2D$ case. All ideas that delivered good results in $2D$ regarding the superposition of EDS would become invalid, such that this concept is discarded, too.

Finally, the concepts of Sec. 7.3.1.4 and Sec. 7.3.1.5 remain. In the following, these concepts are further investigated and the final choice is made after the error of the arbitrary rotation is quantified.

7.3.2. The derivation of the 3D Diffraction Angle Probability Density Function

Different definitions of a $3D$-DAPDF are possible. Since the UBD is based on the uncertainty relation, first the uncertainties have to be defined. Based on the $2D$-approach, where the uncertainty of *position* A is related to the uncertainty of *momentum* in direction of A (see Eqn. 5.5), an additional assumption has to be made for the uncertainty of *position* B in relation to the uncertainty of *momentum* in direction of B

$$\begin{aligned} \Delta A \cdot \Delta p_A &\approx \hbar \\ \Delta B \cdot \Delta p_B &\approx \hbar, \end{aligned} \tag{7.13}$$

which have to be valid at the same time. Without loss in generality, the $A-$ and $B-$ direction vectors are both lying in the $y-z-$ plane, but not necessarily the identities $A \hat{=} y$ and $B \hat{=} z$ have to be valid, as these coordinate systems can be rotated against each other. Nevertheless, these equations are defined in perpendicular planes (both have the $x-axis$ in common). According to the UBD in $2D$, each of these equations corresponds to a pair of perpendicular $2D$-DAPDFs and EDSs. The $3D$-DAPDF is computed by multiplying the two $2D$-DAPDFs in perpendicular planes, as the probabilities multiply. Therefore, an additional diffraction angle η is introduced that diffracts sound particles in the perpendicular plane compared to ε (see Sec. 5.2). With the DAPF, the result of such a multiplication is

$$\frac{\partial DAPF}{\partial \varepsilon} \cdot \frac{\partial DAPF}{\partial \eta} = D_A\left(\varepsilon, b_A\right) \cdot D_B\left(\eta, b_B\right) = D\left(\varepsilon, \eta, b_A, b_B\right) = \frac{\partial^2 DAPF}{\partial \varepsilon \partial \eta}. \tag{7.14}$$

This idea is also directly based on the Fraunhofer diffraction, where the $si-$ functions for the $y-$ and the $z-$ directions are multiplied, because they are orthogonal/independent to each other (see Eqn. 2.44).

It has to be noted that this definition of the $3D$-DAPDF differs from the definition of Eqn. 7.10. Although the DAPF itself is identical, their derivations are not, because

$$\frac{\partial DAPF}{\partial \Omega} \neq \frac{\partial DAPF}{\partial \varepsilon} \cdot \frac{\partial DAPF}{\partial \eta} = \frac{\partial^2 DAPF}{\partial \varepsilon \partial \eta} \tag{7.15}$$

and, more precisely,

$$\partial \Omega \neq \partial \varepsilon \partial \eta. \tag{7.16}$$

The difference between these definitions and a conversion between them is presented in Sec. 7.3.4. The rest of this section assumes the $3D$-DAPDF defined as in Eqn. 7.14.

In order to reduce the computational effort and keep the analogy to the $2D$-derivation, the analytical considerations are restricted to the simpler $2D$-DAPDF $D_b\left(\varepsilon, b\right)$ (see Eqn. 5.15). Two $2D$-DAPDFs are derived for the diffraction in two dimensions A and B

$$\begin{aligned} D_A\left(\varepsilon, b_A\right) &= \frac{D_{0,A}}{1 + 2 \cdot u^2} \text{ with } u = 2 \cdot b_A \cdot \varepsilon \text{ and} \\ D_B\left(\eta, b_B\right) &= \frac{D_{0,B}}{1 + 2 \cdot v^2} \text{ with } v = 2 \cdot b_B \cdot \eta, \end{aligned} \tag{7.17}$$

where $b_{A,B}$ are the *effective* slit widths in the respective directions. The multiplication of these $2D$-DAPDFs results in the $3D$-DAPDF with a general normalization constant $D_0 = D_{0,A} \cdot D_{0,B}$

$$D(\varepsilon, \eta, b_A, b_B) = D_A(\varepsilon, b_A) \cdot D_B(\eta, b_B) = \frac{D_0}{(1 + 2 \cdot u^2)(1 + 2 \cdot v^2)}. \tag{7.18}$$

This $3D$-DAPDF is exemplarily shown in Fig. 7.12.

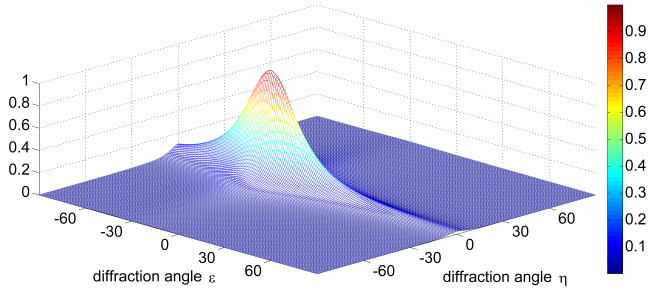

Figure 7.12.: Diffraction Angle Probability Density Function in $3D$ for $b_A = 1$, $b_B = 3$, $\varepsilon_1 = 30°$, $\eta_1 = 0°$ and $D_0 = 1$.

It should be noted that this $3D$-DAPDF is independent of any rotation of the coordinate system as long as the planes A and B are perpendicular to each other in the $y-z-$ plane. Thus, it can be applied to the two diffraction concepts that were described in Sec. 7.3.1.4 and Sec. 7.3.1.5.

In case of the concept of an arbitrary rotation of the coordinate system, the direction A can be defined as the $y-$ direction and the direction B as the $z-$ direction. Then, the two independent *effective* EDSs b_A and b_B are based on, in total, 4 distances $a_{y,1}$, $a_{z,1}$, $a_{y,2}$ and $a_{z,2}$ (see Fig. 7.10). For each distance a, an EDS of Eqn. 5.10 (with the extension of Eqn. 5.63) is computed and the respective EDSs of one dimension are added up by Eqn. 5.34.

$$\begin{aligned} S_A = S_y &= \frac{1}{b_{y,1}} + \frac{1}{b_{y,2}} = \frac{1}{6a_{y,1}cos(\varepsilon_1)} + \frac{1}{6a_{y,2}cos(\varepsilon_1)} = \frac{1}{b_y} = \frac{1}{b_A} \\ S_B = S_z &= \frac{1}{b_{z,1}} + \frac{1}{b_{z,2}} = \frac{1}{6a_{z,1}cos(\eta_1)} + \frac{1}{6a_{z,2}cos(\eta)} = \frac{1}{b_z} = \frac{1}{b_B}, \end{aligned} \tag{7.19}$$

where ε_1 and η_1 are the angles of incidence of the sound particle on the aperture projected on the respective plane (either $y - x-$ or $z - x-$ plane).

Since the orthogonal $2D$-DAPDFs are multiplied with each other, the same multiplication is used to compute the normalization constant D_0 in analogy to Eqn. 5.51 by

$$\int_{-\frac{\pi}{2}+\varepsilon_1}^{\frac{\pi}{2}+\varepsilon_1} \int_{-\frac{\pi}{2}+\eta_1}^{\frac{\pi}{2}+\eta_1} \frac{D_0}{\left(1 + 2\left(2 \cdot b_A \cdot \varepsilon\right)^2\right)\left(1 + 2\left(2 \cdot b_B \cdot \eta\right)^2\right)} d\varepsilon d\eta \stackrel{!}{=} 1 \tag{7.20}$$

D_0 is approximated with $b_A\varepsilon \gg 1$ and $b_B\eta \gg 1$ (according to Eqn. 5.52) by

$$D_0\left(b_A, b_B\right) \overset{b_A\varepsilon\gg 1, b_B\eta\gg 1}{\approx} \frac{8 \cdot b_A \cdot b_B}{\pi^2}. \tag{7.21}$$

In any other case, the normalization constant has to be computed numerically.

7.3.3. Analytical Formulation for Sound Particle Diffraction Through an Aperture

To achieve an analytical expression for the diffraction in $3D$, an analytical equation is derived from a SPSM experiment, similar to the $2D$ case. Without loss in generality, the diffraction plane (aperture represented by the VW) is assumed to be the $y-z$ plane at $x = 0$. This infinite plane is covered by an infinite surface with an arbitrary opening in this surface of size S_{AP}, through which sound particles can propagate. A sound source (x_S, y_S, z_S) is defined at $x_S < 0$ and a receiver (x_R, y_R, z_R) at $x_R > 0$ (it should be noted that this derivation is in analogy to Sec. 5.3.1).

The sound source emits a number of N primary sound particles, from which N_0 intersect with the opening S_{AP} that is represented by the VW. Each intersecting sound particle is split-up into S secondary sound particles. S_0 of these sound particles intersect with the receiver with radius r_D for each of the N_0 sound particles (see Fig. 7.13).

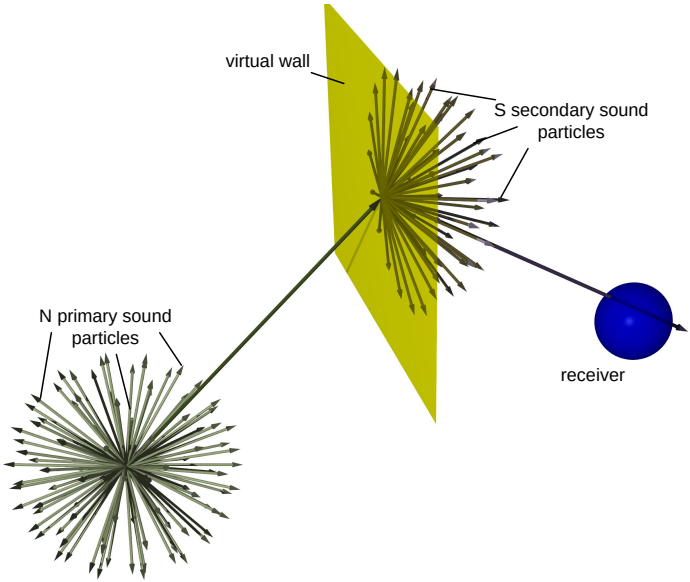

Figure 7.13.: Geometrical definitions of the sound particle diffraction in $3D$ through an aperture (*yellow*).

The detected sound intensity reads (neglecting reflections) with the respective double

sum (according to Eqn. 7.12, compare to Eqn. 5.20)

$$I = \frac{P}{N \cdot V_D} \sum_{i=1}^{N_0} \sum_{j=1}^{S_0} e_{i,j} \cdot w_{i,j}, \tag{7.22}$$

where V_D is the detector volume, $e_{i,j}$ are the relative sound particle energies and $w_{i,j}$ are the inner crossing distances. From Eqn. 7.22 follows with the energy of these sound particles (see Eqn. 7.9), neglecting air attenuation (compare to Eqn. 5.20)

$$I = \frac{P}{N \cdot V_D} \sum_{i=1}^{N_0} \sum_{j=1}^{S_0} w_{i,j} \cdot \int_{\Omega_{SP}} D^* \left(S_{AP}, \vec{I}, \Omega_1, \Omega \right) d\Omega. \tag{7.23}$$

Here, a different definition of the $3D$-DAPDF $D^* \left(S_{AP}, \vec{I}, \Omega_1, \Omega \right)$ than in Eqn. 7.18 is used. For simplification (as in Eqn. 5.22), the inner crossing distances are replaced by the MFPL inside the detector with the surface S_D

$$\overline{w} = 4 \cdot \frac{V_D}{S_D} \rightarrow \frac{w_{i,j}}{V_D} \approx \frac{4}{S_D}. \tag{7.24}$$

As all *pyramids* (see Fig. 7.3) around sound particles are tangent to each other (compare Fig. 5.14 and Eqn. 5.24), the sum over all S_0 sound particles that intersect with the receiver in Eqn. 7.23 is replaced by the integral over the angle range of the detector Ω_R (with Eqn. 7.24) to

$$I = \frac{4 \cdot P}{N \cdot S_D} \sum_{i=1}^{N_0} \int_{\Omega_R} D^* \left(S_{AP}, \vec{I}, \Omega_1, \Omega \right) d\Omega. \tag{7.25}$$

In order to perform the transition to infinitesimally small receivers, the integral over the receiver angle range Ω_R is replaced by a multiplication of $\Delta\Omega_R$, as the $3D$-DAPDF is assumed to be constant in that small angle range

$$I = \frac{4 \cdot P}{N \cdot S_D} \sum_{i=1}^{N_0} D^* \left(S_{AP}, \vec{I}, \Omega_1, \Omega \right) \Delta\Omega_R. \tag{7.26}$$

The solid angle Ω_R of the receiver with radius r_D is expressed for small solid angles by the ratio of a circular disc relative to a sphere with the radius r_2 (distance between the intersection point and the receiver) to (compare to Eqn. 5.25)

$$\frac{\Delta\Omega_R}{4\pi} \approx \frac{\pi r_D^2}{4\pi r_2^2} \rightarrow \frac{4 \cdot \Delta\Omega_R}{S_D} = \frac{1}{r_2^2}. \tag{7.27}$$

This allows the transition to infinitesimally small receivers of Eqn. 7.26 to

$$I = \frac{P}{N} \sum_{i=1}^{N_0} \frac{D^* \left(S_{AP}, \vec{I}, \Omega_1, \Omega \right)}{r_2^2}. \tag{7.28}$$

The number of primary sound particles N is substituted by the solid angle of each sound particle $\Delta\Omega_{SP}$

$$\frac{4\pi}{N} = \Delta\Omega_{SP} \rightarrow N = \frac{4\pi}{\Delta\Omega_{SP}}, \tag{7.29}$$

such that the transition to an infinite number of primary sound particles $N \to \infty$ is performed by $\Delta\Omega_{SP} \to 0$ (compare to Eqn. 5.29),

$$\begin{aligned} I &= \lim_{\Delta\Omega_{SP}\to 0} \frac{P}{4\pi} \sum_{i=1}^{N_0} \frac{D^*\left(S_{AP}, \vec{I}, \Omega_1, \Omega\right)}{r_2^2} \Delta\Omega_{SP} \\ &= \frac{P}{4\pi} \int_{\Omega_{Aperture}} \frac{D^*\left(S_{AP}, \vec{I}, \Omega_1, \Omega\right)}{r_2^2} d\Omega, \end{aligned} \tag{7.30}$$

where the sum over all N_0 sound particles that intersect with the aperture is replaced by an integral over the solid angle range of the aperture $\Omega_{Aperture}$.

Now, for the special case of a plane aperture (VW), the integral over the solid angle is replaced by a surface integral over the aperture (to symmetrize the formulation). The vector from the sound source to the current intersection point at the aperture is defined as $\vec{r_1}$, and $d\vec{A}$ denotes an infinitesimally small surface element of the aperture. In the given coordinate system, the surface element of the VW, i.e., the aperture in the $y-z$ plane, is given by $d\vec{A} = dy \cdot dz \cdot \vec{e_x}$, where $\vec{e_x}$ is the unit vector in $x-$ direction. In analogy to Fig. 5.15b, Eqn. 5.30 reads for $3D$

$$d\Omega = \frac{cos(\beta_1)}{r_1^2} dA = \frac{cos(\beta_1)}{r_1^2} dydz. \tag{7.31}$$

In $3D$, β_1 (instead of α in $2D$) equals the non-projected angle of incidence of the current propagation path at the VW. It has to be noted that β_1 is not equal to both ε_1 or η_1 as long as the other angle is different from $0°$.

Eqn. 7.30 yields directly

$$I = \frac{P}{4\pi} \iint_{Aperture} \frac{D^*\left(S_{AP}, \vec{I}, \Omega_1, \Omega\right) cos\left(\beta_1\right)}{r_1^2 r_2^2} dydz. \tag{7.32}$$

Finally, the transmission degree is computed with Eqn. 5.1 and Eqn. 5.2 to

$$T = \frac{I}{I_F} = R^2 \iint_{Aperture} \frac{D^*\left(S_{AP}, \vec{I}, \Omega_1, \Omega\right) cos\left(\beta_1\right)}{r_1^2 r_2^2} dydz, \tag{7.33}$$

which is in direct analogy to Eqn. 5.32 or Eqn. 5.36. The only differences are:

1. the radii are exchanged from linear ($2D$) to quadratic ($3D$),
2. the angle of incidence is β_1 ($3D$) instead of ε_1 ($2D$) and
3. the line integral ($2D$) is a surface integral ($3D$).

Unfortunately, the $3D$-DAPDF, as derived in Eqn. 7.18, cannot be inserted in Eqn. 7.33 due to different definitions. This difference is explained together with a substitution in the following.

7.3.4. Conversion of the Diffraction Angle Probability Density Function Within Different Definitions

Per definition, the $2D$-DAPDF is a density function per angle. As described in Eqn. 7.10, the $3D$-DAPDF $D^*\left(S_{AP}, \vec{I}, \Omega_1, \Omega\right)$ is derived by the solid angle $\partial\Omega$ (usual description in polar coordinates), whereas the definition of the $3D$-DAPDF $D\left(\varepsilon, b\right)$, Eqn. 7.14, is based on a physical derivation by two diffraction angles $\partial\varepsilon$ and $\partial\eta$ (into orthogonal directions). However, the absolute probabilities (the DAPF) must be identical. Thus, one $3D$-DAPDF can be mathematically expressed by the other with Eqn. 7.10 and 7.14.

$$D^*\left(S_{AP}, \vec{I}, \Omega_1, \Omega\right) = \frac{\partial DAP}{\partial\Omega} = \frac{\partial^2 DAP}{\partial\varepsilon\partial\eta}\frac{\partial\varepsilon\partial\eta}{\partial\Omega} = D\left(\varepsilon, \eta, b_A, b_B\right)\frac{\partial\varepsilon\partial\eta}{\partial\Omega}. \tag{7.34}$$

Therefore, a $3D$-diffraction conversion factor $Q_{3D}\left(\varepsilon, \eta\right) = \frac{\partial\varepsilon\partial\eta}{\partial\Omega}$ has to be determined. For the further investigations, the projected angles of incidence ε_1 and η_1 are assumed to be constant due to a fixed intersection point on the VW and, thus, a constant $\vec{r_1}$. In this case, the $3D$-diffraction conversion factor Q_{3D} is only dependent on the outgoing angles ε_2 and η_2

$$Q_{3D}\left(\varepsilon_2, \eta_2\right) = \frac{\partial\varepsilon\partial\eta}{\partial\Omega} = \frac{\partial\varepsilon_2\partial\eta_2}{\partial\Omega}. \tag{7.35}$$

With this definition and the outgoing angle β_2, a similar equation like Eqn. 7.31 is found that utilizes the relationship between an integration over an angle and an integration over a surface

$$d\Omega = \frac{cos(\beta_2)}{r_2^2}dydz = \frac{1}{r_2^2}\cdot\frac{r_{2,x}}{r_2}dydz,$$

where $r_{2,x}$ is the $x-$component of $\vec{r_2}$. Inserting this in Eqn. 7.35, $Q_{3D}\left(\varepsilon_2, \eta_2\right)$ reads

$$Q_{3D}\left(\varepsilon_2, \eta_2\right) = \frac{\partial\varepsilon_2\partial\eta_2}{\partial\Omega} = \frac{\partial\varepsilon_2\partial\eta_2}{dydz}\frac{r_2^3}{r_{2,x}}. \tag{7.36}$$

In order to compute the $3D$-diffraction conversion factor $Q_{3D}\left(\varepsilon_2, \eta_2\right)$, the diffraction angles on the rear side of the VW ε_2 and η_2 have to be defined in Cartesian coordinates. Based on the diffraction concept with an arbitrary rotation of the coordinate system (see Sec. 7.3.1.5), a coordinate system is assumed as follows (see Fig. 7.14):

$$\begin{aligned}
x &= r_{2,x} \\
y &= r_{2,x}\cdot tan\left(\varepsilon_2\right) \\
z &= r_{2,x}\cdot tan\left(\eta_2\right) \\
\varepsilon_2 &= atan\left(\frac{y}{x}\right) \\
\eta_2 &= atan\left(\frac{z}{x}\right) \\
r_2 &= \sqrt{x^2+y^2+z^2} = r_{2,x}\sqrt{\left(1+tan\left(\varepsilon_2\right)^2+tan\left(\eta_2\right)^2\right)}
\end{aligned} \tag{7.37}$$

(a) ε_2 **(b)** η_2

Figure 7.14.: Conversion from the diffraction coordinate system (ε_2, η_2) on the rear side of the Virtual Wall to Cartesian coordinates.

So, the partial derivations are

$$\begin{aligned} \frac{\partial \varepsilon_2}{\partial y} &= \frac{\partial atan\left(\frac{y}{x}\right)}{\partial y} = \frac{x}{x^2+y^2} = \frac{\frac{1}{x}}{1+tan\left(\varepsilon_2\right)^2} \text{ and} \\ \frac{\partial \eta_2}{\partial z} &= \frac{\partial atan\left(\frac{z}{x}\right)}{\partial z} = \frac{x}{z^2+y^2} = \frac{\frac{1}{x}}{1+tan\left(\eta_2\right)^2} \end{aligned} \tag{7.38}$$

and, thus, Eqn. 7.36 yields

$$\begin{aligned} Q_{3D}\left(\varepsilon_2, \eta_2\right) &= \frac{\partial \varepsilon_2 \partial \eta_2}{dydz} \frac{r_2^3}{r_{2,x}} = \frac{\partial \varepsilon_2}{dy} \cdot \frac{\partial \eta_2}{dz} \frac{r_2^3}{r_{2,x}} \\ &= \frac{\left(1+tan\left(\varepsilon_2\right)^2+tan\left(\eta_2\right)^2\right)^{\frac{3}{2}}}{\left(1+tan\left(\varepsilon_2\right)^2\right) \cdot \left(1+tan\left(\eta_2\right)^2\right)}. \end{aligned} \tag{7.39}$$

This modification factor is shown in Fig. 7.15.

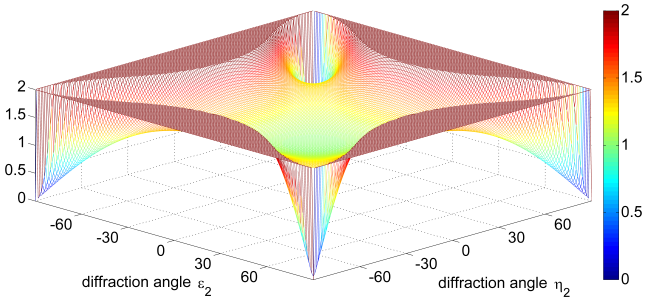

Figure 7.15.: $3D$-diffraction conversion factor $Q_{3D}\left(\varepsilon_2, \eta_2\right)$ (see Eqn. 7.39) between two definitions of the Diffraction Angle Probability Density Function.

For small diffraction angles ε_2 and η_2, this factor can be expressed by

$$Q_{3D}\left(\varepsilon_2,\eta_2\right) \overset{\varepsilon_2,\eta_2\approx 0}{\approx} 1+\frac{tan^2\left(\varepsilon_2\right)}{2}+\frac{tan^2\left(\eta_2\right)}{2} \tag{7.40}$$

and converges to 1 for $\varepsilon_2,\eta_2 \to 0$ (see centre of Fig. 7.15), such that no influence is expected for the targeted angle range of Kirchhoff's diffraction theory (see Sec. 2.3.4.3). If only one angle is 0, it follows

$$Q_{3D}\left(\varepsilon_2,\eta_2=0\right)=\left|\frac{1}{cos\left(\varepsilon_2=\beta_2\right)}\right| \text{ and } Q_{3D}\left(\varepsilon_2=0,\eta_2\right)=\left|\frac{1}{cos\left(\eta_2=\beta_2\right)}\right|. \tag{7.41}$$

Thus, the increase of $Q_{3D}\left(\varepsilon_2,\eta_2\right)\to\infty$ in Fig. 7.15 is explained, which is very problematic for a numerical integration in this region. If both angles tend to $\varepsilon_2,\eta_2\to\pm\frac{\pi}{2}$, the factor $Q_{3D}\left(\varepsilon_2,\eta_2\right)$ drops to zero, which is numerically problematic, too. However, if only one diffraction angle is above 60°, the factor increases rapidly, whereas it rapidly decreases if both angles are above a certain angle (corners in Fig. 7.15). This factor is explained geometrically by the size of the surface elements on a unit sphere. With both definitions, they are approximately at the same size near the equator $\varepsilon_2\approx\eta_2\approx 0°$, but differ significantly near the pole caps.

With this factor, the transmission degree T of Eqn. 7.33 is written with Eqn. 7.34 as

$$\begin{aligned} T &= R^2\iint_{Aperture}\frac{D\left(\varepsilon,\eta,b_A,b_B\right)\frac{\partial\varepsilon\partial\eta}{\partial\Omega}cos\left(\beta_1\right)}{r_1^2r_2^2}dydz \qquad (7.42)\\ &= R^2\iint_{Aperture}\frac{D\left(\varepsilon,\eta,b_A,b_B\right)cos\left(\beta_1\right)}{r_1^2r_2^2}\frac{\left(1+tan\left(\varepsilon_2\right)^2+tan\left(\eta_2\right)^2\right)^{\frac{3}{2}}}{\left(1+tan\left(\varepsilon_2\right)^2\right)\left(1+tan\left(\eta_2\right)^2\right)}dydz. \end{aligned}$$

It is very questionable, if this $3D$-diffraction conversion factor $Q_{3D}\left(\varepsilon_2,\eta_2\right)$ is physically correct, although it has been derived mathematically. Furthermore, the combination of the UBD with the SPSM results in high computation times, because the integral is only computable numerically, such that one approach might be to just omit that conversion factor in the future.

For an analytical comparison to $2D$, $\eta_1=\eta_2=0°$ and $b_B\to\infty$ have to be assumed, such that $\beta_1=\varepsilon_1$ and $\beta_2=\varepsilon_2$. Then, Eqn. 7.42 reads

$$T=R^2\int\int\frac{D\left(\varepsilon,0,b_A,\infty\right)cos\left(\varepsilon_1\right)}{r_1^2r_2^2}\left|\frac{1}{cos\left(\varepsilon_2\right)}\right|dydz. \tag{7.43}$$

As an equivalence to $2D$ cannot be seen directly, the analytical solution (Eqn. 7.42) is validated for some simple aperture shapes in the following.

7.3.5. Validation of the analytical 3D diffraction module

The validation of the analytical equation is performed in several steps. First of all, the agreement with the two dimensional UBD module is investigated in the respective cross-section, because this is an important requirement. As this investigation basically covers the convergence to the infinite wedge length, finite wedges are covered in this section, too. Furthermore, the influence of the arbitrarily chosen coordinate system by the diffraction concept of Sec. 7.3.1.5 is quantified.

In addition, the source and receiver positions are rotated around the $y-axis$ in the third dimension to investigate oblique diffraction around a wedge. Finally, the

investigation is extended to the sound distribution of rectangularly shaped apertures. As no $2D$ equivalent is defined for that case, the wave-theoretical SSM is used as reference here. An extension to arbitrarily shaped apertures is not covered yet, because the integration boundaries of Eqn. 7.42 are dependent on each other then, such that these cases are investigated by the SPR in the future.

7.3.5.1. Comparison with Former 2D Investigations

To validate the three dimensional analytical diffraction model, the shape of the aperture has to be defined at first. In order to solve the analytical Eqn. 7.42, a rectangular aperture parallel to the $y-axis$ and $z-axis$ is assumed. Thus, the boundary of the aperture is defined by the range $y_{Min} < y < y_{Max}$ and $z_{Min} < z < z_{Max}$. The widths are given by $d_y = y_{Max} - y_{Min}$ and $d_z = z_{Max} - z_{Min}$. The sound source and the receivers are defined identically to the $2D$ experiments in the $x-y-$plane at $z = 0$ (see Fig. 7.16). In $3D$, the receivers are on a half circle (arc) and differ by an angle of $1°$ in the range $-89° < \varphi_R < 89°$.

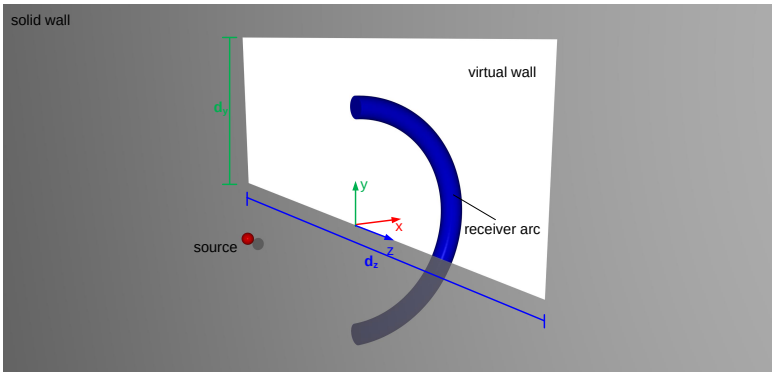

Figure 7.16.: Geometrical definitions for the diffraction in $3D$.

Due to the restriction of the presented analytical $3D$ diffraction model to rectangular apertures, no infinitesimally long wedges are possible as they were assumed in $2D$, because the limits of the integration have to be finite. In addition, the effective slit widths b converge to $b \to \infty$ for infinite wedges, such that the $3D$-DAPDF collapses to a $2D$-DAPDF, which is numerically not computable. However, the aperture has a large width in one direction ($d_z \gg 1$) and the convergence for larger widths is investigated.

First, a single wedge is symmetrically defined to the $z-axis$ ($\left|z_{Min,Max}\right| = d_z/2$) and a large width in $y-direction$ ($y_{Min} = 0$, $y_{Max} = 500$) is assumed. All distances are given in relation to the wavelength λ. The results are shown in Fig. 7.17 for $r_S = r_R = 10\lambda$. Besides the $3D$ experiments, the reference solution in $2D$ of Fig. 5.27 is shown.

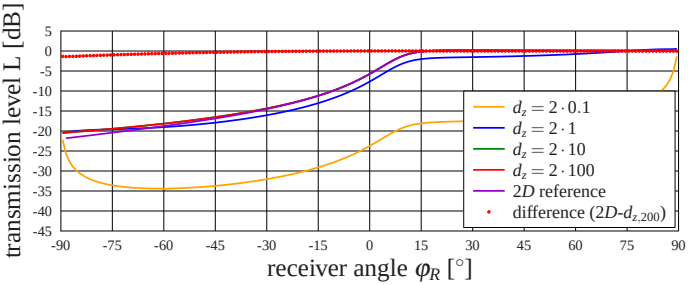

Figure 7.17.: Validation of $3D$ diffraction at an (in)finite wedge ($r_S = r_R = 10$).

The difference between a wedge length of $d_z = 200$ and $d_z = 20$ is not noticeable, because the *green* graph matches the *red* graph exactly. Thus, a convergence is achieved for increasing single wedge lengths d_z. In comparison to the former $2D$-experiments, the same transmission level is computed except for the deep shadow zone, where an increased transmission level is computed (up to $1dB$ greater).

For a smaller wedge length of $d_z = 2$, the overall transmission level decreases quite constantly by about $2dB$. This is reasonable, because both wedges in $y - direction$ are so close to each other that they cause a diffraction of energy in $z - direction$. This energy is missing in direction of the receivers ($y - direction$).

For even shorter wedges ($d_z = 0.2$), this effect increases to a reduction of approximately $17dB$ (also in the visibility region $\varphi_R > 0°$), because even more energy is diffracted in $z - direction$. Unfortunately, very large errors occur in the angle range $|\varphi_R| > 75°$. This is caused by the $3D$-diffraction conversion factor $Q_{3D}(\varepsilon_2, \eta_2)$ (see Eqn. 7.39), due to numerical errors in the integration.

The same behaviour is observed for different source and receiver distances in principle, but the numerical problems occur already for $d_z = 2$ for $r_S = r_R = 100$ (see appendix A.2.5.1).

In a second experiment, the slit case of the $2D$-experiments is repeated, too. Therefore, the dimensions of the aperture remain unaffected in $z - direction$, but a slit is constructed in $y - direction$ ($y_{Min} = -5$, $y_{Max} = 5$, $d_y = 10$). The results are shown in Fig. 7.18.

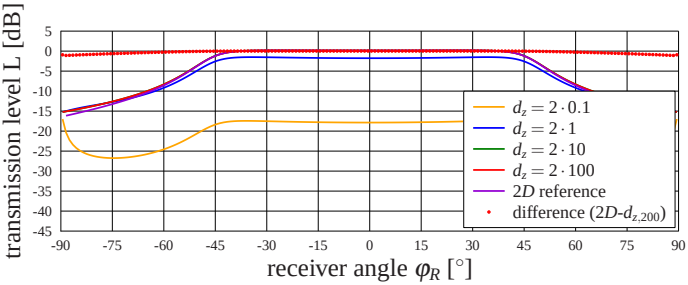

Figure 7.18.: Validation of $3D$ diffraction at an (in)finite slit ($r_S = r_R = d_y = 10$).

No principle difference between the slit and the wedge is noticed. For not too narrow slits in $z - direction$, very good agreements between the $2D$ results and different slit

lengths show a compatibility of the $3D$ diffraction model, too. For $d_z = 0.2$, the same effect as for the wedge occurs. Again, the results for different distances are shown in appendix. A.2.5.1.

7.3.5.2. Influence of an Arbitrarily Chosen Local Coordinate System

In the next experiments, the influence of the local coordinate system is discussed. The reflection pattern behind the aperture should be invariant to a rotation of the two main axes of the $2D$-DAPDFs to make the concept of Sec. 7.3.1.5 usable. Due to the definition of the aperture in Fig. 7.16, the $y-$ and $z-axes$ directly equal the dimensions of the closed distances (such that the diffraction concept of Sec. 7.3.1.4 and 7.3.1.5 are identical in this case). To investigate the effect of a rotated coordinate system, the local coordinate system, and thus the perpendicular diffraction dimensions, are rotated around the $x-axis$ about an angle of α in steps of 15°. Only angles in the range of $0° \leq \alpha \leq 45°$ are investigated, as a rotation of a larger angle geometrically equals a rotation of $90° - \alpha$. This is repeated for a rotation above $\alpha > 90°$, except for an interchange of the axes. The results for a single wedge (or a rather wide slit of $d_y = 200$) are shown in Fig. 7.19.

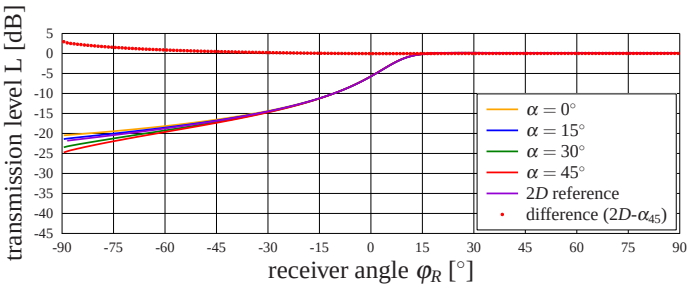

Figure 7.19.: Validation of the local coordinate system at a wedge ($r_S = r_R = 10$). The coordinate system is rotated by an angle of α.

In general, the transmission level is only hardly affected by a rotation of the coordinate system. For all receiver angles $\varphi_R > -45°$, no difference is observed at all. However, for receivers in the deep shadow zone ($\varphi_R < -60°$), the transmission level differs in-between the different rotation angle up to $5dB$ at $\varphi_R = -89°$. Astonishingly, the reference solution of the $2D$ experiment is in the centre of the possible transmission levels (such that the best match is found for $\alpha = 15°$). The biggest difference between the $3D$ and the $2D$ case occurs for $\alpha = 45°$ with up to $2.5dB$ for the lowest receiver ($\varphi_R = -89°$). These results are confirmed for different distances, too (see appendix A.2.5.2).

The same good agreements are expected for the diffraction at a slit. The results are shown in Fig. 7.20.

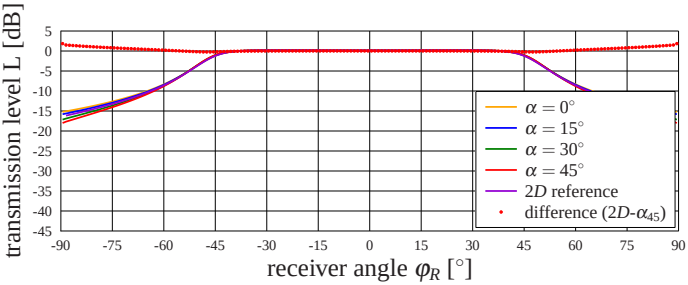

Figure 7.20.: Validation of local coordinate systems at a slit ($r_S = r_R = d_y = 10$). The coordinate system is rotated by an angle of α.

The conclusions for the single wedge experiment are confirmed by the experiments at a slit. Even for different distances (see appendix A.2.5.2), the maximum difference between the $2D$-reference method and the $3D$-results are even smaller than for the single wedge. These results are very astonishing and convincing, because the arbitrary choice of the coordinate system seemed to be a weak point. This might be explained by the *sampling* of the aperture by the intersecting sound particles, such that the choice of the local coordinate system is of minor importance.

7.3.5.3. Oblique Incidence

Although the diffraction module is extended to three dimensions, all validations were restricted to the sound source and receiver in the $x-y-$plane at $z = 0$. This restriction is now abandoned by rotating the plane with the sound source and the receivers around the $y - axis$ by an angle of ϑ (see Fig. 7.21). It should be noted that the SSM yields similar results ($< 0.1dB$) whether a single wedge or the complete aperture is modelled (four wedges). An application of the $2D$-DAPDF would result in a transmission level independent of this rotation, because the geometrical scene in $2D$ can be considered in the rotated plane, such that all distances and angles are constant.

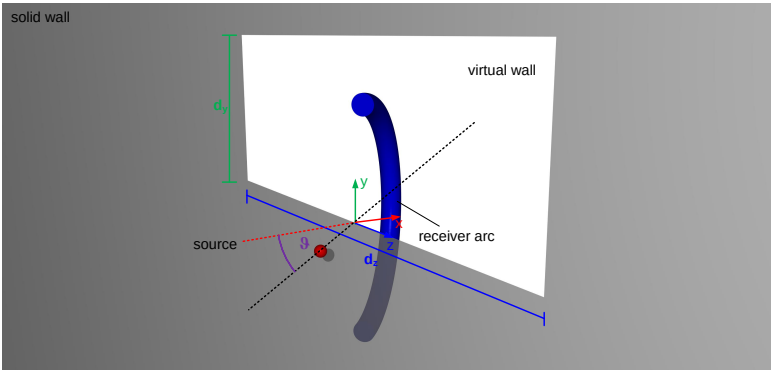

Figure 7.21.: Geometrical definitions of a rotation of the diffraction plane about an angle of ϑ.

Thus, the source and receiver positions read

$$\vec{S} = \begin{pmatrix} -cos\,(\varphi_S) \cdot cos\,(\vartheta) \\ sin\,(\varphi_S) \\ -cos\,(\varphi_S) \cdot sin\,(\vartheta) \end{pmatrix} \text{ and } \vec{R} = \begin{pmatrix} cos\,(\varphi_R) \cdot cos\,(\vartheta) \\ sin\,(\varphi_R) \\ cos\,(\varphi_R) \cdot sin\,(\vartheta) \end{pmatrix}. \tag{7.44}$$

For a single wedge of length $d_z = 200$, the results of the UBD for a rotation of the diffraction plane by an angle of $0° < \vartheta < 75°$ in steps of $15°$ are shown in Fig. 7.22a. Due to the symmetrical geometry, the results of positive rotation angles equal the results of negative rotation angles (not shown here). As these results are not comparable with former $2D$ experiments, the Edge Diffraction ToolBox (EDB) using the SSM is utilized to compute a reference solution for the same setup as shown in Fig. 7.22b. As described above, the SSM shows almost the same results whether a single wedge or the complete aperture is modelled. Thus, only the single wedge is used in this investigation.

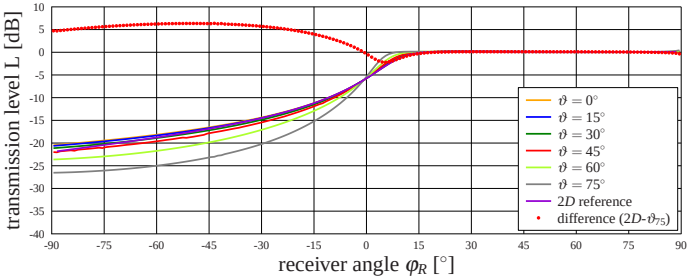

(a) Uncertainty relation Based Diffraction

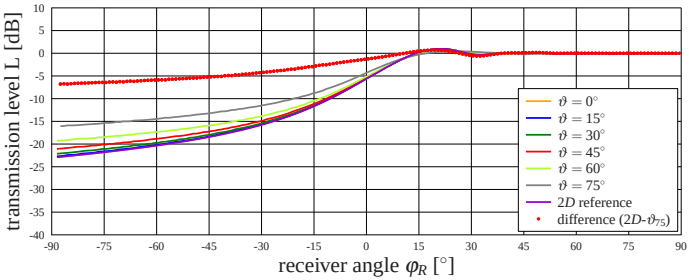

(b) Secondary Source Model

Figure 7.22.: Validation of oblique incidence at a wedge ($r_S = r_R = 10$). The diffraction plane is rotated by an angle of ϑ.

In case of the UBD, the transmission level decreases in the complete shadow zone with increasing rotation angles ϑ. For an almost parallel position of the diffraction plane to the aperture ($\vartheta = 75°$), a decrease of up to $6dB$ is achieved at $\varphi_R = -45°$.

From a physical point of view, even an increase of the transmission level is expected, because for the case of $\vartheta = 90°$, theoretically, the sound wave does not propagate through a slit howsoever. This expectation is confirmed by the SSM, where an increase of up to $7dB$ for the transmission level is achieved at $\vartheta = 75°$. So, there is obviously a strong discrepancy between the UBD and the SSM results.

An explanation for this discrepancy is the $3D$-diffraction conversion factor $Q_{3D}(\varepsilon_2, \eta_2)$ of Eqn. 7.39. With respect to the aperture in the $y-z-$ plane, both receiver positions are located in regions with large secondary diffraction angles $\varepsilon_2, \eta_2 \gg 1$. In this region, $Q_{3D}(\varepsilon_2, \eta_2)$ decreases fast to 0, such that the estimated transmission level of the UBD is way too low. Another explanation is that the SSM includes specular reflections. These reflections cause stronger effects for the sound sources and the receivers that are close to the wedge surface. In these cases, the transmission level is increased by these reflections. In the case of the UBD, this effect would be handled by reflected sound particles when combined with the SPSM, but they are not handled in the evaluated analytical formula. These angle regions contradict to the Kirchhoff assumptions. Thus, a modification of the diffraction algorithm behind the diffraction module might be necessary to achieve reasonable results for these angle ranges, since the Kirchhoff theory is only made for small angles anyway. For example, the $3D$-diffraction conversion factor $Q_{3D}(\varepsilon_2, \eta_2)$ could be neglected. Fortunately, both models are nearly unaffected by a rotation of the diffraction plane up to an angle of $|\vartheta| < 45°$. These observations are confirmed for distances of $r_S = r_R = 1$ and $r_S = r_R = 100$ (see appendix A.2.5.3).

7.3.5.4. Diffraction Through Rectangular Shaped Apertures

The last investigation of the UBD in $3D$ handled only $2D$ cross-sections. In order to investigate the complete angle ranges of the receivers, a whole receiver grid is defined with a constant distance x_R as shown in Fig. 7.23.

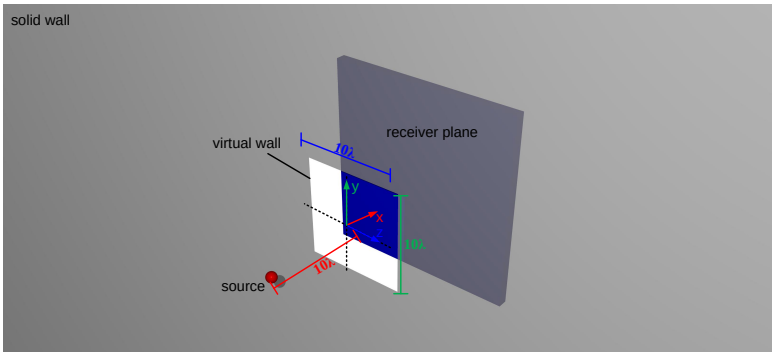

Figure 7.23.: Geometrical definitions for a receiver grid.

The aperture is defined by $d_y = d_z = 10$ and symmetrically positioned around the centre of the coordinate system $(0, 0, 0)$. The sound source is placed in a distance of $r_S = 10$ on the $x - axis$. A grid of 100 receivers is placed in a distance $x_R = 10$ in the opposite direction of the aperture. These receivers are equally distributed within a range of $-20 < y_R < 20$ and $-20 < z_R < 20$. Again, all distances are in wavelength λ.

As reference, the transmission level is computed by the EDB using the SSM. As the geometrical scene has to be defined with finite dimensions when the SSM is applied, the aperture is composed by four rigid wedges with an opening angle of $\varphi_W = 1°$. As the wall containing the aperture has to be of finite size, the height is set to $1000m$ counted from the edges outwards, such that diffraction at the bottom of these wedges is not computed. The conversion from the impulse response to the transmission level is described in Sec. 5.1.1. The results of the SSM and the UBD are compared in Fig. 7.24. Additionally, the absolute level difference between both methods is shown.

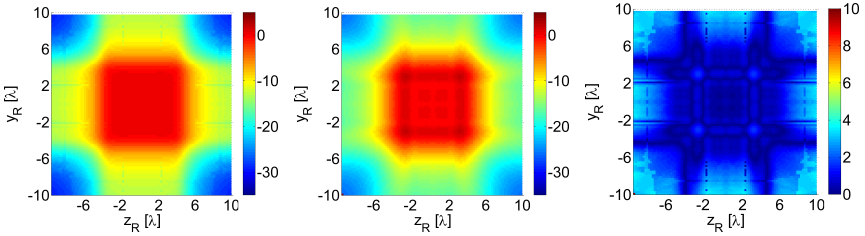

(a) Uncertainty relation Based Diffraction **(b)** Secondary Source Model **(c)** $|UBD - SSM|$

Figure 7.24.: Validation of the transmission level L for $3D$-diffraction of Uncertainty relation Based Diffraction and Secondary Source Model for a rectangular aperture $(10x10)$, $r_S = 10$ and a grid of receivers in the distance of $x_R = 10$.

The transmission level L in the view zone ($|y_R, z_R| < 10$) is about $0dB$ for both methods with one exception: the transmission level of the SSM is up to $1.9dB$ greater due to the interference effect in a small range around $|y_R, z_R| \approx 7$.

In the shadow zone of each wedge pair ($|y_R| < 10$ and $|z_R| > 10$ or vice versa), the transmission levels of the UBD is on average $1.2dB$ above the transmission level of the SSM (maximum $3.5dB$). This difference, however, is caused by the simplified $2D$-DAPDF D_b (see Eqn. 5.15). As shown in Fig. 5.32, the new $2D$-DAPDF D_g (see Eqn. 5.15) increases the transmission level about $2.5dB$ in this region and, thus, is expected to compensate this error at least by part.

A different effect is noticed in the shadow zone of both wedge pairs ($|y_R, z_R| > 10$), where the transmission level of the SSM is on average $2.3dB$ (maximum $3dB$) above the transmission level computed with the UBD. Again the $3D$-diffraction conversion factor $Q_{3D}(\varepsilon_2, \eta_2)$ (see Eqn. 7.39) might be reasonable for this effect as discussed in Sec. 7.3.5.3. The absolute level differences between the UBD and SSM over the complete receiver grid is on average $1.4dB$. Astonishingly, the mean difference, without the neglection of the sign, shows nearly no difference ($0.0dB$) between the SSM and the UBD.

A similar result is computed for distances of the sound source and the receivers $|x_S = x_R| = 1$ as shown in Fig. 7.25. The receiver plane is adjusted to $-2 < y_R, z_R < 2$.

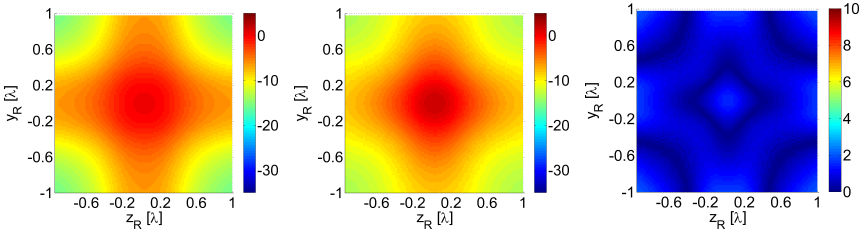

(a) Uncertainty relation Based Diffraction **(b)** Secondary Source Model **(c)** $|UBD - SSM|$

Figure 7.25.: Validation of the transmission level L for $3D$-diffraction of Uncertainty relation Based Diffraction and Secondary Source Model for a rectangular aperture $(1x1)$, $r_S = 1$ and a grid of receivers in the distance of $x_R = 1$.

The effects for $x_R = x_S = 10$ are reproduced, but the errors in the shadow regions are up to $\pm 1dB$ in the same regions. The sign of these differences is equal to the results of $r = 10$. Thus, the absolute difference of all receiver positions is on average only $0.7dB$ (and $-0.3dB$ for an averaging of the signed differences). The results are, as expected in $2D$, even better for smaller distances when the former $2D$-DAPDF D_b is used.

The same results are finally shown for $r = 100$ in Fig. 7.26. Again, the receiver grid is adjusted to the modified distances by $-100 < y_R, z_R < 100$.

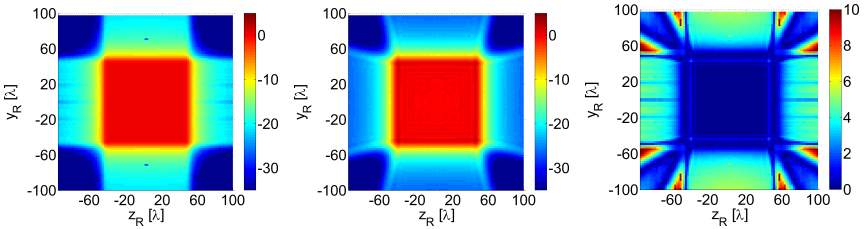

(a) Uncertainty relation Based Diffraction **(b)** Secondary Source Model **(c)** $|UBD - SSM|$

Figure 7.26.: Validation of the transmission level L for $3D$-diffraction of Uncertainty relation Based Diffraction and Secondary Source Model for a rectangular aperture ($100x100$), $r_S = 100$ and a grid of receivers in the distance of $x_R = 100$.

In this case, the difference in the shadow zone of one wedge pair ($|y_R| < 50$ and $|z_R| > 50$ or vice versa) is confirmed. This is caused by a kind of convergence to a far field distribution as discussed in $2D$. Additionally, numerical errors occur when integrating the UBD, which are not resolved yet.

In the shadow zone of both wedge pairs ($|y_R, z_R| > 50$), large differences of up to $10dB$ are computed between the SSM and the UBD in some small regions (*red* triangles in Fig. 7.26c). These systematical differences have to be investigated in more detail in the future.

In summary, the diffraction through a rectangularly shaped aperture showed very good agreements with the wave-theoretical SSM for almost all combinations. In many regions, even better agreements are expected, when the new $2D$-DAPDF D_g is used.

7.4. Summary of the Extension to Three Dimensions

Different concepts of $3D$ convex sub-divisions were presented, which are summarized in Tab. 7.1. The sub-division that extended the $3D$ approach is automatically performed and optimized for diffraction, but not implemented yet.

	Delaunay-Triangulation	extension of $2D$ approach	manual sub-division
optimized for diffraction	✗	✓	✗✓
automatically performed	✓	✓	✗
fully implemented	✓	✗	✗✓

Table 7.1.: Comparison of different sub-division techniques.

The SPR method was extended to $3D$ and it was shown that the core of the algorithm is identical to the $2D$ version. The overall conclusions for the accuracy and the computational effort (see chapter 6) are also applicable to $3D$.

The UBD module was discussed in more detail. Different theoretical concepts of diffraction through a polygonal aperture were presented. It was shown that the new concepts of 1) two perpendicular diffraction planes and 2) its arbitrarily rotated version are superior to the other concepts including the vectorial addition of the EDSs. The arguments are summarized in Tab. 7.2.

	circum-ference	all edges	closest edge	perpendicular edges	arbitrary rotation	vectorial addition
compatible to $2D$	✗	✓	✓	✓	✓	✓
robust for small edges	✓	✗	✗	✗✓	✗✓	✗✓
acceptable complexity	✗	✗✓	✓	✗✓	✗✓	✓
unquestionable closed distance	✓	✗	✓	✓	✓	✗
diffraction in all directions	✓	✓	✗	✓	✓	✗

Table 7.2.: Comparison of different $3D$-diffraction concepts.

These two concepts were applied to both the extended versions ($3D$) of the DAPDF and the EDS. In addition, an analytical equation for the transmission level behind an arbitrarily shaped aperture was analytically derived and numerically validated for a rectangularly shaped aperture. Although the former $2D$-DAPDF was used instead of the optimized $2D$-DAPDF to reduce the mathematical complexity, very good agreements with the $2D$ case were observed for the perpendicular incidence. These agreements were independent of the chosen local coordinate system, but differences occurred in the case of an oblique incidence. A comparison of diffraction through a rectangularly shaped aperture with the wave theoretical SSM showed good agreements for medium and small distances, but errors occurred for large distances in some small angle regions (see Tab. 7.3).

	checked with analytical formula
compatible to $2D$ investigations of the single wedge and the slit	✓
invariant with respect to a rotation of the local coordinate system	✓
oblique incidence meets the results of the Secondary Source Model	✗
diffraction through rectangular aperture meets the results of the Secondary Source Model	✓

Table 7.3.: Results of different numerical experiments.

Some of the occurring problems might be compensated by further investigations of the artificial $3D$-diffraction conversion factor $Q_{3D}(\varepsilon_2, \eta_2)$ and the usage of the new $2D$-DAPDF, but others can only be reduced by further improvement of the $3D$-UBD module.

8. Summary and Outlook

8.1. Summary

The aim of this work was to find an energetic Geometrical Acoustic (GA) simulation method that combines higher order reflections with higher order diffractions without an explosion of the Computation Time (CT). These investigations were restricted to $2D$ at first, because diffraction is a two dimensional effect and the statistical considerations were easier.

The chosen diffraction method in this work was based on the Uncertainty relation Based Diffraction (UBD) theory. It was investigated in detail and many improvements were found. By detailed analytical investigations, both main fundamental functions of the UBD (namely the Diffraction Angle Probability Density Function (DAPDF) and the Edge Diffraction Strength (EDS)) were adjusted, such that good agreements with the wave theoretical Secondary Source Model (SSM) were observed in many more cases than before. Even in regions, where the underlying Kirchhoff diffraction theory failed or other errors were expected, acceptable results were found. Although there were cases of large errors in extreme cases, a significant improvement of the results compared to the former results of Stephenson was presented.

For the combination of the modified diffraction module with the GA simulation methods, an improved spatial sub-division into convex sub-spaces was presented that efficiently detected sound energy carriers that had to be diffracted. It was shown that the CT with simulations using the presented sub-division technique was independent of the number of vertices and, thus, the complexity of the scene.

The necessary split-up of sound particles needed for the simulation of diffraction was compensated by a reunification of sound energy carriers. Both the Sound Particle Radiosity (SPR) and Quantized Pyramidal Beam Tracing (QPBT) were implemented (in $2D$) for the first time. Here, analytical, statistical and numerical investigations revealed that the reunification technique QPBT was both more inefficient and more inaccurate than the SPR. The numerical errors and an estimation of the computational effort of the SPR was given.

The combination of the SPR with the UBD module allowed the computation of higher order diffraction as shown in Fig. 8.1.

(a) without diffraction **(b)** with diffraction

Figure 8.1.: Comparison of intensity maps with and without diffraction (see Fig. 1.1).

Both the SPR and the UBD were extended to $3D$. Very good agreements of the $3D$-UBD with the $2D$-reference were shown already for the perpendicular incidence of sound particles, but discrepancies occurred for oblique incidence. A first investigation of diffraction in $3D$ through a rectangularly shaped aperture showed acceptable results, but a $3D$-diffraction conversion factor $Q_{3D}(\varepsilon_2, \eta_2)$ generated errors in same angle ranges.

8.2. Outlook

Although the UBD was evaluated for many crucial cases in $2D$, still some cases have to be investigated. Certainly to mention here is the definition of multiple wedges passed by. The decisive point for the UBD is the distinction between edges that are passed by simultaneously (forming a slit) or one after another (cascade). This is dependent on the convex sub-division (see Fig. 8.2).

(a) three parallel slits **(b)** four perpendicular wedges

Figure 8.2.: Different solution to define *simultaneously* passed wedges. The physically reasonable convex sub-division is indicated by the *green* Virtual Walls, whereas a different version is indicated by the *red* Virtual Walls.

In spite of the fact that both the rotation of Virtual Walls (VWs) and the passing through multiple VWs was inspected, complicated effects might occur for such cases. More critical cases will occur, when these methods are applied to real scenarios.

To use the method in real scenarios, a pre-processing step is needed to optimize the geometrical scene for acoustical simulations[SLSC08], such that acoustical irrelevant objects are removed out of the typical architectural CAD datasets. For these pre-processing algorithms, it might be appropriate to result in different geometry files for each frequency band[PVM10], because the definition of *acoustical relevant* objects strongly depends on the wavelength since a factor of up to 1000 occurs in the audible frequency range ($20Hz < f < 20kHz$). It might be necessary to fall back to the independent simulation of the single frequency bands. In either case, material data (e.g., from [PSS$^+$12]) has to be assigned to surfaces and objects of a geometrical model.

Once the problem of the huge memory effort of the Reunification Matrix (RUM) is solved (either by more efficient usage or parallelization), the complete algorithm (SPR with the UBD) has to be validated for even higher orders of diffraction. A (frequency-dependent) approximation has to be derived to estimate the quantization parameter $f_P = l_P/\bar{l}$ to a targeted accuracy, which will probably result in a dependency on the patch length per wavelength l_P/λ.

For the usage in $3D$, the presented sub-division concept has to be implemented and the $3D$-diffraction module has to be investigated analytically. Especially the influence of the $3D$-diffraction conversion factor $Q_{3D}(\varepsilon_2, \eta_2)$ in Eqn. 7.39 seems to play an important role and should be the first modification candidate. The optimized $2D$-DAPDF has to be used for further experiments. Furthermore, the UBD has to be introduced in the SPR, such that more complicated apertures instead of just a rectangle can be validated. Again, the Edge Diffraction ToolBox (EDB) by Svensson can be used as reference method for simple test cases. Problems are more complicated cases of cities, where wave-based reference methods fail and measurements are practically impossible. Nevertheless, comparisons with measurements, e.g., in scaled models are aspired.

A. Appendix

A.1. Datastructure

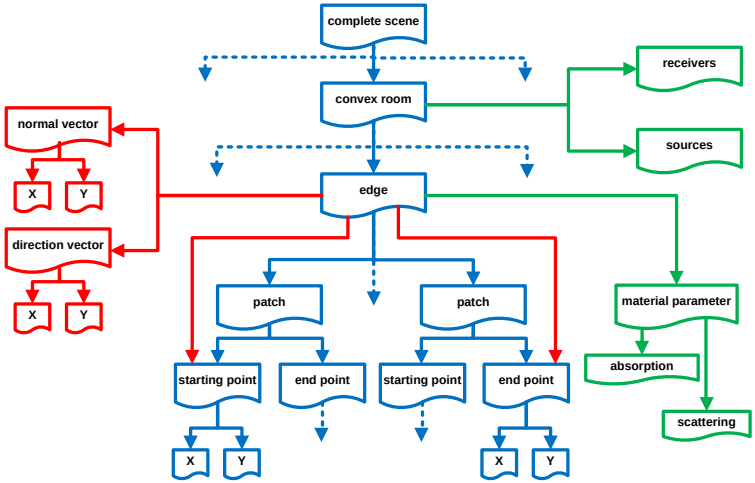

Figure A.1.: Datastructure in $2D$.

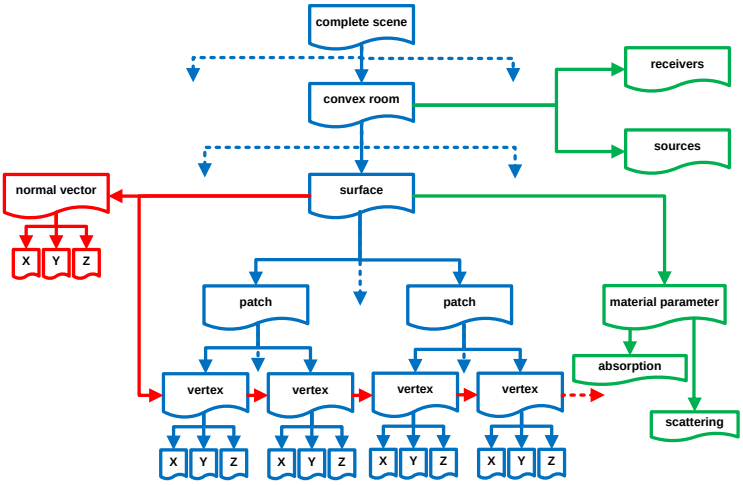

Figure A.2.: Datastructure in $3D$.

A.2. Additional Validation Plots

A.2.1. Analytical Comparison of Diffraction at a Single Wedge (2D)

A.2.1.1. Changing Soure Distance

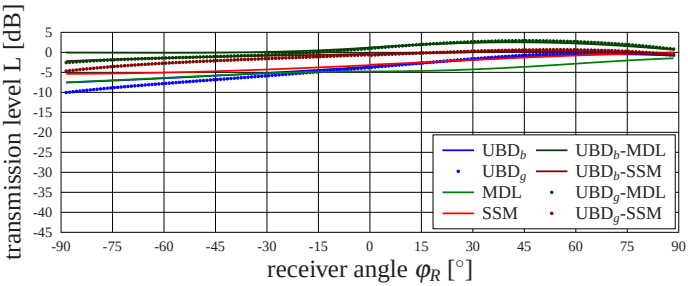

Figure A.3.: Validation of a single wedge as a function of φ_R, with $r_S = \frac{1}{10}\lambda$, $\varphi_S = 0°$ and $r_R = 10\lambda$.

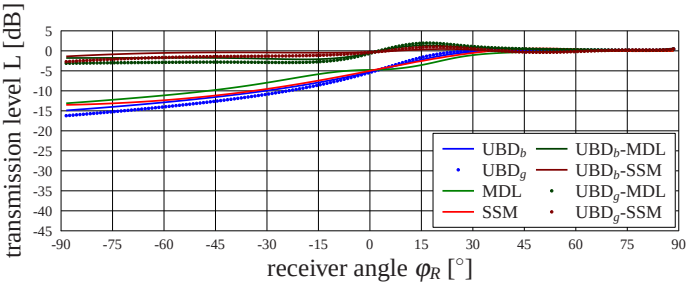

Figure A.4.: Validation of a single wedge as a function of φ_R, with $r_S = 1\lambda$, $\varphi_S = 0°$ and $r_R = 10\lambda$.

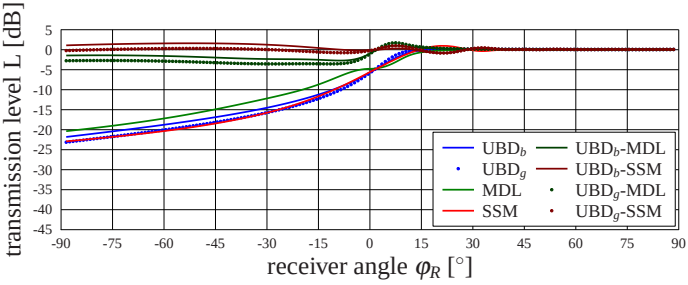

Figure A.5.: Validation of a single wedge as a function of φ_R, with $r_S = 10\lambda$, $\varphi_S = 0°$ and $r_R = 10\lambda$.

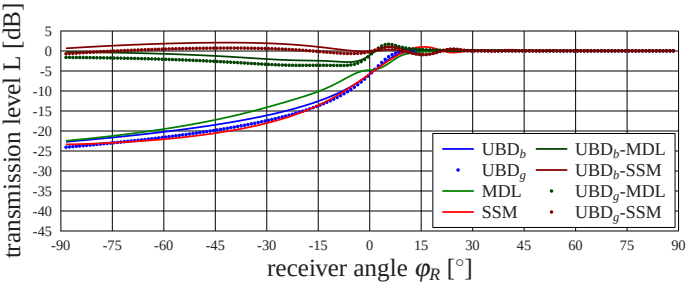

Figure A.6.: Validation of a single wedge as a function of φ_R, with $r_S = 100\lambda$, $\varphi_S = 0°$ and $r_R = 10\lambda$.

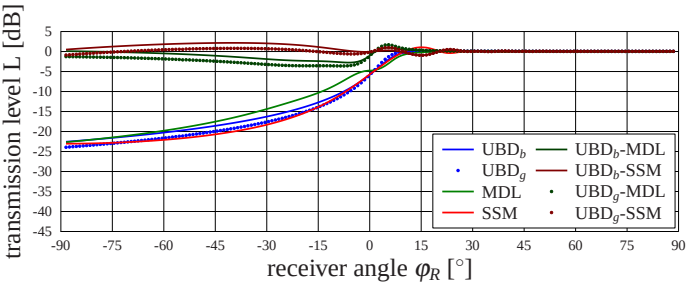

Figure A.7.: Validation of a single wedge as a function of φ_R, with $r_S = 1000\lambda$, $\varphi_S = 0°$ and $r_R = 10\lambda$.

		$r_S[\lambda]$	region $[dB]$ 0	1	2	3	Min$[dB]$	at[°]	Max$[dB]$	at[°]
UBD - MDL	UBD$_b$	$\frac{1}{10}$	−0.1	−0.1	+0.6	+1.0	−0.1	−59	+2.5	+43
		1	−1.8	−1.8	−1.8	−0.6	−2.1	−20	+1.4	+17
		10	−1.4	−2.0	−2.4	−0.9	−2.7	−09	+1.0	+08
		100	−0.4	−1.3	−2.4	−0.6	−2.8	−07	+1.0	+06
		1000	−0.1	−1.1	−2.3	−0.5	−2.8	−07	+1.0	+06
	UBD$_g$	$\frac{1}{10}$	−1.9	−1.0	+0.1	+0.6	−2.6	−89	+2.9	+46
		1	−3.0	−2.8	−2.4	−1.0	−3.1	−89	+1.9	+17
		10	−2.7	−3.2	−3.3	−1.4	−3.6	−29	+1.7	+08
		100	−1.8	−2.6	−3.4	−1.2	−3.6	−09	+1.7	+06
		1000	−1.5	−2.5	−3.4	−1.1	−3.6	−09	+1.7	+06
UBD - SSM	UBD$_b$	$\frac{1}{10}$	−1.8	−1.1	−0.6	−0.6	−2.2	−89	+0.2	+54
		1	−0.9	−0.4	−0.4	−0.2	−1.4	−89	+0.6	+89
		10	+1.4	+1.5	+0.5	+0.6	−0.9	+21	+1.6	−52
		100	+1.3	+2.0	+0.9	+0.7	−0.9	+16	+2.1	−42
		1000	+1.2	+2.1	+1.0	+0.7	−1.0	+15	+2.2	−42
	UBD$_g$	$\frac{1}{10}$	−3.6	−2.1	−1.1	−1.0	−4.7	−89	+0.7	+55
		1	−2.1	−1.4	−1.0	−0.7	−2.7	−89	+1.0	+21
		10	+0.1	+0.3	−0.4	±0.0	−0.8	+21	+1.0	+09
		100	±0.0	+0.7	−0.1	+0.1	−0.9	+16	+1.0	+06
		1000	−0.2	+0.7	±0.0	+0.1	−0.9	+16	+1.0	+06

Table A.1.: Numerical validation of a single wedge with $\varphi_S = 0°$, $r_R = 10\lambda$ and varying source distances r_S.

A.2.1.2. Changing Receiver Distance

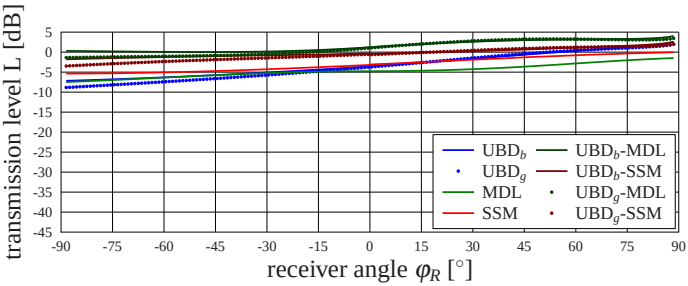

Figure A.8.: Validation of a single wedge as a function of φ_R, with $r_S = 10\lambda$, $\varphi_S = 0°$ and $r_R = \frac{1}{10}\lambda$.

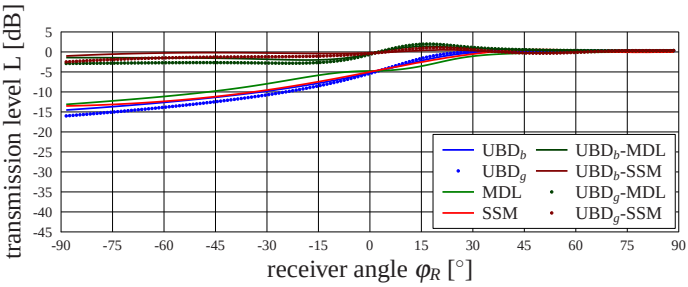

Figure A.9.: Validation of a single wedge as a function of φ_R, with $r_S = 10\lambda$, $\varphi_S = 0°$ and $r_R = 1\lambda$.

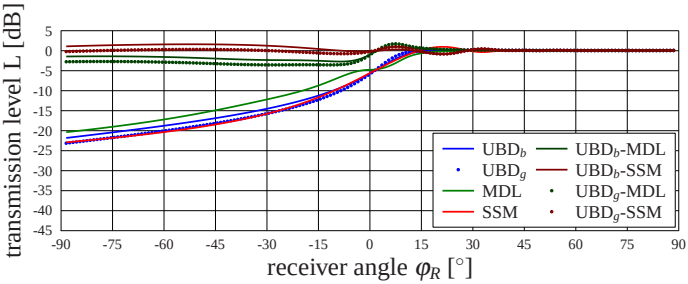

Figure A.10.: Validation of a single wedge as a function of φ_R, with $r_S = 10\lambda$, $\varphi_S = 0°$ and $r_R = 10\lambda$.

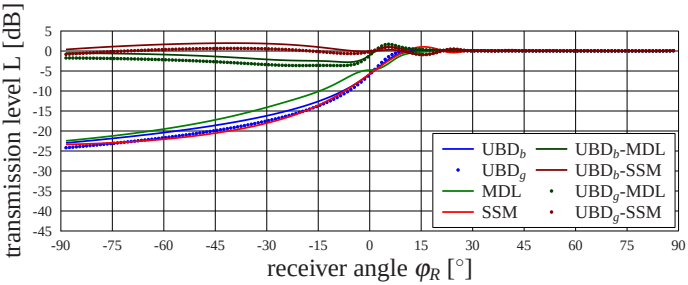

Figure A.11.: Validation of a single wedge as a function of φ_R, with $r_S = 10\lambda$, $\varphi_S = 0°$ and $r_R = 100\lambda$.

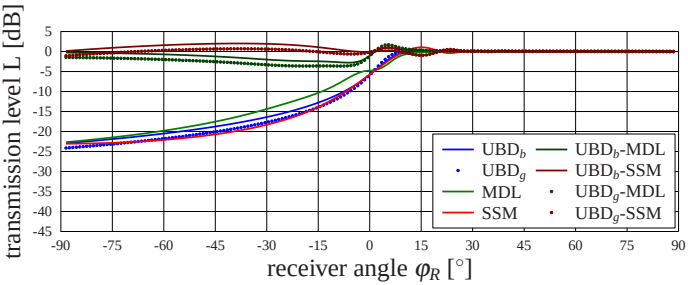

Figure A.12.: Validation of a single wedge as a function of φ_R, with $r_S = 10\lambda$, $\varphi_S = 0°$ and $r_R = 1000\lambda$.

		$r_R[\lambda]$	region $[dB]$ 0	1	2	3	Min$[dB]$	at[°]	Max$[dB]$	at[°]
UBD - MDL	UBD$_b$	$\frac{1}{10}$	+0.2	+0.1	+0.6	+1.5	±0.0	−48	+4.1	+89
		1	−1.4	−1.6	−1.7	−0.5	−2.0	−19	+1.4	+17
		10	−1.4	−2.0	−2.4	−0.9	−2.7	−09	+1.0	+08
		100	−0.7	−1.4	−2.4	−0.7	−2.8	−07	+1.0	+06
		1000	−0.4	−1.3	−2.4	−0.6	−2.8	−07	+1.0	+06
	UBD$_g$	$\frac{1}{10}$	−1.2	−0.8	+0.2	+1.1	−1.4	−89	+3.4	+89
		1	−2.8	−2.7	−2.3	−0.9	−2.9	−89	+2.0	+18
		10	−2.7	−3.2	−3.3	−1.4	−3.6	−29	+1.7	+08
		100	−1.9	−2.7	−3.4	−1.2	−3.6	−09	+1.7	+06
		1000	−1.7	−2.6	−3.4	−1.2	−3.6	−09	+1.7	+06
UBD - SSM	UBD$_b$	$\frac{1}{10}$	−1.5	−1.0	−0.6	−0.2	−1.8	−89	+2.6	+89
		1	−0.6	−0.2	−0.3	−0.1	−1.0	−89	+0.5	+22
		10	+1.4	+1.5	+0.5	+0.6	−0.9	+21	+1.6	−52
		100	+1.1	+1.9	+0.9	+0.7	−0.9	+16	+2.0	−41
		1000	+0.9	+1.9	+1.0	+0.6	−1.0	+15	+2.0	−39
	UBD$_g$	$\frac{1}{10}$	−2.9	−1.9	−1.0	−0.6	−3.5	−89	+2.0	+89
		1	−1.9	−1.3	−1.0	−0.6	−2.5	−89	+1.1	+21
		10	+0.1	+0.3	−0.4	±0.0	−0.8	+21	+1.0	+09
		100	−0.2	+0.6	−0.1	+0.1	−0.9	+16	+1.0	+06
		1000	−0.3	+0.6	±0.0	+0.1	−1.1	−89	+1.0	+06

Table A.2.: Numerical validation of a single wedge with $\varphi_S = 0°$, $r_S = 10\lambda$ and varying receiver distances r_R.

A.2.1.3. Changing All Distances

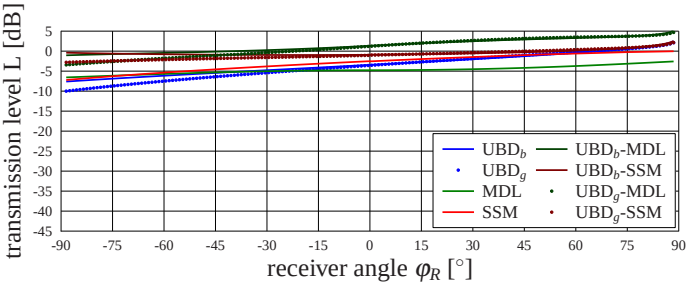

Figure A.13.: Validation of a single wedge as a function of φ_R, with $r_S = \frac{1}{10}\lambda$, $\varphi_S = 0°$ and $r_R = \frac{1}{10}\lambda$.

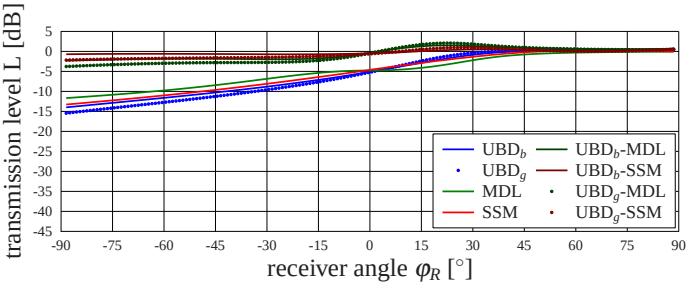

Figure A.14.: Validation of a single wedge as a function of φ_R, with $r_S = 1\lambda$, $\varphi_S = 0°$ and $r_R = 1\lambda$.

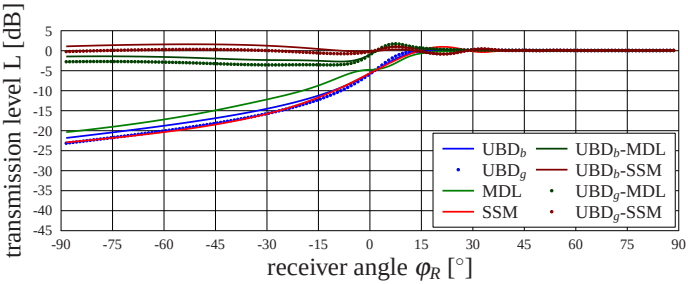

Figure A.15.: Validation of a single wedge as a function of φ_R, with $r_S = 10\lambda$, $\varphi_S = 0°$ and $r_R = 10\lambda$.

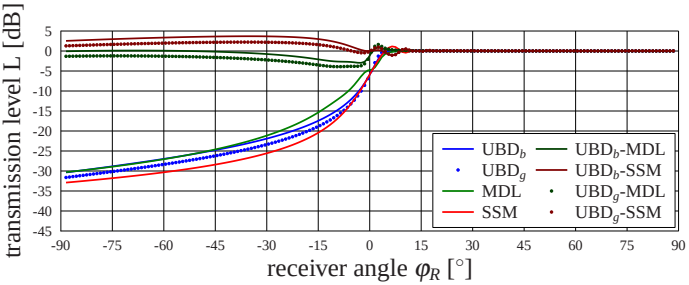

Figure A.16.: Validation of a single wedge as a function of φ_R, with $r_S = 100\lambda$, $\varphi_S = 0°$ and $r_R = 100\lambda$.

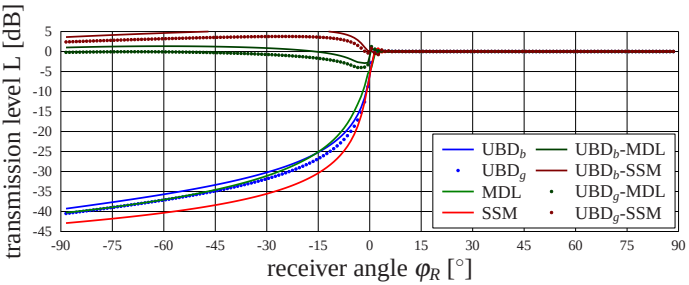

Figure A.17.: Validation of a single wedge as a function of φ_R, with $r_S = 1000\lambda$, $\varphi_S = 0°$ and $r_R = 1000\lambda$.

		r_S	region $[dB]$				Min$[dB]$	at	Max$[dB]$	at
		$= r_R[\lambda]$	0	1	2	3				
UBD - MDL	UBD$_b$	$\frac{1}{10}$	−0.7	−0.1	+0.8	+1.4	−1.0	−89	+5.1	+89
		1	−2.0	−1.9	−1.5	−0.5	−2.3	−89	+1.5	+23
		10	−1.4	−2.0	−2.4	−0.9	−2.7	−09	+1.0	+08
		100	+0.1	−0.2	−2.0	−0.3	−3.0	−03	+0.9	+03
		1000	+1.2	+1.2	−0.5	+0.3	−2.9	−02	+1.3	−60
	UBD$_g$	$\frac{1}{10}$	−2.6	−1.1	+0.4	+0.9	−3.4	−89	+4.7	+89
		1	−3.3	−2.8	−2.0	−0.9	−3.8	−89	+2.1	+23
		10	−2.7	−3.2	−3.3	−1.4	−3.6	−29	+1.7	+08
		100	−1.2	−1.7	−3.2	−1.0	−3.9	−10	+1.6	+03
		1000	−0.1	−0.3	−2.0	−0.4	−4.0	−03	+1.2	+01
UBD - SSM	UBD$_b$	$\frac{1}{10}$	−0.6	−0.9	−1.0	−0.4	−1.0	−19	+2.5	+89
		1	−0.6	−0.7	−0.7	−0.2	−0.7	−23	+0.7	+89
		10	+1.4	+1.5	+0.5	+0.6	−0.9	+21	+1.6	−52
		100	+3.0	+3.6	+2.5	+1.5	−1.1	+07	+3.7	−36
		1000	+4.1	+5.0	+4.5	+2.3	−0.8	+03	+5.4	−25
	UBD$_g$	$\frac{1}{10}$	−2.4	−1.8	−1.3	−0.9	−2.8	−89	+2.1	+89
		1	−1.9	−1.6	−1.2	−0.6	−2.2	−89	+1.0	+29
		10	+0.1	+0.3	−0.4	±0.0	−0.8	+21	+1.0	+09
		100	+1.7	+2.2	+1.2	+0.9	−1.1	+07	+2.2	−37
		1000	+2.8	+3.5	+3.1	+1.6	−0.8	+03	+3.8	−25

Table A.3.: Numerical validation of a single wedge with $\varphi_S = 0°$ and varying source and receiver distances $r_S = r_R$.

A.2.1.4. Changing Source Angle

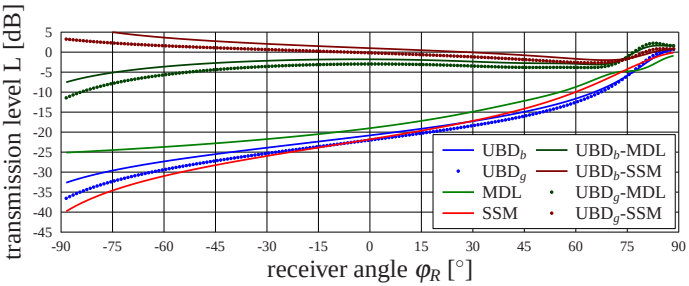

Figure A.18.: Validation of a single wedge as a function of φ_R, with $r_S = 10\lambda$, $\varphi_S = -75°$ and $r_R = 10\lambda$.

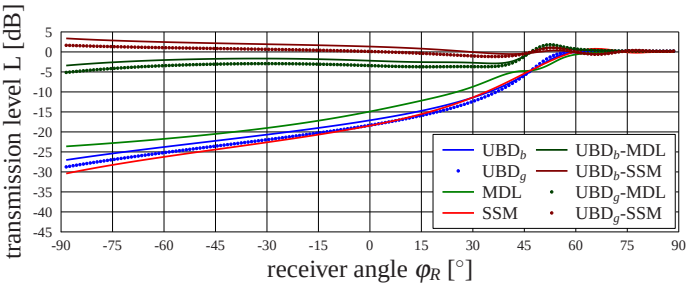

Figure A.19.: Validation of a single wedge as a function of φ_R, with $r_S = 10\lambda$, $\varphi_S = -45°$ and $r_R = 10\lambda$.

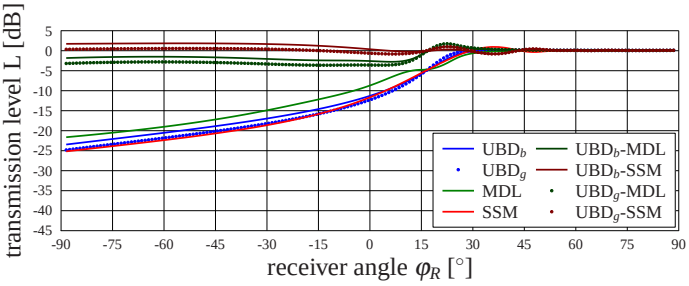

Figure A.20.: Validation of a single wedge as a function of φ_R, with $r_S = 10\lambda$, $\varphi_S = -15°$ and $r_R = 10\lambda$.

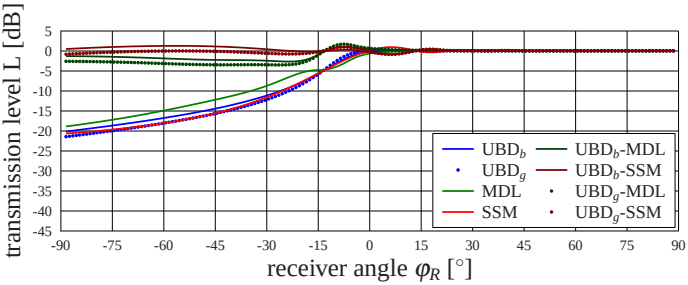

Figure A.21.: Validation of a single wedge as a function of φ_R, with $r_S = 10\lambda$, $\varphi_S = 15°$ and $r_R = 10\lambda$.

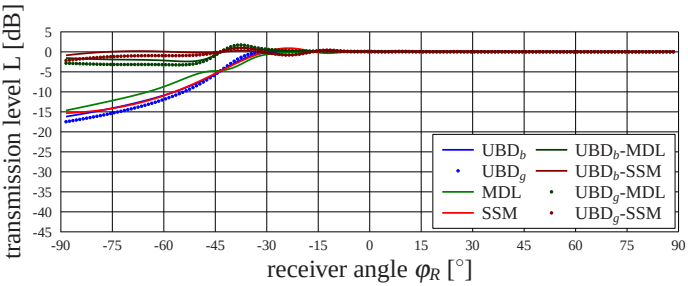

Figure A.22.: Validation of a single wedge as a function of φ_R, with $r_S = 10\lambda$, $\varphi_S = 45°$ and $r_R = 10\lambda$.

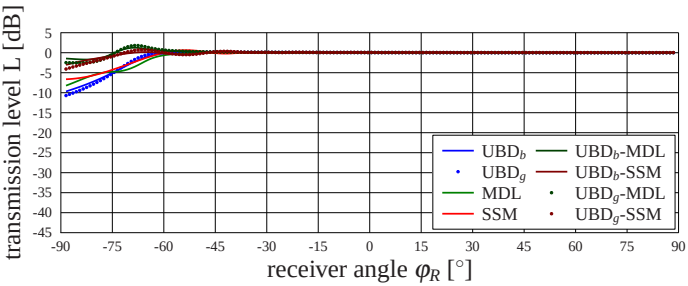

Figure A.23.: Validation of a single wedge as a function of φ_R, with $r_S = 10\lambda$, $\varphi_S = 75°$ and $r_R = 10\lambda$.

		$\varphi_S[^\circ]$	region $[dB]$ 0	1	2	3	Min$[dB]$	at$[^\circ]$	Max$[dB]$	at$[^\circ]$
UBD - MDL	UBD_b	-75°	-5.2	-2.8	-1.9	-2.6	-7.5	-89	$+1.7$	$+89$
		-45°	-2.6	-1.8	-1.9	-1.6	-3.4	-89	$+1.1$	$+53$
		-15°	-1.6	-1.7	-2.4	-1.0	-2.8	$+07$	$+1.1$	$+23$
		$+15^\circ$	-1.5	-2.2	-0.9	-0.7	-2.6	-24	$+1.0$	-08
		$+45^\circ$	-1.9	-0.7	$+0.2$	-0.4	-2.4	-54	$+1.1$	-38
		$+75^\circ$	-0.3	$+0.2$	$+0.1$	$+0.0$	-1.7	-83	$+1.3$	-69
	UBD_g	-75°	-8.0	-4.5	-3.2	-3.9	-11.4	-89	$+2.2$	$+83$
		-45°	-4.2	-3.1	-3.1	-2.5	-5.1	-89	$+1.8$	$+52$
		-15°	-2.9	-3.0	-3.5	-1.7	-3.6	-14	$+1.7$	$+23$
		$+15^\circ$	-2.8	-3.4	-1.0	-1.1	-3.5	-27	$+1.7$	-08
		$+45^\circ$	-3.1	-0.9	$+0.2$	-0.6	-3.3	-56	$+1.7$	-38
		$+75^\circ$	-0.4	$+0.2$	$+0.1$	± 0.0	-2.5	-85	$+1.8$	-69
UBD - SSM	UBD_b	-75°	$+5.1$	$+2.8$	$+1.5$	$+1.3$	-2.0	$+69$	$+7.2$	-89
		-45°	$+2.9$	$+2.2$	$+1.7$	$+1.2$	-0.6	$+66$	$+3.4$	-89
		-15°	$+1.8$	$+1.8$	$+1.2$	$+0.8$	-0.8	$+36$	$+1.8$	-57
		$+15^\circ$	$+1.0$	$+1.0$	$+0.1$	$+0.3$	-0.9	$+06$	$+1.3$	-57
		$+45^\circ$	-0.1	± 0.0	-0.1	± 0.0	-0.9	-89	$+0.5$	-13
		$+75^\circ$	-0.9	± 0.0	$+0.1$	-0.1	-3.0	-89	$+0.4$	-43
	UBD_g	-75°	$+2.3$	$+1.1$	$+0.2$	± 0.0	-2.7	$+65$	$+3.3$	-89
		-45°	$+1.3$	$+0.9$	$+0.4$	$+0.3$	-1.2	$+37$	$+1.7$	-89
		-15°	$+0.5$	$+0.5$	± 0.0	$+0.1$	-0.8	$+07$	$+1.0$	$+24$
		$+15^\circ$	-0.3	-0.2	-0.1	-0.1	-0.8	$+06$	$+1.0$	-07
		$+45^\circ$	-1.3	-0.1	-0.1	-0.2	-2.1	-89	$+0.9$	-37
		$+75^\circ$	-1.1	± 0.0	$+0.1$	-0.2	-4.1	-89	$+0.7$	-67

Table A.4.: Numerical validation of a single wedge with $r_S = r_R = 10\lambda$ and varying source angles φ_S.

A.2.2. Analytical Comparison of Diffraction at a Slit (2D)

A.2.2.1. Changing Source Distance

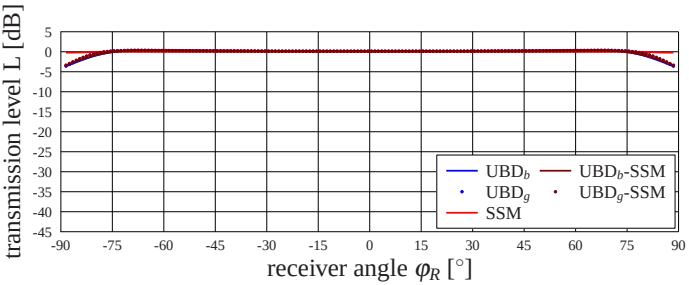

Figure A.24.: Validation of a slit ($d = 10\lambda$) as a function of φ_R, with $r_S = \frac{1}{10}\lambda$, $\varphi_S = 0°$ and $r_R = 10\lambda$.

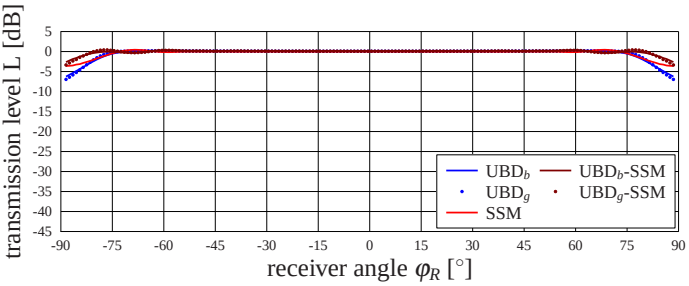

Figure A.25.: Validation of a slit ($d = 10\lambda$) as a function of φ_R, with $r_S = 1\lambda$, $\varphi_S = 0°$ and $r_R = 10\lambda$.

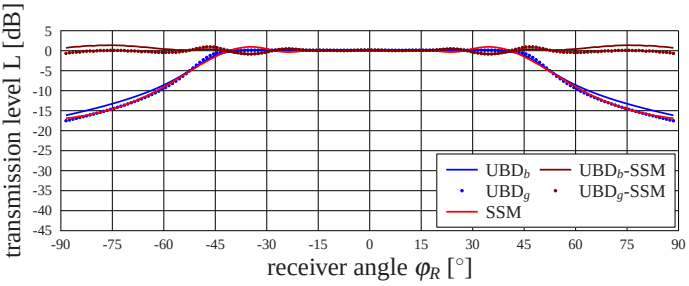

Figure A.26.: Validation of a slit ($d = 10\lambda$) as a function of φ_R, with $r_S = 10\lambda$, $\varphi_S = 0°$ and $r_R = 10\lambda$.

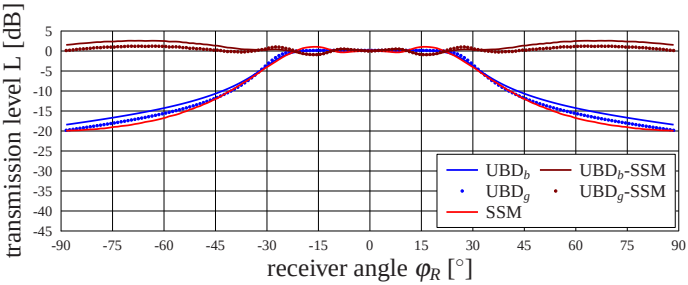

Figure A.27.: Validation of a slit ($d = 10\lambda$) as a function of φ_R, with $r_S = 100\lambda$, $\varphi_S = 0°$ and $r_R = 10\lambda$.

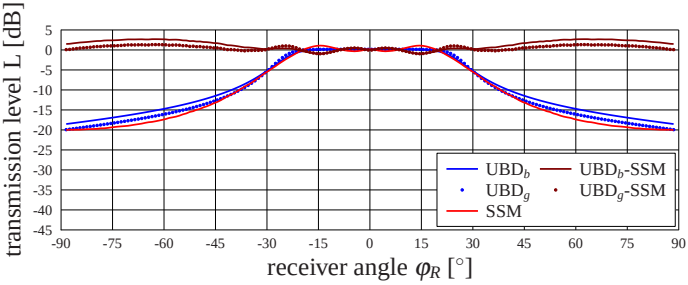

Figure A.28.: Validation of a slit ($d = 10\lambda$) as a function of φ_R, with $r_S = 1000\lambda$, $\varphi_S = 0°$ and $r_R = 10\lambda$.

		$r_S[\lambda]$	region $[dB]$ 0	1	2	3	Min$[dB]$	at[°]	Max$[dB]$	at[°]
UBD - SSM	UBD$_b$	$\frac{1}{10}$	-0.6	$+0.3$	$+0.2$	±0.0	-3.4	±89	$+0.4$	±65
		1	-0.5	$+0.2$	$+0.1$	-0.1	-2.6	±89	$+0.4$	±59
		10	$+1.1$	-0.1	$+0.2$	$+0.4$	-0.9	±36	$+1.4$	±76
		100	$+2.3$	$+1.3$	-0.1	$+1.2$	-0.9	±17	$+2.6$	±68
		1000	$+2.3$	$+1.6$	-0.1	$+1.3$	-1.0	±15	$+2.7$	±63
	UBD$_g$	$\frac{1}{10}$	-0.4	$+0.2$	$+0.1$	±0.0	-3.4	±89	$+0.4$	±68
		1	-0.4	$+0.1$	$+0.1$	-0.1	-3.4	±89	$+0.4$	±77
		10	-0.2	±0.0	$+0.2$	±0.0	-0.8	±36	$+1.0$	±47
		100	$+0.9$	$+0.4$	$+0.1$	$+0.4$	-0.9	±17	$+1.2$	±64
		1000	$+0.9$	$+0.5$	$+0.1$	$+0.5$	-0.9	±15	$+1.3$	±63

Table A.5.: Numerical validation of a slit with $\varphi_S = 0°$, $r_R = d = 10$ and varying source distance r_S.

A.2.2.2. Changing Receiver Distance

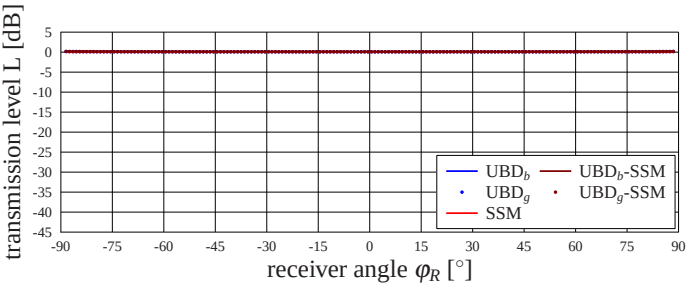

Figure A.29.: Validation of a slit ($d = 10\lambda$) as a function of φ_R, with $r_S = 10\lambda$, $\varphi_S = 0°$ and $r_R = 1\lambda$.

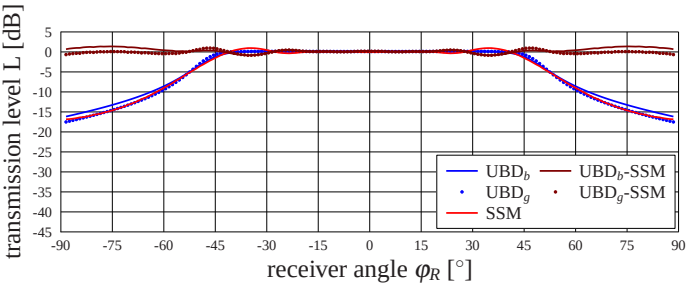

Figure A.30.: Validation of a slit ($d = 10\lambda$) as a function of φ_R, with $r_S = 10\lambda$, $\varphi_S = 0°$ and $r_R = 10\lambda$.

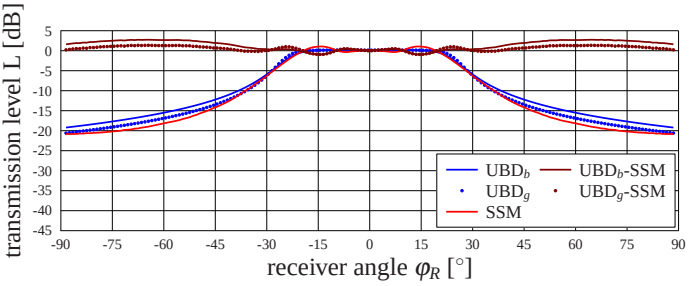

Figure A.31.: Validation of a slit ($d = 10\lambda$) as a function of φ_R, with $r_S = 10\lambda$, $\varphi_S = 0°$ and $r_R = 100\lambda$.

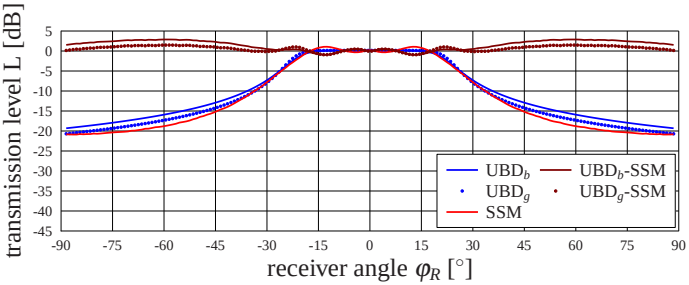

Figure A.32.: Validation of a slit ($d = 10\lambda$) as a function of φ_R, with $r_S = 10\lambda$, $\varphi_S = 0°$ and $r_R = 1000\lambda$.

		$r_R[\lambda]$	region $[dB]$ 0	1	2	3	Min$[dB]$	at[°]	Max$[dB]$	at[°]
UBD - SSM	UBD$_b$	$\frac{1}{10}$	+0.2	+0.2	+0.2	+0.2	+0.2	±25	+0.3	±89
		1	+0.2	+0.1	+0.1	+0.1	+0.1	±35	+0.2	±89
		10	+1.1	−0.1	+0.2	+0.4	−0.9	±36	+1.4	±76
		100	+2.4	+1.8	±0.0	+1.4	−1.0	±15	+2.7	±65
		1000	+2.4	+2.1	±0.0	+1.5	−1.0	±14	+2.9	±60
	UBD$_g$	$\frac{1}{10}$	+0.2	+0.1	+0.1	+0.1	+0.1	±25	+0.2	±89
		1	+0.1	+0.1	+0.1	+0.1	+0.1	±35	+0.2	±89
		10	−0.2	±0.0	+0.2	±0.0	−0.8	±36	+1.0	±47
		100	+1.0	+0.6	+0.1	+0.6	−0.9	±15	+1.4	±65
		1000	+1.0	+0.8	+0.1	+0.6	−0.9	±13	+1.5	±60

Table A.6.: Numerical validation of a slit with $\varphi_S = 0°$, $r_S = d = 10$ and varying receiver distance r_R.

A.2.2.3. Changing Wedge Distance

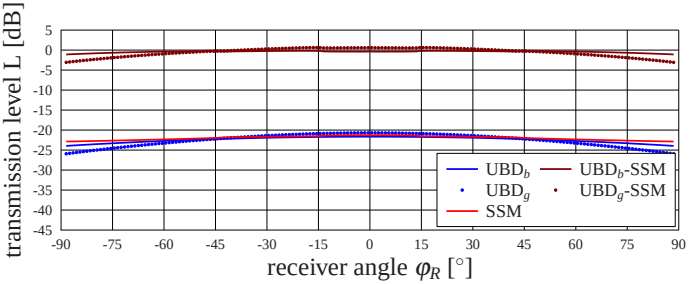

Figure A.33.: Validation of a slit ($d = \frac{1}{10}\lambda$) as a function of φ_R, with $r_S = 10\lambda$, $\varphi_S = 0°$ and $r_R = 10\lambda$.

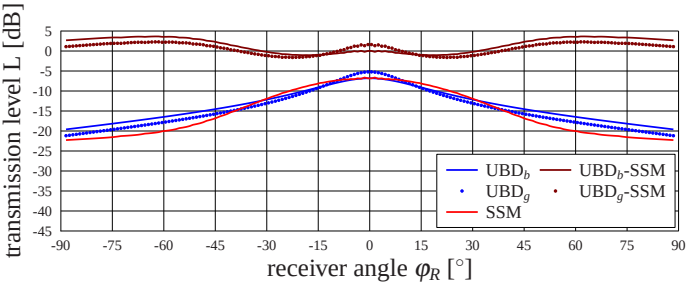

Figure A.34.: Validation of a slit ($d = 1\lambda$) as a function of φ_R, with $r_S = 10\lambda$, $\varphi_S = 0°$ and $r_R = 10\lambda$.

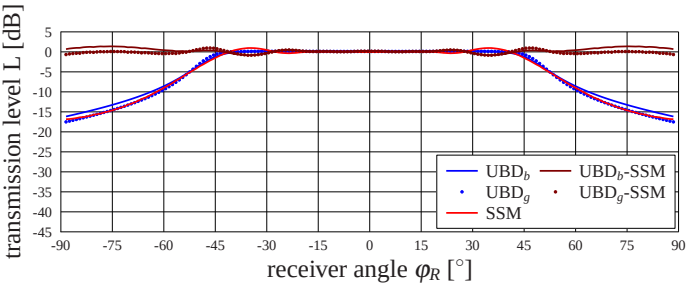

Figure A.35.: Validation of a slit ($d = 10\lambda$) as a function of φ_R, with $r_S = 10\lambda$, $\varphi_S = 0°$ and $r_R = 10\lambda$.

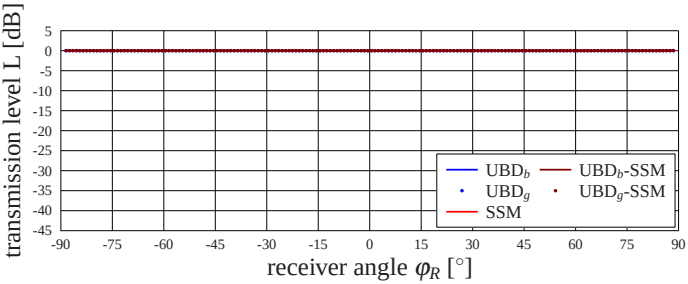

Figure A.36.: Validation of a slit ($d = 100\lambda$) as a function of φ_R, with $r_S = 10\lambda$, $\varphi_S = 0°$ and $r_R = 10\lambda$.

		$d[\lambda]$	region $[dB]$ 0	1	2	3	Min$[dB]$	at$[^\circ]$	Max$[dB]$	at$[^\circ]$
UBD - SSM	UBD_b	$\frac{1}{10}$	-0.7	-0.3	-0.3	-0.4	-1.1	± 89	-0.2	± 19
		1	$+3.3$	$+2.1$	-0.6	$+1.6$	-1.0	± 18	$+3.6$	± 63
		10	$+1.1$	-0.1	$+0.2$	$+0.4$	-0.9	± 36	$+1.4$	± 76
		100	± 0.0	± 0.0	± 0.0	± 0.0	± 0.0	± 01	± 0.0	± 01
		1000	± 0.0	± 0.0	± 0.0	± 0.0	± 0.0	± 01	± 0.0	± 01
	UBD_g	$\frac{1}{10}$	-1.9	-0.3	$+0.5$	-0.5	-3.1	± 89	$+0.6$	± 16
		1	$+1.8$	$+0.9$	-0.5	$+0.7$	-1.6	± 23	$+2.3$	± 62
		10	-0.2	± 0.0	$+0.2$	± 0.0	-0.8	± 36	$+1.0$	± 47
		100	± 0.0	± 0.0	± 0.0	± 0.0	± 0.0	± 1	± 0.0	± 1
		1000	± 0.0	± 0.0	± 0.0	± 0.0	± 0.0	± 1	± 0.0	± 1

Table A.7.: Numerical validation of a slit with $\varphi_S = 0^\circ$, $r_S = r_R = 10$ and varying slit width d.

A.2.2.4. Changing All Distances

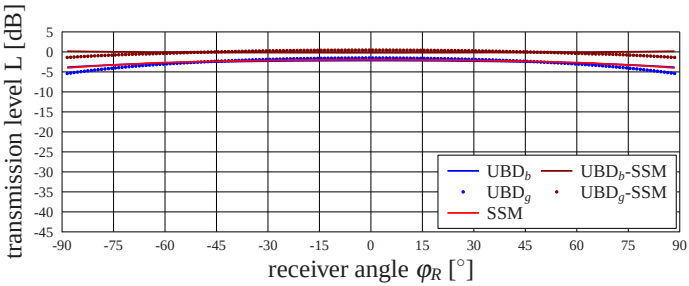

Figure A.37.: Validation of a slit ($d = \frac{1}{10}\lambda$) as a function of φ_R, with $r_S = \frac{1}{10\lambda}$, $\varphi_S = 0^\circ$ and $r_R = \frac{1}{10}\lambda$.

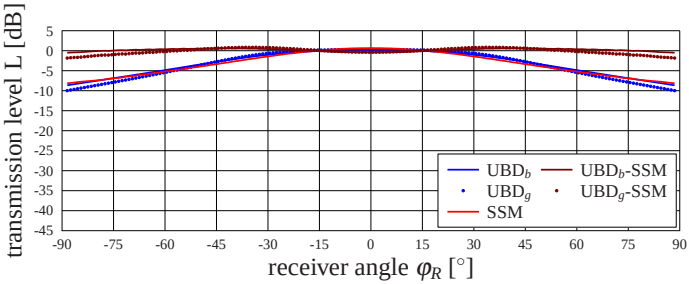

Figure A.38.: Validation of a slit ($d = 1\lambda$) as a function of φ_R, with $r_S = 1\lambda$, $\varphi_S = 0^\circ$ and $r_R = 1\lambda$.

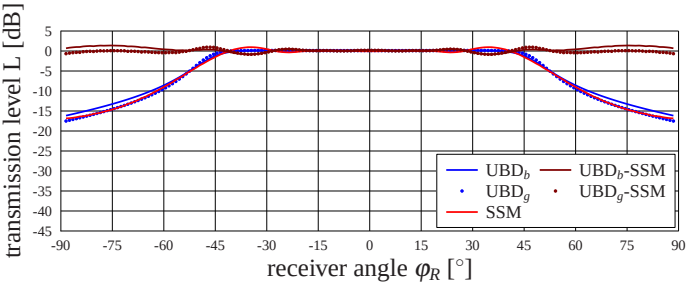

Figure A.39.: Validation of a slit ($d = 10\lambda$) as a function of φ_R, with $r_S = 10\lambda$, $\varphi_S = 0°$ and $r_R = 10\lambda$.

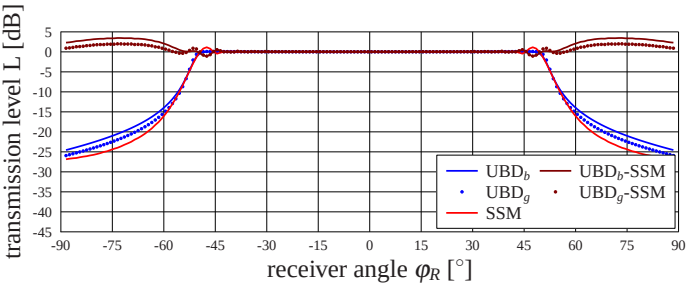

Figure A.40.: Validation of a slit ($d = 100\lambda$) as a function of φ_R, with $r_S = 100\lambda$, $\varphi_S = 0°$ and $r_R = 100\lambda$.

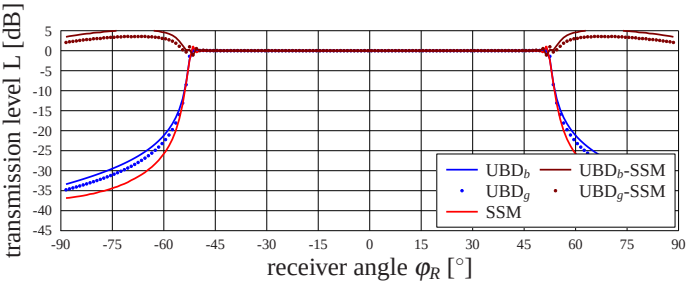

Figure A.41.: Validation of a slit ($d = 1000\lambda$) as a function of φ_R, with $r_S = 1000\lambda$, $\varphi_S = 0°$ and $r_R = 1000\lambda$.

		$\varphi_S[^\circ]$	region $[dB]$ 0	1	2	3	Min$[dB]$	at$[^\circ]$	Max$[dB]$	at$[^\circ]$
UBD - SSM	UBD_b	$\frac{1}{10}$	±0.0	-0.2	-0.2	-0.1	-0.2	±10	$+0.2$	±89
		1	±0.0	$+0.5$	-0.1	$+0.1$	-0.5	±89	$+0.6$	±42
		10	$+1.1$	-0.1	$+0.2$	$+0.4$	-0.9	±36	$+1.4$	±76
		100	$+3.0$	$+0.2$	±0.0	$+1.1$	-1.1	±48	$+3.5$	±74
		1000	$+4.7$	$+0.7$	±0.0	$+1.7$	-1.2	±52	$+5.2$	±66
	UBD_g	$\frac{1}{10}$	-0.8	±0.0	$+0.4$	-0.1	-1.4	±89	$+0.5$	±01
		1	-1.0	$+0.5$	$+0.1$	-0.1	-1.8	±89	$+0.9$	±34
		10	-0.2	±0.0	$+0.2$	±0.0	-0.8	±36	$+1.0$	±47
		100	$+1.6$	±0.0	±0.0	$+0.5$	-1.1	±48	$+2.0$	±74
		1000	$+3.1$	$+0.4$	±0.0	$+1.2$	-1.1	±52	$+3.6$	±66

Table A.8.: Numerical validation of a slit with $\varphi_S = 0^\circ$ and varying source and receiver distances as well as slit width $r_S = r_R = d$.

A.2.2.5. Changing Source Angle

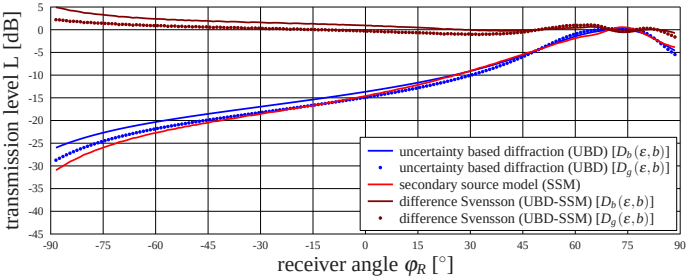

Figure A.42.: Validation of a slit ($d = 10\lambda$) as a function of φ_R, with $r_S = 10\lambda$, $\varphi_S = -75^\circ$ and $r_R = 10\lambda$.

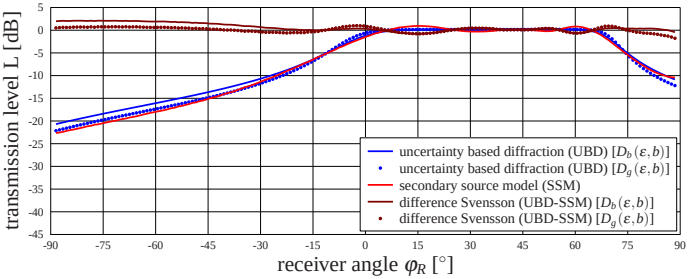

Figure A.43.: Validation of a slit ($d = 10\lambda$) as a function of φ_R, with $r_S = 10\lambda$, $\varphi_S = -45^\circ$ and $r_R = 10\lambda$.

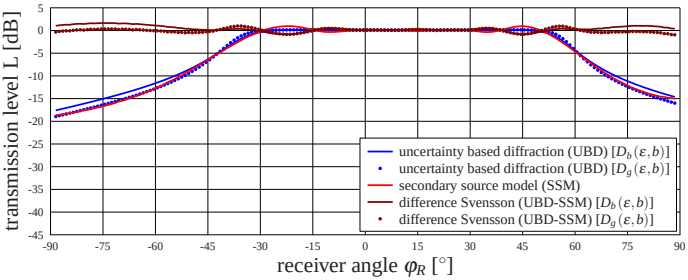

Figure A.44.: Validation of a slit ($d = 10\lambda$) as a function of φ_R, with $r_S = 10\lambda$, $\varphi_S = -15°$ and $r_R = 10\lambda$.

		φ_S[°]	region [dB] 0	1	2	3	Min[dB]	at[°]	Max[dB]	at[°]
UBD - SSM	UBD_b	−75°	+3.4	+1.9	+1.3	+1.2	−0.7	+89	+4.9	−89
		−45°	+2.0	+1.4	+0.2	+0.6	−0.8	+15	+2.1	−77
		−15°	+1.4	+0.4	−0.1	+0.4	−0.9	−23	+1.6	−76
		+15°	+0.7	±0.0	+0.1	+0.4	−0.9	+23	+1.6	+76
		+45°	+0.1	+0.2	−0.3	+0.6	−0.8	−15	+2.1	+77
		+75°	±0.0	±0.0	+0.5	+1.2	−0.7	−89	+4.9	+89
	UBD_g	−75°	+1.4	+0.6	±0.0	+0.2	−1.6	+89	+2.2	−89
		−45°	+0.7	+0.2	±0.0	+0.1	−1.8	+89	+1.0	−03
		−15°	+0.1	+0.1	−0.1	±0.0	−1.0	+89	+1.0	−37
		+15°	−0.4	+0.1	+0.1	±0.0	−1.0	−89	+1.0	+37
		+45°	−0.3	+0.2	−0.2	+0.1	−1.8	−89	+1.0	+03
		+75°	+0.1	−0.3	−0.7	+0.2	−1.6	−89	+2.2	+89

Table A.9.: Numerical validation of a slit with $r_S = r_R = d = 10$ and varying source angles φ_S.

A.2.3. Analytical Comparison of Diffraction at a Double Wedge (2D)

A.2.3.1. Changing Source Distance

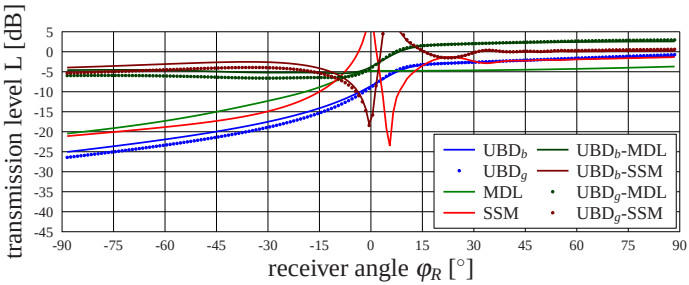

Figure A.45.: Validation of a double wedge ($d = 10\lambda$) as a function of φ_R, with $r_S = \frac{1}{10}\lambda$, $\varphi_S = 0°$ and $r_R = 10\lambda$.

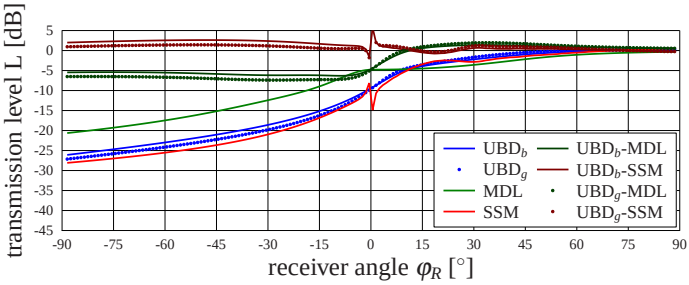

Figure A.46.: Validation of a double wedge ($d = 10\lambda$) as a function of φ_R, with $r_S = 1\lambda$, $\varphi_S = 0°$ and $r_R = 10\lambda$.

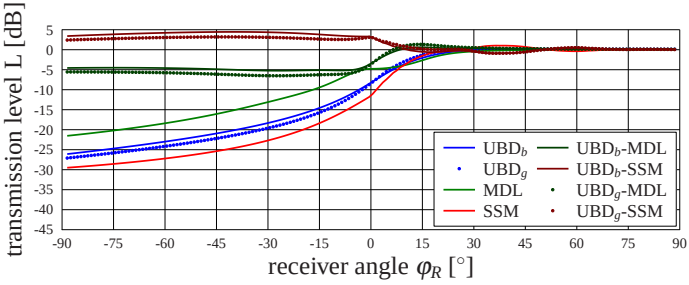

Figure A.47.: Validation of a double wedge ($d = 10\lambda$) as a function of φ_R, with $r_S = 10\lambda$, $\varphi_S = 0°$ and $r_R = 10\lambda$.

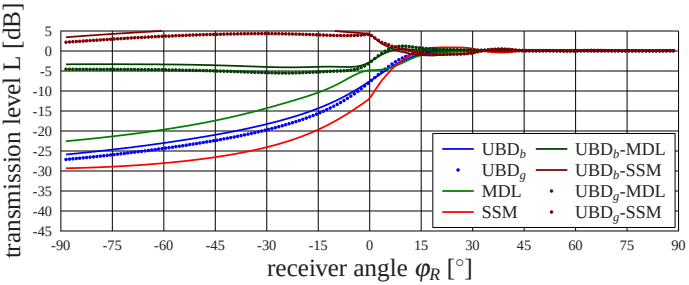

Figure A.48.: Validation of a double wedge ($d = 10\lambda$) as a function of φ_R, with $r_S = 100\lambda$, $\varphi_S = 0°$ and $r_R = 10\lambda$.

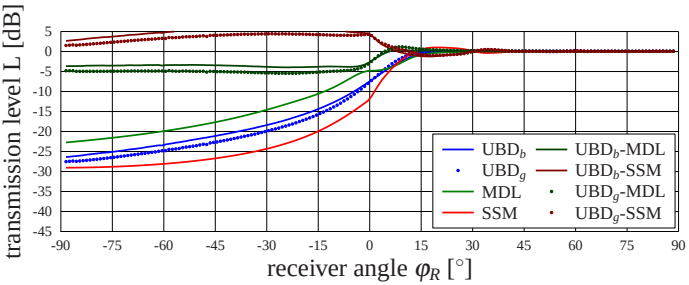

Figure A.49.: Validation of a double wedge ($d = 10\lambda$) as a function of φ_R, with $r_S = 1000\lambda$, $\varphi_S = 0°$ and $r_R = 10\lambda$.

		$r_S[\lambda]$	region $[dB]$ 0	1	2	3	Min$[dB]$	at[°]	Max$[dB]$	at[°]
UBD - MDL	UBD$_b$	$\frac{1}{10}$	−4.6	−4.9	−5.2	−1.5	−5.4	−09	+2.6	+89
		1	−5.4	−5.9	−6.1	−2.6	−6.3	−09	+1.4	+34
		10	−4.5	−4.9	−5.0	−2.4	−5.2	−27	+0.6	+15
		100	−3.3	−3.6	−3.9	−1.8	−4.1	−23	+0.5	+10
		1000	−3.5	−3.5	−3.8	−1.8	−4.0	−24	+0.4	+09
	UBD$_g$	$\frac{1}{10}$	−6.0	−6.4	−6.2	−2.1	−6.6	−31	+3.0	+89
		1	−6.5	−7.1	−7.1	−3.0	−7.4	−29	+2.0	+34
		10	−5.6	−6.1	−6.1	−2.8	−6.5	−28	+1.3	+15
		100	−4.6	−5.0	−5.1	−2.4	−5.5	−25	+1.2	+10
		1000	−4.9	−5.0	−5.0	−2.4	−5.4	−25	+1.2	+09
UBD - SSM	UBD$_b$	$\frac{1}{10}$	−3.5	−2.7	−5.6	−1.8	−1.8	−01	+17.6	+06
		1	+2.3	+2.6	+1.6	+1.2	+1.2	−01	+5.7	+01
		10	+3.8	+4.4	+3.8	+2.0	+2.0	+37	+4.5	−41
		100	+4.3	+5.5	+5.2	+2.5	+2.5	+19	+5.8	−33
		1000	+3.8	+5.5	+5.4	+2.5	+2.5	+18	+5.9	−33
	UBD$_g$	$\frac{1}{10}$	−4.9	−4.1	−6.7	−2.4	−18.4	−01	+18.0	+06
		1	+1.2	+1.4	+0.6	+0.8	−1.8	−01	+5.6	+01
		10	+2.8	+3.2	+2.8	+1.5	−0.9	+37	+3.2	−42
		100	+3.0	+4.1	+4.1	+1.9	−0.9	+19	+4.3	−31
		1000	+2.4	+4.0	+4.2	+1.8	−1.0	+19	+4.4	−29

Table A.10.: Numerical validation of a double wedge with $\varphi_S = 0°$, $r_R = d = 10$ and varying source distance r_S.

A.2.3.2. Changing Receiver Distance

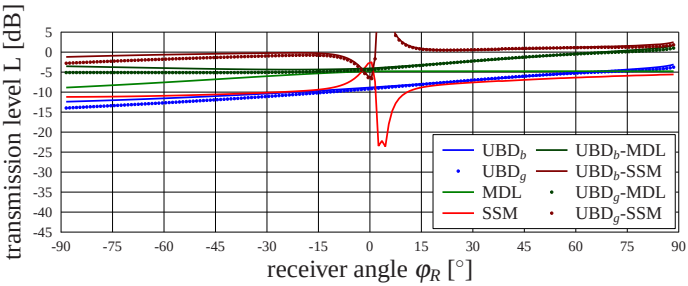

Figure A.50.: Validation of a double wedge ($d = 10\lambda$) as a function of φ_R, with $r_S = 10\lambda$, $\varphi_S = 0°$ and $r_R = \frac{1}{10}\lambda$.

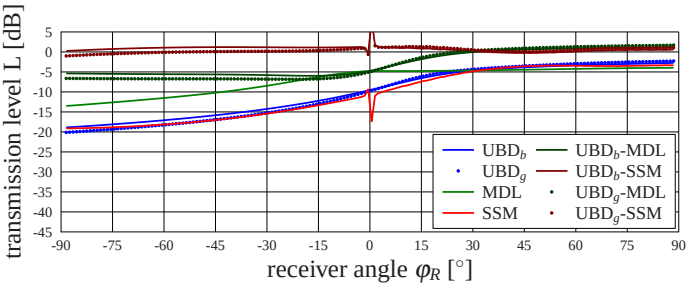

Figure A.51.: Validation of a double wedge ($d = 10\lambda$) as a function of φ_R, with $r_S = 10\lambda$, $\varphi_S = 0°$ and $r_R = 1\lambda$.

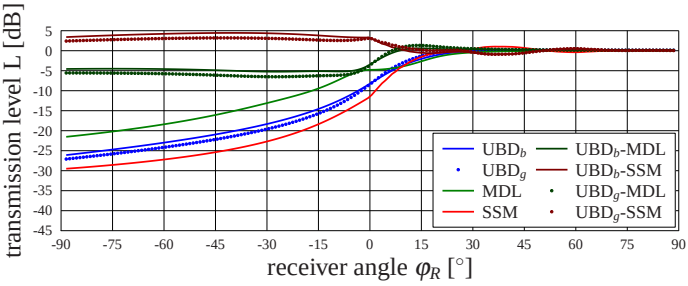

Figure A.52.: Validation of a double wedge ($d = 10\lambda$) as a function of φ_R, with $r_S = 10\lambda$, $\varphi_S = 0°$ and $r_R = 10\lambda$.

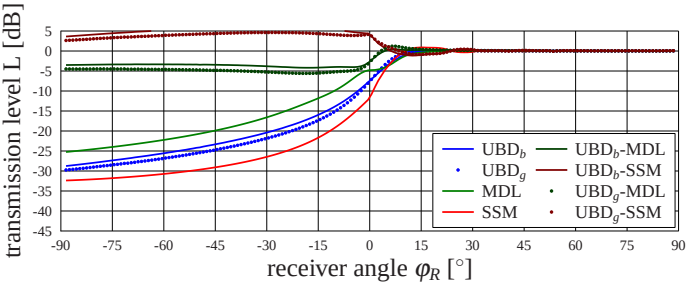

Figure A.53.: Validation of a double wedge ($d = 10\lambda$) as a function of φ_R, with $r_S = 10\lambda$, $\varphi_S = 0°$ and $r_R = 100\lambda$.

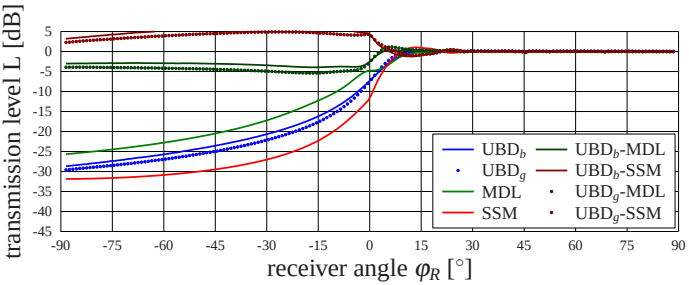

Figure A.54.: Validation of a double wedge ($d = 10\lambda$) as a function of φ_R, with $r_S = 10\lambda$, $\varphi_S = 0°$ and $r_R = 1000\lambda$.

		$r_R[\lambda]$	region $[dB]$ 0	1	2	3	Min$[dB]$	at[°]	Max$[dB]$	at[°]
UBD - MDL	UBD$_b$	$\frac{1}{10}$	−3.8	−4.2	−4.3	−2.7	−4.4	−24	+1.7	+89
		1	−5.5	−5.6	−5.7	−2.9	−6.0	−18	+1.2	+89
		10	−4.5	−4.9	−5.0	−2.4	−5.2	−27	+0.6	+15
		100	−3.4	−3.5	−4.0	−1.8	−4.2	−18	+0.4	+08
		1000	−2.9	−3.1	−3.7	−1.6	−3.9	−16	+0.4	+07
	UBD$_g$	$\frac{1}{10}$	−5.1	−5.1	−4.8	−3.3	−5.1	−48	+1.0	+89
		1	−6.7	−6.7	−6.4	−3.2	−6.8	−23	+1.7	+89
		10	−5.6	−6.1	−6.1	−2.8	−6.5	−28	+1.3	+15
		100	−4.5	−4.9	−5.2	−2.4	−5.6	−20	+1.2	+07
		1000	−4.0	−4.5	−5.0	−2.3	−5.4	−18	+1.2	+07
UBD - SSM	UBD$_b$	$\frac{1}{10}$	−0.9	−0.4	−1.1	+0.4	−6.3	+01	+15.0	+05
		1	+0.7	+1.2	+1.1	+0.7	−0.4	−01	+8.0	+01
		10	+3.8	+4.4	+3.8	+2.0	−0.9	+37	+4.5	−41
		100	+4.4	+5.7	+5.5	+2.6	−1.2	+13	+6.1	−28
		1000	+4.2	+5.9	+5.8	+2.7	−1.2	+13	+6.4	−25
	UBD$_g$	$\frac{1}{10}$	−2.3	−1.3	−1.6	−0.1	−6.6	+01	+14.8	+05
		1	−0.5	+0.1	+0.4	+0.4	−1.0	−89	+7.8	+01
		10	+2.8	+3.2	+2.8	+1.5	−0.9	+37	+3.2	−42
		100	+3.3	+4.3	+4.3	+2.1	−0.8	+14	+4.6	−29
		1000	+3.1	+4.5	+4.6	+2.1	−1.0	+13	+4.9	−27

Table A.11.: Numerical validation of a double wedge with $\varphi_S = 0°$, $r_S = d = 10$ and varying receiver distance r_R.

A.2.3.3. Changing Wedge Distance

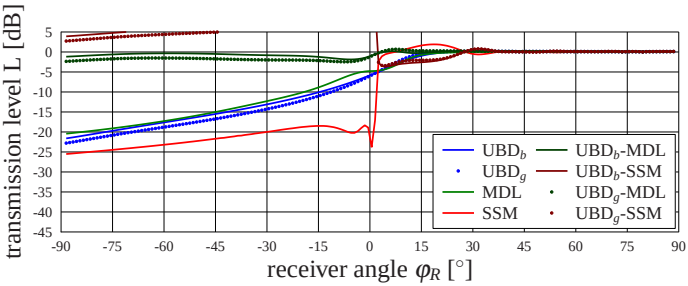

Figure A.55.: Validation of a double wedge ($d = \frac{1}{10}\lambda$) as a function of φ_R, with $r_S = 10\lambda$, $\varphi_S = 0°$ and $r_R = 10\lambda$.

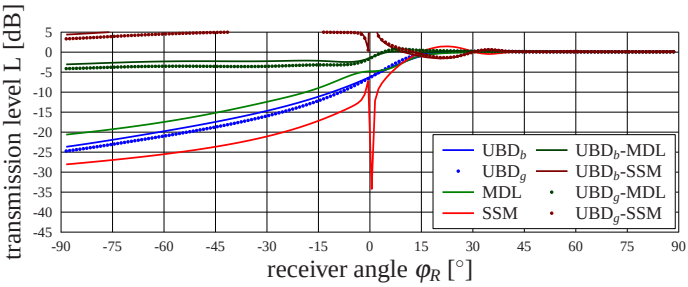

Figure A.56.: Validation of a double wedge ($d = 1\lambda$) as a function of φ_R, with $r_S = 10\lambda$, $\varphi_S = 0°$ and $r_R = 10\lambda$.

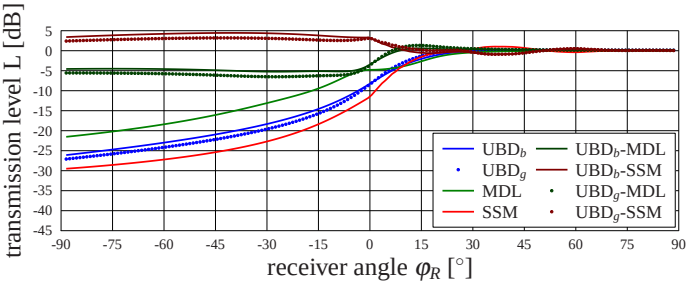

Figure A.57.: Validation of a double wedge ($d = 10\lambda$) as a function of φ_R, with $r_S = 10\lambda$, $\varphi_S = 0°$ and $r_R = 10\lambda$.

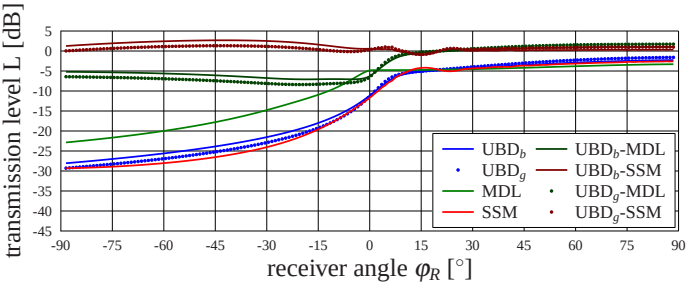

Figure A.58.: Validation of a double wedge ($d = 100\lambda$) as a function of φ_R, with $r_S = 10\lambda$, $\varphi_S = 0°$ and $r_R = 10\lambda$.

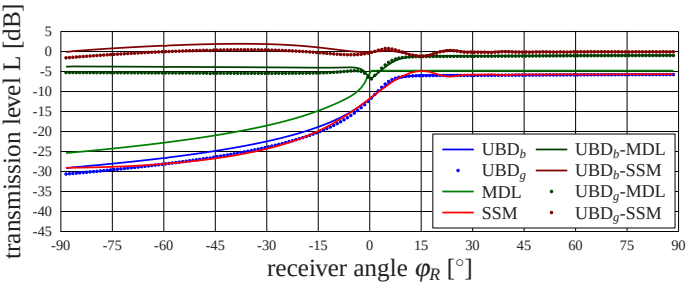

Figure A.59.: Validation of a double wedge ($d = 1000\lambda$) as a function of φ_R, with $r_S = 10\lambda$, $\varphi_S = 0°$ and $r_R = 10\lambda$.

		$d[\lambda]$	region $[dB]$ 0	1	2	3	Min$[dB]$	at$[°]$	Max$[dB]$	at$[°]$
UBD - MDL	UBD$_b$	$\frac{1}{10}$	−0.7	−0.5	−1.3	−0.4	−1.9	−06	+0.2	+33
		1	−2.7	−2.3	−2.2	−1.1	−3.1	−89	+0.2	+30
		10	−4.5	−4.9	−5.0	−2.4	−5.2	−27	+0.6	+15
		100	−5.4	−6.1	−7.0	−3.0	−7.1	−19	+1.0	+89
		1000	−3.8	−3.9	−4.1	−2.6	−6.7	+01	−0.9	+89
	UBD$_g$	$\frac{1}{10}$	−1.8	−1.7	−2.1	−0.9	−2.5	−08	+0.7	+08
		1	−3.8	−3.6	−3.1	−1.7	−4.1	−89	+0.8	+09
		10	−5.6	−6.1	−6.1	−6.1	−6.5	−28	+1.3	+15
		100	−6.6	−7.5	−8.1	−3.4	−8.4	−21	+1.7	+89
		1000	−5.3	−5.4	−5.3	−3.4	−6.8	+01	−1.0	+89
UBD - SSM	UBD$_b$	$\frac{1}{10}$	+4.8	+6.2	+9.3	+3.3	−3.7	+05	+18.2	+01
		1	+5.1	+6.2	+5.7	+3.1	−1.6	+21	+28.3	+01
		10	+3.8	+4.4	+3.8	+2.0	−0.9	+37	+4.5	−41
		100	+1.9	+2.6	+1.5	+1.1	−0.9	+15	+2.7	−43
		1000	+0.8	+1.8	+0.9	+0.5	−1.1	+15	+1.9	−37
	UBD$_g$	$\frac{1}{10}$	+3.6	+5.0	+8.4	+2.8	−3.4	+05	+18.1	+08
		1	+3.9	+4.9	+4.8	+2.5	−1.3	+23	+28.2	+09
		10	+2.8	+3.2	+2.8	+1.5	−0.9	+37	+3.2	+15
		100	+0.6	+1.3	+0.4	+0.7	−0.8	+16	+1.3	+89
		1000	−0.8	+0.3	−0.2	−0.2	−1.6	−89	+0.8	+89

Table A.12.: Numerical validation of a double wedge with $\varphi_S = 0°$, $r_R = r_S = 10$ and varying wedge distance d.

A.2.3.4. Changing All Distances

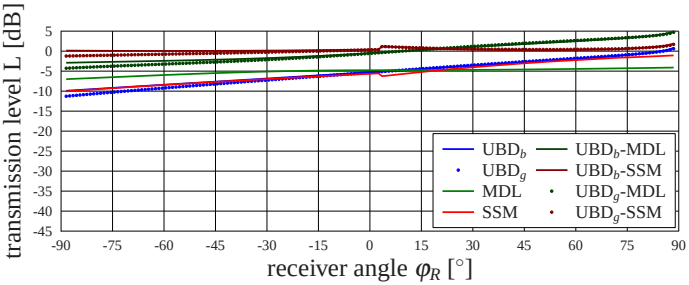

Figure A.60.: Validation of a double wedge ($d = \frac{1}{10}\lambda$) as a function of φ_R, with $r_S = \frac{1}{10}\lambda$, $\varphi_S = 0°$ and $r_R = \frac{1}{10}\lambda$.

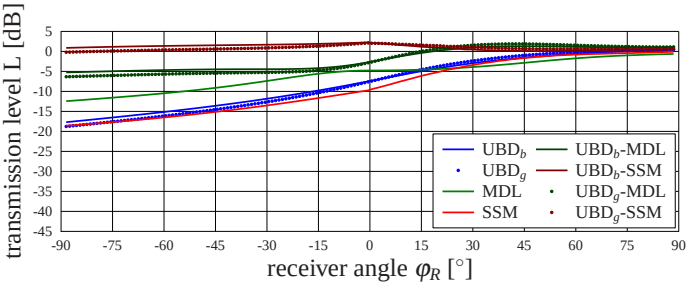

Figure A.61.: Validation of a double wedge ($d = 1\lambda$) as a function of φ_R, with $r_S = 1\lambda$, $\varphi_S = 0°$ and $r_R = 1\lambda$.

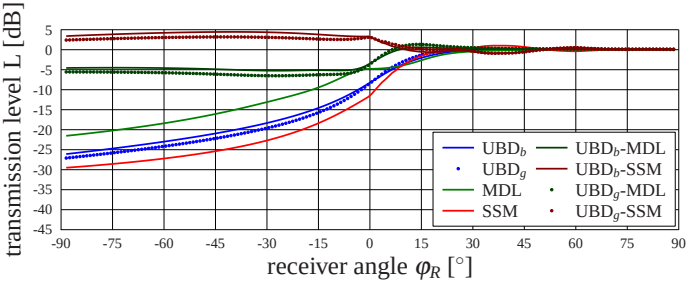

Figure A.62.: Validation of a double wedge ($d = 10\lambda$) as a function of φ_R, with $r_S = 10\lambda$, $\varphi_S = 0°$ and $r_R = 10\lambda$.

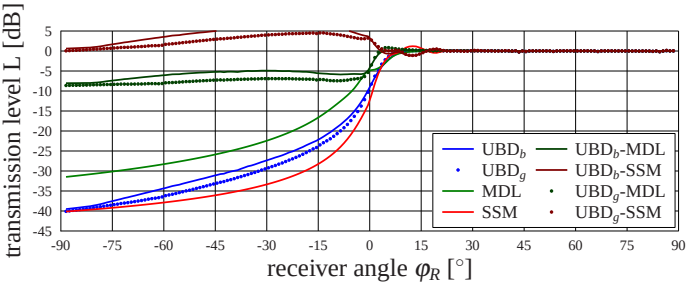

Figure A.63.: Validation of a double wedge ($d = 100\lambda$) as a function of φ_R, with $r_S = 100\lambda$, $\varphi_S = 0°$ and $r_R = 100\lambda$.

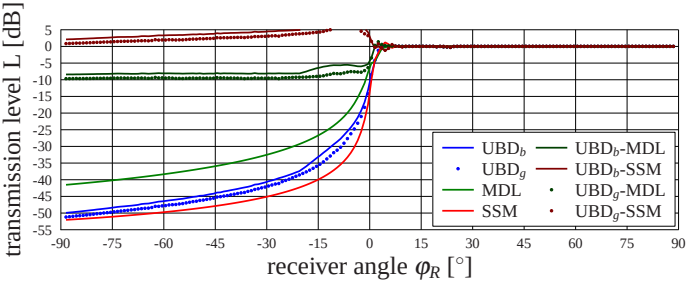

Figure A.64.: Validation of a double wedge ($d = 1000\lambda$) as a function of φ_R, with $r_S = 1000\lambda$, $\varphi_S = 0°$ and $r_R = 1000\lambda$.

		$r_S = r_R = d[\lambda]$	region [dB] 0	1	2	3	Min[dB]	at[°]	Max[dB]	at[°]
UBD - MDL	UBD$_b$	$\frac{1}{10}$	−2.7	−2.1	−1.2	−0.1	−2.9	−89	+4.9	+89
		1	−5.0	−4.5	−4.0	−1.9	−5.3	−89	+1.3	+45
		10	−4.5	−4.9	−4.0	−2.4	−5.2	−27	+0.6	+15
		100	−7.3	−5.3	−5.4	−3.0	−8.0	−89	+0.2	+12
		1000	−8.2	−8.1	−6.8	−3.9	−8.4	−89	+0.7	+03
	UBD$_g$	$\frac{1}{10}$	−3.7	−2.7	−1.4	−0.4	−4.3	−89	+4.7	+89
		1	−6.0	−5.4	−4.5	−2.2	−6.3	−89	+1.9	+43
		10	−5.6	−6.1	−6.1	−2.8	−6.5	−28	+1.3	+15
		100	−8.4	−7.4	−7.0	−3.8	−8.6	−89	+0.9	+06
		1000	−9.5	−9.5	−8.6	−4.6	−9.7	−89	+1.4	+03
UBD - SSM	UBD$_b$	$\frac{1}{10}$	+0.1	+0.1	0.03	+0.4	+0.1	−60	+1.9	+89
		1	+1.1	+1.5	+1.9	+1.1	+0.1	+49	+2.3	−01
		10	+3.8	+4.4	+3.8	+2.0	−0.9	+37	+4.5	−41
		100	+1.8	+4.9	+5.7	+2.1	−1.2	+13	+6.3	−19
		1000	+2.7	+3.8	+6.1	+2.1	−1.2	+05	+7.8	−08
	UBD$_g$	$\frac{1}{10}$	−1.0	−0.5	±0.0	+0.1	−1.2	−89[°]	+1.7	+89
		1	+0.1	+0.6	+1.4	+0.8	−0.2	−89[°]	+2.1	−01
		10	+2.8	+3.2	+2.8	+1.5	−0.9	+37[°]	+3.2	−42
		100	+0.7	+2.9	+4.0	+1.3	−1.1	+13[°]	+4.5	−14
		1000	+1.4	+2.4	+4.2	+1.4	−1.2	+05[°]	+5.7	−06

Table A.13.: Numerical validation of a double wedge with $\varphi_S = 0°$ and varying source and receiver distances as well as wedge distance $r_S = r_R = d$.

A.2.3.5. Changing Source Angle

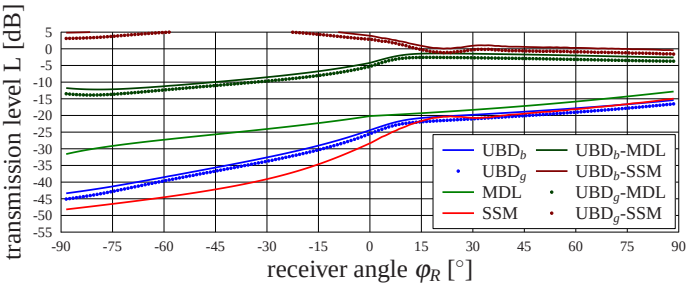

Figure A.65.: Validation of a double wedge ($d = 10\lambda$) as a function of φ_R, with $r_S = 10\lambda$, $\varphi_S = -75°$ and $r_R = 10\lambda$.

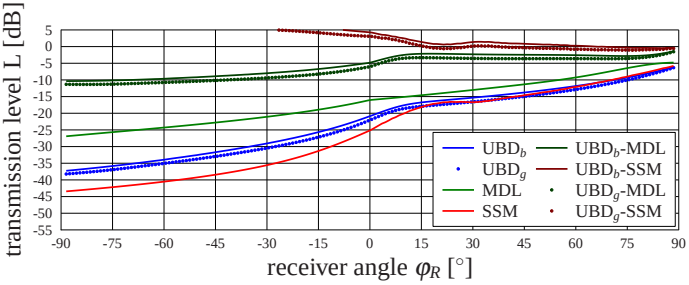

Figure A.66.: Validation of a double wedge ($d = 10\lambda$) as a function of φ_R, with $r_S = 10\lambda$, $\varphi_S = -45°$ and $r_R = 10\lambda$.

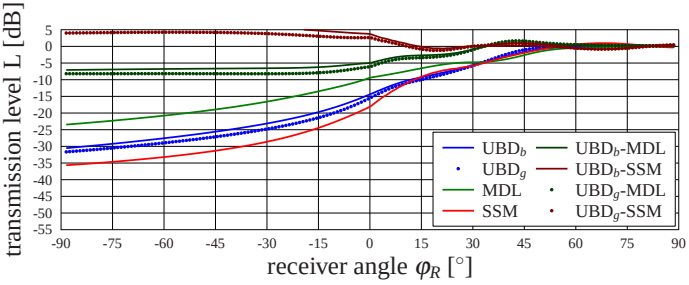

Figure A.67.: Validation of a double wedge ($d = 10\lambda$) as a function of φ_R, with $r_S = 10\lambda$, $\varphi_S = -15°$ and $r_R = 10\lambda$.

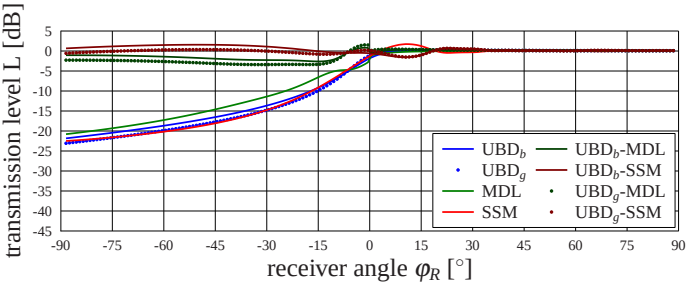

Figure A.68.: Validation of a double wedge ($d = 10\lambda$) as a function of φ_R, with $r_S = 10\lambda$, $\varphi_S = +15°$ and $r_R = 10\lambda$.

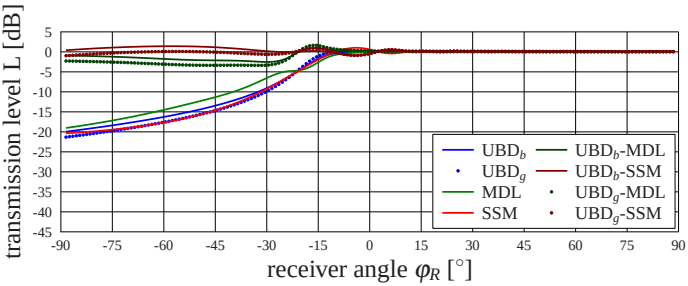

Figure A.69.: Validation of a double wedge ($d = 10\lambda$) as a function of φ_R, with $r_S = 10\lambda$, $\varphi_S = +75°$ and $r_R = 10\lambda$.

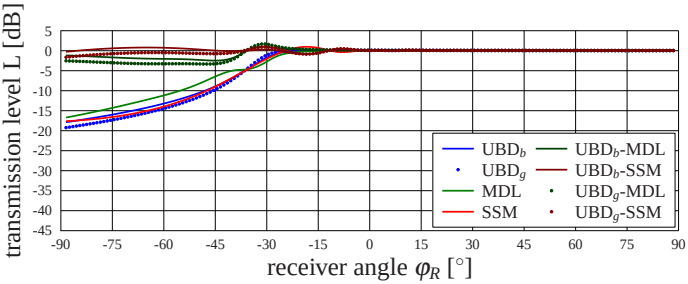

Figure A.70.: Validation of a double wedge ($d = 10\lambda$) as a function of φ_R, with $r_S = 10\lambda$, $\varphi_S = +75°$ and $r_R = 10\lambda$.

		$\varphi_S[^\circ]$	region $[dB]$ 0	1	2	3	Min$[dB]$	at$[^\circ]$	Max$[dB]$	at$[^\circ]$
UBD - MDL	UBD_b	−75	−11.9	−9.9	−6.6	−5.7	−12.2	−80	−1.4	+20
		−45	−10.1	−8.9	−6.6	−5.5	−10.4	−89	−1.4	+89
		−15	−6.9	−6.7	−6.0	−3.6	−7.1	−89	+1.0	+43
		+15	−1.2	−1.9	−1.6	−0.7	−2.6	−15	+0.8	−02
		+45	−1.3	−2.1	−0.2	−0.5	−2.5	−30	+1.0	−17
		+75	−1.7	−1.5	+0.3	−0.4	−2.5	−46	+1.0	−32
	UBD_g	−75°	−13.4	−11.0	−7.8	−6.9	−13.9	−82	−2.6	+17
		−45°	−11.2	−10.1	−8.1	−6.7	−11.4	−83	−1.5	+89
		−15°	−8.2	−8.2	−7.6	−4.4	−8.2	−34	+1.7	+43
		+15°	−2.4	−3.1	−2.1	−1.2	−3.4	−33	+1.5	−02
		+45°	−2.6	−3.3	−0.1	−0.9	−3.4	−33	+1.6	−17
		+75°	−3.0	−2.0	+0.4	−0.7	−3.4	−48	+1.7	−31
UBD - SSM	UBD_b	−75	+5.3	+6.5	+5.5	+3.2	−0.4	+89	+6.6	−39
		−45	+6.4	+6.7	+5.6	+3.5	−0.5	+86	+6.7	−45
		−15	+5.4	+5.7	+4.7	+2.7	−0.9	+67	+5.7	−46
		+15	+1.1	+1.5	+0.1	+0.4	−1.6	+11	+1.6	−50
		+45	+1.0	+1.0	−0.2	+0.4	−0.9	−05	+1.4	−58
		+75	+0.5	+0.2	−0.1	+0.1	−0.9	−19	+0.8	−65
	UBD_g	−75	+3.9	+5.4	+4.2	+2.0	−1.6	+89	+5.5	−42
		−45	+5.3	+5.4	+4.1	+2.4	−1.1	+77	+5.5	−52
		−15	+4.1	+4.1	+3.1	+1.9	−1.2	+19	+4.3	−57
		+15	−0.1	+0.3	−0.4	±0.0	−1.5	+11	+0.7	+23
		+45	−0.3	−0.2	−0.1	±0.0	−1.0	−89	+0.9	−16
		+75	−0.8	−0.3	±0.0	−0.2	−1.6	−89	+0.9	−31

Table A.14.: Numerical validation of a double wedge with $r_S = r_R = d = 10$ and varying source angles φ_S.

A.2.4. Analytical Comparison of Diffraction at a Single Wedge with a Reflecting Floor (2D)

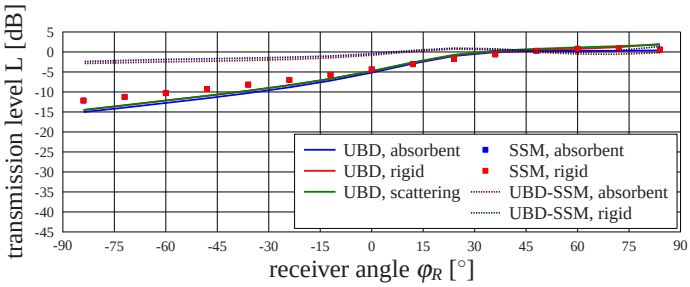

Figure A.71.: Influence of a reflecting floor in front of wedge ($r = 1\lambda$).

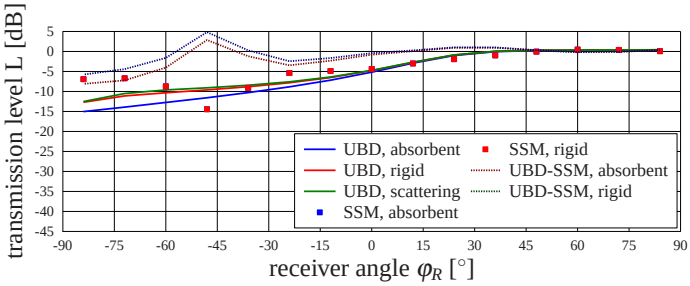

Figure A.72.: Influence of a reflecting floor behind wedge ($r = 1)\lambda$.

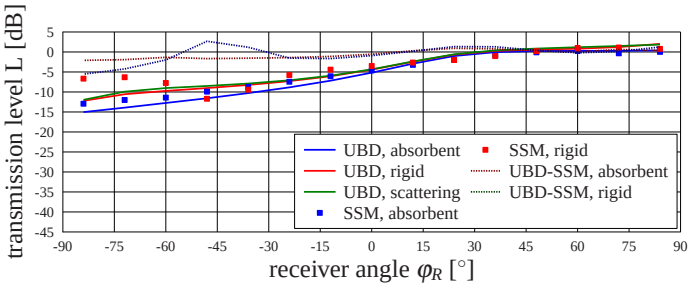

Figure A.73.: Influence of a reflecting floor in front and behind a wedge ($r = 1\lambda$).

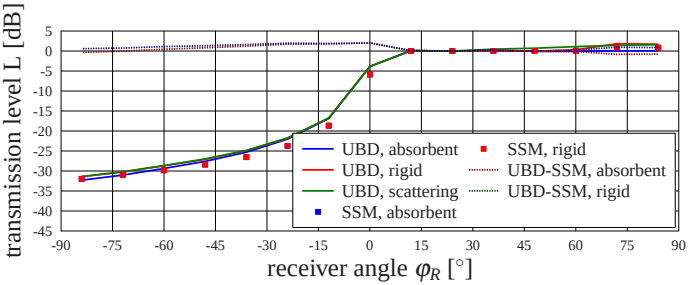

Figure A.74.: Influence of a reflecting floor in front of wedge ($r = 100\lambda$).

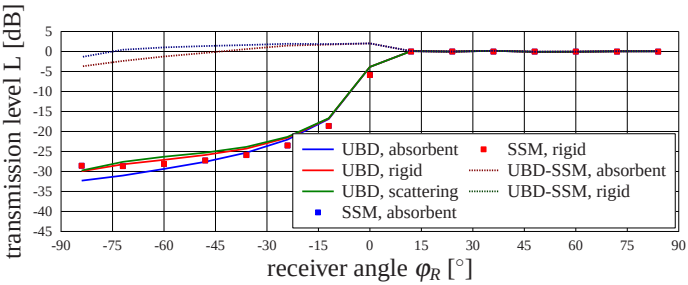

Figure A.75.: Influence of a reflecting floor behind wedge ($r = 100\lambda$).

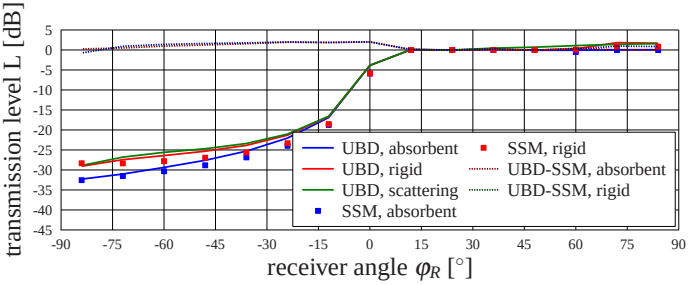

Figure A.76.: Influence of a reflecting floor in front and behind a wedge ($r = 100\lambda$).

A.2.5. Analytical Comparison of Diffraction at a rectangular Aperture (3D)

A.2.5.1. Finite Wedge

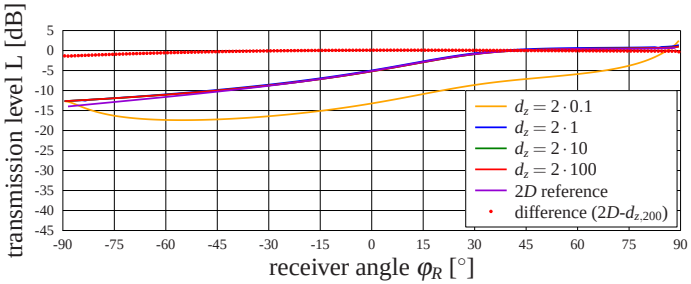

Figure A.77.: Validation of $3D$ diffraction at an (in)finite wedge ($r_S = r_R = 1$).

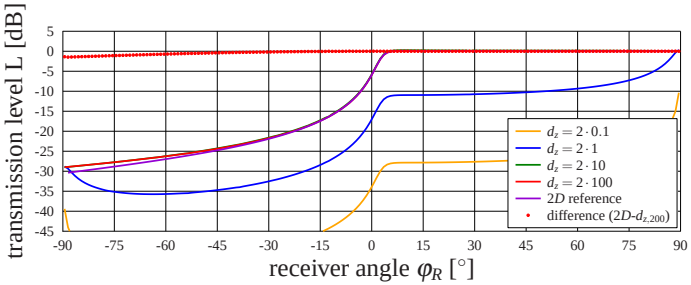

Figure A.78.: Validation of $3D$ diffraction at an (in)finite wedge ($r_S = r_R = 100$).

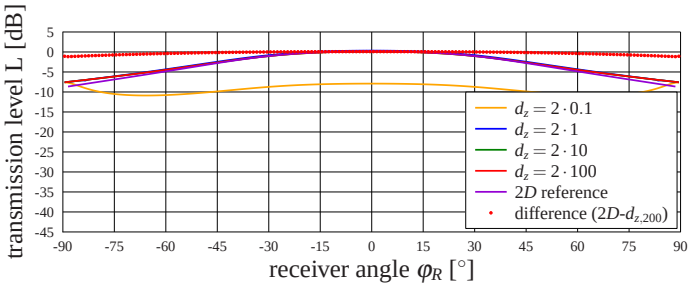

Figure A.79.: Validation of $3D$ diffraction at an (in)finite slit ($r_S = r_R = d_y = 1$).

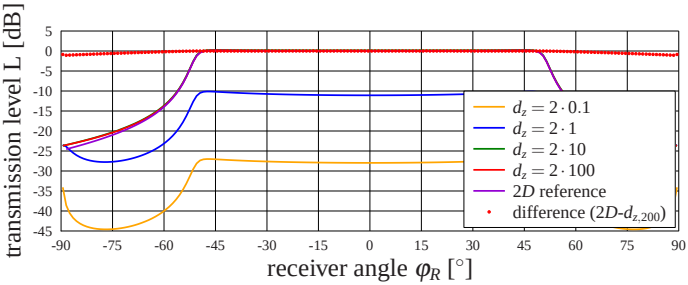

Figure A.80.: Validation of $3D$ diffraction at an (in)finite slit ($r_S = r_R = d_y = 100$).

A.2.5.2. Local Coordiante System

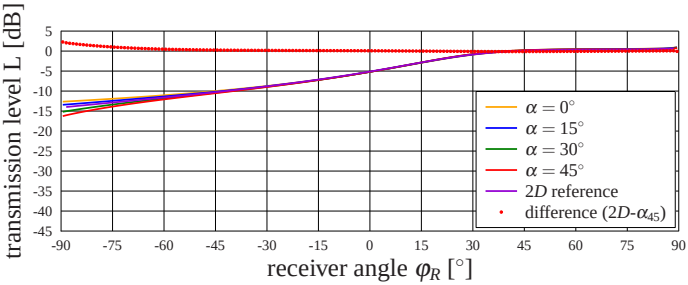

Figure A.81.: Validation of the local coordinate system at a wedge ($r_S = r_R = 1$). The coordiante system is rotated by an angle of α.

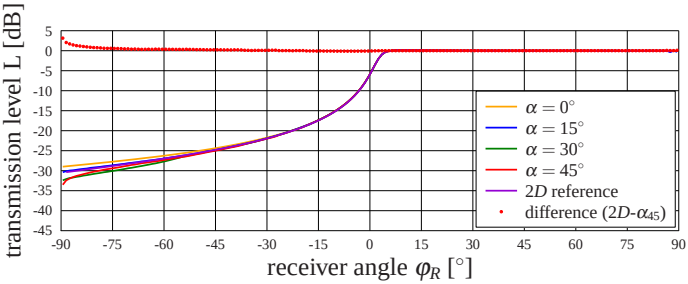

Figure A.82.: Validation of the local coordinate system at a wedge ($r_S = r_R = 100$). The coordiante system is rotated by an angle of α.

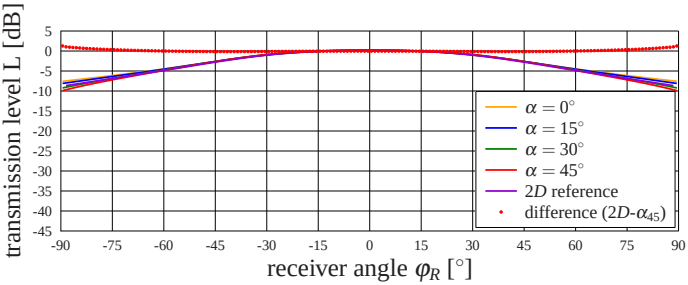

Figure A.83.: Validation of the local coordinate system at a slit ($r_S = r_R = d_y = 1$). The coordiante system is rotated by an angle of α.

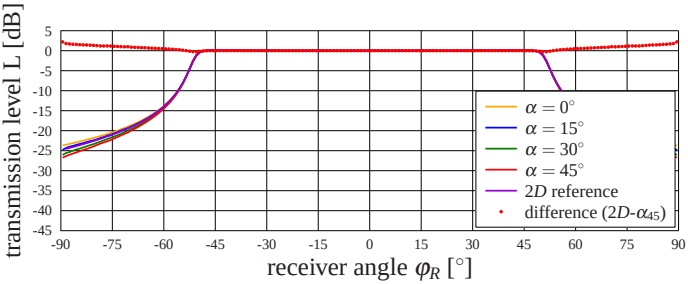

Figure A.84.: Validation of the local coordinate system at a slit ($r_S = r_R = d_y = 100$). The coordiante system is rotated by an angle of α.

A.2.5.3. Oblique Incidence

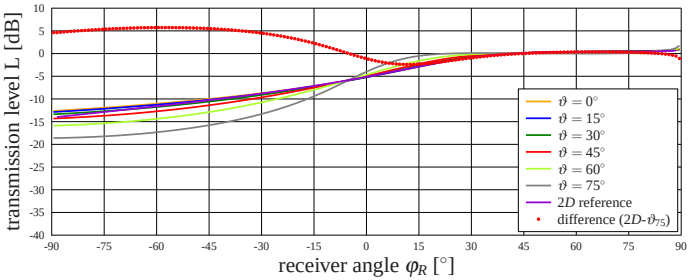

(a) Uncertainty relation Based Diffraction

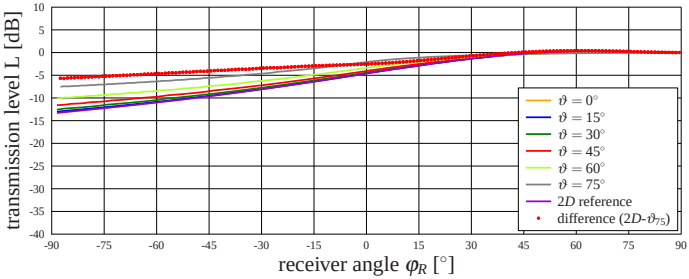

(b) Secondary Source Model

Figure A.85.: Validation of oblique incidence at a wedge ($r_S = r_R = 1$). The diffraction plane is rotated by an angle of ϑ.

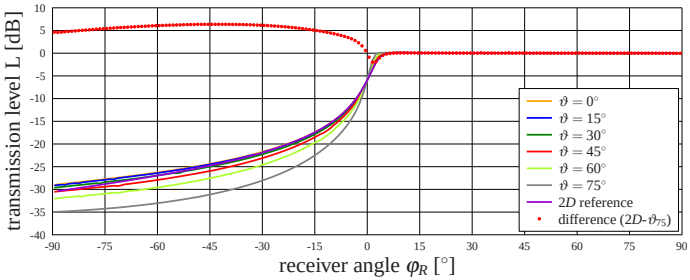

(a) Uncertainty relation Based Diffraction

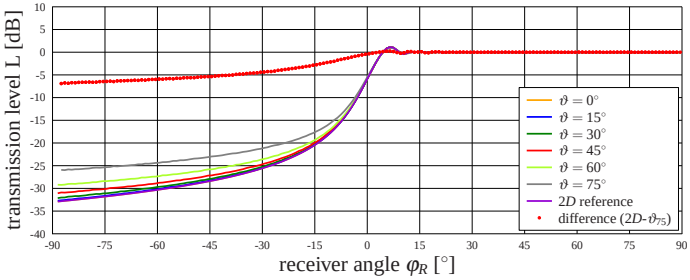

(b) Secondary Source Model

Figure A.86.: Validation of oblique incidence at a wedge ($r_S = r_R = 100$). The diffraction plane is rotated by an angle of ϑ.

A.2.6. Sound Intensity Maps for Diffraction at a Single Wedge Computed with Sound Particle Radiosity

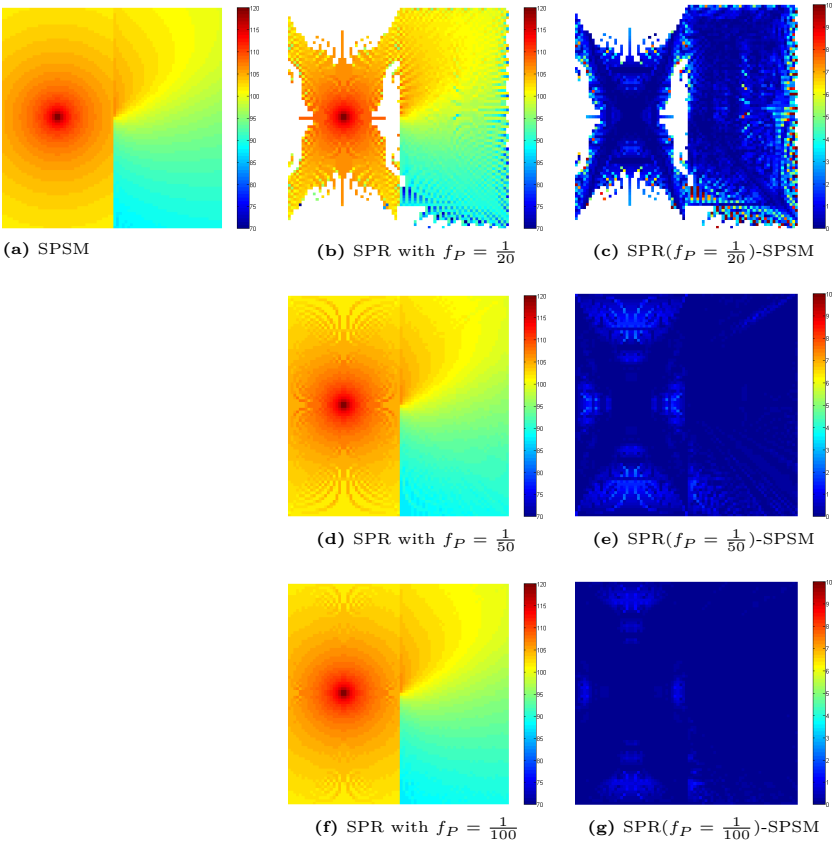

(a) SPSM **(b)** SPR with $f_P = \frac{1}{20}$ **(c)** SPR($f_P = \frac{1}{20}$)-SPSM

(d) SPR with $f_P = \frac{1}{50}$ **(e)** SPR($f_P = \frac{1}{50}$)-SPSM

(f) SPR with $f_P = \frac{1}{100}$ **(g)** SPR($f_P = \frac{1}{100}$)-SPSM

Figure A.87.: The influence of the applied discretization in Sound Particle Radiosity on diffraction simulation compared with the Sound Particle Simulation Method for $f = 31.5Hz$.

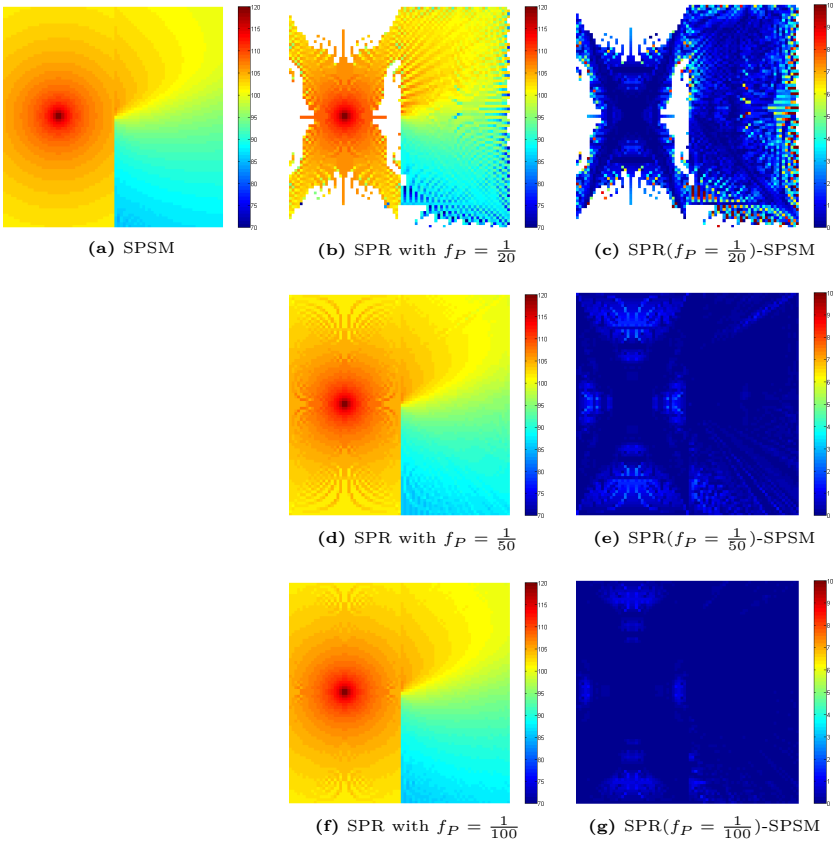

(a) SPSM **(b)** SPR with $f_P = \frac{1}{20}$ **(c)** SPR($f_P = \frac{1}{20}$)-SPSM

(d) SPR with $f_P = \frac{1}{50}$ **(e)** SPR($f_P = \frac{1}{50}$)-SPSM

(f) SPR with $f_P = \frac{1}{100}$ **(g)** SPR($f_P = \frac{1}{100}$)-SPSM

Figure A.88.: The influence of the applied discretization in Sound Particle Radiosity on diffraction simulation compared with the Sound Particle Simulation Method for $f = 63Hz$.

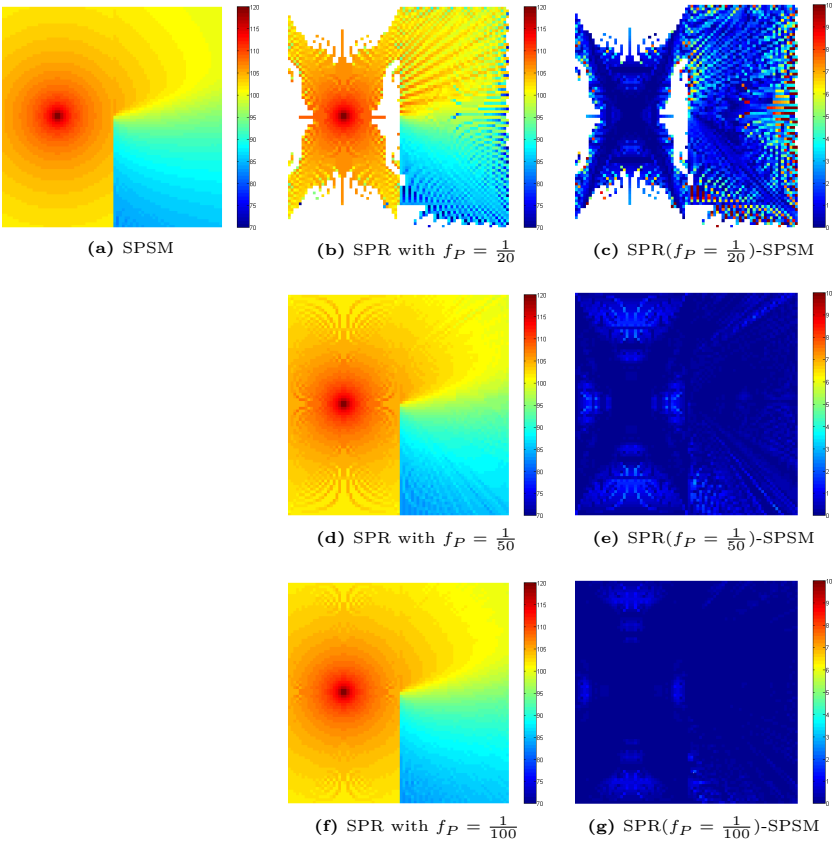

(a) SPSM **(b)** SPR with $f_P = \frac{1}{20}$ **(c)** SPR($f_P = \frac{1}{20}$)-SPSM

(d) SPR with $f_P = \frac{1}{50}$ **(e)** SPR($f_P = \frac{1}{50}$)-SPSM

(f) SPR with $f_P = \frac{1}{100}$ **(g)** SPR($f_P = \frac{1}{100}$)-SPSM

Figure A.89.: The influence of the applied discretization in Sound Particle Radiosity on diffraction simulation compared with the Sound Particle Simulation Method for $f = 125Hz$.

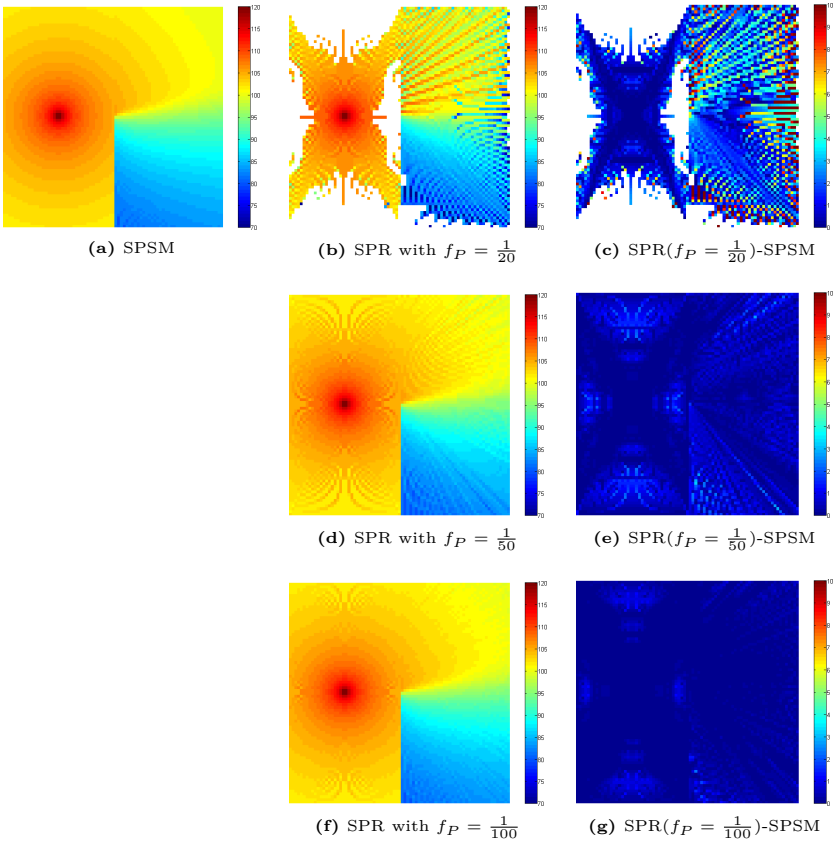

(a) SPSM **(b)** SPR with $f_P = \frac{1}{20}$ **(c)** SPR($f_P = \frac{1}{20}$)-SPSM

(d) SPR with $f_P = \frac{1}{50}$ **(e)** SPR($f_P = \frac{1}{50}$)-SPSM

(f) SPR with $f_P = \frac{1}{100}$ **(g)** SPR($f_P = \frac{1}{100}$)-SPSM

Figure A.90.: The influence of the applied discretization in Sound Particle Radiosity on diffraction simulation compared with the Sound Particle Simulation Method for $f = 250Hz$.

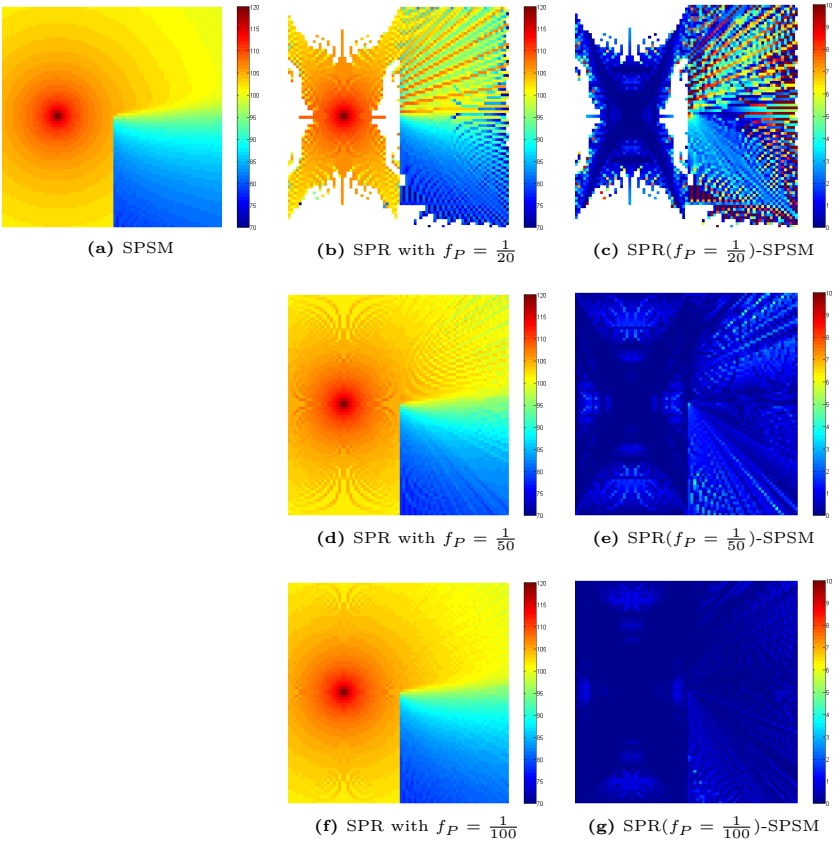

(a) SPSM **(b)** SPR with $f_P = \frac{1}{20}$ **(c)** SPR($f_P = \frac{1}{20}$)-SPSM

(d) SPR with $f_P = \frac{1}{50}$ **(e)** SPR($f_P = \frac{1}{50}$)-SPSM

(f) SPR with $f_P = \frac{1}{100}$ **(g)** SPR($f_P = \frac{1}{100}$)-SPSM

Figure A.91.: The influence of the applied discretization in Sound Particle Radiosity on diffraction simulation compared with the Sound Particle Simulation Method for $f = 500Hz$.

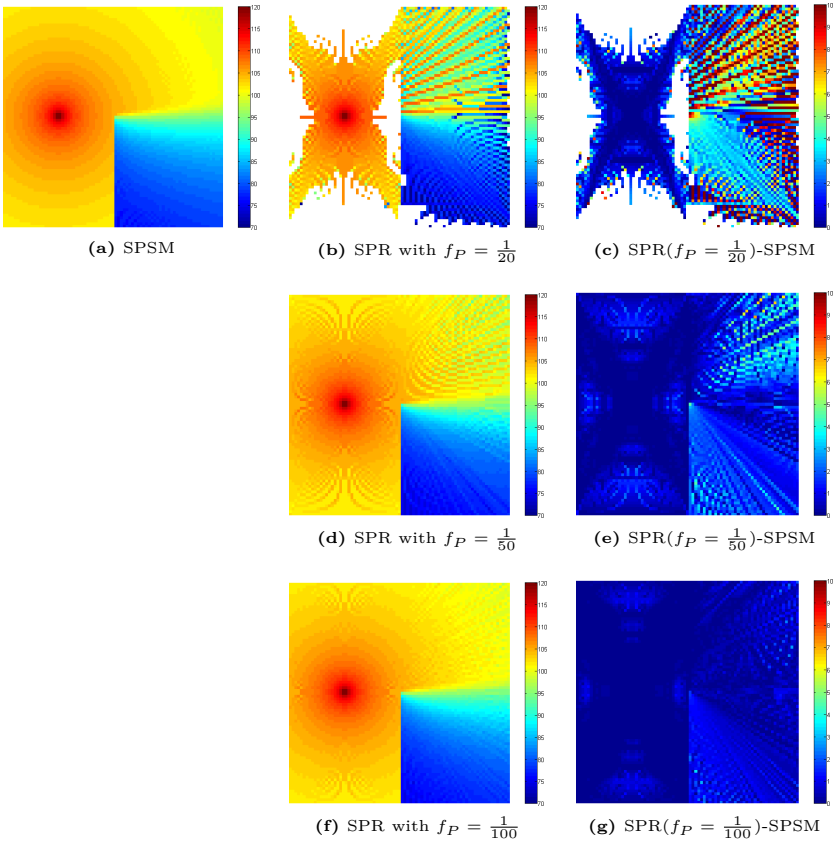

(a) SPSM **(b)** SPR with $f_P = \frac{1}{20}$ **(c)** SPR($f_P = \frac{1}{20}$)-SPSM

(d) SPR with $f_P = \frac{1}{50}$ **(e)** SPR($f_P = \frac{1}{50}$)-SPSM

(f) SPR with $f_P = \frac{1}{100}$ **(g)** SPR($f_P = \frac{1}{100}$)-SPSM

Figure A.92.: The influence of the applied discretization in Sound Particle Radiosity on diffraction simulation compared with the Sound Particle Simulation Method for $f = 1000Hz = 1kHz$.

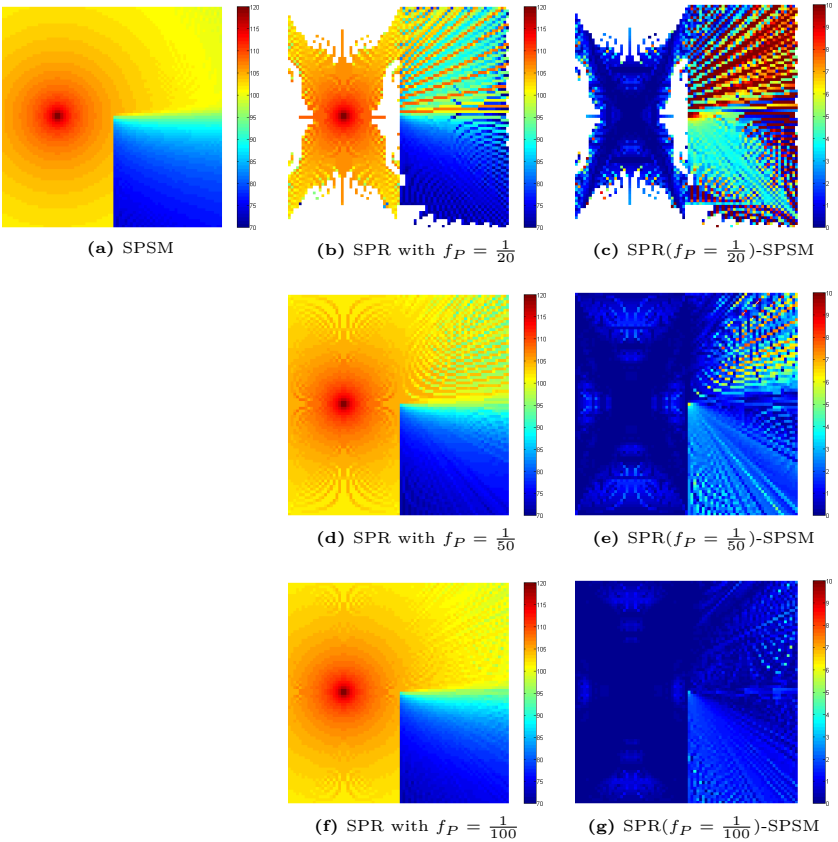

(a) SPSM **(b)** SPR with $f_P = \frac{1}{20}$ **(c)** SPR($f_P = \frac{1}{20}$)-SPSM

(d) SPR with $f_P = \frac{1}{50}$ **(e)** SPR($f_P = \frac{1}{50}$)-SPSM

(f) SPR with $f_P = \frac{1}{100}$ **(g)** SPR($f_P = \frac{1}{100}$)-SPSM

Figure A.93.: The influence of the applied discretization in Sound Particle Radiosity on diffraction simulation compared with the Sound Particle Simulation Method for $f = 2kHz$.

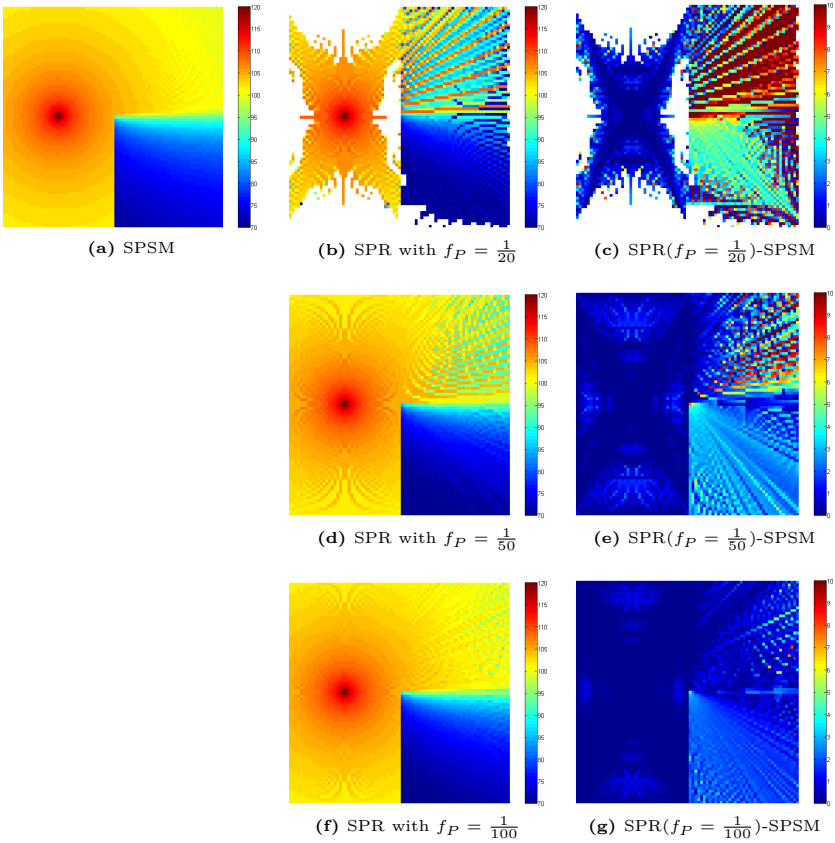

(a) SPSM **(b)** SPR with $f_P = \frac{1}{20}$ **(c)** SPR($f_P = \frac{1}{20}$)-SPSM

(d) SPR with $f_P = \frac{1}{50}$ **(e)** SPR($f_P = \frac{1}{50}$)-SPSM

(f) SPR with $f_P = \frac{1}{100}$ **(g)** SPR($f_P = \frac{1}{100}$)-SPSM

Figure A.94.: The influence of the applied discretization in Sound Particle Radiosity on diffraction simulation compared with the Sound Particle Simulation Method for $f = 4kHz$.

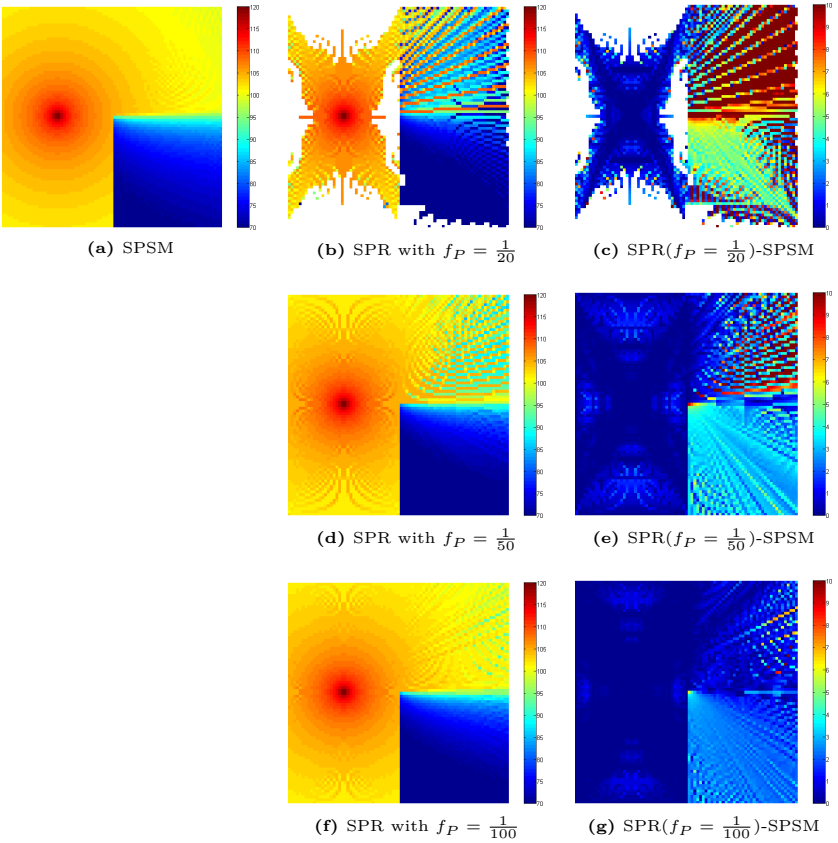

(a) SPSM **(b)** SPR with $f_P = \frac{1}{20}$ **(c)** SPR($f_P = \frac{1}{20}$)-SPSM

(d) SPR with $f_P = \frac{1}{50}$ **(e)** SPR($f_P = \frac{1}{50}$)-SPSM

(f) SPR with $f_P = \frac{1}{100}$ **(g)** SPR($f_P = \frac{1}{100}$)-SPSM

Figure A.95.: The influence of the applied discretization in Sound Particle Radiosity on diffraction simulation compared with the Sound Particle Simulation Method for $f = 8kHz$.

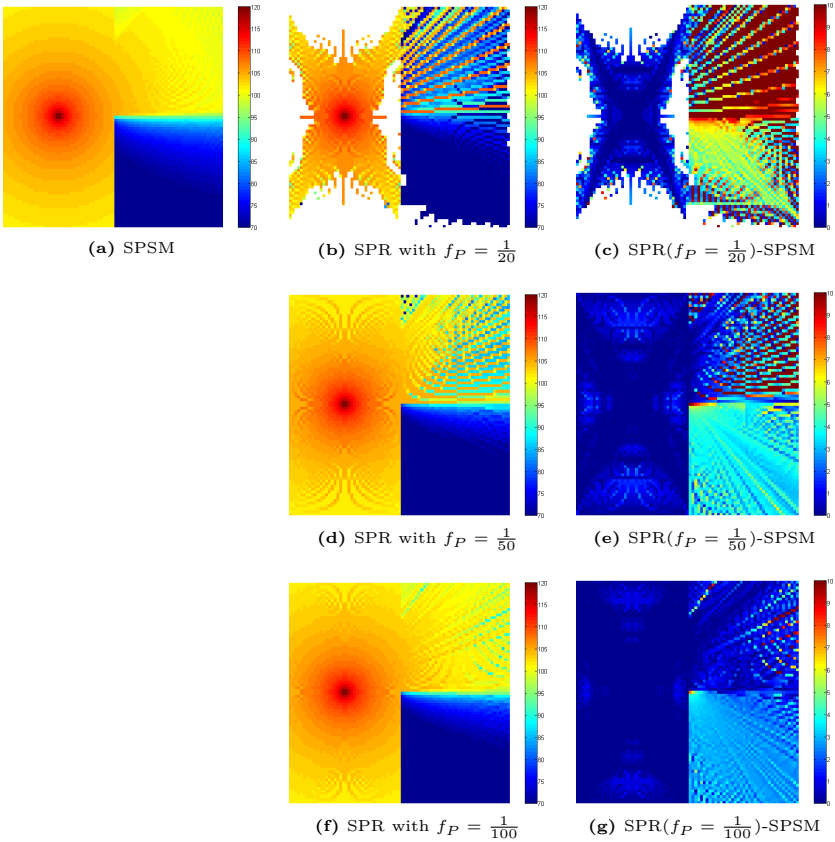

(a) SPSM **(b)** SPR with $f_P = \frac{1}{20}$ **(c)** SPR($f_P = \frac{1}{20}$)-SPSM

(d) SPR with $f_P = \frac{1}{50}$ **(e)** SPR($f_P = \frac{1}{50}$)-SPSM

(f) SPR with $f_P = \frac{1}{100}$ **(g)** SPR($f_P = \frac{1}{100}$)-SPSM

Figure A.96.: The influence of the applied discretization in Sound Particle Radiosity on diffraction simulation compared with the Sound Particle Simulation Method for $f = 16kHz$.

Bibliography

[AB79] J. B. Allen and D. A. Berkley. Image method for efficiently simulating small-room acoustics. *The Journal of the Acoustical Society of America*, 65(4):943–950, 1979.

[Ama84] John Amanatides. Ray tracing with cones. In *Proceedings of the 11th Annual Conference on Computer Graphics and Interactive Techniques*, pages 129–135, New York, NY, USA, 1984.

[AS64] Milton Abramowitz and Irene A. Stegun. *Handbook of Mathematical Functions with Formulas, Graphs, and Mathematical Tables*. Dover, New York, 10th edition edition, 1964.

[Bab37] Jacques Babinet. *Memoires d'optique meteorologique*, volume 4. Comptes rendus hebdomadaires des séances de l'Académie des sciences, 1837.

[Ber75] J. M. Berman. Behaviour of sound in a bounded space. *The Journal of the Acoustical Society of America*, 57(6):1275–1291, 1975.

[BIm02] Bundes-Immissionsschutzgesetz (BImSchG): Gesetz zum Schutz vor schädlichen Umwelteinwirkungen durch Luftverunreinigungen, Geräusche, Erschütterungen und ähnlichen Vorgängen, 2002.

[Bla96] Jens Blauert. *Spatial Hearing - The Psychophysics of Human Sound Localization*. MIT Press, 2nd revised edition, 1996.

[BLs95] Birgitta Berglund, Thomas Lindvall, and Dietrich H schwela. *Guidelines for community noise*. Stockholm University and Karolinska Institute, 1995.

[BoA96] L.L. Beranek and Acoustical Society of America. *Acoustics*. American Institute of Physics for the Acoustical Society of America, 1996.

[Bor84] J. Borish. Extension of the image model to arbitrary polyhedra. *The Journal of the Acoustical Society of America*, 75(6):1827–1836, 1984.

[BS66] Nikolai Panteleimonovich Buslenko and YU. A. Shreider. *The Monte Carlo Method*. Pergamon Press, Oxford, 1966.

[BSU69] J. J. Bowman, T. B. A. Senior, and P. L. E. Uslenghi. *Electromagnetic and Acoustic Scattering by Simple Shapes*. North-Holland Publishing Company, 1969.

[BSZ+95] H. E. Bass, L. C. Sutherland, A. J. Zuckerwar, D. T. Blackstock, and D. M. Hester. Atmospheric absorption of sound: further developments. *The Journal of the Acoustical Society of America*, 97(1):680–683, 1995.

[BT57] M. A. Biot and I. Tolstoy. Formulation of wave propagation in infinite media by normal coordinates with an application to diffraction. volume 29, pages 381–391. ASA, 1957.

[CADa] CadnaA 4.4. `http://www.datakustik.com`.

[CADb] CadnaR 2.2. `http://www.datakustik.com`.

[Cal09] Paul Thomas Calamia. *Advances in Edge-Diffraction Modeling for Virtual Acoustic simulations*. PhD thesis, Princeton University, 2009.

[CAT] CATT-Acoustic v9. `http://www.catt.se`.

[CD09] Trevor J. Cox and Peter D'Antonio. *Acoustic Absorbers and Diffusers*. Taylor & Francis, 2nd edition edition, 2009.

[CDD+06] Trevor J. Cox, Bengt-Inge L. Dalenbäck, Peter D'Antonio, Jean-Jacques Embrechts, Jin Y. Jeon, E. Mommertz, and Michael Vorländer. A tutorial on scattering and diffusion coefficients for room acoustic surfaces. *Acta acustica united with acustica*, 92(1):1–15, 2006.

[CSDS94] Per H. Christensen, Eric J. Stollnitz, Tony D. Derose, and David H. Salesin. Wavelet radiance. In *In Fifth Eurographics Workshop on Rendering*, pages 287–302, 1994.

[Dal95] Bengt-Inge L. Dalenbäck. *A New Model for Room Acoustic Prediction and Auralization*. PhD thesis, Chalmers University of Technology, 1995.

[Dal96] Bengt-Inge L. Dalenbäck. Room acoustic prediction based on a unified treatment of diffuse and specular reflection. *The Journal of the Acoustical Society of America*, 100(2):899–909, 1996.

[Dal02] Bengt-Inge L. Dalenbäck. Software user manual catt-acoustic v8, 2002.

[Dal11] Bengt-Inge Dalenbäck. Scattering distributions in geometrical acoustics. In *Proceedings of EAA Forum Acusticum*, pages 1493–1498, Aalborg, 2011.

[Dam02] Jens J. Dammerud. *Stage Acoustics for Symphony Orchestras in Concert Halls*. PhD thesis, The University of Bath, 2002.

[DIN02] DIN 18005: Schallschutz im Städtebau. Teil 1: Grundlagen und Hinweise für die Planung, 2002.

[DIN03] DIN EN ISO 354: Measurement of sound absorption in a reverberation room, 2003.

[DIN06] DIN 45684: Ermittlung von Fluggeräuschimmissionen an Landeplätzen. Teil 1: Berechnungsverfahren, 2006.

[DKW85] Norm Dadoun, David G. Kirkpatrick, and John P. Walsh. The geometry of beam tracing. In *Proceedings of the First Annual Symposium on Computational Geometry*, pages 55–61, New York, USA, 1985. ACM.

[DL00] I. A. Drumm and Y. W. Lam. The adaptive beam-tracing algorithm. *The Journal of the Acoustical Society of America*, 107:1405–1412, 2000.

[dVV05] Paul de Vos and Margreet Beuving Edwin Verheijen. Harmonised accurate and reliable methods for the eu directive on the assessment and management of environmental noise. Technical report, HARMONOISE, 2005.

[EAS] EASE 4.3. `http://ease.afmg.eu`.

[Emb80] T. F. W. Embleton. Line integral theory of barrier attenuation in the presence of the ground. *The Journal of the Acoustical Society of America*, 67:42–45, 1980.

[END02] DIRECTIVE 2002/49/EC OF THE EUROPEAN PARLIAMENT AND OF THE COUNCIL of 25 June 2002 relating to the assessment and management of environmental noise, 2002.

[Eri04] Christer Ericson. *Real-Time Collision Detection*. Morgan Kaufmann Publishers Inc., San Francisco, CA, USA, 2004.

[Far00] Angelo Farina. Introducing the surface diffusion and edge scattering in a pyramid tracing numerical model for room acoustics. In *Audio Engineering Society Convention 108*, 2000.

[FGH99] Edward R. Freniere, G. Groot Gregory, and Richard A. Hassler. Edge diffraction in monte carlo ray tracing. *Proceedings of SPIE: Optical Design and Analysis Software*, 3780:151–157, 1999.

[FTC+04] Thomas Funkhouser, Nicolas Tsingos, Ingrid Carlbom, Gary Elko, Mohan Sondhi, James E. West, Gopal Pingali, Patrick Min, and Addy Ngan. A beam tracing method for interactive architectural acoustics. *The Journal of the Acoustical Society of America*, 115(2):739–756, 2004.

[Gib72] B. M. Gibbs. A simple image method for calculating the distribution of sound pressure levels within an enclosure. *Acustica*, 26:24–32, 1972.

[Gla89] Andrew S. Glassner, editor. *An Introduction to Ray Tracing*. Academic Press Ltd., London, UK, 1989.

[Gla90] Andrew S. Glassner. *Graphics Gems*. Academic Press, Inc., Orlando, FL, USA, 1990.

[GLM96] S. Gottschalk, M. C. Lin, and D. Manocha. OBBTree: a hierarchical structure for rapid interference detection. In *Proceedings of the 23th Annual Conference on Computer Graphics and Interactive Techniques*, pages 171–180, New Orleans, LA, USA, 1996. ACM.

[Gor75] W.B. Gordon. Far-field approximations to the kirchoff-helmholtz representations of scattered fields. *Antennas and Propagation, IEEE Transactions on*, 23(4):590–592, 1975.

[Got73] Dieter Gottlob. *Verglich objektiver akustischer Parameter mit Ergebnissen subjektiver Untersuchungen an Konzertsälen*. PhD thesis, Georg-August-Universität Göttingen, 1973.

[Gre01] Walter Greiner. *Quantum Mechanics: An Introduction*. Springer, 4th edition edition, 2001.

[GTGB84] Cindy M. Goral, Kenneth E. Torrance, Donald P. Greenberg, and Bennett Battaile. Modeling the interaction of light between diffuse surfaces. In *Proceedings of the 11th Annual Conference on Computer Graphics and Interactive Techniques*, pages 213–222, New York, NY, USA, 1984. ACM.

[HC71] R. P. Heinisch and T. S. Chou. Numerical experiments in modeling diffraction phenomena. *Applied Optics*, 10(10):2248–2251, 1971.

[HC99] Ching-Jer Huang and Chao-Yi Chen. Diffracted acoustic fields about circular apertures in soft and hard baffles. *Acta Acustica united with Acustica*, 85:301–311, 1999.

[Hec01] Eugene Hecht. *Optics*. Addison Wesley, 4th edition edition, 2001.

[Hei27] Werner Heisenberg. Über den anschaulichen Inhalt der quantentheoretischen Kinematik und Mechanik. *Zeitschrift für Physik*, 43(3–4):172–198, 1927.

[HH84] Paul S. Heckbert and Pat Hanrahan. Beam tracing polygonal objects. In *Proceedings of the 11th Annual Conference on Computer Graphics and Interactive Techniques*, pages 119–127, New York, NY, USA, 1984. ACM.

[HLM90] C. Huygens, E. Lommel, and R. Mewes. *Traité de la lumière (1690)*. Ostwalds Klassiker der exakten Wissenschaften. W. Engelmann, 1890.

[Hub96] Philip M. Hubbard. Approximating polyhedra with spheres for time-critical collision detection. *ACM Transactions on Graphics*, 15:179–210, 1996.

[IMM] IMMI 2013. `http://www.woelfel.de`.

[ISO96] ISO 9613: Attenuation of sound during propagation outdoors. Part 2: General method of calculation, 1996.

[ISO04] ISO 17497: Sound-scattering properties of surfaces. Part 1: Measurement of random-incidence scattering coefficient in a reverberation room, 2004.

[JIR08] Cheol-Ho Jeong, Jeong-Guon Ih, and Jens Holger Rindel. An approximate treatment of reflection coefficient in the phased beam tracing method for the simulation of enclosed sound fields at medium frequencies. *Applied Acoustics*, 69(7):601–613, 2008.

[JM82] Gary M. Jebsen and Herman Medwin. On the failure of the kirchhoff assumption in backscatter. *The Journal of the Acoustical Society of America*, 72:1607–1611, 1982.

[KBA01] N. Korany, J. Blauert, and O. Abdel Alim. Acoustic simulation of rooms with boundaries of partially specular reflectivity. *Applied Acoustics*, 62(7):875 – 887, 2001.

[Kel54] Joseph B. Keller. Geometrical acoustics. I. the theory of weak shock waves. *Journal of Applied Physics*, 25(8):938–947, 1954.

[Kel62] Joseph B. Keller. Geometrical theory of diffraction. *The Journal of the Optical Society of America*, 52(2):116–130, 1962.

[KHM+98] James T. Klosowski, Martin Held, Joseph S. B. Mitchell, Henry Sowizral, and Karel Zikan. Efficient collision detection using bounding volume hierarchies of k-DOPs. *IEEE Transactions on Visualization and Computer Graphics*, 4:21–36, 1998.

[KKF93] U.R. Kristiansen, A. Krokstad, and T. Follestad. Extending the image method to higher-order reflections. *Applied Acoustics*, 38(2–4):195–206, 1993.

[Kos60] C. W. Kosten. The mean free path in room acoustics. *Acustica*, 10:245–250, 1960.

[KP74] R. G. Kouyoumjian and P. H. Pathak. A uniform geometrical theory of diffraction for an edge in a perfectly conducting surface. *Proceedings of the IEEE*, 62(11):1448–1461, 1974.

[KSS68] A. Krokstad, S. Strom, and S. Sørsdal. Calculating the acoustical room response by the use of a ray tracing technique. *Journal of Sound and Vibration*, 8(1):118 – 125, 1968.

[Kur74] Ulrich J. Kurze. Noise reduction by barriers. *The Journal of the Acoustical Society of America*, 55(3):504–518, 1974.

[Kut71] Heinrich Kuttruff. Simulierte Nachhallkurven in Rechteckräumen mit diffusem Schallfeld. *Acustica*, 25:333–342, 1971.

[Kut95] H. Kuttruff. A simple iteration scheme for the computation of decay constants in enclosures with diffusely reflecting boundaries. *The Journal of the Acoustical Society of America*, 98(1):288–293, 1995.

[Kut07] Heinrich Kuttruff. *Acoustics: An Introduction*. Taylor & Franscis, 2007.

[Kut09] Heinrich Kuttruff. *Room acoustics*. Taylor & Franscis, 5th edition edition, 2009.

[LA92] J.H. Lambert and E. Anding. *Photometrie: Photometria, sive De mensura et gradibus luminis, colorum et umbrae (1760)*. Ostwald's Klassiker der exakten Wissenschaften. W. Engelmann, 1892.

[Leo07a] Paul Leopardi. *Distributing points on the sphere: Partitions, separation, quadrature and energy*. PhD thesis, The University of New South Wales, 2007.

[Leo07b] Recursive Zonal Equal Area Sphere Partitioning Toolbox by Paul Leopardi. `http://eqsp.sourceforge.net/`, 2007.

[Lew93] T. Lewers. A combined beam tracing and radiatn exchange computer model of room acoustics. *Applied Acoustics*, 38(2–4):161–178, 1993.

[LIM] Predictor-LimA Software Suite Type 7810. `http://www.bksv.com`.

[LS09] Keunhwa Lee and Woojae Seong. Time-domain kirchhoff model for acoustic scattering from an impedance polygon facet. *JASA Express Letters*, 6 2009.

[LSLS09] Samuli Laine, Samuel Siltanen, Tapio Lokki, and Lauri Savioja. Accelerated beam tracing algorithm. *Applied Acoustics*, 70(1):172–181, 2009.

[Mac15] H. M. MacDonald. A class of diffraction problems. In *Proceedings of London Mathematical Society*, London, Great Britain, 1915.

[Mae68] Z. Maekawa. Noise reduction by screens. *Applied Acoustics*, 1(3):157–173, 1968.

[Mar72] G. Marsaglia. Choosing a point from the surface of a sphere. *The Annals of Mathematical Statistics*, 43(2):645–646, 1972.

[McA54] William Henry McAdams. *Heat Transmission*. McGraw-Hill, New York, 3rd edition, 1954.

[Mec08] Fridolin P. Mechel. *Raumakustische Felder*. Hirtzel, 2008.

[Med81] Herman Medwin. Shadowing by finite noise barriers. *The Journal of the Acoustical Society of America*, 69:1060–1064, 1981.

[Mey09] J. Meyer. *Acoustics and the Performance of Music*. Springer, 5th edition edition, 2009.

[Mil84] R. N. Miles. Sound field in a rectangular enclosure with diffusely reflecting boundaries. *Journal of Sound and Vibration*, 92:223–226, 1984.

[Min50] David Mintzer. Transient sounds in rooms. *The Journal of the Acoustical Society of America*, 22(3):341–352, 1950.

[MMOD96] Michael Monks, Byong Mok Oh, and Julie Dorsey. Acoustic simulatin and visualization using a new unified beam tracing and image source approach. In *Audio Engineering Society Convention 101*, 11 1996.

[Mös08] M. Möser. *Technische Akustik*. Springer, 8th edition edition, 2008.

[NHA04] Eva-Marie Nosal, Murray Hodgson, and Ian Ashdown. Improved algorithms and methods for room sound-field prediction by acoustical radiosity in arbitrary polyhedral rooms. *The Journal of the Acoustical Society of America*, 116(2):970–980, 2004.

[ODE] ODEON Room Acoustics Modelling Software. `http://www.odeon.dk`.

[OL07] Jens-Rainer Ohm and Hans Dieter Lüke. *Signalübertragung: Grundlagen der digitalen und analogen Nachrichtenübertragungssysteme*. Springer, 11th edition edition, 2007.

[Pie74] Allan D. Pierce. Diffraction of sound around corners and over wide barriers. *The Journal of the Acoustical Society of America*, 55(5):941–955, 1974.

[Pie89] Allan D. Pierce. *Acoustics: An Introduction to Its Physical Principles and Applications*. Acoustical Society of America, 1989.

[PS10a] Alexander Pohl and Uwe M. Stephenson. A combination of the sound particle simulation and the radiosity method. In *Proceedings of the International Symposium on Room Acoustics (ISRA)*, Melbourne, Australia, 2010.

[PS10b] Alexander Pohl and Uwe M. Stephenson. Efficient simulation of sound propagation including multiple diffractions in urban geometries by convex sub-division. In *Proceedings of Internoise*, Lisbon, Portugal, 2010.

[PS10c] Alexander Pohl and Uwe M. Stephenson. From ray to beam tracing and diffraction - an analytical prognosis formula for the trade-off between accuracy and computation time. In *Proceedings of DAGA*, Berlin, Germany, 2010.

[PS10d] Alexander Pohl and Uwe M. Stephenson. Room division into convex subspaces and its benefits to calculation time and diffraction simulation with ray tracing. In *Proceedings of DAGA*, Berlin, Germany, 2010.

[PS11a] Alexander Pohl and Dirk Schröder. Comparison of edge diffraction simulation methods with measurements from a scaled noise barrier model. In *Proceedings of DAGA*, Düsseldorf, Germany, 2011.

[PS11b] Alexander Pohl and Uwe M. Stephenson. A combination of the sound particle simulation method and the radiosity method. *The Journal of Building Acoustics*, 18(1):97–122, 2011.

[PS11c] Alexander Pohl and Uwe M. Stephenson. Introduction of diffraction into geometrical acoustics: comparison of different sound energy reunification techniques. In *Proceedings of EAA Forum Acusticum*, Aalborg, Denmark, 2011.

[PS12] Alexander Pohl and Uwe M. Stephenson. Combining ray tracing with higher order diffraction based on the uncertainty relation. In *Proceedings of DAGA*, Darmstadt, Germany, 2012.

[PSS+12] Alexander Pohl, S.Drechsler, U. Peter Svensson, Michael Vorländer, and Uwe M. Stephenson. openMat - an open xml-database for acoustical properties of materials and objects. In *Proceedings of Internoise 2012*, New York, NY, USA, 2012.

[PVM10] Sönke Pelzer, Michael Vorländer, and Hans-Joachim Maempel. Room modeling for acoustic simulation and auralization tasks: resolution of structural detail. In *Proceedings of DAGA*, Berlin, Germany, 2010.

[PWS13] Alexander Pohl, Jan Winkelmann, and Uwe M. Stephenson. Parallel sound particle radiosity: reunification of diffracted and scattered sound particles on parallel computers. In *Proceedings of DAGA*, Meran, Italy, 2013.

[RAV] RAVEN - A framework for dynamic real-time auralization of virtual environments. `http://www.ravenaudio.de/`.

[Red40] S.W. Redfearn. Some acoustic source-observer problems. *Phil. Mag.*, 30(4), 1940.

[RJBJ13] Jana Rückert-John, Inka Bormann, and Rene John. *Umweltbewusstsein in Deutschland 2012 – Ergebnisse einer repräsentativen Bevölkerungsumfrage*. Bundesministerium für Umwelt, Naturschutz und Reaktorsicherheit (BMU), 2013.

[RLBPL04] Emeline Reboul, A. Le Bot, and J. Perret-Liaudet. Introduction of acoustical diffraction in the radiative transfer method. *Comptes rendus mécanique*, 332(7):505–511, 2004.

[RLS90] RLS-90: Richtlinien für den Lärmschutz an Strassen, 1990.

[Sch03] Schall03: Richtlinie zur Berechnung der Schallimmissionen von Schienenwegen, 2003.

[Sch11] Dirk Schröder. *Physically based real-time auralization of interactive virtual environments*. PhD thesis, RWTH Aachen, 2011.

[SFV99] U. P. Svensson, R. I. Fred, and J. Vanderkooy. An analytic secondary source model of edge diffraction impulse responses. *The Journal of the Acoustical Society of America*, 106:2331–2344, 1999.

[She96] Jonathan Richard Shewchuk. Robust Adaptive Floating-Point Geometric Predicates. In *Proceedings of the Twelfth Annual Symposium on Computational Geometry*, pages 141–150. Association for Computing Machinery, 1996.

[She05] Triangle: A Two-Dimensional Quality Mesh Generator and Delaunay Triangulator by Jonathan Richard Shewchuk. `http://www.cs.cmu.edu/~quake/triangle.html`, 2005.

[Si08] Hang Si. *Three Dimensional Boundary Conforming Delaunay Mesh Generation*. PhD thesis, Technische Universität Berlin, 2008.

[Si11] TetGen Toolbox by Hang Si. `http://wias-berlin.de/software/tetgen/`, 2011.

[SL08] Samuel Siltanen and Tapio Lokki. Diffraction modeling in acoustic radiance transfer method. In *Joint ASA/EAA Meeting, Acoustics 2008*, pages 5625–5630, Paris, France, 2008.

[SLKS07] Samuel Siltanen, Tapio Lokki, Sami Kiminki, and Lauri Savioja. The room acoustic rendering equation. *The Journal of the Acoustical Society of America*, 122(3):1624—1645, 2007.

[SLS09] Samuel Siltanen, Tapio Lokki, and Lauri Savioja. Frequency domain acoustic radiance transfer for real-time auralization. *Acta Acustica united with Acustica*, 95(1):106–117, 2009.

[SLS10] Samuel Siltanen, Tapio Lokki, and Lauri Savioja. Room acoustics modeling with acoustic radiance transfer. In *Proceedings of International Symposium on Room Acoustics*, Melbourne, Australia, 2010.

[SLSC08] Samuel Siltanen, Tapio Lokki, Lauri Savioja, and Claus Lynge Christensen. Geometry reduction in room acoustics modeling. *Acta Acustica united with Acustica*, 94(3):410–418, 2008.

[SN81] Y. Sakurai and K. Nagata. Sound reflections of a rigid plane panel and of the "live-end" composed by those panels. *The Journal of the Acoustical Society of Japan*, 2:5–14, 1981.

[SN04] A. Sommerfeld and R.J. Nagem. *Mathematical Theory of Diffraction*. Birkhäuser, 2004.

[Sou] SoundPLAN 7.3. `http://www.soundplan.eu`.

[SP09] Dirk Schröder and Alexander Pohl. Real-time hybrid simulation method including edge diffraction. In *Proceedings of EAA Symposium on Auralization*, Espoo, Finland, 2009.

[SP11] Uwe M. Stephenson and Alexander Pohl. Introduction of diffraction into ray tracing based on the uncertainty relation - some new results concerning reciprocity. In *Proceedings of EAA Forum Acusticum*, Aalborg, Denmark, 2011.

[SP13] Dirk Schröder and Alexander Pohl. Modeling (non-)uniform scattering distributions in geometrical acoustics. In *Proceedings of International Congress on Acoustics*, Montreal, Canada, 2013.

[SPD+13] Dirk Schröder, Alexander Pohl, Stefan Drechsler, Peter Svensson, Michael Vorländer, and Uwe M. Stephenson. openMat - management of acoustic material (meta-)properties using an open source database format. In *Proceedings of DAGA*, Meran, Italy, 2013.

[SPS+12] Dirk Schröder, Alexander Pohl, Peter Svensson, Uwe M. Stephenson, and Michael Vorländer. On the accuracy of edge diffraction simulation methods in geometrical acoustics. In *Proceedings of Internoise 2012*, New York, NY, USA, 2012.

[SS07] Uwe M. Stephenson and U. Peter Svensson. An improved energetic approach to diffraction based on the uncertainty principle. In *Proceedings of International Congress on Acoustics*, Madrid, Spain, 2007.

[Ste85] Uwe M. Stephenson. Eine Schallteilchen-Computer-Simulation zur Berechnung der für die Hörsamkeit in Konzertsälen maßgebenden Parameter. *Acustica*, 59:1–20, 1985.

[Ste86] Uwe M. Stephenson. Wie werden Schallteilchen gebeugt? In *Proceedings of DAGA*, Oldenburg, Germany, 1986.

[Ste90] Uwe M. Stephenson. Comparison of the mirror image source method and the sound particle simulation method. *Applied Acoustics*, 29(1):35–72, 1990.

[Ste96] Uwe M. Stephenson. Quantized pyramidal beam tracing - a new algorithm for room acoustics and noise immission prognosis. *Acta Acustica united with Acustica*, 82:517–525, 1996.

[Ste01] Uwe M. Stephenson. Simulation von Streuung und Beugung ohne Rechenzeitexplosion? Lösung durch Kombination der Schallteilchen- mit der Radiosity-Methode. In *Proceedings of DAGA*, Hamburg, Germany, 2001.

[Ste03a] Uwe M. Stephenson. *Beugungssimulation ohne Rechenzeitexplosion: die Methode der quantisierten Pyramidenstrahlen (Urfassung)*. PhD thesis, RWTH Aachen, 2003.

[Ste03b] Uwe M. Stephenson. Quantisierte Pyramidenstrahlen oder Schallteilchen-Radiosity-Methode? Lösung der Probleme der Quantisierung und der Quasi-Simultanverfolgung. In *Proceedings of DAGA*, Aachen, Germany, 2003.

[Ste04] Uwe M. Stephenson. *Beugungssimulation ohne Rechenzeitexplosion: die Methode der quantisierten Pyramidenstrahlen.* PhD thesis, RWTH Aachen, 2004.

[Ste06] Uwe M. Stephenson. Analytical derivation of a formula for the reduction of computationtime by the voxelcrossingtechnique used in room acoustical simulation. *Applied Acoustics*, 67(10):959–981, 2006.

[Ste08] Uwe M. Stephenson. Can also diffracted sound be handled as flow of particles? - some new results of a beam tracing approach based on the uncertainty principle. In *Proceedings of Acoustics '08*, Paris, France, 2008.

[Ste09] Uwe M. Stephenson. Introducing diffraction into beam tracing - some new results. In *Proceedings of NAG/DAGA*, Rotterdam, Netherlands, 2009.

[Ste10a] Uwe M. Stephenson. An energetic approach for the simulation of diffraction within ray tracing based on the uncertainty relation. *Acta Acustica united with Acustica*, 96:516–535, 2010.

[Ste10b] Uwe M. Stephenson. Some further experiments with the beam diffraction model based on the uncertainty relation - is it valid also with double diffraction? In *Proceedings of DAGA*, Berlin, Germany, 2010.

[Ste11] Uwe M. Stephenson. Introducing higher order diffraction into beam tracing based on the uncertainty relation. *The Journal of Building Acoustics*, 18(1):59–82, 2011.

[Ste14] Uwe M. Stephenson. Particle, ray and beam detection in room acoustical ray tracing methods - their difference and though physical equivalence (not published yet). *Acta Acustica united with Acustica*, ?:?, 2014.

[Sve10] Edge Diffraction Matlab Toolbox by U. Peter Svensson. `http://www.iet.ntnu.no/~svensson/software/index.html`, 2010.

[TFAC00] Nicolas Tsingos, Thomas A. Funkhouser, N. Addy, and Ingrid Carlbom. Geometrical theory of diffraction for modeling acoustics in virtual environments, 2000.

[TFNC01] Nicolas Tsingos, Thomas Funkhouser, Addy Ngan, and Ingrid Carlbom. Modeling acoustics in virtual environments using the uniform theory of diffraction. In *Proceedings of the 28th annual conference on Computer graphics and interactive techniques*, pages 545–552, New York, NY, USA, 2001. ACM.

[THM+03] M. Teschner, B. Heidelberger, M. Müller, D. Pomeranets, M. Gross, and H. Hubinsky. Optimized Spatial Hashing for Collision Detection of Deformable Objects. In *Proceedings of the Vision, Modeling, and Visualization Conference*, pages 47–54, Munich, Germany, 2003. Aka GmbH.

[Tho88] Eric I. Thorsos. The validity of the kirchhoff approximation for rough surface scattering using a gaussian roughness spectrum. *The Journal of the Acoustical Society of America*, 83(1):78–92, 1988.

[Ufi89] P. Y. Ufimtsev. Theory of acoustical edge waves. *The Journal of the Acoustical Society of America*, 86:463–474, 1989.

[vdB98] Gino van den Bergen. Efficient collision detection of complex deformable models using AABB trees. *Journal of Graphics Tools*, 2(4):1–13, 1998.

[VDI88] VDI 2714: Schallausbreitung im Freien, 1988.

[VDI97] VDI 2720 Blatt 1: Schallschutz durch Abschirmung im Freien, 1997.

[VEdG+04] Michael Vorländer, Jean Jaques Embrechts, Lieven de Geetere, Gerrit Vermeir, and Márcio Henrique de Avelar Gomes. Case studies in measurement of random incidence scattering coefficients. *Acta acustica united with Acustica*, 90(5):858–867, 2004.

[VM00] Michael Vorländer and Eckhard Mommertz. Definition and measurement of random-incidence scattering coefficients. *Applied Acoustics*, 60(2):187 – 199, 2000.

[Vor88] Michael Vorländer. Die Genauigkeit von Berechnungen mit dem raumakustischen Schallteilchenmodell und ihre Abhängigkeit von der Rechenzeit. *Acustica*, 66:90–96, 1988.

[Vor89] Michael Vorländer. Simulation of transient and steady-state sound propagation in rooms using a new combined ray-tracing/image-source algorithm. *The Journal of the Acoustical Society of America*, 86(7):172–178, 1989.

[Vor08] Michael Vorländer. *Auralization: fundamentals of acoustics, modelling, simulation, algorithms and acoustic virtual reality*. RWTHedition. Springer, 2008.

[VvM86] Jean-Paul Vian and Dirk van Maerke. Calculation of the room response using a ray tracing method. In *Proceedings of ICA Symposium on Acoustics and Theater Planning for the Performing Arts*, Vancouver, Canada, 1986.

[WD81] John P. Walsh and Norman Dadoun. The Design and Development of Godot: A System for Computer-Aided Room Acoustics Modelling and Simulation. *The Journal of the Acoustical Society of America*, 69:S36, 1981.

[Win12] Jan Winkelmann. A data partitioning algorithm for sound particle radiosity, 2012.

In both room and city acoustics, the simulation of sound propagation is still challenging. The handling of diffraction is still topic of current research, especially the diffraction of higher orders. Due to the large scale of the environment compared to the typical wavelengths of sound, Geometrical Acoustic (GA) simulation methods are used rather than exact wave theoretical simulation methods. These GA methods handle sound as particles instead of waves (wave-particle dualism as known from optics). Based on this restriction, wave effects such as diffraction have to be modelled explicitly.

In this work, a diffraction formulation called Uncertainty relation Based Diffraction (UBD) by Stephenson is investigated and extended. The UBD is based on Heisenberg's uncertainty relation and the Fraunhofer diffraction theory. The great advantage of this formulation is that the straight forward propagation technique of particles can be used and integrated as a module in the simulation. However, it will be shown that some assumptions of former publications are not well founded, such that alternative formulations are presented. Good agreements with the wave theoretical reference methods are shown in almost all cases. In addition to former publications, the UBD method is extended to 3D.

Unfortunately, the usage of the UBD diffraction module causes a split-up of particles, such that the computation time increases exponentially. To overcome this split-up, the reunification of particles is aspired. Quantized Pyramidal Beam Tracing (QPBT) and the Sound Particle Radiosity (SPR) aim at this reunification. It will be shown that SPR is both more efficient and more accurate than QPBT. However, the memory effort of the SPR yields a major bottleneck. First optimizations to decrease the memory effort will be presented to overcome this issue.

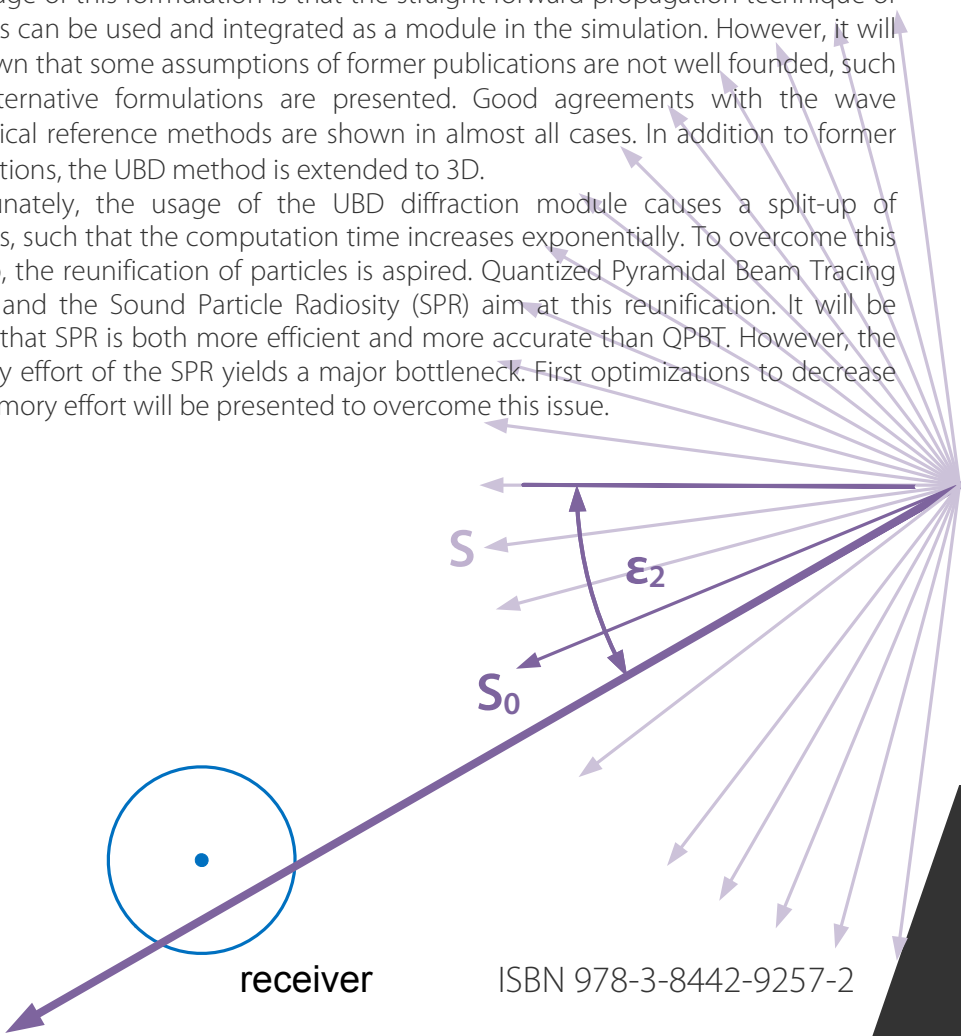

ISBN 978-3-8442-9257-2